Application de la théorie des similitudes en turbulence à l'interface océan atmosphère

Benoît Pinier

THÈSE DE DOCTORAT DE

L'UNIVERSITE DE RENNES 1
COMUE **U**NIVERSITE **B**RETAGNE **L**OIRE

Ecole Doctorale N°601
Mathématique et Sciences et Technologies de l'Information et de la Communication
Spécialité : *Mathématiques et leurs Interactions*

Par

« Benoît PINIER »

« Application de la théorie des similitudes en turbulences à l'interface océan atmosphère. »

Thèse présentée et soutenue à RENNES , le 12/02/2019
Unité de recherche : IRMAR UMR CNRS 6625, INRIA

Rapporteurs avant soutenance :

Didier BRESCH - Directeur de recherche - Université de Haute Savoie
Eric BLAYO - Professeur des universités - Université Grenoble Alpes

Composition du jury :

Examinateurs : Didier BRESCH - Directeur de recherche - Université de Haute Savoie
Eric BLAYO - Professeur des universités - Université Grenoble Alpes
Jocelyne ERHEL - Directrice de recherche - INRIA Rennes
Frédéric HECHT - Professeur des universités - Université Paris VI
Bruno DESPRES - Professeur des universités - Université Paris VI

Dir. de thèse : Roger LEWANDOWSKI, Professeur des universités, Université de Rennes 1

Co-dir. de thèse : Étienne MEMIN, Directeur de recherche, INRIA Rennes

REMERCIEMENTS

En ouverture à ce manuscrit, je tiens à remercier celles et ceux qui m'ont permis d'arriver à l'écriture de celui-ci. En premier lieu ; mes directeurs de thèse Roger Lewandowski et Etienne Mémin pour avoir présenté ce sujet, leur patience et exigence dans ce travail. Je pense également à Valentin Resseguier et Sylvain Laizet pour les collaborations scientifiques. Un remerciement pour les rapporteurs Didier Bresch et Eric Blayo pour leur lecture du manuscrit et leurs bienveillance. Un grand remerciement aussi au membre du jury pour avoir accepté de passer du temps sur l'étude de ce texte. Je pense remercie également celles qui m'ont souvent apporté un soutien administratif Huguette Béchu, Marie-Aude Verger, Chantal Halet.

Je tiens à remercier ma famille qui m'a permis d'étudier dans un confort optimal, ainsi qu'un fort soutien durant cette expérience. Á Morgane pour m'avoir supporté pendant cette thèse. Charly s'il ne m'avait pas montré le développement informatique en fin de licence 1, je n'aurais pas pris cette voie. Je remercie aussi pour leur présence quelques inclassables Pierrick, Morgane, Alice, Alban, Gaëlle, Elodie, David, Chloë, Stéphane, Thibault.

Je fais un clin d'œil à celles et ceux avec qui j'ai partagé cette experience que ce soit à l'IRMAR ou à INRIA ; la liste sera un peu longue et non-exhaustive Hélene, Blandine, Ophélie, Julie, Arnaud, Tristan, Gwenezheg, Nestor, Alexandre, Damien, Charles, Anca, Pranav (mention spéciale pour m'avoir les 3 ans dans co-bureau), Valentin, Manu, Vincent, Sandeep, Long, Yacine, Thibault, Pierre. A ma nouvelle équipe de recherche à l'OSUR, la délicieuse Fractory : Philippe, Caroline, Romain, Etienne, Diane, Justine.

Je pense aussi à mon équipe de tennis de table pendant cette periode Jeremy, Renaud, Antoine, Bertrand. Mes nombreux partenaires de scènes à l'ASCREB : Simon, Mélisande, Arthur, Pablo, Yann, Gwendoline, Malo, Marina, Amélie, Jérôme, Lauragondin, Elise, Rémi, Kevin, Maxou, Paola, Thomas, Etienne, Melaine, Louna, Teddy et les autres..

Enfin, je conclurai ces remerciements en pensant à mes anciens professeurs de mathématiques et directeurs de stages Dominique Heitz et Pascal Rosenblatt.

TABLE OF CONTENTS

Introduction **1**

1 The Kolmogorov Law of turbulence. What can rigorously be proved ? **9**
1.1 Introduction 10
1.2 About the 3D Navier Stokes equations 12
1.3 Mean Navier-Stokes Equations 15
1.4 Law of the $-5/3$ 17
1.5 Numerical experiments 22

2 Généralités sur la turbulence **31**
2.1 Modélisations mathématiques de la turbulence 31
2.2 Modélisation "Under location Uncertainty" 35
2.3 Couche limite turbulente 40
2.4 Résolutions numériques des équations de Navier Stokes 48
2.5 Fonction à la paroi (wall-functions) 63

3 A NS-TKE model with wall law and physical mixing length **67**
3.1 Introduction 69
3.2 Boundary condition modeling 73
3.3 Direct Numerical Simulations 77
3.4 NSTKE simulations and conclusions 89
3.5 Theoretical analysis of the NSTKE model 95

4 A model under location uncertainty for the mean velocity in wall bounded flows **109**
4.1 introduction 111
4.2 Boundary layer and wall laws 113
4.3 Numerical validation 119

Conclusion **131**

Appendices **133**

A Determination of the numerical viscosity and diffusivity inherent to the discretization for the advection term in Openfoam **134**

A.1 Numerical framework 134

A.2 Expression of the numerical viscosity 137

A.3 Verification of the expression 139

Bibliography **162**

INTRODUCTION

Dans ce mémoire, nous allons vous présenter un ensemble de modélisations de la turbulence mathématiquement justifiées. Le cadre d'étude sera principalement la couche limite turbulente.

Contexte

L'étude de l'évolution de fluides en régime turbulent est un enjeu essentiel dans notre époque. Tout d'abord, les systèmes climatiques correspondent à des écoulements turbulents, que ce soit l'océan ou l'atmosphère. Chaque échelle de turbulence est importante, au niveau régional, des phénomènes locaux exceptionnels sont susceptibles d'avoir des conséquences notables (épisodes cévenols, tempêtes pouvant provoquer des raz de marée, inondations etc). De plus, sur l'océan, une bonne prévision est essentielle notamment pour assurer la sécurité en mer. Au niveau planétaire, l'étude de la turbulence permet de comprendre l'évolution du système climatique et d'anticiper au mieux les modifications anthropologiques. Une vue d'ensemble des échelles en espace et en temps de différents phénomènes est présentée sur la figure 1.

La turbulence est un phénomène chaotique dépendant de chaque échelle. Calculer un écoulement turbulent revient donc à saisir l'ensemble des tourbillons jusqu'à la plus petite taille possible (dite échelle de Kolmogorov) où ces derniers sont dissipés par la friction moléculaire. Á haut nombre de Reynolds, le calcul de ces tourbillons est un problème toujours complexe. Pour simuler correctement un écoulement atmosphérique dans un domaine d'une superficie de $100km^2$, il est nécessaire d'utiliser un maillage comprenant $O(10^{18})$ nœuds. Cela est irréaliste pour la puissance de calcul disponible. Á l'heure actuelle, le système atmosphérique est calculé à diverses échelles, au niveau mondial, le modèle WRF (Weather Research and Forecasting) utilisé par la NOAA aux Etats-Unis admet des mailles de calcul allant de 15 à 2km de large à l'horizontale [Skamarock et al., 2005]. Chez Météo-France, le modèle ARPEGE (Action de Recherche Petite Echelle Grande Echelle) est utilisé pour les simulations au niveau

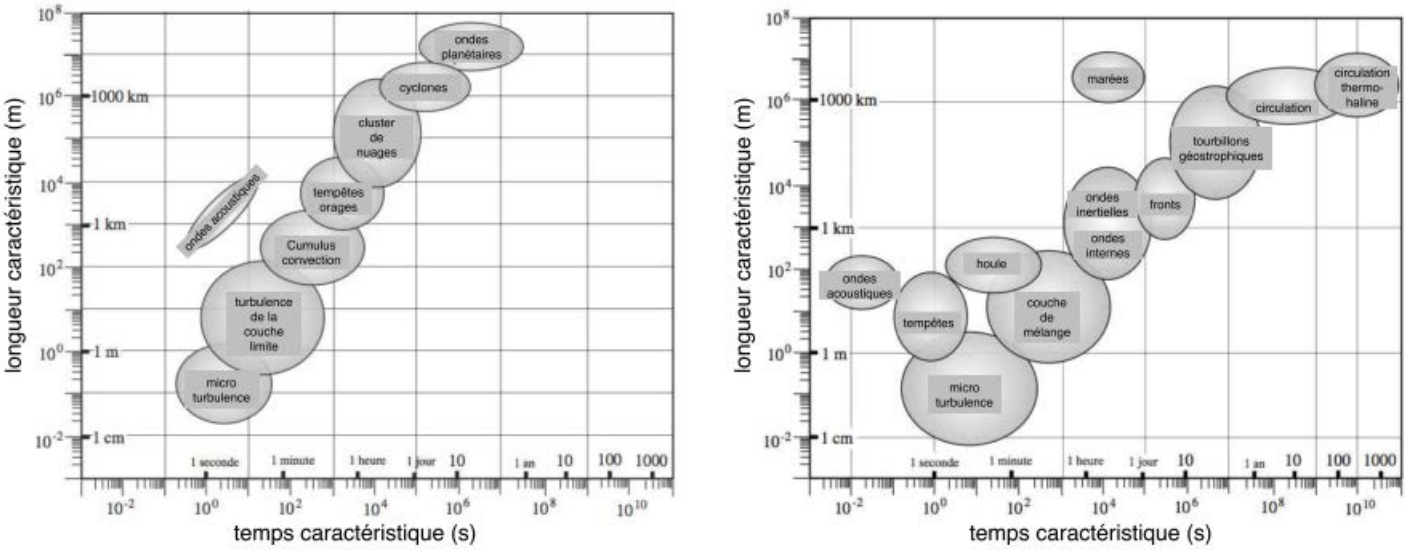

FIGURE 1 – Temps et longueurs caractéristiques de la turbulence dans l'océan (gauche) et dans l'atmosphère (droite). (source : [Lemarie, 2008] [Von Storch et al., 2013])

mondial avec un maillage de résolution 7.5 km en moyenne en Europe. Pour calculer des solutions plus fines, le modèle AROME (Application of Research to Operations at MEsoscale) est utilisé au niveau national avec une maille de taille 1.3 km en moyenne.

Pour montrer l'évolution et la quantité d'articles traitant de la turbulence, nous avons résumé dans le tableau 1 le nombre d'articles disponibles sur la plateforme Google Scholar qui incluent le mot clef "Turbulence".

Malgré le nombre d'études publiées, de nombreux problèmes sont soulevés pour déterminer les profils de vitesse et des autres variables inhérentes aux équations de turbulence dans la couche limite. De plus, afin qu'une loi soit valide, il est nécessaire qu'elle soit universelle, autrement dit qu'elle soit valide pour n'importe quel nombre de Reynolds. Concernant les écoulements stratifiés, ces profils sont aussi dépendant des nombre de Prandtl (de Rossby dans une couche d'Ekman), il s'agit des modélisation à la Monin-Obukhov.

De surcroît, les systèmes d'équations inhérents à la turbulence sont complexes. Les

Début	Fin	Nombre d'articles sur la période
1910	1920	1230
1920	1930	1590
1930	1940	3380
1940	1950	5330
1950	1960	14100
1960	1970	27300
1970	1980	70100
1980	1990	195000
1990	2000	608000
2000	2005	528000
2005	2010	664000
2010	2014	479000

TABLE 1 – Nombre d'article paru contenant le mot "Turbulence" - référence Google Scholar

équations de Navier Stokes sont de type advection - diffusion non linéaires, couplées à une ou plusieurs variables (pression, énergie cinétique turbulente, dissipation, température, salinité ...). Il est cependant impératif de s'assurer que le problème mathématique soit bien posé pour mener correctement des campagnes de simulations numériques. Pour cela, dans ce manuscrit, chaque modèle sera associé à un raisonnement mathématique cohérent.

Afin de répondre à la problématique exposée ci-dessus, nous avons mené un travail de modélisation basé sur nos propres simulations numériques de références ainsi que d'autres bases de données afin de tester l'universalité des théories, mais aussi assurer la robustesse de nos propos.

Simulations numériques Depuis les années 1930, des expériences en laboratoire, sur le terrain ou numériques ont été menées afin d'obtenir les profils dans la couche limite.

Les expériences In-Situ ont démarré avec des mesures par anémomètres suivie par des mesures par LIDAR (laser detection and ranging) [Behrendt et al., 2015] [Frehlich and Kelley, 2008]. Le caractère universel de la turbulence permet de reproduire les écoulement de taille atmosphérique dans des souffleries. Parmi les

techniques éprouvées pour obtenir les informations nécessaires sur les statistiques de la turbulence, citons les relevés anénométriques [Klebanoff, 1955]. Citons également la PIV (particle image velocimetry) combiné au flot optique. Le principe est le suivant, un écoulement est envoyé dans une soufflerie avec des traceurs les plus légers possibles, par exemple, de la fumée de spectacle. Des images de l'écoulement éclairé par laser sont prises à des intervalles très courts ($\approx 10^{-3}s$) [Carlier and Stanislas, 2005] [Hambleton et al., 2006]. Suite à cela, le flot optique reproduit le champs de vitesses. Concernant des fluides à échelles plus élevées comme l'océan, d'autres traceurs sont utilisés et repérés par satellite, par exemple, la salinité, la température.

Au niveau numérique, les expériences de canal ont augmenté en nombre de Reynolds depuis les travaux de [Kim et al., 1987]. Les simulations ont été menées par un $Re_* \approx 590$ par [Moser et al., 1999], à $Re_* \approx 1990$ par [Del Alamo et al., 2004], à 5200 dans [Lee and Moser, 2015].

Aux débuts des années 2000, deux types de profil de vitesses prédominaient dans la littérature, un profil logarithmique hérité de [Millikan, 1938] et un profil de type puissance provenant de [George and Castillo, 1997] et [Barenblatt and Chorin, 1998]. L'existence d'un profil logarithmique est aujourd'hui dominant dans la communauté scientifique.

Dans un même temps, des campagnes de simulations numériques ont été développé pour des problèmes de couche limite au-dessus d'une plaque. Citons les simulation à $Re_\theta \approx 4200$ [Schlatter et al., 2010], [Diaz-Daniel et al., 2017], $Re_\theta \approx 8300$ [Eitel-Amor et al., 2014].

Chacune des simulations précédentes admettaient un fond plat. Plusieurs campagnes de simulations sont aussi menés sur des fond rugueux, citons [Orlandi and Leonardi, 2006] pour des rugosités composés de parallélépipèdes reproduisant un milieu urbain, [Busse et al., 2015] où les auteurs ont testé des fonds plus ou moins lisses.

Au cours des dernières années, des DNS ont été menées pour des écoulements stratifiés en rotation qui simulent une atmosphère ou un océan, [Coleman et al., 1992], [Spalart et al., 2008], [Taylor and Sarkar, 2008]

,[Marlatt et al., 2011] et [Shah and Bou-zeid, 2014].

Enfin, nous pouvons évoquer les écoulements en interface. Un premier article mène des DNS avec un fond plat mais assurant la continuité à l'interface [Lombardi et al., 1996], puis avec une interface non stationnaire [Fulgosi et al., 2003], [Kawamura, 2000]. De nombreuses simulations LES ont été menées sur le sujet, citons dernièrement [López Castaño et al., 2018].

Modèles de turbulences Afin de résoudre les écoulements turbulents, il est nécessaire de modéliser soit les tourbillons de tailles inférieures à la grille de calcul (LES) ou de résoudre des variables statistiques (RANS).

Les premiers modèles LES héritent du modèle de Smagorinsky [Smagorinsky, 1963]. Ce dernier est connu pour surévaluer la viscosité. Une pléïade de modèle ont été écrits pour évaluer plus finement l'énergie sous-grille [Métais and Lesieur, 1992], une revue des méthode est disponible dans [Sagaut, 2006].

Ces modèles sont très régulièrement utilisés en simulations atmosphériques. [Kirkil et al., 2012] , [Gullbrand and Chow, 2003], [Zhou and Chow, 2011], [Zhou and Chow, 2014], [Porté-agel et al., 2000], [Porté-agel and chi C., 2015], [Zhang et al., 2013], [Cheng and Porté-agel, 2016], [Lu and Porte-Agel, 2013] , [Fang and Porté-Agel, 2015], [Shamsoddin and Porté-agel, 2017], [Lu and Porte-Agel, 2014].

Dans ce manuscrit, nous nous intéressons à la seconde famille de modèle de turbulence. Les modèles RANS forment un ensemble de fermetures d'équations afin de modéliser physiquement le tenseur de stress de Reynolds. Une revue sur les modèles RANS est disponible dans [Argyropoulos and Markatos, 2015]. La capacité des modèles RANS pour prédire les écoulements de couche limite (pipeline, canal, plaque) a été étudiée dans de nombreux articles, [Sarkar and So, 1997], [Gorji et al., 2014] où sont testés un large éventail de systèmes de fermetures à 2 équations.

Il est également proposé par des auteurs [Sogachev et al., 2012] des paramétrisations de modèles $k - \mathscr{E}$ pour des simulations d'atmosphères stratifiées.

Conditions de bords Différents types de conditions de bords sont utilisés en simulations. Premièrement, quand la résolution de calcul est suffisamment fine, une condition de type Dirichlet $\mathbf{v} = 0$ est appliquée (no slip boundary condition). Une même condition s'applique pour l'énergie cinétique turbulente.

Parmi les conditions de Dirichlet existantes, citons [Richards and Hoxey, 1993], [Blocken et al., 2007], [Parente et al., 2011]. Ces conditions de Dirichlet considèrent comme paramètres un hauteur de rugosité ainsi qu'un coefficient dépendant du type de rugosité. Ces conditions de bords sont surtout applicables aux problèmes RANS.

Afin d'apporter une physique supplémentaire au sein de la condition de bords, des auteurs [Podvin and Fraigneau, 2011] utilisent des décompositions de type POD afin de générer des conditions de bords pour produire des simulations dans un domaine réduit.

Modélisations stochastiques Les raisonnements et simulations exprimés ci-dessus sont basés sur des équations déterministes avec possiblement l'ajout d'aléatoire. Cependant comme les modèles LES et RANS nécessitent de résoudre des équations supplémentaires aux équations de Navier Stokes, ces dernières sont gourmandes en ressource et en temps de calcul. Pour des projets industriel ou de météorologie à court terme, il est nécessaire d'approcher autant que possible du temps réel.

Plusieurs approches sont développées en ce sens, les méthodes dites de réduction d'ordre où la plus connue est la POD (proper orthogonal decomposition) dans laquelle les équations sont résolus dans une base de Galerkin tronqués pour conserver les niveaux d'énergie suffisants [Cammilleri et al., 2013], [Wang et al., 2012]. Un autre cadre est développé et notre travail s'inscrit ici, est une formulation dans un contexte stochastique des équations de la mécanique des fluides.

En 2014, le modèle "Under location uncertainty" [Mémin, 2014] est développé dans ce sens. Ici, la modélisation de la turbulence se fait à travers des opérateurs aléatoires. Plus récemment [Holm, 2015], a développé un autre système de loi pour des équations de type Eulériennes.

Organisation du mémoire

Ce mémoire est organisé de la façon suivante : Dans le premier chapitre, nous avons redémontré algébriquement la règle fondamentale des -5/3 décrivant la décroissance de la taille des tourbillons dans un écoulement homogène et isotrope. Pour arriver au problème algébrique, nous reviendrons sur l'obtention des modèles RANS avec notamment le développement des équation développées par les moyennes de Reynolds.

Cette loi de puissance est toujours considéré comme une référence dans l'ensemble des simulations proposées dans la littérature. Par un ensemble de simulations numériques, nous montrons l'écart existant entre ce profil en -5/3 et le profil existant dans un écoulement de couche limite, ce dernier n'étant pas spatialement isotrope. En utilisant un canal à très haut nombre de Reynolds, nous montrons l'évolution de cette loi de puissance en fonction de la hauteur. L'évolution de la loi de puissance s'explique par le changement de physique entre les différentes sections de la couche limite turbulente.

Dans le deuxième chapitre, nous reviendrons sur des généralités sur la couche limite turbulente. Ce chapitre est divisé en 3 sections. En premier lieu, nous présenterons les autres modèles de turbulence (Large Eddy Simulations et le modèle "Under Location Uncertainty"), ainsi l'ensemble des modèles de turbulences évoqués dans ce manuscrit seront présentés. En deuxième lieu, nous reviendrons sur la physique de la couche limite turbulente, nous présenterons une ouverture vers la couche limite atmosphérique. Dans cette section, nous reviendrons sur l'obtention des lois de profils dans la couche limite. Ce chapitre sera conclu par un exposé des méthodes numériques implémentées au sein des codes de calculs utilisés dans nos études.

Le troisième chapitre est consacré au développement d'une nouvelle formule universelle pour la longueur de mélange. Il sera testé dans un écoulement de canal, cette longueur de mélange ainsi qu'une condition de bord obtenues à partir de l'analyse dimensionnelle. De plus, nous avons testé tant les écoulements au dessus d'une plaque ainsi qu'au dessus d'un fond rugueux. En fin de chapitre, nous démontrons l'existence de solution au système NS-TKE inhérent à ce problème. Il s'agit d'un problème EDP avec un terme source dans $L^1(\Omega)$ avec une condition de bord de type Neumann et

periodique.

Au quatrième chapitre, nous utilisons le nouveau modèle de turbulence "Under Location Uncertainty" pour obtenir de nouvelles lois de profil au sein de la couche limite turbulente. Nous allons utiliser nos simulations numériques tant eulérienne que lagrangienne pour démontrer nos résultats. Les lois que nous obtenons seront mathématiquement cohérentes.

Enfin, nous proposons en annexe un travail revenant sur la diffusivité numérique générée par les schémas volumes finis dans le solveur OpenFoam utilisés ici. Ce travail permettra de comparer la viscosité numérique et la viscosité physique.

Publications

Le travail fourni a mené aux publications suivantes :

— Lewandowski Roger, Pinier Benoît, Mémin Etienne, Chandramouli Pranav ;
Testing a one-closure equation turbulence model in neutral boundary layers, soumis à Journal of Computational Physics.

— Lewandowski Roger, Pinier Benoît ;
The Kolmogorov law of turbulence : what can rigorously be proved ? Part II, The foundations of chaos revisited : from Poincaré to recent advancements, 2016.

— Pinier Benoît, Mémin Etienne, Laizet Sylvain, Lewandowski, Roger ;
A model under location uncertainty for the mean velocity in wall bounded flows, soumis

CHAPITRE 1

THE KOLMOGOROV LAW OF TURBULENCE. WHAT CAN RIGOROUSLY BE PROVED ?

Nous apportons une justification algébrique de la théorie des -5/3 de Kolmogorov. Cette loi utilisée pour caractériser la distribution des tourbillons dans un écoulement est trouvée dans un article de 1949 écrit par Onsager [Onsager, 1949] et non pas dans la série d'articles écrite par Kolmogorov dans les années 1940. Dans ces derniers ; Kolmogorov a introduit la loi des 2/3 via les échelles nécessaires dans le cas d'un écoulement isotrope et homogène.

Il est connu que cette loi est comprise dans l'intervalle inertiel (intervalle de nombres d'ondes pour lesquels les tourbillons se dissipent en tourbillons de tailles inférieures jusqu'á ce que ces derniers soient dissipés par la diffusion moléculaire). La densité d'énergie pour un nombre d'onde k est donc $E(k) = Ck^{-5/3}$.

Dans la première partie de ce chapitre, il sera exposé l'algèbre nécessaire à l'analyse d'un écoulement homogène et isotrope préparant á une démonstration rigoureuse permettant d'obtenir la loi des $-5/3$ de Kolmogorov.

Dans la seconde partie du chapitre, nous mettrons en valeur la nécessité d'isotropie d'un écoulement pour obtenir cette loi, nous menons une simulation dans un canal avec une rugosité correlée dans la direction horizontale. Le spectre d'énergie calculé montre une tendance assez éloignée des $-5/3$.

1.1 Introduction

We focus in this paper on the law of the $-5/3$, which attracted a lot of attention from the fluid mechanics community these last decades, since it is a basis for many turbulence models, such as Large Eddy Simulation models (see for instance in [Germano et al., 1991, Germano, 2000, Pope, 2000, Sagaut, 2006]). Although it is usually known as the Kolmogorov law, it seems that it appears for the first time in a paper by Onsager [Onsager, 1949] in 1949, and not in the serie of papers published by Kolmogorov in 1941 (see in [Tikhomirov, 1992]), where the author focuses on the $2/3$'s law, by introducing the essential scales related to homogeneous and isotropic turbulent flows (see formula (1.32) below). In this major contribution to the field, Kolmogorov opened the way for the derivation of laws based on similarity principles such as the $-5/3$'s law (see also in [Chacòn Rebollo and Lewandowski, 2014, Lewandowski, 2016]).

Roughly speaking, the $-5/3$'s law states that in some inertial range $[k_1, k_2]$, the energy density of the flow $E(k)$ behaves like $C^{te}k^{-5/3}$, where k denotes the current wave number (see figure 1.1 below and the specific law (1.39)).

This paper is divided in a theoretical part and a numerical part, in which we aim at :

i) carrefully express what is the appropriate similarity assumption that must satisfy an homogeneous and istropic turbulent flow in order to derive the $-5/3$'s law (assumptions 1.4.1 and 1.4.2 below),

ii) to theoretically derive the $-5/3$ law from the similarity assumption (see Theorem 1.4.2 below),

iii) to discuss the numerical validity of such a law from a numerical simulation in a test case, using the software OpenFoam and the ices turbulence database for simulations at very high Reynolds number.

Before processing items i) and ii), we discuss on different results about the Navier-Stokes equations (1.1) (NSE in what follows), that are one of the main tools in fluid mechanics, as well as the Reynolds stress (1.13) derived by taking the expectation of the NSE, once the appropriate probabilistic frame is specified. We then define the density energy $E(k)$, which is the energy of the flow in the sphere $\{k = |\mathbf{k}|\}$ in the Fourier space. Furthermore, we introduce the concept of dimensional bases in order to properly set Assumptions 1.4.1 and 1.4.2.

The numerical simulation takes place in a computational box (see 1.2a) with a non trivial topography (see figure 1.2b), by using the mean NSE (1.12), the $k - \mathscr{E}$

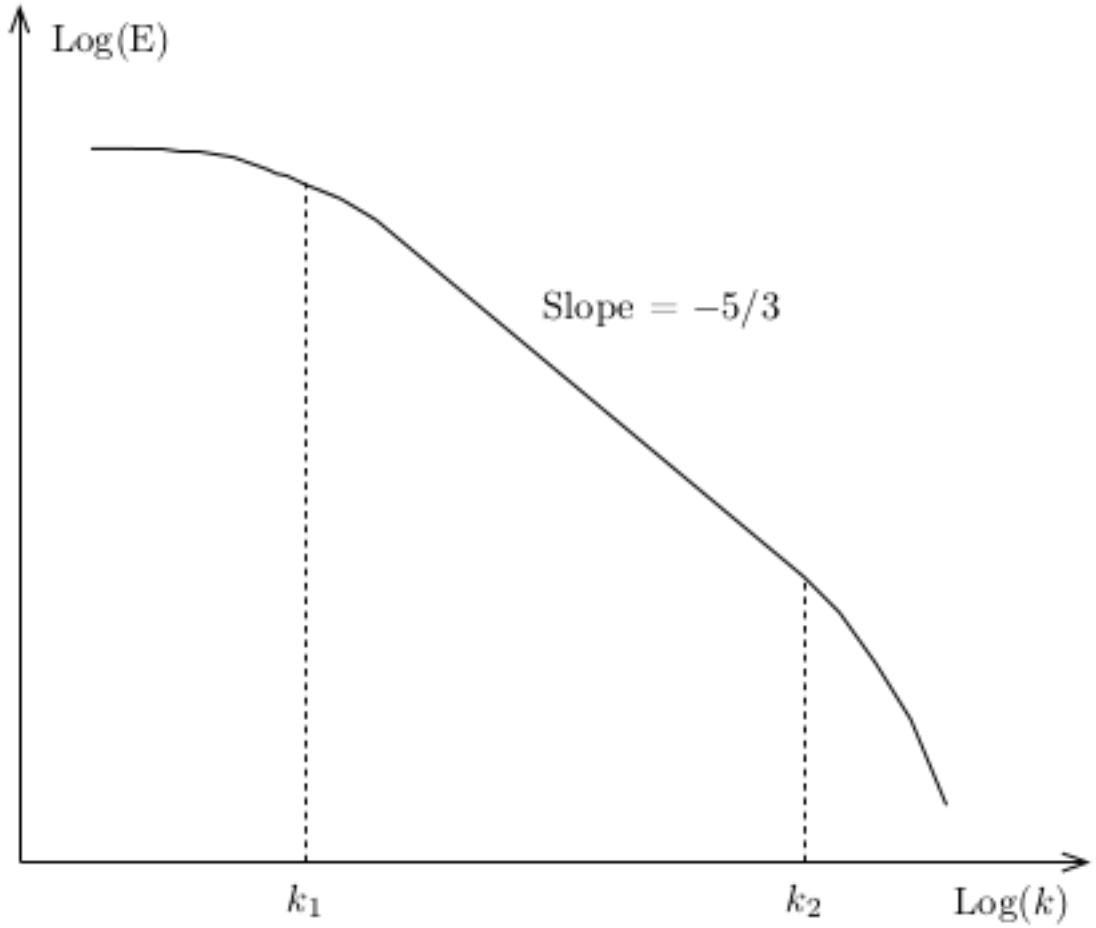

FIGURE 1.1 – Energy spectrum Log-Log curve

model (1.19), and appropriate boundary conditions supposed to model the dynamics of the atmospheric boundary layer. Atmospheric boundary layer modeling is a modern challenge because of its significance in climate change issues. We find in the literature many simulations carried out in different configurations. Of course, this flows is not homogeneous nor isotropic. However, the simulations shows that the curve of $\log_{10}(E(k))$ exhibits an inertial range over 4 decades, in which the regression straight line has a slope equal to $-2.1424 \neq -5/3$ (see figure 1.4), suggesting that the $-5/3$'s law is not satisfied in this case. The deviation from the $-5/3$ law is also illustrated with a DNS of a high Reynolds channel flow at the end of this chapter.

1.2 About the 3D Navier Stokes equations

1.2.1 Framework

Let $\Omega \subseteq \mathbb{R}^3$ be a C^1 bounded convex smooth domain, Γ its boundary, $T \in \mathbb{R}_+$ (enventually $T = +\infty$), and $Q = [0, T] \times \Omega$. The velocity of the flow is denoted by $\mathbf{v}$, its pressure by p. The incompressible Navier Stokes equation satisfied by $(\mathbf{v}, p)$ (NSE in the remainder) are as follows :

$$\left\{\begin{array}{rcll} \partial_t \mathbf{v} + (\mathbf{v}\cdot\nabla)\,\mathbf{v} - \nabla\cdot(2\nu D\mathbf{v}) + \nabla p &=& \mathbf{f} & \text{in } Q, \quad \text{(i)} \\ \nabla\cdot\mathbf{v} &=& 0 & \text{in } Q, \quad \text{(ii)} \\ \mathbf{v} &=& 0 & \text{on } \Gamma, \quad \text{(iii)} \\ \mathbf{v} &=& \mathbf{v}_0 & \text{at } t = 0, \quad \text{(iv)} \end{array}\right. \tag{1.1}$$

where $\mathbf{v}_0$ is any divergence free vector fields such that $\mathbf{v}_0 \cdot \mathbf{n}|_\Gamma = 0$, $\nu > 0$ denotes the kinematic viscosity, that we suppose constant for the simplicity, $\mathbf{f}$ is any external force (such as the gravity for example), $D\mathbf{v}$ denotes the deformation tensor, $\nabla\cdot$ the divergence operator and $(\mathbf{v}\cdot\nabla)\,\mathbf{v}$ is the nonlinear transport term, specifically

$$\begin{aligned} &D\mathbf{v} = \frac{1}{2}\left(\nabla\mathbf{v} + \nabla\mathbf{v}^t\right), \quad \nabla\mathbf{v} = (\partial_j v_i)_{1\le ij\le 3}, \quad \mathbf{v} = (v_1, v_2, v_3), \quad \partial_i = \frac{\partial}{\partial x_i}, \\ &\nabla\cdot\mathbf{v} = \partial_i v_i, \\ &[(\mathbf{v}\cdot\nabla)\,\mathbf{v}]_i = v_j\partial_j v_i, \end{aligned}$$

by using the Einstein summation convention. We recall that it is easily deduced from the incompressibilty condition (see [Chacòn Rebollo and Lewandowski, 2014]) :

$$\begin{aligned} &(\mathbf{v}\cdot\nabla)\,\mathbf{v} = \nabla\cdot(\mathbf{v}\otimes\mathbf{v}), \quad \mathbf{v}\otimes\mathbf{v} = (v_i v_j)_{1\le i,j\le 3}, \\ &\nabla\cdot(2\nu D\mathbf{v}) = \nu\Delta\mathbf{v}. \end{aligned}$$

In the following, we will consider the functional spaces

$$\mathbf{W} = \{\mathbf{v} \in H_0^1(\Omega)^3, \nabla\cdot\mathbf{v} = 0\} \hookrightarrow \mathbf{V} = \{\mathbf{v} \in L^2(\Omega)^3,\, \mathbf{v}\cdot\mathbf{n}|_\Gamma = 0, \nabla\cdot\mathbf{v} = 0\}, \tag{1.2}$$

Throughout the paper, we assume $\mathbf{v}_0 \in \mathbf{V}$.

1.2.2 Strong solutions to the NSE

Let P be the orthogonal projection $L^2(\Omega)^3 \hookrightarrow \mathbf{V}$, A and F the operators

$$A\mathbf{v} = -\nu P\Delta\mathbf{v}, \quad F\mathbf{v} = P((\mathbf{v}\cdot\nabla)\,\mathbf{v}).$$

By applying P to (1.1.i) in noting that $P(\nabla p) = 0$, we are led to the following initial value problem

$$\begin{cases} \dfrac{d\mathbf{v}}{dt} = -A\mathbf{v} + F\mathbf{v} + P\mathbf{f}(t), & \text{(i)} \\ \mathbf{v}(0) = \mathbf{v}_0, & \text{(ii)} \end{cases} \tag{1.3}$$

where $t \to \mathbf{v}(t)$ and $t \to \mathbf{f}(t)$ are considered as functions valued in $\mathbf{W}$ and $\mathbf{V}$ respectively.

Definition 1.2.1. *We say that $\mathbf{v} = \mathbf{v}(t)$ is a strong solution to the NSE in a time interval $[0, T^\star]$ if $d\mathbf{v}/dt$ and $A\mathbf{v}$ exist and are continuous in $[0, T^\star]$ and (1.3.i) is satisfied there.*

Remark 1.2.1. *In definition 1.2.1, the pressure is not involved. It can be reconstructed by the following equation*

$$\Delta p = -\nabla\cdot((\mathbf{v}\cdot\nabla)\,\mathbf{v}) + \nabla\cdot\mathbf{f}, \tag{1.4}$$

derived from equation (1.1.i) by taking its divergence.

The existence of a strong solution is proved in Fujita-Kato [Fujita and Kato, 1964]. It is subject to regularity conditions regarding the initial data $\mathbf{v}_0$ and the source $\mathbf{f}$. The result is stated as follows.

Theorem 1.2.1. *We assume*

i) $\mathbf{v}_0 \in \mathbf{V} \cap H^{1/2}(\Omega)^3$,

ii) $\mathbf{f}$ *is Hölder continuous in* $[0, T]$.

Then there exists $T^\star = T^\star(\nu, ||\mathbf{v}_0||_{1/2,2,\Omega}, ||\mathbf{f}||_{C^{0,\alpha}(\Omega)})$ such that the NSE admits a unique strong solution $\mathbf{v} = \mathbf{v}(t)$. Moreover, if $\mathbf{f} = \mathbf{f}(t, \mathbf{x})$ is Hölder continuous in $Q = [0, T^\star] \times \Omega$, then $\mathbf{v}(t, \mathbf{x})$, $\nabla\mathbf{v}(t, \mathbf{x})$, $\Delta\mathbf{v}(t, \mathbf{x})$ and $\partial\mathbf{v}(t, \mathbf{x})/\partial t$ are Hölder continous in $]0, T^\star[\times\Omega$.

Remark 1.2.2. *The strong solution is solution of the equation*

$$\mathbf{v}(t) = e^{-tA}\mathbf{v}_0 - \int_0^t e^{-(t-s)A}F(\mathbf{v}(s))ds + \int_0^t e^{-(t-s)A}P\mathbf{f}(s)ds, \tag{1.5}$$

which is approached by the sequence $(\mathbf{v}_n)_{n\in\mathbf{N}}$ *expressed by*

$$\mathbf{v}_n(t) = e^{-tA}\mathbf{v}_0 - \int_0^t e^{-(t-s)A}F(\mathbf{v}_{n-1}(s))ds + \int_0^t e^{-(t-s)A}P\mathbf{f}(s)ds, \tag{1.6}$$

The reader is referred to [Cannone, 2004, Chemin and Gallagher, 2009, Lemarié-Rieusset, 2002] for more details concerning the question of strong solutions.

1.2.3 Turbulent solutions

Definition 1.2.2. *We say that* $\mathbf{v}$ *is a turbulent solution of NSE (1.1) in* $[0,T]$ *if*

i) $\mathbf{v} \in L^2([0,T],\mathbf{W}) \cap L^\infty([0,T],L^2(\Omega))$*,*

ii) $\partial_t\mathbf{v} \in L^{4/3}([0,T],\mathbf{W}') = [L^4([0,T],\mathbf{W})]'$ *(by writing* $\partial_t = \dfrac{\partial}{\partial t}$ *for the simplicity),*

iii) $\lim\limits_{t\to 0} ||\mathbf{v}(\cdot,t) - \mathbf{v}_0(\cdot)||_{0,2,\Omega} = 0$*,*

iv) $\forall\, \mathbf{w} \in L^4([0,T],\mathbf{W})$,

$$\int_0^T < \partial_t\mathbf{v},\mathbf{w} > dt + \int_0^T\int_\Omega (\mathbf{v}\otimes\mathbf{v}) : \nabla\mathbf{w}\, d\mathbf{x}dt + \int_0^T\int_\Omega \nabla\mathbf{v} : \nabla\mathbf{w}\, d\mathbf{x}dt = \int_0^T < \mathbf{f},\mathbf{w} > dt,$$

where for $\mathbf{u} \in \mathbf{W}$*,* $\mathbf{F} \in \mathbf{W}'$*,* $< \mathbf{F},\mathbf{u} >$ *denotes the duality pairing between* $\mathbf{F}$ *and* $\mathbf{u}$*,*

v) $\mathbf{v}$ *satisfies the energy inequality at each* $t > 0$*,*

$$\frac{1}{2}\int_\Omega |\mathbf{v}(t,\mathbf{x})|^2 d\mathbf{x} + \nu\int_0^t\int_\Omega |\nabla\mathbf{v}(t',\mathbf{x})|^2 d\mathbf{x}dt' \le \int_0^t < \mathbf{f},\mathbf{v} > dt'.$$

Remark 1.2.3. *Once again, the pressure is not involved in this formulation. It this frame, it is recovered by the De Rham Theorem (see for instance in [Temam, 2001]).*

The existence of a turbulent solution was first proved by Leray [Leray, 1934] in the whole space, then by Hopf [Hopf, 1951] in the case of a bounded domain with the no slip boundary condition, which is the case under conderation here. This existence result can be stated as follows.

Theorem 1.2.2. *Assume that* $\mathbf{v}_0 \in \mathbf{V}$*,* $\mathbf{f} \in L^{4/3}([0,T],\mathbf{W}')$*. Then the NSE (1.1) has a turbulent solution.*

Remark 1.2.4. *The turbulent solution is global in time, which means that it may be extended to* $t \in [0,\infty[$ *depending on a suitable assumption on* $\mathbf{f}$*. However it is not*

known whether it is unique or not. Moreover, it is not known if the energy inequality is an equality.

The reader is also referred to [Constantin and Foias, 1988, Feireisl, 2004, Lions, 1996, Temam, 2001] for further results on turbulent (also weak) solutions of the NSE.

1.3 Mean Navier-Stokes Equations

1.3.1 Reynolds decomposition

Based on strong or turbulent solutions, it is known that it is possible to set a probabilistic framework in which we can decompose the velocity v and the pressure as a the sum of the statistical mean and a fluctuation, namely

$$\mathbf{v} = \overline{\mathbf{v}} + \mathbf{v}', \quad p = \overline{p} + p'. \tag{1.7}$$

More generally, any tensor field ψ related to the flow can be decomposed as

$$\psi = \overline{\psi} + \psi'. \tag{1.8}$$

The statistical filter is linear and subject to satisfy the Reynolds rules :

$$\overline{\partial_t \psi} = \partial_t \overline{\psi}, \tag{1.9}$$

$$\overline{\nabla \psi} = \nabla \overline{\psi}, \tag{1.10}$$

as well as

$$\overline{\overline{\psi}} = \overline{\psi} \text{ leading to } \overline{\psi'} = 0. \tag{1.11}$$

We have studied in [Chacòn Rebollo and Lewandowski, 2014] different examples of such filters. Historically, such a decomposition was first considered in works by Stokes [Stokes, 1851], Boussinesq [Boussinesq, 1877], Reynolds [Reynolds, 1883], Prandtl [Prandtl, 1925], in the case of the « long time average »(see also in [Lewandowski, 2015]). Later on, Taylor [Taylor, 1935], Kolmogorov [Kolmogorov, 1941] and Onsager [Onsager, 1949] have considered such decompositions when the fields related to the flow are considered as random variables, which was one of the starting

point for the development of modern probability theory.

1.3.2 Reynolds Stress and closure equations

We take the mean of the NSE (1.1) by using (1.9), (1.10) and (1.11). We find out the following system :

$$\begin{cases} \partial_t \overline{\mathbf{v}} + (\overline{\mathbf{v}} \cdot \nabla)\, \overline{\mathbf{v}} - \nu \Delta \overline{\mathbf{v}} + \nabla \overline{p} &= -\nabla \cdot \boldsymbol{\sigma}^{(\mathsf{R})} + \mathbf{f} \quad \text{in } Q, \\ \nabla \cdot \overline{\mathbf{v}} &= 0 \quad \text{in } Q, \\ \overline{\mathbf{v}} &= 0 \quad \text{on } \Gamma, \\ \overline{\mathbf{v}} &= \overline{\mathbf{v}_0} \quad \text{at } t = 0, \end{cases} \tag{1.12}$$

where

$$\boldsymbol{\sigma}^{(\mathsf{R})} = \overline{\mathbf{v}' \otimes \mathbf{v}'} \tag{1.13}$$

is the Reynolds stress. The big deal in turbulence modeling is to express $\boldsymbol{\sigma}^{(\mathsf{R})}$ in terms of averaged quantities. The most popular model is derived from the Boussinesq assumption which consists in writing :

$$\boldsymbol{\sigma}^{(\mathsf{R})} = -\nu_t D\overline{\mathbf{v}} + \frac{2}{3} k \,\mathrm{Id}, \tag{1.14}$$

where

i) $k = \dfrac{1}{2}\mathrm{tr}\, \boldsymbol{\sigma}^{(\mathsf{R})} = \dfrac{1}{2}\overline{|\mathbf{v}'|^2}$ is the turbulent kinetic energy (TKE),

ii) ν_t is an eddy viscosity.

In order to close the system, the eddy viscosity remains to be modeled.

We next mention the so-called TKE model, given by

$$\nu_t = C_k \ell \sqrt{k}, \tag{1.15}$$

which gives accurate results for the simulation of realistic flows (see for instance [Lewandowski and Pichot, 2007]). In model (1.15), ℓ denotes the Prandtl mixing length, C_k is a dimensionless constant that must be fixed according to experimental data. In practice, ℓ is taken to be equal to the local mesh size in a numerical simulation, and k is computed by using the closure equation (see in [Mohammadi and Pironneau, 1994])

$$\partial_t k + \overline{\mathbf{v}} \cdot \nabla k - \nabla \cdot (\nu_t \nabla k) = \nu_t |D\overline{\mathbf{v}}|^2 - \frac{k\sqrt{k}}{\ell}. \tag{1.16}$$

The reader will find a bunch of mathematical result concerning the coupling of the TKE equation to the mean NSE in [Brossier and Lewandowski, 2002, Bulíček et al., 2011, Chacòn Rebollo and Lewandowski, 2014, Gallouët et al., 2003, Lederer and Lewandowski, 2007, Lewandowski, 1997a].

Finally, we mention the famous $k-\mathscr{E}$ model that is used for the numerical simulations carried out in Section 1.5. In this model, $\mathscr{E}$ denotes the turbulent dissipation

$$\mathscr{E} = 2\nu\overline{|D\mathbf{v}'|^2}, \tag{1.17}$$

and dimensional analysis leads to write

$$\nu_t = C_\mu \frac{k^2}{\mathscr{E}}. \tag{1.18}$$

The coupled system used to compute k and $\mathscr{E}$ is the following (see [**?**, Mohammadi and Pironneau, 1994] for the derivation of these equations) :

$$\left\{\begin{array}{rcl} \partial_t k + \overline{\mathbf{v}}\cdot\nabla k - \nabla\cdot(\nu_t\nabla k) &=& \nu_t|D\overline{\mathbf{v}}|^2 - \mathscr{E}. \\ \partial_t \mathscr{E} + \overline{\mathbf{v}}\cdot\nabla \mathscr{E} - \nabla\cdot(\nu_t\nabla \mathscr{E}) &=& c_\eta k|D\overline{\mathbf{v}}|^2 - c_{\mathscr{E}}\dfrac{\mathscr{E}^2}{k}, \end{array}\right. \tag{1.19}$$

where $C_\nu = 0.09$, $c_{\mathscr{E}} = 1.92$ and $c_\eta = 1.44$ are dimensionless constants.

1.4 Law of the $-5/3$

The idea behind the law of the $-5/3$ for homogeneous and isotropic turbulence is that in the « inertial range », the energy density $E = E(k)$ at a given point $(t, \mathbf{x})$ is driven by the dissipation $\mathscr{E}$. In this section, we properly define the energy density E for homogeneous and isotropic turbulent flows. We then set the frame of the dimensional bases and the similarity principle in order to rigorously derive the law of the $-5/3$.

Remark 1.4.1. *For homogeneous and isotropic turbulence, one can show the identity* $\mathscr{E} = 2\nu\overline{|D\mathbf{v}'|^2} = 2\nu\overline{|D\mathbf{v}|^2}$ *(see in [Chacòn Rebollo and Lewandowski, 2014]).*

1.4.1 Energy density of the flow

Roughly speaking, homogeneity and isotropy means that the correlations in the flows are invariant under translations and isometries (see in [Batchelor, 1959, Chacòn Rebollo and Lewandowski, 2014, Lewandowski, 2016]), which we assume throughout this section, as well as the stationarity of the mean flow for simplicity. Let

$$\boldsymbol{E} = \frac{1}{2}\overline{|\mathbf{v}|^2}, \tag{1.20}$$

be the total mean kinetic energy at a given point $\mathbf{x} \in \Omega$, which we not specify in what follows.

Theorem 1.4.1. *There exists a measurable function $E = E(k)$, defined over $\mathbb{R}_+$, the integral of which over $\mathbb{R}_+$ is finite, and such that*

$$\boldsymbol{E} = \int_0^\infty E(k)dk. \tag{1.21}$$

Démonstration. Let $\boldsymbol{B}_2$ be the two order correlation tensor expressed by :

$$\boldsymbol{B}_2 = \boldsymbol{B}_2(\mathbf{r}) = (\overline{v_i(\mathbf{x})v_j(\mathbf{x}+\mathbf{r})})_{1\leq i,j\leq 3} = (B_{ij}(\mathbf{r}))_{1\leq i,j\leq 3}, \tag{1.22}$$

which only depend on $\mathbf{r}$ by the homogeneity assumption, nor on t because of the stationarity assumption. It is worth noting that

$$\boldsymbol{E} = \frac{1}{2}\mathrm{tr}\boldsymbol{B}_2(0). \tag{1.23}$$

Let $\widehat{\boldsymbol{B}}_2$ denotes the Fourier transform of $\boldsymbol{B}$ expressed by

$$\forall\, \mathbf{k} \in \mathbb{R}^3, \quad \widehat{\boldsymbol{B}}_2(\mathbf{k}) = \frac{1}{(2\pi)^3}\int_{\mathbf{R}^3} \boldsymbol{B}_2(\mathbf{r})e^{-i\,\mathbf{k}\cdot\mathbf{r}}d\mathbf{r}, \tag{1.24}$$

We deduce from the Plancherel formula,

$$\forall\, \mathbf{r} \in \mathbb{R}^3, \quad \boldsymbol{B}_2(\mathbf{r}) = \frac{1}{(2\pi)^3}\int_{\mathbf{R}^3} \widehat{\boldsymbol{B}}_2(\mathbf{k})e^{i\,\mathbf{k}\cdot\mathbf{r}}d\mathbf{k}, \tag{1.25}$$

which makes sense for both types of solutions to the NSE, strong or turbulent (see the section 1.2). It is easily checked that the isotropy of $\boldsymbol{B}_2$ in $\mathbf{r}$ yields the isotropy of $\widehat{\boldsymbol{B}}_2$ in $\mathbf{k}$. Therefore, according to Theorem 5.1 in [Chacòn Rebollo and Lewandowski, 2014] we

deduce the existence of two real valued functions $\widetilde{B}_d$ and $\widetilde{B}_n$ of class C^1 such that [1]

$$\forall \mathbf{k} \in \mathbb{R}^3, \quad |\mathbf{k}| = k, \quad \widehat{\boldsymbol{B}}_2(\mathbf{k}) = (\widetilde{B}_d(k) - \widetilde{B}_n(k))\frac{\mathbf{k} \otimes \mathbf{k}}{k^2} + \widetilde{B}_n(k)\mathrm{I}_3. \tag{1.26}$$

Using formula (1.26) yields

$$\widehat{B}_{ii}(\mathbf{k}) = \widetilde{B}_d(k) + 2\widetilde{B}_n(k), \tag{1.27}$$

which combined with Fubini's Theorem, (1.23) and (1.25), leads to

$$\int_{\mathbf{R}^3} \widehat{B}_{ii}(\mathbf{k})\, d\mathbf{k} = \int_0^\infty \left(\int_{|\mathbf{k}|=k} \widehat{B}_{ii}(\mathbf{k}) d\boldsymbol{\sigma} \right) dk = \int_0^\infty 4\pi k^2 (\widetilde{B}_d(k) + 2\widetilde{B}_n(k))\, dk, \tag{1.28}$$

by noting $d\boldsymbol{\sigma}$ the standard measure over the sphere $\{|\mathbf{k}| = k\}$. This proves the result, where $E(k)$ is given by

$$E(k) = \left(\frac{k}{2\pi}\right)^2 (\widetilde{B}_d(k) + 2\widetilde{B}_n(k)). \tag{1.29}$$

□

Remark 1.4.2. *From the physical point of view, $E(k)$ is the amount of kinetic energy in the sphere $S_k = \{|\mathbf{k}| = k\}$. As such, it is expected that $E \geq 0$ in $\mathbb{R}$, and we deduce from (1.21) that $E \in L^1(\mathbb{R}_+)$. Unfortunately, we are not able to prove that $E \geq 0$ from formula (1.29), which remains an open problem.*

1.4.2 Dimensional bases

Only length and time are involved in this frame, since we do not consider heat transfers and the fluid is incompressible. Therefore, any field ψ related to the flow has a dimension $[\psi]$ encoded as :

$$[\psi] = (\text{length})^{d_\ell(\psi)} (\text{time})^{d_\tau(\psi)}, \tag{1.30}$$

1. k already denotes the TKE, and from now also the wavenumber, $k = |\mathbf{k}|$. This is commonly used in turbulence modeling, although it might sometimes be confusing.

which we express through the couple

$$\mathbb{D}(\psi) = (d_\ell(\psi), d_\tau(\psi)) \in \mathbb{Q}^2. \tag{1.31}$$

Definition 1.4.1. *A length-time basis is a couple $b = (\lambda, \tau)$, where λ is a given constant length and τ a constant time.*

Definition 1.4.2. *Let $\psi = \psi(t, \mathbf{x})$ (constant, scalar, vector, tensor...) be defined on $Q = [0, T] \times \Omega$. Let ψ_b be the dimensionless field defined by :*

$$\psi_b(t', \mathbf{x}') = \lambda^{-d_\ell(\psi)} \tau^{-d_\tau(\psi)} \psi(\tau t', \lambda \mathbf{x}'),$$

where

$$(t', \mathbf{x}') \in Q_b = \left[0, \frac{T}{\tau}\right] \times \frac{1}{\lambda}\Omega,$$

is dimensionless. We say that $\psi_b = \psi_b(t', \mathbf{x}')$ is the b-dimensionless field deduced from ψ.

1.4.3 Kolmogorov scales

Let us consider the length-time basis $b_0 = (\lambda_0, \tau_0)$, given by

$$\lambda_0 = \nu^{\frac{3}{4}} \mathscr{E}^{-\frac{1}{4}}, \quad \tau_0 = \nu^{\frac{1}{2}} \mathscr{E}^{-\frac{1}{2}}, \tag{1.32}$$

where $\mathscr{E}$ is the dissipation defined by (1.17) (see also Remark 1.4.1). The scale λ_0 is kown as the Kolmogorov scale. The important point here is that

$$\mathscr{E}_{b_0} = \nu_{b_0} = 1. \tag{1.33}$$

Moreover, for all wave number k, and because

$$\mathbb{D}(E) = (3, -2), \tag{1.34}$$

we get

$$E(k) = \lambda_0^3 \tau_0^{-2} E_{b_0}(\lambda_0 k) = \nu^{\frac{5}{4}} \mathscr{E}^{\frac{1}{4}} E_{b_0}(\lambda_0 k), \tag{1.35}$$

by using (1.32). We must determine the universal profil E_{b_0}.

1.4.4 Proof of the $-5/3$'s law

The law of the $-5/3$ is based on two assumptions about the flow :

i) the separation of the scales (assumption 1.4.1 below),

ii) the similarity assumption (assumption 1.4.2 below).

Assumption 1.4.1. *Let ℓ be the Prandtl mixing length. Then*

$$\lambda_0 << \ell. \tag{1.36}$$

Assumption 1.4.2. *There exists an interval*

$$[k_1, k_2] \subset \left[\frac{2\pi}{\ell}, \frac{2\pi}{\lambda_0}\right] \quad \textit{s.t.} \;\; k_1 << k_2 \;\; \textit{and on} \;\; [\lambda_0 k_1, \lambda_0 k_2],$$

$$\forall\, b_1 = (\lambda_1, \tau_1),\, b_2 = (\lambda_2, \tau_2) \;\; \textit{s.t.} \;\; \mathscr{E}_{b_1} = \mathscr{E}_{b_2}, \;\; \textit{then} \;\; E_{b_1} = E_{b_2}. \tag{1.37}$$

Theorem 1.4.2. *Scale separation and similarity assumptions 1.4.1 and 1.4.2 yield the existence of a constant C such that*

$$\forall\, k' \in [\lambda_0 k_1, \lambda_0 k_2] = J_r, \quad E_{b_0}(k') = C(k')^{-\frac{5}{3}}. \tag{1.38}$$

Corollary 1. *The energy spectrum satisfies the $-5/3$ law*

$$\forall\, k \in [k_1, k_2], \quad E(k) = C\mathscr{E}^{\frac{2}{3}} k^{-\frac{5}{3}}, \tag{1.39}$$

where C is a dimensionless constant.

Démonstration. Let

$$b^{(\alpha)} = (\alpha^3 \lambda_0, \alpha^2 \tau_0).$$

As

$$\mathscr{E}_{b^{(\alpha)}} = 1 = \mathscr{E}_{b_0},$$

the similarity assumption yields

$$\forall\, k' \in J_r, \quad \forall \alpha > 0, \quad E_{b^{(\alpha)}}(k') = E_{b_0}(k'),$$

which leads to the functional equation,

$$\forall\, k' \in J_r, \quad \forall\, \alpha > 0, \quad \frac{1}{\alpha^5} E_{b_0}(k') = E_{b_0}(\alpha^3 k'),$$

whose unique solution is given by

$$\forall\, k' \in J_r, \quad E_{b_0}(k') = C(k')^{-\frac{5}{3}}, \quad C = \left(\frac{k_1}{\lambda_0}\right)^{\frac{5}{3}} E_{b_0}\left(\frac{k_1}{\lambda_0}\right),$$

hence the result. Corollary 1 is a direct consequence of (1.35) combined with (1.38). □

1.5 Numerical experiments

1.5.1 Simulation setting

The computational domain Ω is a box, the size $L_x \times L_y \times L_z$ of which is equal to $(1024m, 512m, 200m)$ (see figure 1.2b). The number of nodes is $(256, 128, 64)$. The bottom of the box, plotted in figure 1.2b, has a non trivial topography modeled by gaussian smooth domes, the height of which being equal to 50 m. We perform the simulation with $\nu = 2.10^{-5} m^2 s^{-1}$, which yields a Reynolds number equal to 9.10^7. We use the mean NSE with the Boussinesq assumption, coupled to the $k - \mathscr{E}$ model, namely the PDE system (1.12)-(1.14)-(1.18)-(1.19). We specify in what follows the boundary conditions, by considering the following decomposition of $\Gamma = \partial\Omega$:

$$\Gamma = \Gamma_t \cup \Gamma_f \cup \Gamma_b \cup \Gamma_g \cup \Gamma_i \cup \Gamma_o,$$

where

— Γ_t is the top of the box,
— Γ_f is the front face,
— Γ_b is the back face,
— Γ_g is the bottom of the box (the ground),
— Γ_i is the inlet,
— Γ_o is the outlet.

The condition on Γ_i is prescribed by the Monin Obukhov similitude law [Monin and Obukhov, 1954] :

$$\mathbf{v}(x,y,z,t)|_{\Gamma_i} = \left(\frac{u_\star}{\kappa}\ln\left(\frac{z+z_0}{z_0}\right), 0, 0\right)^t, \tag{1.40}$$

where $\kappa = 0.4$ is the Von Karman constant, z denotes the distance from the ground level, the aerodynamic roughness length z_0 is equal to $0.1m$, the friction velocity is expressd by :

$$u_\star = \kappa U_{ref}\left[\ln\left(\frac{H_{ref}+z_0}{z_0}\right)\right]^{-1}, \tag{1.41}$$

by taking $U_{ref} = 36ms^{-1}$ and $H_{ref} = 200m$. The turbulent kinetic energy and turbulent dissipation are setted by

$$\begin{cases} k|_{\Gamma_i} = u_\star^{1/2} C_\nu^{-1/2}, \\ \mathscr{E}|_{\Gamma_i} = \dfrac{u_\star^3}{\kappa(z+z_0)}. \end{cases} \tag{1.42}$$

On Γ_g, velocity, TKE and turbulent dissipation are subject to verify the no slip and homogeneous boundary conditions,

$$\begin{cases} \mathbf{v}|_{\Gamma_g} &= (0,0,0)^t, \\ k|_{\Gamma_g} &= 0, \\ \mathscr{E}|_{\Gamma_g} &= 0. \end{cases} \tag{1.43}$$

On the top and lateral boundaries, we put

$$\begin{cases} \mathbf{v}\cdot\mathbf{n} &= 0 \quad on \quad \Gamma_t \cup \Gamma_b \cup \Gamma_f, \\ \nabla k \cdot \mathbf{n} &= 0 \quad on \quad \Gamma_t \cup \Gamma_b \cup \Gamma_f, \\ \nabla \mathscr{E} \cdot \mathbf{n} &= 0 \quad on \quad \Gamma_t \cup \Gamma_b \cup \Gamma_f. \end{cases} \tag{1.44}$$

Finally a null gradient condition is prescribed at the outlet Γ_o

$$\begin{cases} \nabla(\mathbf{v}\cdot\mathbf{n}) &= 0 \quad on \quad \Gamma_o, \\ \nabla k \cdot \mathbf{n} &= 0 \quad on \quad \Gamma_o, \\ \nabla \mathscr{E} \cdot \mathbf{n} &= 0 \quad on \quad \Gamma_o. \end{cases} \tag{1.45}$$

Remark 1.5.1. *The PDE system (1.12)-(1.14)-(1.18)-(1.19) with the boundary conditions (1.40)-(1.42)-(1.43)-(1.44)-(1.45) yields a very hard mathematical problem. The*

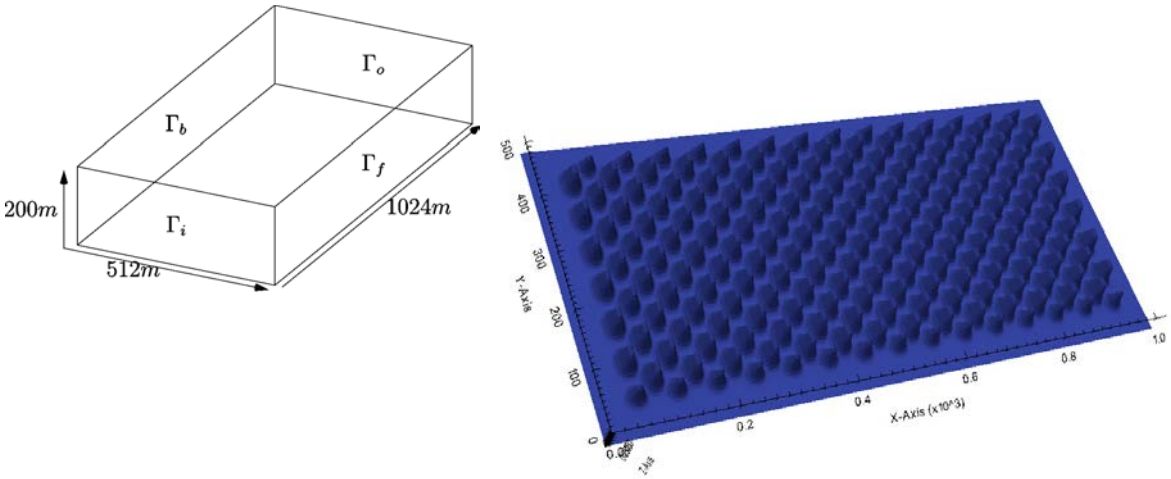

(a) (b)

FIGURE 1.2 – Computational Box and the ground

existence and the uniqueness of a solution is a difficult issue, whether for global weak solutions or local time strong solutions.

1.5.2 Results

The numerical scheme we use for the simulation is based on the standard finite volume method (FVM) in space, and a Euler method for the time discretization. For the simplicity, we will not write here this technical part of the work. The reader will find comprehensive presentations of the FVM in [Jasak, 1996].

In figures 1.3a and 1.3b, are plotted the values of the streamwise and spanwise components of the velocity at $z = 50m$, which corresponds to the dome height.

In Figure 1.4, we have plotted the energy spectrum of the flow at $(x, y, z) = (500, 200, 50)$ using a log-log scale, together with a straight line whose slope is equal to $-5/3 = -1,666....$ and the regression straight line of $\log_{10}(E(k))$, whose slope is about equal to -2.1424.

Then, we focus on the turbulent spectra built from channel flow at $Re_* \approx 5200$

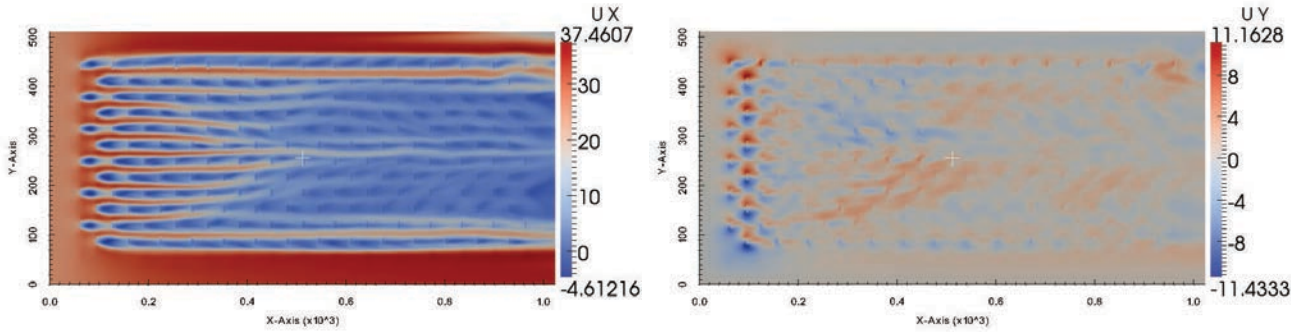

(a) (b)

FIGURE 1.3 – Streamwise and spanwise direction of the mean flow at the $z = 50m$ cutplane.

[Lee and Moser, 2015]. In figures from 1.5a to 1.7b we show turbulent spectra in the streamwise direction. The figures 1.5a and 1.5b show the results in the viscous section. In particular, the figure 1.5b show the $E(k)k^{5/3}$ function, it highlights the difference of the slope as the $-5/3$ section is the section where $E(k)k^{5/3}$ is constant. In 1.6a and 1.6b, the spectra come from the middle of the logarithmic section and then in the figures 1.7a and 1.7b, the spectra come from the top of the boundary layer (middle of the channel here).

In order to summarize the optimal power laws at every sections of the turbulent boundary layer, we show in figure 1.8 the optimal power laws at every heigh, the slope begins at 0.5 in the viscous sublayer and converge toward the 1.5. As a consequence, there are not any z where the spectrum from the streamwise section admits a $-5/3$ slope.

i) The simulation reveals a certain reliability of the code, which suggests the convergence of the numerical method. However, the mathematical convergence of the sheme remains an open question, closely related to the question of the existence of solutions mentionned in Remark 1.5.1.

ii) The curve $\log_{10}(E(k))$ is an irregular curve which substancially differs from a straight line, so that we cannot conclude that numerically $E(k)$ behaves like $C^{te}k^{\alpha}$ in some interval $[k_1, k_2]$. Moreover, there is a gap between the slope of the regression straight line of the curve and $-5/3$. However, something that looks like an inertial range can be identified between $k = 10^{-5}m^{-1}$ and $k = 10^{-1}m^{-1}$. This departure from the $-5/3$ law asks for the following comments and questions.

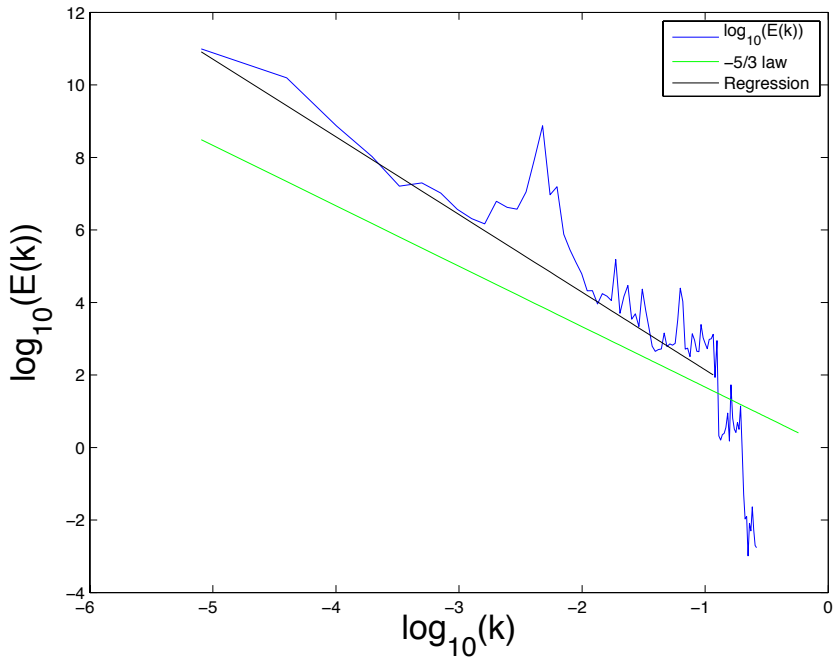

FIGURE 1.4 – Energy spectrum at the point $(x, y, z) = (500, 200, 50)$

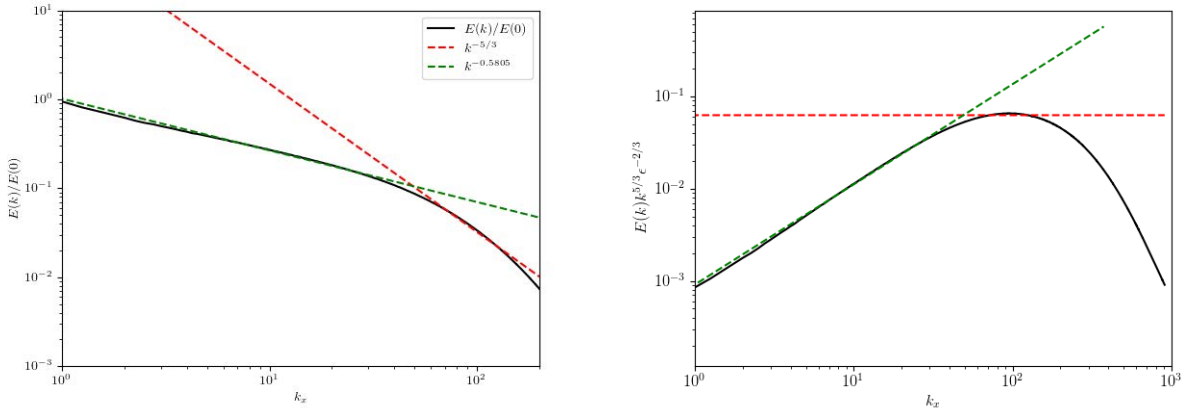

(a) (b)

FIGURE 1.5 – Spectra of turbulent kinetic energy in the streamwise direction in the viscous section. The black line is the spectrum from the dns whereas the green line is the slope of the optimal exposant, the red line is the $-5/3$ slope. The right figure is the non dimensional spectrum

— The case under consideration yields a turbulence which is not homogeneous nor isotropic, which may explain the slope equal to 1424 we found.

— This simulation does not validate the Kolmogorov law or any law like $E(k) \approx C^{te}k^{\alpha}$. We cannot infer that such a law holds or not. Many parameters may generate the oscillations we observe in the curve $\log_{10}(E(k))$, such as any eventual numerical dissipation, a wrong choice of the constants in the $k-\mathscr{E}$ model which also may be not accurate, the boundary conditions we used and which may be questionable.

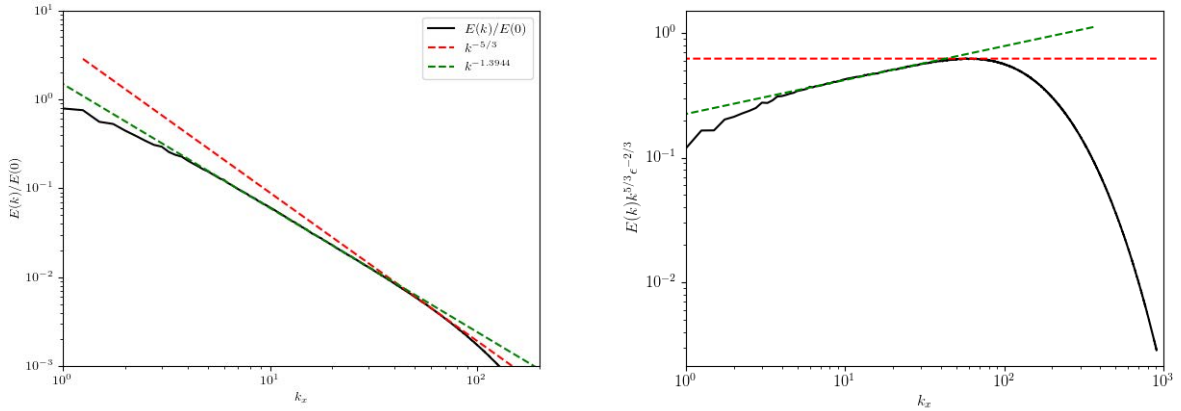

(a) (b)

FIGURE 1.6 – Spectra of turbulent kinetic energy in the streamwise direction in the logarithmic section. The black line is the spectrum from the dns whereas the green line is the slope of the optimal exposant, the red line is the $-5/3$ slope. The right figure is the non dimensional spectrum

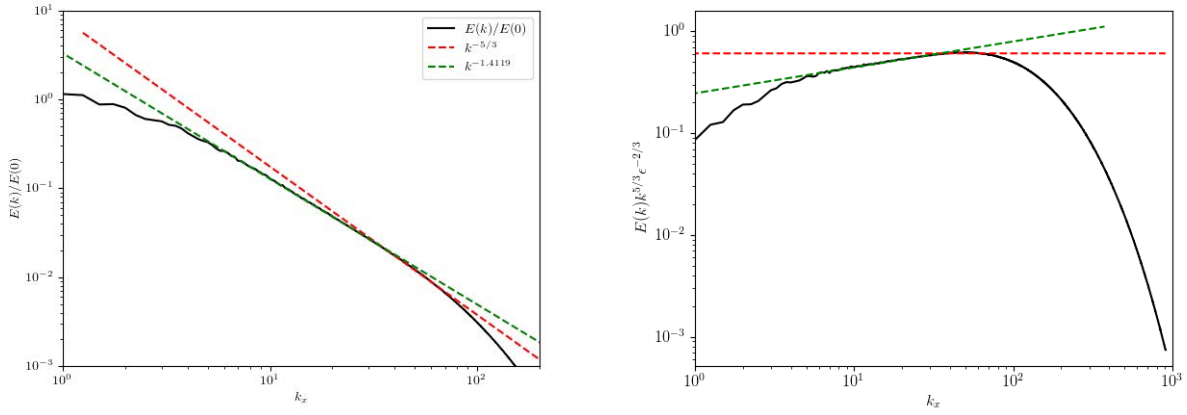

(a) (b)

FIGURE 1.7 – Spectra of turbulent kinetic energy in the streamwise direction in the top of the logarithmic section. The black line is the spectrum from the dns whereas the green line is the slope of the optimal exposant, the red line is the $-5/3$ slope. The right figure is the non dimensional spectrum

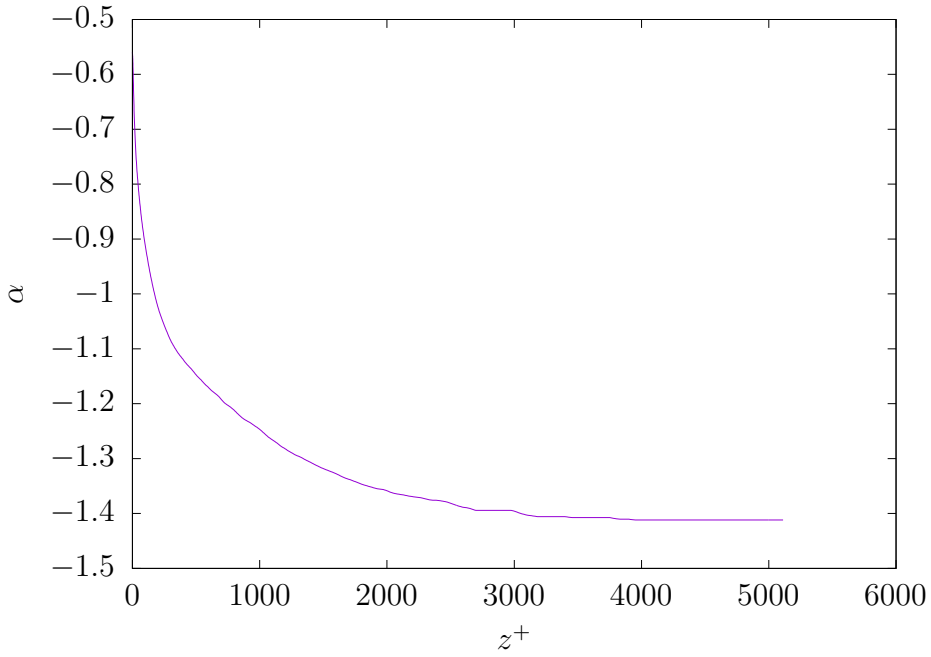

FIGURE 1.8 – Evolution of the optimal power law such that $E(k) = ck^{\alpha}$ in the channel flow at $Re_* \approx 5200$. The wavelength are only in the streamwise direction.

CHAPITRE 2

GÉNÉRALITÉS SUR LA TURBULENCE

Dans ce chapitre, nous introduisons les outils utilisés dans le reste de ce mémoire. Premièrement, nous revenons sur les modèles de turbulence. Nous proposons, ensuite, une introduction à la physique de la couche limite turbulente. Enfin nous expliquerons les méthodes numériques implémentées dans les codes de simulations utilisés afin de vérifier les théories de ce mémoire.

2.1 Modélisations mathématiques de la turbulence

2.1.1 Large Eddy Simulations

L'idée des Large Eddy simulation est de résoudre les grandes échelles (les grands tourbillons) et de modéliser les tourbillons petites échelles. Cette séparation d'échelle est effectuée par une opération de filtrage. L'écoulement s'écrit :

$$\mathbf{v} = \widetilde{\mathbf{v}}(\mathbf{x}, t) + \mathbf{v}'(\mathbf{x}, t), \tag{2.1}$$

où $\tilde{\mathbf{v}}(\mathbf{x}, t)$ est dépendant du temps et représente les grandes échelles de l'écoulement, tandis que $\mathbf{v}'(\mathbf{x}, t)$ représente le terme sous grille (subgrid-scale SGS dans le reste du texte).

Le filtrage est effectué par convolution [Leonard, 1975] :

$$\widetilde{\mathbf{v}} = \int_{\Omega} G(\mathbf{r}, \mathbf{x}) \mathbf{v}(\mathbf{x} - \mathbf{r}, t) d\mathbf{r}. \tag{2.2}$$

Le filtre G est normalisé de sorte que :

$$\int_{\Omega} G(\mathbf{r}, \mathbf{x}) d\mathbf{r} = 1. \tag{2.3}$$

On peut citer comme filtres, le filtre "box"

$$G(\mathbf{r},\mathbf{x}) = \begin{cases} \frac{1}{\Delta} & \text{si } ||\mathbf{x}-\mathbf{r}|| < \frac{1}{2\Delta}, \\ 0 & \text{sinon.} \end{cases} \tag{2.4}$$

Le filtre gaussien

$$G(\mathbf{r},\mathbf{x}) = \left(\frac{6}{\pi\Delta^2}\right) exp\left(\frac{-6||\mathbf{x}-\mathbf{r}||^2}{\Delta^2}\right). \tag{2.5}$$

Le filtre "sharp spectral" :

$$G(\mathbf{x},\mathbf{r}) = \frac{sin(\pi||\mathbf{x}-\mathbf{r}||/\Delta)}{\pi||\mathbf{x}-\mathbf{r}||}. \tag{2.6}$$

Une fois l'opération de filtrage effectuée, une équation de Navier Stokes est déduite pour l'écoulement filtré.

$$\begin{cases} \nabla\cdot\widetilde{\mathbf{v}} &= 0 \\ \partial_t\widetilde{\mathbf{v}} + \nabla\cdot(\widetilde{\mathbf{v}}\otimes\widetilde{\mathbf{v}}) + \nabla\widetilde{p} &= -\nabla\cdot\tau + \mathbf{f}. \end{cases} \tag{2.7}$$

Dans l'équation , le terme τ est un équivalent du tenseur de Reynolds.

$$\tau = \widetilde{\mathbf{v}\otimes\mathbf{v}} - \widetilde{\mathbf{v}}\otimes\widetilde{\mathbf{v}}. \tag{2.8}$$

Au même titre que pour les modèles RANS, l'objectif est de modéliser le terme non linéaire convectif. Une modélisation classique est apportée par Germano [Germano, 1986] :

$$\tau_{ij}^R = \mathcal{L}_{ij}^0 + \mathcal{C}_{ij}^0 + \mathcal{R}_{ij}^0, \tag{2.9}$$

composée des stress de Leonard :

$$\mathcal{L}_{ij}^0 = \widetilde{\widetilde{\mathbf{v}}_i\widetilde{\mathbf{v}}_j} - \widetilde{\widetilde{\mathbf{v}}}_i\widetilde{\widetilde{\mathbf{v}}}_j, \tag{2.10}$$

qui représentent l'interaction entre les grandes échelles. Du stress croisé :

$$\mathcal{C}_{ij}^0 = \widetilde{\widetilde{\mathbf{v}}_i\mathbf{v}'_j} + \widetilde{\mathbf{v}'_i\widetilde{\mathbf{v}}_j} - \widetilde{\widetilde{\mathbf{v}}_i}\widetilde{\mathbf{v}'}_j - \widetilde{\mathbf{v}'}_i\widetilde{\widetilde{\mathbf{v}}_j}, \tag{2.11}$$

qui lui représente les interactions entre les grandes échelles et les petites échelles.

Enfin, le stress de Reynolds sous-grille représentant les petites échelles :

$$\mathcal{R}_{ij}^{0} = \widetilde{\mathbf{v}_i'\mathbf{v}_j'} - \widetilde{\mathbf{v}_i'}\widetilde{\mathbf{v}_j'}. \tag{2.12}$$

Historiquement, une autre décomposition était apportée par Leonard [Leonard, 1975], de sortent que dans cette définition les termes étaient :

$$\mathcal{L}_{ij}^{0} = \widetilde{\widetilde{\mathbf{v}}_i\widetilde{\mathbf{v}}_j} - \widetilde{\mathbf{v}}_i\widetilde{\mathbf{v}}_j, \tag{2.13}$$

$$\mathcal{C}_{ij}^{0} = \widetilde{\widetilde{\mathbf{v}}_i\mathbf{v}_j'} + \widetilde{\mathbf{v}_i'\widetilde{\mathbf{v}}_j}, \tag{2.14}$$

$$\mathcal{R}_{ij}^{0} = \widetilde{\mathbf{v}_i'\mathbf{v}_j'}. \tag{2.15}$$

Cette décomposition n'était pas invariante par transformation Galiléenne [Speziale, 1985]. Cela fut corrigé par la décomposition de Germano, cette dernière est préférée dans les modèles LES.

Modèle de Smagorinsky

Le modèle de Smagorinsky [Smagorinsky, 1963] est le plus simple des modèles de LES. Le "filtrage" généralement utilisé est la grille de calcul. Il n'y a pas de filtrage explicite dans le modèle de Smagorinsky.

Le modèle sous-grille s'écrit :

$$\nu_{SGS} = 2C_s\Delta|D\mathbf{v}|D\mathbf{v}. \tag{2.16}$$

Dans l'équation (2.16), le coefficient C_s est une constante déterminée empiriquement. Par exemple, dans le cas d'un écoulement homogène et isotrope, $C_s = 0.2$ [Clark et al., 1979], tandis que pour un écoulement de couche limite, une valeur de 0.1 peut être utilisée [Deardorff, 1970]. Enfin Δ est la racine cubique du volume de la cellule de calcul.

Le modèle de Smagorinsky est cependant trop dissipatif ne résolvant que des gros tourbillons. De plus, il surévalue le stress près des parois [Juneja and Brasseur, 1999].

Modèle de Smagorinsky dynamique

Le problème du modèle classique de Smagorinsky est la détermination de la constante C_s. Pour pallier ce problème, des modèles dynamiques ont été implémentée. Un second filtrage est effectué par un filtre "test" de taille $\alpha\Delta$ où α est souvent aux alentours de 2.

Dans cette partie, le filtre de la grille sera de taille Δ tandis que le filtre test sera de taille $\widetilde{\Delta}$. Ici, $\overline{\mathbf{v}}$ sera le champ des vitesses filtré par la taille de la grille et l'écoulement $\widetilde{\mathbf{v}}$ sera filtré par le filtre de taille $\widetilde{\Delta}$.

Le modèle de Smagorinsky dynamique [Germano et al., 1991] est basé sur la décomposition de Germano, (2.9), (2.10),(2.11). Nous définissons ici une décomposition de Germano pour les modèles dynamiques [Germano, 1992] : Le stress pour le filtre $\overline{\Delta}$

$$\tau_{ij}^R = \overline{\mathbf{v}_i\mathbf{v}_j} - \overline{\mathbf{v}}_i\overline{\mathbf{v}}_j, \tag{2.17}$$

et le stress pour le filtre test :

$$T_{ij}^R = \widetilde{\overline{\mathbf{v}_i\mathbf{v}_j}} - \widetilde{\overline{\mathbf{v}}}_i\widetilde{\overline{\mathbf{v}}}_j. \tag{2.18}$$

On en déduit le stress :

$$\mathcal{L}_{ij}^0 = T_{ij} - \widetilde{\tau_{ij}^R} \tag{2.19}$$

$$= \widetilde{\overline{\mathbf{v}}_i\overline{\mathbf{v}}_j} - \widetilde{\overline{\mathbf{v}}}_i\widetilde{\overline{\mathbf{v}}}_j. \tag{2.20}$$

Nous écrivons le modèle de Smagorinsky pour la partie deviatorique des différents stress :

$$\tau_{ij}^r = \tau_{ij}^R - \frac{1}{3}\tau_{kk}^R\delta_{ij} \tag{2.21}$$

$$= -2c_s\overline{\Delta}^2||\overline{D\mathbf{v}}||\overline{D\mathbf{v}}_{ij}. \tag{2.22}$$

De même pour T_{ij}^R :

$$T_{ij}^r = T_{ij}^R - \frac{1}{3}T_{kk}^R\delta_{ij} \tag{2.23}$$

$$= -2c_s\widetilde{\overline{\Delta}}^2||\widetilde{\overline{D\mathbf{v}}}||\widetilde{\overline{D\mathbf{v}}}_{ij}. \tag{2.24}$$

Nous définissons le tenseur M tel que

$$M_{ij} = -2c_s\overline{\Delta}^2\widetilde{||\overline{D\mathbf{v}}||\overline{D\mathbf{v}}}_{ij} - 2c_s\widetilde{\overline{\Delta}}^2||\widetilde{\overline{D\mathbf{v}}}||\widetilde{\overline{D\mathbf{v}}}_{ij}. \tag{2.25}$$

Il est maintenant possible d'exprimer la partie deviatorique de $\mathcal{L}$ en fonction des quantités filtrées.

$$\mathcal{L}^S = c_s M. \tag{2.26}$$

Par conséquent, dans un code LES, les quantités M et $\mathcal{L}$ sont calculées en fonction de $\overline{\mathbf{v}}$. La constante c_s est calculée comme un minimiseur d'erreur en spécifiant [Lilly, 1992] :

$$c_s = \frac{M_{ij}\mathcal{L}_{ij}}{M_{kl}\mathcal{L}_{kl}}. \tag{2.27}$$

Modèle WALE

Le modèle WALE pour Wall adaptive local eddy viscosity [Ducros et al., 1998] est un modèle dessiné pour adapter les modèles LES pour les problèmes proche paroi dans le cas des géométries complexes. En effet, il est à signaler que dans les zones proches paroi, les tourbillons peuvent être de taille inférieure au filtre.

La viscosité s'exprime comme :

$$\nu_{SGS} = (C_m\Delta_s)^2\frac{(S_ij^dS_ij^d)^{3/2}}{(\overline{S}_ij\overline{S}_ij)^{5/2} + (S_ij^dS_ij^d)^{5/4}}. \tag{2.28}$$

2.2 Modélisation "Under location Uncertainty"

Le modèle dit "Under location Uncertainty" décrit dans l'article fondateur [Mémin, 2014] revisite les équation de Navier Stokes. L'idée est la suivante. Dans une simulation grossièrement résolu, d'un point de vue Lagrangien, la position réelle de

la particule est connu à une composante aléatoire près. Cette position se décrit par l'équation suivante :

$$d\mathbf{X}_t = \mathbf{w}(t, \mathbf{X}_t)dt + \sigma(t, \mathbf{X}_t)W(t) \tag{2.29}$$

où $W(t)$ est un processus stochastique. Quelques ouvrages utiles sur le sujet peuvent être cités : [Kunita, 1997], [Øksendal, 2003], [Chow, 2007], [Protter, 2005].

W_t est traditionnellement un processus de Wiener, c'est à dire qu'il correspond aux critères suivants :

— $W_0 = 0$,
— Les accroissements sont stationnaires et indépendants en temps,
— Continu à droite (Cadlag),
— $W_{t+s} - W_t$ suit la loi $\mathcal{N}(0, s)$.

Le mouvement Brownien est un processus de Wiener non différentiable en temps, les équations ULU se dérive de :

$$d\mathbf{X}_t = \tilde{\boldsymbol{u}}(t, \mathbf{X}_t)dt + \boldsymbol{\sigma}(t, \mathbf{X}_t)d\mathbf{B}_t. \tag{2.30}$$

Dans cette expression, les fonctions $u(t, \mathbf{X}_t)$ et $\boldsymbol{\sigma}(t, \mathbf{X}_t)$ sont déterministes. La fonction $\boldsymbol{\sigma}(t, \mathbf{X}_t)$ est déterminée par un noyau $\breve{\boldsymbol{\sigma}}$ de sorte que dans un domaine 3D Ω :

$$\boldsymbol{\sigma}(t, \mathbf{X}_t)d\mathbf{B}_t = \int_\Omega \breve{\boldsymbol{\sigma}}^{i,j}(\mathbf{x}_t, \mathbf{x}')d\mathbf{B}_t^j(\mathbf{x}')d\mathbf{x}' \tag{2.31}$$

Un mouvement brownien est à variation quadratique finie, on définit le tenseur de variation quadratique qui se définie par :

$$\langle X_t, X_t\rangle = \sum_{i=1}^{N} \mathbb{E}[(\mathbf{X}_{t_{i+1}} - \mathbf{X}_{t_i})(\mathbf{X}_{t_{i+1}} - \mathbf{X}_{t_i})^t]. \tag{2.32}$$

Comme le mouvement brownien est un processus gaussien centré, décorrelé en temps, il est possible d'écrire son tenseur de covariance :

$$Cov(\mathbf{x}, \mathbf{y}, t, t') = \mathbb{E}\left[(\boldsymbol{\sigma}(\mathbf{x}, t)d\mathbf{B}_t)(\boldsymbol{\sigma}(\mathbf{y}, t)d\mathbf{B}_t)^t\right] \tag{2.33}$$

$$= \int_\Omega \breve{\boldsymbol{\sigma}}(\mathbf{x}, \mathbf{x}')\breve{\boldsymbol{\sigma}}(\mathbf{y}, \mathbf{x}')^t d\mathbf{x}'\delta(t - t'). \tag{2.34}$$

Une fois défini le tenseur de covariance, le tenseur de variance peut être définie :

$$a^{i,j} = d\left\langle X_t^i, X_t^j \right\rangle \tag{2.35}$$

$$= \int_\Omega \breve{\boldsymbol{\sigma}}^{i,k}(\mathbf{x}, \mathbf{x}')\breve{\boldsymbol{\sigma}}^{k,j}(\mathbf{x}, \mathbf{x}')d\mathbf{x}'. \tag{2.36}$$

Parmi les propriétés essentielles du mouvement brownien nous utiliserons l'isométrie d'Itô. Cette dernière permet d'exprimer de façon déterministes l'espérance du mouvement des particules dans un fluide.

$$E\left[\left(\int_0^t f(\mathbf{X}_t, t)dB_t\right)^2\right] = E\left[\int_0^t f^2(\mathbf{X}_t, t)dt\right]. \tag{2.37}$$

La différentielle d'un processus stochastique ϕ est donnée par la formule d'Itô : Soit ϕ un processus stochastique 2 fois différentiable

$$d\phi(t, \mathbf{X}_t) = \frac{\partial \phi}{\partial t}(t, \mathbf{X}_t) + \sum_{i=0}^{3} \frac{\partial \Phi}{\partial x_i}(t, \mathbf{X}_t)d\mathbf{X}_t^i + \frac{1}{2}\sum_{i,j=1}^{3} \frac{\partial^2 \phi}{\partial x_i x_j} d < \mathbf{X}_t^i, \mathbf{X}_t^j > . \tag{2.38}$$

Nous définissons une dérivée matérielle (ici stochastique). Elle est nommée d'Ito-Wendell dans le contexte d'un flot. Avant cela, nous définissons l'opérateur de transport stochastique :

Soit un traceur θ (température, salinité ...),

$$\mathbb{D}\theta = d_t\theta + (\widetilde{\boldsymbol{u}}^* + \boldsymbol{\sigma} d\mathbf{B}_t) \cdot \nabla\theta - \nabla \cdot (\frac{1}{2}a\nabla\theta)dt. \tag{2.39}$$

Dans la partie droite de l'équation précédente, le premier terme est l'incrément en temps (nous rappelons que la fonction n'est pas différentiable en temps), le deuxième terme est l'advection et enfin le dernier terme est la diffusion.

Si le traceur est passif, par exemple un flotteur dans un courant (il ne modifie pas la dynamique), l'expression de ses moments d'ordre 1 et 2 s'obtiennent par :

$$\partial_t \mathbb{E}(\theta) + \widetilde{\boldsymbol{u}}^* \cdot \mathbb{E}(\theta) = \nabla \cdot (\frac{1}{2}a\nabla\mathbb{E}(\theta)), \tag{2.40}$$

$$\partial_t Var(\theta) + \widetilde{\boldsymbol{u}}^* \cdot Var(\theta) = \nabla \cdot (\frac{1}{2}a\nabla Var(\theta)) + (\nabla\mathbb{E}(\theta))^t a\mathbb{E}(\theta). \tag{2.41}$$

Si le traceur est actif, (c'est le cas de la température, salinité, polluant ...) il est nécessaire de décomposer le traceur en deux parties, l'une régulière $\widetilde{\theta}$e t la seconde oscillante θ' . Cette décomposition est appelée décomposition semi-martingale [Kunita, 1997]. Chaque composante satisfait donc aux équations de transport suivantes :

$$\partial_t \widetilde{\theta} + \widetilde{\boldsymbol{u}}^* \cdot \theta = \nabla \cdot (a \nabla \theta), \tag{2.42}$$

$$d_t \theta' + \boldsymbol{\sigma} d\mathbf{B}_t \cdot \nabla \theta = 0. \tag{2.43}$$

Nous utiliserons les expressions précédentes pour écrire les équation de Navier Stokes avec un traceur menant aux systèmes géophysiques.

Dans l'article [Mémin, 2014], l'équation de Navier Stokes stochastique est obtenue, nous notons ici les principales étapes du raisonnement. La preuve est une adaptation de la preuve habituelle d'obtention des équation de Navier Stokes dans un cas déterministe.

Premièrement, le théorème de transport de Reynolds s'exprime par l'expression suivante :

$$\frac{d}{dt} \int_\Omega q(\mathbf{x}, t) d\mathbf{x} = \int_\Omega \left[d_t q + \left(\nabla \cdot (q \widetilde{\boldsymbol{u}}) - \frac{1}{2} \Delta (aq) dt \right] + \nabla q \cdot \boldsymbol{\sigma} d\mathbf{B}_t \right] d\mathbf{x}. \tag{2.44}$$

A partir de ce théorème, une équation de l'évolution de masse dans un fluide est obtenue, de surcroît, comme il est attendu que la masse totale soit constante, la masse volumique satisfait donc l'équation suivante :

$$d_t \rho + \nabla \cdot (\rho \widetilde{\boldsymbol{u}}) = \frac{1}{2} \left(\Delta (a\rho)|_{\nabla \cdot \boldsymbol{\sigma} = 0} + \frac{1}{2} ||\nabla \boldsymbol{\sigma}||^2 \rho \right) dt - \nabla \cdot (\rho \boldsymbol{\sigma} d\mathbf{B}_t). \tag{2.45}$$

La seconde étape est la conservation du moment. Le principe fondamental de la dynamique se lit ici :

$$d \int_\Omega \rho (\widetilde{\boldsymbol{u}}(\mathbf{x}, t) dt + \boldsymbol{\sigma}(\mathbf{x}, t) d\mathbf{B}_t) d\mathbf{x} = \int_\Omega \boldsymbol{f}(\mathbf{x}, t) d\mathbf{x}. \tag{2.46}$$

Comme l'accélération est très oscillante, l'équation (2.46) doit être vue au sens des distributions, donc soit $h \in C_0^\infty (\mathbb{R}^+$:

$$\int_{\mathbb{R}^+} h(t) d \int_\Omega \rho (\widetilde{\boldsymbol{u}}(\mathbf{x}, t) dt - \int_{\mathbb{R}^+} h'(t) \boldsymbol{\sigma}(\mathbf{x}, t) d\mathbf{B}_t) d\mathbf{x} = \int_{\mathbb{R}^+} h(t) \int_\Omega \boldsymbol{f}(\mathbf{x}, t) d\mathbf{x}. \tag{2.47}$$

En joignant la conservation de la masse et le principe fondamental de la dynamique stochastique, on obtient une équation pour la vitesse :

$$d\int_\Omega \rho w_i d\mathbf{x} = \int_\Omega \Bigg[d_t(\rho w_i) + \nabla\cdot(\rho w_i \widetilde{\boldsymbol{u}}) + ||\nabla\boldsymbol{\sigma}||^2 \rho w_i - \sum_{j,k}\frac{1}{2}\frac{\partial^2}{\partial x_j \partial x_k}(a^{j,k}\rho w_i)|_{\nabla\cdot\boldsymbol{\sigma}=0} dt + \nabla\cdot(\rho w_i \boldsymbol{\sigma} d\mathbf{B}_t) d\mathbf{x} \quad (2.48)$$

Les forces agissant sur le fluide sont les efforts de surface, une extension stochastique s'obtient par l'équation suivante :

$$\Sigma = \int_\Omega -\nabla(pdt + d\widehat{p}_t) + \mu(\Delta\mathbf{U} + \frac{1}{3}\nabla\left(\nabla\cdot\mathbf{U}\right)). \quad (2.49)$$

Dans le premier terme du membre de droite, $d\widehat{p}_t$ est un processus stochastique de moyenne nulle décrivant une contribution aléatoire à la pression provenant de la composante aléatoire de la vitesse. Désormais, il est possible d'écrire une équation de Navier Stokes stochastique :

$$\left(\frac{\partial\widetilde{\boldsymbol{u}}}{\partial t} + \widetilde{\boldsymbol{u}}\nabla^t\widetilde{\boldsymbol{u}}\right)\rho - \frac{1}{2}\sum_{i,j} a_{i,j}\rho\frac{\partial^2\widetilde{\boldsymbol{u}}}{\partial x_i\partial x_j} - \sum_{i,j}\frac{\partial(a_{i,j})\rho}{\partial x_j}\frac{\partial\widetilde{\boldsymbol{u}}}{\partial x_i} = \rho\nabla - \nabla p + \mu\left(\nabla^2\widetilde{\boldsymbol{u}} + \frac{1}{3}\nabla(\nabla\cdot\widetilde{\boldsymbol{u}})\right) \quad (2.50)$$

$$\nabla dp_t = -\rho\widetilde{\boldsymbol{u}}\nabla^t\boldsymbol{\sigma}d\mathbf{B}_t + \mu\left(\nabla^2\widetilde{\boldsymbol{u}} + \frac{1}{3}\nabla(\nabla\cdot\widetilde{\boldsymbol{u}})\right) \quad (2.51)$$

Dans le cas d'un fluide incompressible avec une densité constante, la contrainte appliquée est

$$\nabla\cdot\widetilde{\boldsymbol{u}} = 0. \quad (2.52)$$

Si de plus la composante de vitesse à grande échelle est à divergence nulle :

$$\nabla\cdot\widetilde{\boldsymbol{u}} = 0, \quad (2.53)$$

alors on obtient les contraintes suivantes :

— Contrainte sur la partie aléatoire :

$$\nabla(\boldsymbol{\sigma}dBv_t) = 0. \quad (2.54)$$

— Contrainte sur la variance :

$$\nabla \cdot (\nabla \cdot a) = 0. \tag{2.55}$$

Nous écrivons donc une équation de la mécanique des fluides incompressibles à densité constante :

$$\begin{cases} \left(\dfrac{\partial \widetilde{\boldsymbol{u}}}{\partial_t} + \widetilde{\boldsymbol{u}}\nabla^t\widetilde{\boldsymbol{u}} - \dfrac{1}{2}\displaystyle\sum_{i,j}\partial_i\partial_j(a^{i,j}\widetilde{\boldsymbol{u}})\right) = \rho g - \nabla p + \mu(\Delta\widetilde{\boldsymbol{u}}) \\ \nabla d\widehat{p}_t = -\rho(\widetilde{\boldsymbol{u}}\nabla^t)\boldsymbol{\sigma}d\mathbf{B}_t + \mu\Delta\boldsymbol{\sigma}d\mathbf{B}_t. \end{cases} \tag{2.56}$$

En fonction du choix du tenseur de variance a, il est possible de simuler des Large Eddy simulations.

2.3 Couche limite turbulente

La couche limite turbulente naît du frottement d'un fluide contre une surface ou un autre fluide (l'atmosphère sur le continent ou sur l'océan par exemple). La couche limite est divisée en plusieurs section :

— Zone visqueuse : La turbulence y est majoritairement 2D.
— Zone "buffer"
— Zone logarithmique : Cette partie de la couche limite est aussi nommé turbulente, la turbulence y est 3D. Le profil moyen de la vitesse y est logarithmique.
— Zone "wake" : C'est la zone tampon entre la couche limite et le reste de l'écoulement, la turbulence y décroît continûment.

2.3.1 Section visqueuse

Dans la section visqueuse, la turbulence est 2D. Étant donné que l'écoulement est freiné par le mur, des zones d'écoulement sont ralentie par rapport au reste, c'est ce que l'on nomme "low speed streaks" [Kline et al., 1967] [Smith and Metzler, 1983], ce phénomène est mis en valeur sur la figure 2.1.

En plus des structures streaks, des tourbillons "streamwise" sont présent dans la section visqueuse [Kim et al., 1987] [Jeong et al., 1997]. Ces mouvements "streaks"

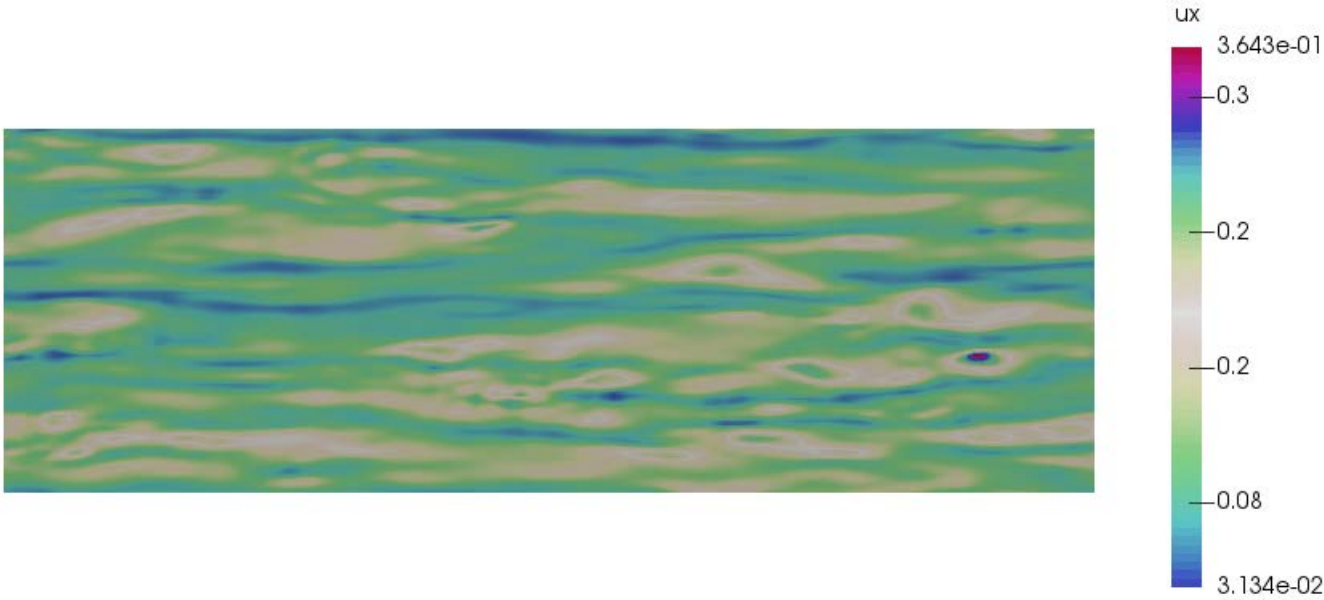

FIGURE 2.1 – Champs de vitesse dans la zone visqueuse d'un canal. Cette image montre des zones plus rapides et plus lentes ce qui corresponds aux streaks. Image tiré d'une simulation à Reynolds 590 à distance 0.0033 H du mur (H étant la hauteur de la couche limite).

sont capable de se maintenir et sont producteurs d'énergie cinétique dans la sous section visqueuse. Les tourbillons cités avant sont le mécanisme qui permet de maintenir les structures streaks. L'énergie cinétique turbulente provient d'un effet "lift-up". Un cycle intervient alors pour les structures cohérentes, les streaks.

2.3.2 Section "buffer"

Entre la zone visqueuse et la zone turbulente, il y a une zone tampon : la zone "buffer". Cette section est caractérisé par la tridimensionnalisation de la turbulence. En effet, les streaks, présents dans la zone visqueuse, s"éloignent lentement du bord avant de s'en échapper rapidement dans la section de buffer. Ce phénomène est nommé éjection. Il s'agit d'une vitesse positive dans le sens du courant et en hauteur ($u'v'$>0). Comme la vitesse doit être conservée, pour chaque éjection, un phénomène tel que $u'v'$<0 coexiste, ce phénomène est appelé sweep.

Sur la figure 2.2, nous montrons une décomposition de l'énergie cinétique turbulente

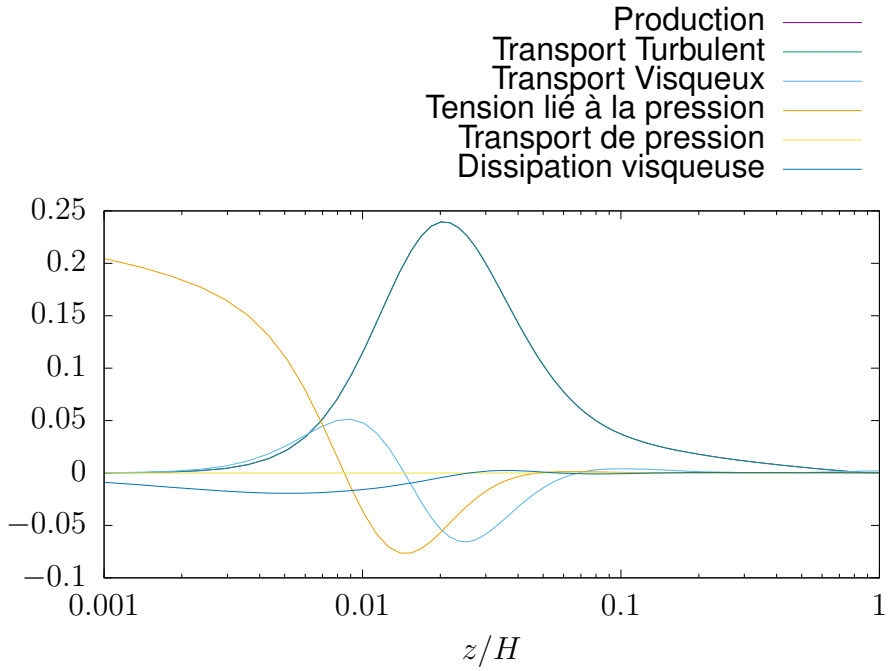

FIGURE 2.2 – Décomposition de la création et dissipation d'énergie cinétique dans un canal $Re_* = 550$

dans la couche limite. Ici c'est un canal à Reynolds 550 qui est proposé. La zone buffer est dans l'intervalle $\frac{z}{H} \in [0.01, 0.05]$. On remarque que la production d'énergie cinétique est bien effectuée dans la zone de buffer alors que la dissipation moléculaire est plus forte dans la zone visqueuse.

2.3.3 Section logarithmique

L'objectif des théories de similitude est d'exprimer de façon universelle les propriétés de la couche limite. L'analyse dimensionnelle basée sur le théorème de Vashy-Buckingham permet d'exprimer les grandeurs physiques (longueur [L], temps [T], masse [M], température [θ]) par de nouveaux paramètres.

Theorem 2.3.1. *Si un problème dépend de n paramètres a_i tels que*

$$f(a_1, a_2, ..., a_n) = 0$$

qui font intervenir p grandeurs physiques, alors, il existe $(n-p)$ variables sans dimensions

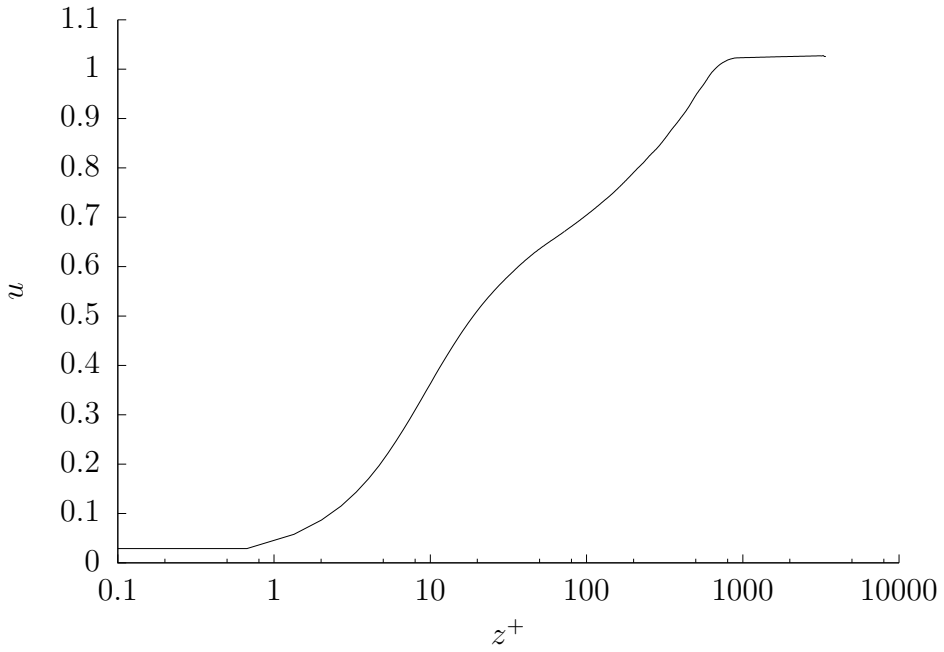

FIGURE 2.3 – Profile de vitesse moyenne dans la couche limite d'un écoulement au dessus d'une plaque laissant apparaître les différente section.

π_i *tel que*

$$f(\pi_1, ..., \pi_{n-p}) = 0$$

.

Une analyse dimensionnelle montre que les paramètres suffisant pour exprimer les grandeurs physiques sont :

— u_* la vitesse de friction $[L][T]^{-1}$,
— ν, ν_t les viscosités moléculaires et turbulentes$[L]^2[T]^{-1}$
— z la coordonnée verticale $[L]$.

Il est convenu que le profil de vitesse dans la section turbulente de la couche limite suit un profil logarithmique. Différentes obtentions de cette hypothèse sont écrites dans [Millikan, 1938], [Monin and Obukhov, 1954].
Une analyse dimensionnelle du gradient de vitesse $\frac{\partial \overline{u}}{\partial z}$ montre que l'on peut construire un paramètre sans dimension :

$$\pi_1 = \frac{z}{u_*}\frac{\partial \overline{u}}{\partial z} \tag{2.57}$$

L'objectif est de définir une fonction sans dimension telle que

$$\frac{z}{u_*}\frac{\partial \overline{u}}{\partial z} = f\left(\frac{z}{\delta}\right) \tag{2.58}$$

où δ est la hauteur de la couche limite.

$$\frac{z}{u_*}\frac{\partial \overline{u}}{\partial z} = \alpha_0 + \sum_{i=1}^{N} \alpha_i \left(\frac{z}{\delta}\right)^i + O(z^{N+1}). \tag{2.59}$$

L'obtention de la loi logarithmique est dans ce cas, une troncature au premier ordre de (2.59) où α_0 est noté κ la constante de Van Karman.
Plus récemment, de nombreux articles développent des fonctions empiriques sans dimensions d'un ordre supérieur, Mizuno et al [Mizuno and Jiménez, 2011], Jimenez [Jimenez and Moser, 2007], Lee et al [Lee and Moser, 2015], [Mckeon et al., 2004], résumé aussi dans Marusic et al [Marusic et al., 2010, Marusic et al., 2013].

Dans [Lee and Moser, 2015], il est proposé une comparaison à très haut nombre de Reynolds de deux formulations de la fonction f :

$$f(z^+) = \frac{z^+}{\kappa(z^+ - a_1)} + a_2 \frac{z^{+2}}{Re_*^2}, \tag{2.60}$$

ainsi que

$$f(z^+) = \left(\frac{1}{\kappa} + \frac{a_1}{Re_*} + a_2 \frac{z^+}{Re_*}\right). \tag{2.61}$$

Il est admis que la couche limite turbulente admet un profil logarithmique, d'autres lois ont co-existé et furent source de polémiques [Cipra, 1996]. Dans leur article référence, Moser, Kim et Mansour [Moser et al., 1999] citent une loi de puissance provenant de [Barenblatt et al., 1997] dans laquelle

$$\overline{u} = u_* A \left(y \frac{u_*}{\nu}\right)^n. \tag{2.62}$$

Ces profils ont été étudiés dans des écoulements de couche limite [George and Castillo, 1997] qui a suggeré que la zone "overlap" contenait cette loi de puissance.

Dans leur article, [Barenblatt et al., 1997] ont argumenté que les lois de puissance contrairement à loi logarithmique ont été écarté sans fondement théoriques, ils vérifient

leur profils sur les données de Nikuradse et le valide sur quasiment l'entièreté du pipe.

Dans une expérience mené à l'université de Princeton, [Zagarola et al., 1997], [Zagarola and Smits, 1998], ils ont montré la coexistence des lois logarithmiques et de puissance. Pour un écoulement à bas nombre de Reynolds, il existe une loi de puissance proche paroi alors que pour un écoulement à haut nombre de Reynolds, il y a une de loi de puissance suivie d'une loi logarithmique. Barenblatt répondant que les données expérimentales de [Zagarola et al., 1997] sont biaisées par une rugosité [Barenblatt and Chorin, 1998]. Cette argument sera infirmé dans [Zagarola and Smits, 1998] et [Mckeon et al., 2004] qui ont répété cette expérience avec un materiel et des méthodes améliorés. Les lois de puissance de [Zagarola et al., 1997] ont été affirmées mais sur un intervalle plus restreint.

Entre temps, un essai mené dans [Wosnik et al., 2000] consiste à considérer que le profil de vitesse est logarithmique dans la région "overlap" selon $(1-r)+c$ où c est un paramètre dépendant du nombre de Reynolds. Cependant, dans une étude plus récente [Wu and Moin, 2008], cet essai s'avère infructueux.

Cette théorie est en terme de similitude incomplète puisque les quantités n et A sont dépendantes du nombre de Reynolds [Pope, 2000].

2.3.4 Zone "wake"

Une fois sortie de la zone logarithmique, l'interface entre cette dernière section et le reste de l'écoulement suit une autre loi et la turbulence y est plus libre et éparse. Le profil de vitesse dans cette section a été étudiée par Coles [Coles, 1956]. Par argument de similitude, le profil de vitesse est modifié :

$$\overline{u} = \frac{1}{\kappa} ln\left(z\frac{u_*}{\nu}\right) + \frac{\Pi}{\kappa} w\left(\frac{z}{\delta}\right). \tag{2.63}$$

L'expression communément employée est : [Pope, 2000]

$$\overline{u} = \frac{1}{\kappa} ln\left(z\frac{u_*}{\nu}\right) + \frac{2\Pi}{\kappa} sin^2\left(\frac{\pi}{2}\frac{z}{\delta}\right). \tag{2.64}$$

Le paramètre Π est dépendant du gradient de pression.

Loi de paroi dans un écoulement stratifié

Dans le cas d'un écoulement de couche limite stratifiée, les hypothèses d'homogénéités spatiales et de stationnarité sont toujours valables. Comme pour la couche limite neutre, nous définissons les variables dimensionnelles qui pilotent la couche limite turbulente stratifiée [Monin et al., 2007] :

L'équation de Navier Stokes simplifiée devient :

$$\frac{\partial}{\partial z}\left((\alpha+\alpha_t)\frac{\partial\overline{\theta}}{\partial z}\right)=0. \tag{2.65}$$

Ce qui revient à noter

$$(\alpha+\alpha_t)\frac{\partial\overline{\theta}}{\partial z}=Q_0. \tag{2.66}$$

C'est l'hypothèse de flux de température turbulente constant.

Par analyse dimensionnelle, il est possible d'exprimer les quantités physiques par 4 paramètres :

— $u_*=\sqrt{\nu\frac{\partial\overline{u}}{\partial n}}$,
— Un paramètre de buoyancy $\frac{g}{\theta_0}$,
— Flux de surface de température Q_0,
— La hauteur z.

Une température et une longueur sont obtenues

$$\theta_*=\frac{Q_0}{u_*}. \tag{2.67}$$

$$L=\frac{u_*^2}{\kappa\beta\theta_*}=\frac{u_*^3}{\kappa\beta Q_0}. \tag{2.68}$$

La longueur (2.68) est la longueur de Monin Obukhov définie dans [Monin and Obukhov, 1954]. Les gradients de vitesses et de températures sont obtenus par des profils sans dimensions tels que

$$\frac{z}{u_*}\frac{\partial\overline{u}}{\partial z}=\phi_m\left(\frac{z}{L}\right) \tag{2.69}$$

et

$$\frac{z}{\theta_*}\frac{\partial\overline{\theta}}{\partial z}=\phi_h\left(\frac{z}{L}\right). \tag{2.70}$$

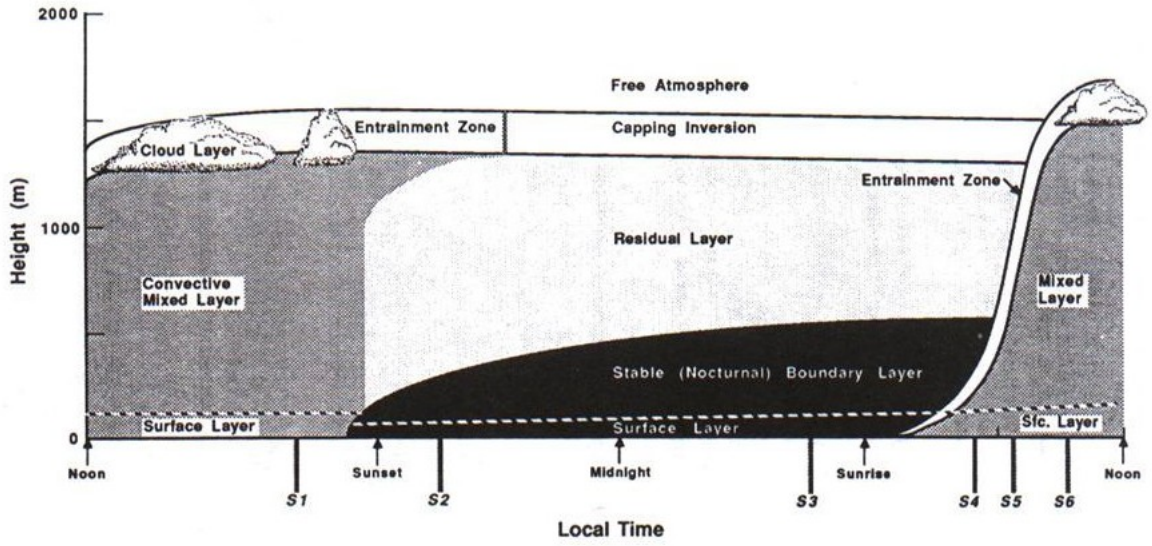

FIGURE 2.4 – Cycle diurne de la couche limite atmosphérique, la journée est régie par un régime convectif (instable) due au réchauffement du sol par le Soleil. La nuit, le régime se stabilise bien qu'il subsiste un régime résiduel instable au dessus. La couche d'inversion est une altitude à laquelle le gradient de température change de signe (négatif en dessous et positif au dessus) assurant une stabilisation de la hauteur de la couche limite.

Les fonctions sans dimensions ϕ_m et ϕ_h définies dans les équations (2.69) et (2.70) sont dépendants de l'état physique de la couche limite. Cet état est divisé en 3 catégories :

- Neutre : La température au sol est égal avec la température dans le reste de la couche limite, dans ce cas, $\phi_h = 0$ et le profil de vitesse reste classique.
- Stable : La température au sol est plus basse que dans la couche limite turbulente. Dans ce cas, par effet de densité, la couche limite devient moins turbulente. C'est le cas pour les écoulements atmosphériques au milieu de la nuit.
- Instable : La température au sol est plus élevée que dans le reste de la couche limite. On parle d'un écoulement convectif. C'est le phénomène qui touche l'atmosphère en journée, l'atmosphère au dessus d'un phénomène El-nino, ou dans une casserole chauffée par le bas.

Les différents régimes au cours d'un cycle diurne sont résumés sur la figure 2.4.

Une atmosphère instable est régie par la force inhérente à la poussée d'Archimède

étant donné qu'il n'y a plus de cisaillement. Par conséquent, les profils de températures et de vitesses sont formellement censés être indépendants de u_*.

Le seul profil de température pouvant être indépendant de u_* est :

$$\overline{\theta} = \theta_0 Q_0^{2/3} \beta^{-1/3} z^{-1/3}. \tag{2.71}$$

Si l'atmosphère est stable, les gradients de vitesses sont différents du cas neutre. En effet, une fonction dite de stabilisation est introduite, il s'agit dans le développement en série entière de pousser d'un ordre supplémentaire par rapport à la loi logarithmique. Les profils sont majoritairement obtenus par expériences sur le terrain, une revue est disponible dans [Högström, 1988]. Citons ici quelques profils souvent utilisés :

— $\phi_m = 1 + 4.7\frac{z}{L}$, $\phi_h = 0.74 + 4.7\frac{z}{L}$ [Businger et al., 1971],

— $\phi_m = \phi_h = 1 + 5\frac{z}{L}$ [Dyer, 1974].

2.4 Résolutions numériques des équations de Navier Stokes

2.4.1 Méthodes des différences finies

La méthode des différences finies est la méthode numérique la plus simple à appréhender. Le principe est d'évaluer chacun des opérateurs différentielle d'une équation différentielle par un schéma dépendant du voisinage d'un point de calcul. Bien évidemment chacun des schéma s'écrit pour des ordres de précisions souhaités.
L'idée qui permet de construire des schémas est le développement de Taylor d'une fonction, cette dernière sera alors exprimée en fonction de ses dérivées.

L'élément central de la méthode des différences finies est la discrétisation des dérivées Nous proposons ici une liste de ces schémas :

— centré

$$\frac{\partial f}{\partial x} = \frac{f(x_{i+1}) - f(x_{i-1})}{x_{i+1} - x_{i-1}}. \tag{2.72}$$

— Décentré En-avant

$$\frac{\partial f}{\partial x} = \frac{f(x_{i+1}) - f(x_i)}{x_{i+1} - x_i} \tag{2.73}$$

Schema	α	β	γ
CDS-2	0	1	0
CDS-4	0	4/3	-1/3
CDS-6	1/3	14/9	1/9
Padé-4	1/4	3/2	0
Padé-6	1/3	14/9	1/9

TABLE 2.1 – Coefficient des schémas compacts pour la dérivée première

— Décentré En-arrière

$$\frac{\partial f}{\partial x} = \frac{f(x_i) - f(x_{i-1})}{x_i - x_{i-1}} \tag{2.74}$$

Pour des maillages réguliers, les schémas d'ordre superieur pour la dérivée d'ordre 2 sont [Ferziger and Peric, 2001] :

— Ordre 3

$$\frac{\partial f}{\partial x} = \frac{2f(x_{i+1}) + 3f(x_i) - 6f(x_{i-1}) + f(x_{i-2})}{6\Delta x} \tag{2.75}$$

— Ordre 4

$$\frac{\partial f}{\partial x} = \frac{-f(x_{i+2}) + 8f(x_{i+1}) - 8f(x_{i-1}) + f(x_{i-2})}{12\Delta x} \tag{2.76}$$

Les équations de Navier Stokes utilisent également un opérateur de Laplacien, ainsi, la dérivée seconde se discrétise par :

$$\frac{\partial^2 f}{\partial x^2} = \frac{f(x_{i-1})(x_i - x_{i-1}) - f(x_i)(x_{i+1} - x_i) + f(x_{i+1})(x_{i+1} - x_i)}{\frac{1}{2}(x_{i+1} - x_{i-1})(x_{i+1} - x_i)(x_i - x_{i-1})} \tag{2.77}$$

Pour des maillages uniformes, des schémas compacts ont été écrits et sont utilisé dans le solveur Incompact3d présentés à la fin de cette sous-section. Ces schémas sont écris sous la forme suivante :

$$\alpha\frac{\partial f(x_{i+1})}{\partial x} + \frac{\partial f(x_i)}{\partial x} + \alpha\frac{\partial f(x_{i-1})}{\partial x} = \beta\frac{f(x_{i+1}) - f(x_{i-1})}{2\Delta_x} + \gamma\frac{f(x_{i+2}) - f(x_{i-2})}{4\Delta_x} \tag{2.78}$$

La précision du schéma est uniquement dépendante des coefficients α, β, γ. L'avantage est certain, il est possible d'augmenter l'ordre de précision en conservant une matrice tri-diagonale et donc aisément inversible. Les coefficients sont notés dans le tableau2.1.

	CDS-6	CDS-6 anti-aliasing
α	2/11	0.47959871686180711
β	12/11	0.42090288706093404
γ	3/11	1.7020738409366740
δ	0	0.16377929427399390

TABLE 2.2 – Coefficient des schémas compacts pour la dérivée seconde

Il est également possible d'écrire un schéma compact pour la dérivée seconde :

$$\alpha\frac{\partial f(x_{i+1})}{\partial x}+\frac{\partial f(x_i)}{\partial x}+\alpha\frac{\partial f(x_{i-1})}{\partial x}=\beta\frac{f(x_{i+1})-f(x_{i-1})}{2\Delta_x^2} + \gamma\frac{f(x_{i+2})-f(x_{i-2})}{4\Delta_x^2}+\delta\frac{f(x_{i+3})-f(x_{i-3})}{9\Delta_x^2} \quad (2.79)$$

Un schéma d'ordre 6 est obtenue par les coefficients présentés dans le tableau 2.2. Le second jeu de paramètre est une discrétisation utile dans l'espace de Fourier pour baisser l'aliasing [Laizet and Lamballais, 2009].

De très nombreux autres schémas jusqu'à une précision d'ordre 10 sont listés dans [Lele, 1992].

Enfin, il reste à écrire un schéma pour la dérivée en temps. Les schéma d'ordre 1 d'Euler sont soit implicite, soit explicite :

— Explicite

$$\frac{u^{n+1}-u^n}{\delta t}=F(u^n) \quad (2.80)$$

— Implicite

$$\frac{u^{n+1}-u^n}{\delta t}=F(u^{n+1}) \quad (2.81)$$

D'autres schémas tels que, par exemple, Runge-Kutta, Adam-Bashford sont aussi implémentables pour les schémas en différences finies.

Les DNS sont résolues par un solveur semi-spectral, autrement dit, résolu en espace dans l'espace de Fourier et dans l'espace physique en temps.

Les équations de la mécanique des fluides étant un problème couplée entre plusieurs variables, de nombreux algorithmes existent, nous avons utilisé le solveur Incompact3d

developpé par Laizet et Lamballais [Laizet and Lamballais, 2009]. Les équations résolues sont :

$$\partial_t \mathbf{v} + \frac{1}{2}\left[\nabla \cdot (\mathbf{v} \otimes \mathbf{v}) + (\mathbf{v} \cdot \nabla)\mathbf{v}\right] - \nabla \cdot (\nu \nabla \mathbf{v}) + \nabla p = \mathbf{f}, \tag{2.82}$$

$$\nabla \cdot \mathbf{v} = 0, \tag{2.83}$$

où $\mathbf{f}$ est le terme de force dans lequel est implémenté la méthode IBM modélisant un fond rugueux, la vitesse y est imposée nulle, plus d'informations sur disponibles dans Gautier [Gautier et al., 2014], Peskin [Peskin, 2002]. La pression est obtenu en résolvant une équation de Poisson dans l'espace de Fourier. Le terme convectif est écrit sous forme skew-symmetric afin de réduire les erreurs d'aliasing et d'assurer la conservation d'énergie [Kravchenko and Moin, 1997].

Premièrement, une vitesse est prédite $\mathbf{v}^*$:

$$\frac{\mathbf{v}^* - \mathbf{v}(t)}{\Delta t} = a_k F(t) - b_k F(t-1) - c_k \nabla p(t) + c_k \mathbf{f}(t),$$

où $F(t) = -\frac{1}{2}\left[\nabla \cdot (\mathbf{v}(t) \otimes \mathbf{v}(t)) - (\mathbf{v}(t) \cdot \nabla)\mathbf{v}(t)\right]$, a_k, b_k et c_k sont les constantes décrivant le schéma temporel. Le terme de pression est obtenu par :

$$\frac{\mathbf{v}^{**} - \mathbf{v}^*}{\Delta t} = c_k \nabla p(t).$$

Afin de satisfaire à la condition de divergence nulle, $p(t + \Delta t)$est calculée par l'équation suivante :

$$\Delta p(t + \Delta t) = \frac{\nabla \cdot \mathbf{v}^{**}}{c_k \delta t}.$$

Enfin , la vitesse est corrigée de sorte que : $\tilde{u}(\mathbf{x}, t) = u^{**}(\mathbf{x}, t) + (U_b - U_t), \tilde{v} = v^{**}, \tilde{w} = w^{**}$.

La nouvelle vitesse est obtenue par :

$$\frac{\mathbf{v}(t + \Delta t) - \tilde{\mathbf{v}}}{\Delta t} = c_k \nabla p(t + 1).$$

2.4.2 Méthodes des volumes finis

La bibliographie sur la méthode des volumes finis pour la résolution de la mécanique des fluides est volumineuse [Krell, 2010], cette méthode est particulièrement populaire chez les ingénieurs, le logiciel Fluent utilise cette méthode. En plus d'Incompact3d, nous avons dans ce travail mené des simulations avec le logiciel OpenSource OpenFoam.[Hrvoje, 1996], [Moukalled et al., 2016] [Holzmann, 2016]. Les notations de cette partie suivent le cours de Eymard, Gallouët et Herbin [Eymard et al., 2000] [Herbin, 2011].

A l'instar des autres méthodes de résolution numérique d'équations différentielles aux dérivées partielles, la méthode des volumes finis a pour objet la transformation d un problème d analyse en un problème algébrique de la forme $A\mathbf{U} = \mathbf{b}$.
A cette fin, le domaine de calcul noté Ω, un convexe borné de dimension d, est divisé en volumes finis dont nous décidons que les points de calculs sont les centres de gravites de ces volumes. Nous adopterons dans la suite de ce document les conventions suivantes :

- Soit une famille d'ouverts convexes polygonaux de dimension d (dimension du problème) $\{K_i, \forall i \in \{1, N\} = I\}$ telle que $\overline{\Omega} = \overline{\cup_{i\in I} K_i}$, nous notons $\mathscr{T} = \{K_i, \forall i \in I\}$ le maillage.
- Chacun des $K \in \mathscr{T}$ est un volume de contrôle,
- $\forall K \in \mathscr{T}$, nous notons $\mathbf{x}_k$ les coordonnées du centre de gravite de K,
- $\forall K \in \mathscr{T}$, nous noterons ϵ_K l'ensemble de ses bords c'est à dire $\epsilon_K = \partial K = \overline{K} \setminus K = \cup_{\sigma\in\epsilon_K} \overline{\sigma}$,
- $\forall K \in \mathscr{T}$, nous notons $\mathscr{N}_K = \{L \in \mathscr{T} \setminus \overline{K} \cap \overline{L} \neq \emptyset\}$, l'ensemble des volumes de contrôles voisins de K,
- $\forall (K, L) \in (\mathscr{T}, \mathscr{N}_K)$, nous notons le bord commun $\sigma_{K,L}$ tel que $\overline{K} \cap \overline{L} = \overline{\sigma}_{K,L}$
- $\forall (K, L) \in (\mathscr{T}, \mathscr{N}_K)$, notons $\mathcal{D}_{K,L}$ le segment liant x_K et x_L. A cela nous associons la distance $d_{K,\sigma}$ entre x_K et le bord $\sigma = \{\sigma \in \epsilon_K | \epsilon_K \cap \mathcal{D}_{K,L} \neq 0\}$.

Remark 2.4.1. *Par souci de simplicité, le segment $[x_K, x_L]$ est une médiatrice de σ. C est le cas pour les maillages structurés.*

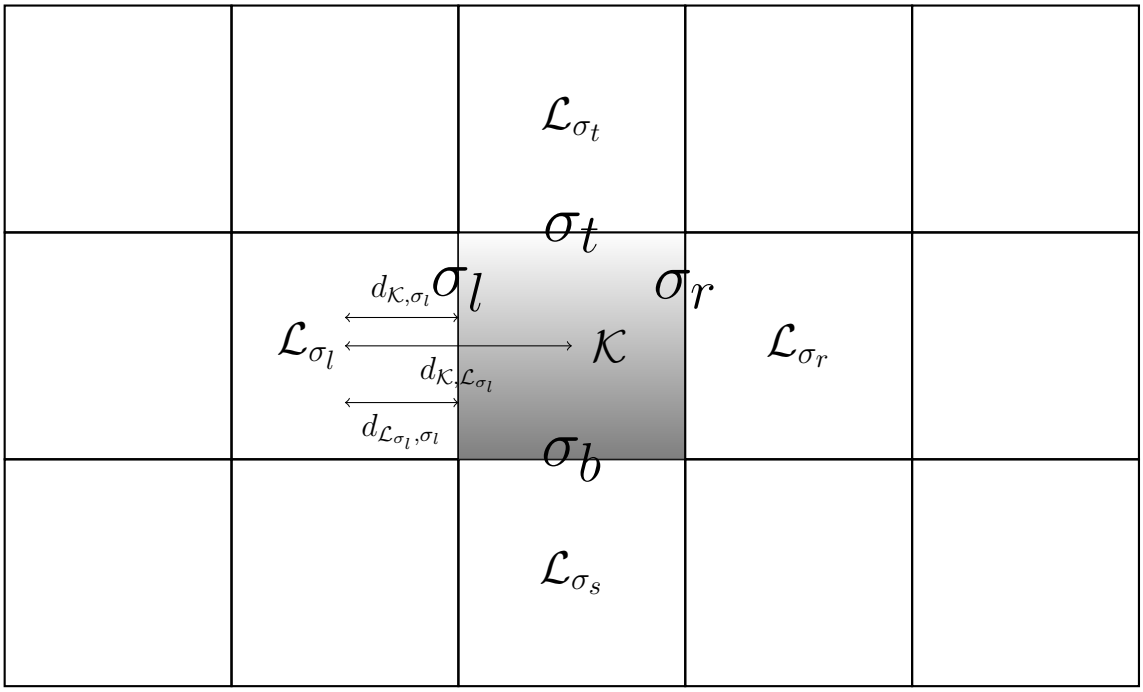

FIGURE 2.5 – Représentation d'un volume de controle $\mathcal{K}$ avec les nomenclatures écrites ci-avant. Ses bords sont σ_i et $\mathcal{L}_{\sigma_i}$ sont les volumes voisins associés à chaque bord.

Le temps est divisé en N intervalles réguliers de longueur Δt de sorte que

$$[0,T] = \cup_{i=0}^{N}[i\Delta t,(i+1)\Delta t]$$

Nous prenons comme exemple la résolution d'un problème de convection diffusion avec condition de Dirichlet nulle sur le bord où l'inconnue est le champ scalaire ψ convecté par une vitesse $\mathbf{v}$

$$\left\{\begin{array}{rcll} \dfrac{\partial\psi}{\partial t} + \nabla\cdot(\mathbf{v}\psi) - \nabla\cdot(\nu\nabla\psi) & = & \mathbf{f} & \Omega, \\ \psi & = & 0 & \Gamma. \end{array}\right. \tag{2.84}$$

Nous recherchons une approximation de ψ constante par morceaux où dans chaque volume de contrôle $K \in \mathscr{T}$, et pour $n \in [0,N]$

$$\forall \mathbf{x} \in K, \quad \psi(t_n,\mathbf{x}) = \psi_K^n$$

.

Remark 2.4.2. *Nous cherchons une approximation à l'ordre 2 quand le problème le permet.*

La méthode des volumes finis se base sur une discrétisation de la forme intégrale du probléme, là où la méthode des différence finie discrétise les formes différentielles et où la méthode des éléments finis utilise une forme faible. Le problème 2.84 en forme intégrale s' écrit :

$$\int_{t_n}^{t_{n+1}} \int_K \frac{\partial \psi}{\partial t} + \nabla \cdot (\mathbf{v}\psi) - \nabla \cdot (\nu \nabla \psi) dt d\mathbf{x} = \int_{t_n}^{t_{n+1}} \int_K \mathbf{f} dt d\mathbf{x} \tag{2.85}$$

La transformation de la forme intégrale vers un problème algébrique en fonction de $\{\psi_K^n, (n, K) \in ([0, T], \mathscr{T})$ sera d'abord en espace puis en temps.

2.4.3 Discrétisation spatiale

Pour le moment, nous nous focalisons sur le problème en espace, nous notons $\psi_K^n = \psi_K$.

La première étape dans le processus est d'approcher l'intégrale calculée. Pour cela, nous avons a disposition l'ensemble des formules de quadrature de Newton-Cotes, de Gauss etc. La méthode la plus élémentaire et la plus simple en terme de calcul est la méthode du point milieu qui utilise la valeur de ψ_K comme polynôme d'interpolation. En se rappelant que x_K est choisi pour être le centre de gravité de K, nous avons la formule suivante :

$$\int_K (\mathbf{x} - \mathbf{x}_K) d\mathbf{x} = 0 \tag{2.86}$$

Proposition 2.4.1. *Soit K un volume de contrôle, si ψ_K est la valeur de ψ au centre de gravité de K, alors la méthode du point milieu est une méthode de quadrature d'ordre 2*

Démonstration. Nous tachons de calculer l'erreur commise en utilisant

$$\int_K \psi(\mathbf{x}) d\mathbf{x} \approx |K| \psi_K$$

oú nous notons $|K|$ le cardinal de K (volume en 3D, aire en 2D, longueur en 1D). En utilisant une formule de Taylor d'ordre 2 centre en x_K, il vient :

$$\psi(\mathbf{x}) = \psi_K + (\mathbf{x} - \mathbf{x}_K) \cdot \nabla\psi(\mathbf{x}_K) + O(||\mathbf{x} - \mathbf{x}_K||^2).$$

Ainsi, en injectant cette série dans

$$\int_K \psi(\mathbf{x}) - \psi_K d\mathbf{x},$$

il vient

$$\int_K \psi(\mathbf{x}) - \psi_K d\mathbf{x} = \int_K (\mathbf{x} - \mathbf{x}_K) \cdot \nabla\psi(\mathbf{x}_K) + O(||\mathbf{x} - \mathbf{x}_K||^2) d\mathbf{x}.$$

Nous savons que x_K est le centre de gravité de K, donc

$$\int_K \psi(\mathbf{x}) - \psi_K d\mathbf{x} = \int_K O(||\mathbf{x} - \mathbf{x}_K||^2) d\mathbf{x}.$$

$$\int_K \psi(\mathbf{x}) = |K|\psi_K + O(|K|^3). \tag{2.87}$$

□

La méthode des trapèzes est une autre méthode de quadrature d'ordre 2 très utilise, si K est un pavé et nous nommons a_i ses sommets, l'intégrale sera calculée par

$$\int_K \psi(\mathbf{x}) \approx \frac{|K|}{8} \sum_{i=0}^{8} \psi_{a_i} d\mathbf{x}$$

L'ordre de l'erreur est similaire, cependant, il est nécessaire par cette méthode de connaître les valeurs sur 8 points de qui ne sont pas des points de calculs qui devront donc être interpolés. Ainsi, pour un gain en précision négligeable, la complexité du calcul serait bien trop augmentée. Le problème de la complexité est augmenté si l'on cherche a approcher l'intégrale par une formule d'ordre encore plus élevée. Ainsi, dans le reste de ce document, nous utiliserons la formule de point milieu pour l'ensemble des intégrations.

Le terme source de notre problème est calculé ainsi :

$$\int_K \mathbf{f} d\mathbf{x} = |K|\overline{f_K}. \tag{2.88}$$

oú $\overline{f_K}$ désigne la moyenne de f dans le volume K.

Terme de convection

Dans cette sous partie, mous nous intéressons à la discrétisation du terme de convection, nous utilisons la formule de la divergence

$$\int_K \nabla \cdot (\mathbf{v}(\mathbf{x})\psi(\mathbf{x}))d\mathbf{x} = \int_{\partial K} \mathbf{v}(\mathbf{x})\psi(\mathbf{x})d\mathbf{x}.$$

Le bord de K est divise en hyperplans réguliers de sorte que

$$\int_K \nabla \cdot (\mathbf{v}(\mathbf{x})\psi(\mathbf{x}))d\mathbf{x} = \sum_{\sigma \in \epsilon_K} \int_\sigma \mathbf{v}(\mathbf{x}) \cdot \mathbf{n}_{K,\sigma}(\mathbf{x})\psi(\mathbf{x})d\mathbf{x}.$$

Où $\mathbf{n}_{K,\sigma}$ le vecteur normal sortant de K sur le bord σ. Nous approchons chacune des intégrales par une formule de point milieu

$$\int_K \nabla \cdot (\mathbf{v}(\mathbf{x})\psi(\mathbf{x}))d\mathbf{x} = \sum_{\sigma \in \epsilon_K} |\sigma|\mathbf{v}(\mathbf{x}_\sigma) \cdot \mathbf{n}_{K,\sigma}(\mathbf{x}_\sigma)\psi_\sigma + O(|\sigma|^3).$$

A ce stade, nous devons exprimer les valeurs de ψ_σ en fonction des points de calculs. Pour cela, diverses techniques d'interpolation de 2e ordre ont été développées avec chacune leurs caractéristiques.

Interpolation linéaire Notons L le volume de contrôle adjacent à K partageant σ comme bord. La méthode la plus évidente pour interpoler ψ_σ est de prendre une moyenne de ψ_K et ψ_L.

$$\psi_\sigma \approx \frac{d_{L,\sigma}}{d_{K,L}}\psi_K + \left(1 - \frac{d_{L,\sigma}}{d_{K,L}}\right)\psi_L \tag{2.89}$$

Dans la littérature, ce schéma est nomme "central differencing" (CD), nous montrons c'est un schéma d'interpolation d'ordre 2. Cependant, ce schéma n'est pas borne, au sens oú il fait apparaître des oscillations numériques n'ayant aucun sens physique rendant nulle toute simulation pour lesquelles la résolution serait trop faible, nous verrons quel sont les caractéristiques permettant d'assurer la cohérence du schéma.

Proposition 2.4.2. *Dans le cas d'un maillage structure, le schéma d'interpolation linéaire est une approximation d'ordre 2.*

Démonstration. Soit $\nabla\cdot$ le vecteur directeur du segment reliant les points $\mathbf{x}_L$ et $\mathbf{x}_K$.

Reprenons un développement de Taylor centre en $\mathbf{x}_K$ à l'ordre 3 de $\psi(\mathbf{x})$

$$\psi(\mathbf{x}) = \psi_K + (\mathbf{x} - \mathbf{x}_K) \cdot \nabla\psi(\mathbf{x}_K) + \frac{1}{2}(\mathbf{x} - \mathbf{x}_K)^2 : \nabla^2\psi(\mathbf{x}_K) + o(||\mathbf{x} - \mathbf{x}_K||^2).$$

En écrivant ce développement en $\mathbf{x}_\sigma$ et en remarquant que $(\mathbf{x}_\sigma - \mathbf{x}_K) = d_{K,\sigma}\nabla\cdot$ il vient

$$\psi_\sigma = \psi_K + d_{K,\sigma}(\nabla \cdot \cdot \nabla\psi(\mathbf{x}_K)) + \frac{1}{2}d_{K,\sigma}^2(\nabla\cdot^2 : \nabla^2\psi(\mathbf{x}_K)) + o(d_{K,\sigma}^2)$$

De même pour ψ_L :

$$\psi_L = \psi_K + d_{K,L}(\nabla \cdot \cdot \nabla\psi(\mathbf{x}_K)) + \frac{1}{2}d_{K,L}^2(\nabla\cdot^2 : \nabla^2\psi(\mathbf{x}_K)) + o(d_{K,L}^2)$$

Utilisant ces deux dernières formules, nous concluons par :

$$\psi_\sigma = \frac{d_{L,\sigma}}{d_{K,L}}\psi_K + \left(1 - \frac{d_{L,\sigma}}{d_{K,L}}\right)\psi_L - \frac{1}{2}d_{L,\sigma}d_{K,\sigma}(\nabla\cdot^2 : \nabla^2\psi(\mathbf{x}_K)) + o(d_{L,\sigma}d_{K,\sigma})$$

□

Terme de diffusion

De la même façon que nous avons discrétisé le terme de convection, nous utilisons le théorème de la divergence :

$$\int_K \nabla \cdot (\nu(\mathbf{x})\nabla\psi(\mathbf{x}))d\mathbf{x} = \sum_{\sigma\in\epsilon_K}\int_\sigma \nu(\mathbf{x})\nabla\psi(\mathbf{x})d\mathbf{x}$$

On utilise la formule de point milieu :

$$\int_K \nabla \cdot (\nu(\mathbf{x})\nabla\psi(\mathbf{x}))d\mathbf{x} = \sum_{\sigma\in\epsilon_K} |\sigma|\nu(\mathbf{x}_\sigma)(\nabla\psi)_\sigma + O(|\sigma|^3) \tag{2.90}$$

Pour conclure le processus pour la diffusion, il nous faut exprimer $(\nabla\psi)_\sigma$ en fonction des points de calcul. Dans le cas où la viscosité est connue, l'interpolation pour la viscosité a une importance moindre, une interpolation linéaire suffira. Dans le cas contraire, le schéma choisi dépendra des variables en jeu (énergie cinétique turbulente, dissipation etc ...).

A partir de là, il est possible d'écrire une procédure résolvant l'équation de Navier

Stokes couplée avec des équations de fermeture à la RANS.

La procédure pour résoudre ce problème est l'algorithme SIMPLEC, acronyme pour "Semi-Implicit Method for Pressure Linked Equations", la lettre C signifie consistant, c'est une amélioration de l'algorithme présenté dans [Patankar, 1980].

Input : Vitesse $\mathbf{v}$
pression$p$
l'énergie cinétique turbulente k
Viscosité turbulente $\nu_t(k)$
Initialisation : $\mathbf{v}$ aux bords
p aux bords
k aux bords
while *Les variables ne convergent pas* **do**
Prédire une vitesse à divergence non nulle $\mathbf{v}$
Appliquer les conditions de bords
Calculer le champ de pression
Correction de la vitesse pour la rendre à divergence nulle
Calculer les équations de fermetures Mise à jour de la viscosité turbulente
end

Algorithm 1: Etapes de l'algorithme SIMPLEC

Nous expliquons en détail l'algorithme. Les prochaines étapes sont répétées tant que la convergence n'est pas achevée.

Predictor Tout d'abord, nous prédisons la vitesse par :

$$\nabla \cdot (\mathbf{v}^{(n)} \otimes \mathbf{v}^{(n-1)}) - \nabla \cdot \left[(2\nu + \nu_t(k^{(n-1)}))\, D\mathbf{v}^{(n)} \right] + \nabla p^{(n-1)} = \mathbf{f}. \tag{2.91}$$

L'équation précédente est discrétisée par le formalisme suivant : Soit $\mathcal{T}$ le maillage, $\mathcal{K}$ un volume de contrôle, l'objectif est d'exprimer chaque vecteur de (2.91) comme :

$$\mathbf{v}_{\mathcal{K}} = \sum_{\mathcal{L} \in \mathcal{N}(\mathcal{K})} \Psi(\mathbf{v}_{\mathcal{L}}). \tag{2.92}$$

où $\mathcal{N}(\mathcal{K})$ est le voisinage de $\mathcal{K}$.

L'équation du moment est résolue dans chaque triangle $\mathcal{K}$ par :

$$\int_{\mathcal{K}} \nabla\cdot(\mathbf{v}(\mathbf{x})^{(n)} \otimes \mathbf{v}(\mathbf{x})^{(n-1)}) - \nabla\cdot((2\nu + \nu_t(k(\mathbf{x}))^{(n-1)})\nabla\cdot\mathbf{v}(\mathbf{x})^{(n)}) + \nabla p^{(n-1)}(\mathbf{x}) d\mathbf{x} = \int_{\mathcal{K}} \mathbf{f}(\mathbf{x}) d\mathbf{x}. \tag{2.93}$$

Par application de la condition de divergence nulle, l'équation précédente devient :

$$\int_{\partial\mathcal{K}}[(\mathbf{v}(\mathbf{x})^{(n)}\otimes\mathbf{v}(\mathbf{x})^{(n-1)})-((2\nu+\nu_t(k(\mathbf{x}))^{(n-1)})\nabla\cdot\mathbf{v}(\mathbf{x})^{(n)})]\cdot\mathbf{n}_{\partial K}(\mathbf{x})d\mathbf{x}+\int_{\mathcal{K}}\nabla p(\mathbf{x})^{(n-1)}d\mathbf{x}=\int_{\mathcal{K}}\mathbf{f}(\mathbf{x})d\mathbf{x}, \tag{2.94}$$

où $\mathbf{n}_{\partial K}$ est le vecteur normal extérieur à $\mathcal{K}$. Dans la suite, le terme R_2 est l'erreur provenant de la discrétisation due au schéma d'ordre 2. Les schémas d'advection sont :

$$\int_{\partial\mathcal{K}}[(\mathbf{v}(\mathbf{x})^{(n)}\otimes\mathbf{v}(\mathbf{x})^{(n-1)})d\mathbf{x}=\sum_{\sigma\in\partial\mathcal{K}}\int_{\sigma}(\mathbf{v}(\mathbf{x})^{(n)}\otimes\mathbf{v}(\mathbf{x})^{(n-1)})\cdot\mathbf{n}_{\sigma}(\mathbf{x})d\mathbf{x}. \tag{2.95}$$

Où σ est une face du volume $\mathcal{K}$, Un schéma centré mène à :

$$\int_{\partial\mathcal{K}}[(\mathbf{v}(\mathbf{x})^{(n)}\otimes\mathbf{v}(\mathbf{x})^{(n-1)})d\mathbf{x}=\sum_{\sigma\in\partial\mathcal{K}}|\sigma|(\mathbf{v}_{\sigma}^{(n)}\otimes\mathbf{v}_{\sigma}^{(n-1)})\cdot\mathbf{n}_{\sigma}(\mathbf{x}). \tag{2.96}$$

Où $\mathbf{v}_\sigma$ est la valeur de $\mathbf{v}$ au centre de σ.

$$\int_{\partial\mathcal{K}}(\mathbf{v}(\mathbf{x})^{(n)}\otimes\mathbf{v}(\mathbf{x})^{(n-1)})d\mathbf{x}=\sum_{\sigma\in\partial\mathcal{K}}|\sigma|(\mathbf{v}_{\sigma}^{(n)}\otimes\mathbf{v}_{\sigma}^{(n-1)})\cdot\mathbf{n}_{\sigma}(\mathbf{x})+R_2, \tag{2.97}$$

$$\int_{\partial\mathcal{K}}(\mathbf{v}(\mathbf{x})^{(n)}\otimes\mathbf{v}(\mathbf{x})^{(n-1)})=\sum_{\sigma\in\partial\mathcal{K}}|\sigma|\mathbf{v}_{\sigma}^{(n)}\cdot\mathbf{n}_{\sigma}\mathbf{v}_{\sigma}^{(n-1)}+R_2. \tag{2.98}$$

Nous notons $\phi_\sigma=|\sigma|\mathbf{v}_\sigma^{(n-1)}\cdot\mathbf{n}_\sigma$ le flux à travers σ, cependant, il manque une équation pour résoudre cette variable. Il reste à exprimer $\mathbf{v}_\sigma$ comme une fonction de $\mathbf{v}_\mathcal{K}$ pour chaque $\mathcal{K}\in\mathcal{T}$. Par exemple, un schéma linéaire peut être utilisé :

$$\mathbf{v}_{\sigma}^{(n)}=f_{\mathcal{K}}\mathbf{v}_{\mathcal{K}}^{(n)}+(1-f_{\mathcal{K}})\mathbf{v}_{\mathcal{L}_\sigma}^{(n)}, \tag{2.99}$$

où

$$f_{\mathcal{K}_\sigma}=\frac{d_{\mathcal{L}_\sigma}}{d_{\mathcal{L}_\sigma\mathcal{K}}},$$

$d_{\mathcal{L}_\sigma}$ est la distance entre les barycentres des volumes $\mathcal{L}_\sigma$ (voisinage de $\mathcal{K}$) séparés par σ.

Soit $C=\int_{\partial\mathcal{K}}(\mathbf{v}(\mathbf{x})^{(n)}\otimes\mathbf{v}(\mathbf{x})^{(n-1)})$, nous obtenons :

$$C=\sum_{\sigma\in\partial\mathcal{K}}\phi_\sigma\left(f_{\mathcal{K}_\sigma}\mathbf{v}_{\mathcal{K}}^{(n)}+(1-f_{\mathcal{K}_\sigma})\mathbf{v}_{\mathcal{L}_\sigma}^{(n)}\right). \tag{2.100}$$

Le terme de diffusion est discrétisé par :

$$\int_{\partial\mathcal{K}}((2\nu+\nu_t(k(\mathbf{x})^{(n-1)})\nabla\cdot\mathbf{v}(\mathbf{x})^{(n)})]\cdot\mathbf{n}_{\partial K}(\mathbf{x}) = \sum_{\sigma\in\partial\mathcal{K}}|\sigma|(2\nu+\nu_{t\sigma})(\nabla\mathbf{v}^{(n)})_\sigma\cdot\mathbf{n}_\sigma+R_2, \quad (2.101)$$

où $\nu_{t\sigma}$ est la viscosité turbulente sur la face. Afin de conserver la linéarité, la viscosité turbulente est calculée ultérieurement. Le gradient est calculé de la façon suivante :

$$|\sigma|(\nabla\mathbf{v})^{(n)}_\sigma\cdot\mathbf{n}_\sigma = |\sigma|\frac{\mathbf{v}^{(n)}_{\mathcal{L}_\sigma}-\mathbf{v}^{(n)}_{\mathcal{K}}}{d_{\mathcal{L}_\sigma\mathcal{K}}}. \quad (2.102)$$

Soit $D = \int_{\partial\mathcal{K}}((2\nu+\nu_t(k(\mathbf{x})^{(n-1)})\nabla\cdot\mathbf{v}(\mathbf{x})^{(n)})]\cdot\mathbf{n}_{\partial K}(\mathbf{x})$, nous obtenons,

$$D = \sum_{\sigma\in\partial\mathcal{K}}|\sigma|(2\nu+\nu_{t\sigma})\frac{\mathbf{v}^{(n)}_{\mathcal{L}_\sigma}-\mathbf{v}^{(n)}_{\mathcal{K}}}{d_{\mathcal{L}_\sigma\mathcal{K}}}. \quad (2.103)$$

Dans l'esprit de [Rhie and Chow, 1983],le gradient de pression n'est pas discrétisé à ce stade. L'intégrale de force est :

$$\int_{\mathcal{K}}\mathbf{f}(\mathbf{x})d\mathbf{x} = \frac{\mathbf{f}_K}{|\mathcal{K}|}. \quad (2.104)$$

Nous utilisons l'ensemble des équations (2.100),(2.102) and (2.104) pour former le problème algébrique

$$A_K\mathbf{v}^n_K = \Phi(\mathbf{v}^n, k^{n-1}) + \nabla p^{n-1}, \quad (2.105)$$

où A_k est la matrice des inconnues et des conditions de Dirichlet, $\Phi(\mathbf{v})$ est le vecteur contenant les informations sur les voisins.

Le problème algébrique mène à une solution prédite $\mathbf{v}^{(n)}$ nommée $\mathbf{v}^{(n-1/2)}$ qui n'assure pas une condition à divergence nulle.

Pressure equation Nous nous intéressons maintenant à l'obtention du champ de pression à travers la résolution de l'équation de Poisson suivante :

$$\Delta p^{(n)} = -\nabla\cdot\left(\nabla\cdot(\mathbf{v}^{(n)}\otimes\mathbf{v}^{(n-1)}) - \nabla\cdot\left[(2\nu+\nu_t(k^{(n-1)}))\,D\mathbf{v}^{(n)}\right] - \mathbf{f}\right). \quad (2.106)$$

Proposition 2.4.1. *Le champs de pression est une solution du système algébrique*

suivant :

$$\nabla \cdot \left(\frac{1}{(A_{\mathcal{K}} - \sum_{\sigma \in \partial \mathcal{K}} A_{\mathcal{L}_\sigma})} \nabla p^{(n)} \right) = \nabla \cdot \left[\frac{1}{A_{\mathcal{K}}} \left(\sum_{\sigma \in \partial \mathcal{K}} A_{\mathcal{L}_\sigma} \mathbf{v}_{\mathcal{L}_\sigma}^{(n-1/2)} \right) - \left(\frac{1}{A_{\mathcal{K}}} - \frac{1}{A_{\mathcal{K}} - \sum_{\sigma \in \partial \mathcal{K}} A_{\mathcal{L}_\sigma}} \nabla p^{(n-1/2)} \right) \right]. \quad (2.107)$$

Démonstration. Considérons l'équation suivante (2.105) :

$$A_{\mathcal{K}} \mathbf{v}_{\mathcal{K}}^{(n-1/2)} = \sum_{\sigma \in \partial \mathcal{K}} A_{\mathcal{L}_\sigma} \mathbf{v}_{\mathcal{L}_\sigma}^{(n-1/2)} + \nabla p^{(n-1)}. \quad (2.108)$$

Soit $\widetilde{\mathbf{v}_{\mathcal{K}}}$ la correction de la vitesse telle que :

$$\mathbf{v}_{\mathcal{K}}^{(n)} = \mathbf{v}_{\mathcal{K}}^{(n-1/2)} + \widetilde{\mathbf{v}_{\mathcal{K}}}, \quad (2.109)$$

est une solution à divergence nulle de

$$\nabla \cdot (\mathbf{v}^{(n)} \otimes \mathbf{v}^{(n-1)}) - \nabla \cdot \left[(2\nu + \nu_t(k^{(n-1)})) \, D\mathbf{v}^{(n)} \right] + \nabla p^{(n)} = \mathbf{f}, \quad (2.110)$$

qui est discrétisée comme suit :

$$A_{\mathcal{K}} \mathbf{v}_{\mathcal{K}}^{(n)} = \sum_{\sigma \in \partial \mathcal{K}} A_{\mathcal{L}_\sigma} \mathbf{v}_{\mathcal{L}_\sigma}^{(n)} + \nabla p^{(n)}. \quad (2.111)$$

Nous soustrayons (2.108)et (2.111) pour obtenir :

$$A_{\mathcal{K}} \widetilde{\mathbf{v}_{\mathcal{K}}} = \sum_{\sigma \in \partial \mathcal{K}} A_{\mathcal{L}_\sigma} \widetilde{\mathbf{v}_{\mathcal{L}_\sigma}} + \nabla \widetilde{p}, \quad (2.112)$$

où $\widetilde{p}$ est la correction de la pression. Le point particulier de l'algorithme SIMPLEC qui provient de [Van Doormaal and Raithby, 1984] est de soustraire $\sum_{\sigma \in \partial \mathcal{K}} A_{\mathcal{K}}$ dans chaque coté de l'équation 2.112. Cette équation devient :

$$\left(A_{\mathcal{K}} - \sum_{\sigma \in \partial \mathcal{K}} A_{\mathcal{L}_\sigma} \right) \widetilde{\mathbf{v}_{\mathcal{K}}} = \sum_{\sigma \in \partial \mathcal{K}} A_{\mathcal{L}_\sigma} \left(\widetilde{\mathbf{v}_{\mathcal{L}_\sigma}} - \widetilde{\mathbf{v}_{\mathcal{K}}} \right) + \nabla \widetilde{p}. \quad (2.113)$$

L'expression suivante est consistante :

$$\sum_{\sigma \in \partial \mathcal{K}} A_{\mathcal{L}_\sigma} \left(\widetilde{\mathbf{v}_{\mathcal{L}_\sigma}} - \widetilde{\mathbf{v}_{\mathcal{K}}} \right) = 0. \quad (2.114)$$

Nous écrivons la condition de divergence nulle dans le triangle $\mathcal{K}$ comme

$$\nabla \cdot \mathbf{v}_{\mathcal{K}}^{(n)} = 0. \tag{2.115}$$

Nous arrangeons l'équation (2.108), pour obtenir (2.113) avec l'approximation (2.114) et la contrainte (2.115).

$$\mathbf{v}_{\mathcal{K}}^{(n)} = -\frac{1}{(A_{\mathcal{K}} - \sum_{\sigma\in\partial\mathcal{K}} A_{\mathcal{L}_\sigma})}\nabla\widetilde{p} + \frac{1}{A_{\mathcal{K}}}\left(\sum_{\sigma\in\partial\mathcal{K}} A_{\mathcal{L}_\sigma}\mathbf{v}_{\mathcal{L}_\sigma}^{(n-1/2)} - \nabla p^{(n-1)}\right). \tag{2.116}$$

Nous arrangeons la partie droite de l'équation (2.116) de sorte à obtenir $p^{(n)}$:

$$\begin{aligned}\mathbf{v}_{\mathcal{K}}^{(n)} = -\frac{1}{(A_{\mathcal{K}} - \sum_{\sigma\in\partial\mathcal{K}} A_{\mathcal{L}_\sigma})}\nabla p^{(n)} + \\ \frac{1}{A_{\mathcal{K}}}\left(\sum_{\sigma\in\partial\mathcal{K}} A_{\mathcal{L}_\sigma}\mathbf{v}_{\mathcal{L}_\sigma}^{(n-1/2)}\right) - \left(\frac{1}{A_{\mathcal{K}}} - \frac{1}{A_{\mathcal{K}} - \sum_{\sigma\in\partial\mathcal{K}} A_{\mathcal{L}_\sigma}}\nabla p^{(n-1)}\right).\end{aligned} \tag{2.117}$$

Finalement, nous appliquons l'opérateur divergence à l'équation (2.117) pour obtenir l'équation sur la pression.

$$\begin{aligned}\nabla \cdot \left(\frac{1}{(A_{\mathcal{K}} - \sum_{\sigma\in\partial\mathcal{K}} A_{\mathcal{L}_\sigma})}\nabla p^{(n)}\right) = \nabla \cdot \left[\frac{1}{A_{\mathcal{K}}}\left(\sum_{\sigma\in\partial\mathcal{K}} A_{\mathcal{L}_\sigma}\mathbf{v}_{\mathcal{L}_\sigma}^{(n-1/2)}\right) - \right. \\ \left.\left(\frac{1}{A_{\mathcal{K}}} - \frac{1}{A_{\mathcal{K}} - \sum_{\sigma\in\partial\mathcal{K}} A_{\mathcal{L}_\sigma}}\nabla p^{(n-1)}\right)\right].\end{aligned} \tag{2.118}$$

□

A ce stade, les flux sur les bords ϕ_σ^n sont mis à jour.

Correction Maintenant, nous avons une vitesse non corrigée qui ne satisfait pas l'incompressibilité ainsi qu'une pression, nous allons utiliser cette pression pour corriger la vitesse :

$$\nabla \cdot (\mathbf{v}^{(n)} \otimes \mathbf{v}^{(n-1)}) - \nabla \cdot \left[(2\nu + \nu_t(k^{(n-1)}))\, D\mathbf{v}^{(n)}\right] + \nabla p^{(n)} = \mathbf{f}. \tag{2.119}$$

Nous obtenons une vitesse à divergence nulle $\mathbf{v}$. Dans l'algorithme SIMPLEC ,la correction est réalisée ainsi : nous considérons l'équation (2.117) de sorte que :

$$\begin{aligned}\mathbf{v}_{\mathcal{K}}^{(n)} &= \mathbf{v}_{\mathcal{K}}^{(n-1/2)} + \widetilde{\mathbf{v}_{\mathcal{K}}} \\ \mathbf{v}_{\mathcal{K}}^{(n)} &= \frac{1}{A_{\mathcal{K}}}\left(\sum_{\sigma\in\partial\mathcal{K}} A_{\mathcal{L}_\sigma}\mathbf{v}_{\mathcal{L}_\sigma}^{(n-1/2)}\right) - \left(\frac{1}{A_{\mathcal{K}}} - \frac{1}{\sum_{\sigma\in\partial\mathcal{K}} A_{\mathcal{L}_\sigma}}\right)\nabla p^{(n-1)} - \left(\frac{1}{A_{\mathcal{K}} - \sum_{\sigma\in\partial\mathcal{K}} A_{\mathcal{L}_\sigma}}\nabla p\right).\end{aligned} \tag{2.120}$$

Ceci termine le couplage entre la vitesse et la pression.

Équation de fermeture La dernière tâche est de résoudre les variables de fermetures turbulentes.

Prenons une modélisation à 1 équation, l'énergie cinétique turbulente est calculée par l'équation suivante :

$$\int_{\mathcal{K}} \mathbf{v}(\mathbf{x})^{(n)}\cdot\nabla k(\mathbf{x})^{(n)} - \nabla\cdot((2\mu + \mu_t(k(\mathbf{x})^{(n-1)})\nabla k(\mathbf{x})^{(n)}) - \frac{k(\mathbf{x})^{(n)}\sqrt{k(\mathbf{x})^{(n-1)}}}{l(\mathbf{x})}d\mathbf{x} = \int_{\mathcal{K}} 2\nu_t(k(\mathbf{x})^{(n)}|D\mathbf{v}(\mathbf{x})^{(n)}|^2 d\mathbf{x}. \tag{2.121}$$

Les termes d'advection et de diffusion sont discrétisés comme ci-dessus. Le problème algébrique à résoudre devient :

$$B_{\mathcal{K}}k_{\mathcal{K}}^{(n)} = \sum_{\sigma\in\partial\mathcal{K}} B_{\mathcal{L}_\sigma}k_{\mathcal{L}_\sigma}^{(n)} + \Psi(\mathbf{v}_{\mathcal{K}}^{(n)}). \tag{2.122}$$

Ceci termine le calcul de k^n, p^n and $\mathbf{v}^n$.

2.5 Fonction à la paroi (wall-functions)

La turbulence est régie par deux sections différentes. Cependant, c'est la section visqueuse qui génère par friction la turbulence. Cependant, cette zone est très confinée et donc afin de la résoudre correctement, il est nécessaire d'avoir un maillage très raffiné au niveau du sol, cela est trop coûteux. Voir la figure 2.6 . De fait, dans l'ensemble des simulations géophysiques, le premier point de calcul est dans la section turbulente. Par conséquent, au lieu d'implémenter une condition $\mathbf{v} = 0$ au sol, il est nécessaire d'écrire une autre relation. Cette propriété est aussi vraie pour les autres variables de la turbulence.

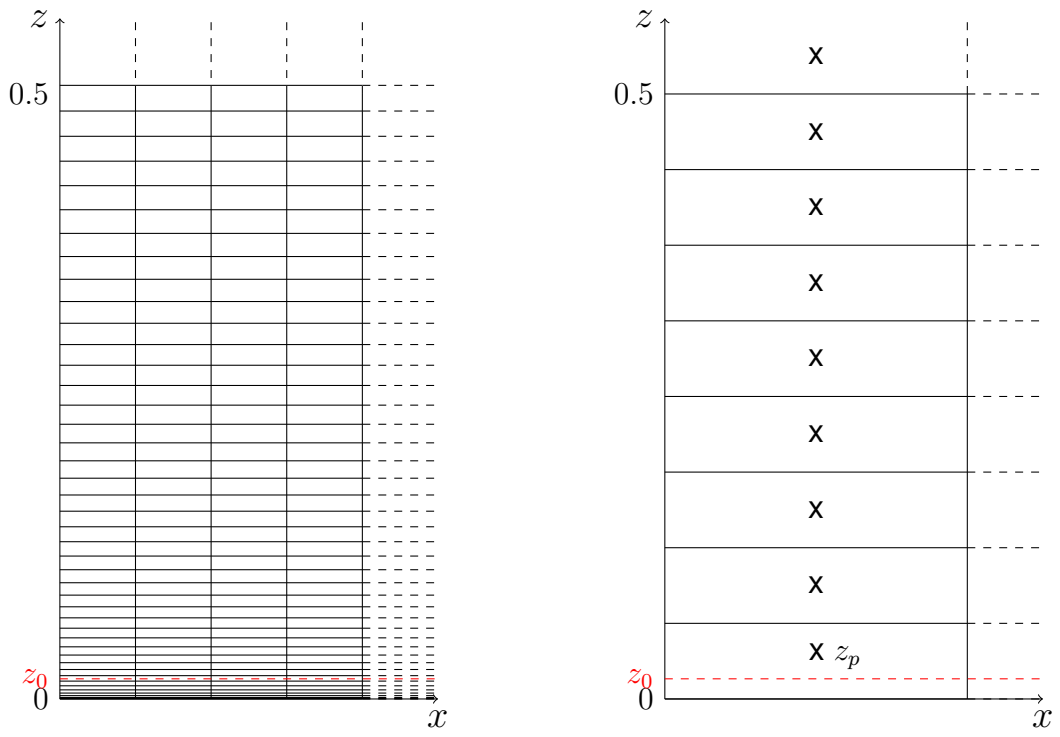

FIGURE 2.6 – Résolution en z d'un maillage de DNS à gauche et d'un maillage de LES ou RANS à droite.

Citons par exemple Blocken [Blocken et al., 2007], dans cette publication, les chercheurs se sont intéressés à l'implémentation des fonctions à la paroi dans le cas où cette dernière n'est pas plate. La rugosité de la paroi est quantifiée par un paramètre k_s (qui est nul si la paroi est lisse), ils obtiennent pour un écoulement non stratifié les lois suivantes :

$$U_p = \frac{u_\tau^2}{\kappa u^*} ln\left(\frac{E u^* y_p}{\nu(1 + C_s k_s^+)}\right) \tag{2.123}$$

$$k_p = \frac{u_*^2}{\sqrt{C_\mu}} \tag{2.124}$$

$$\varepsilon_p = \frac{u_*^3}{\kappa y_p} \tag{2.125}$$

Dans l'équation 2.123, la modification due à la rugosité est le terme $(1 + C_s k_s^+)$, on déduit aisément la fonction sans rugosité, E est une constante empirique ≈ 9.793 selon

les auteurs) et $u^* = C_\mu^{1/4} k_p^{1/2}$ est une autre vitesse de friction.

Concernant les équations des modèles RANS, Kalitzin [Kalitzin et al., 2005] publie un ensemble de conditions pouvant être satisfaites au dessus ou dans la zone visqueuse. Par exemple, pour le modèle $k - \omega$, ils obtiennent

$$\omega_p^+ = \frac{1}{\kappa \sqrt{C_\mu} y_p^+}$$
$$k_p^+ = \frac{1}{\sqrt{C_\mu}}$$

CHAPITRE 3

A NS-TKE MODEL WITH WALL LAW AND PHYSICAL MIXING LENGTH

Dans le troisième chapitre de ce manuscrit ; nous nous focaliserons sur le modèle RANS à une équation de fermeture. L'intérêt d'un tel modèle par rapport aux modèles à 2 ainsi que 3 équations réside dans la quantité de calcul économisée. Le modèle RANS à une équation dépend de la longueur de mélange de Prandtl. Cette notion provenant de la cinétique des gaz, l'analogie en turbulence n'est pas triviale. Plusieurs solutions simples existent, premièrement en considérant la longueur comme étant égale à la longueur du maillage, c'est une propriété utilisée par les modèles de Smagorinsky (LES) ; cependant, elle n'utilise pas les différences de physique à travers la couche limite. Une autre modélisation populaire est une longueur de mélange linéaire, celle-ci mène algébriquement à la loi logarithmique suivie par le profil des vitesses. Nous allons proposer dans ce chapitre une nouvelle formule universelle obtenue par simulations numériques pour des écoulements de canal allant jusqu'à $Re_* \approx 5200$.

Une autre levée dans la résolution des problèmes à haut nombre de Reynolds est la condition de bords aux parois. En effet ; une condition écrite de sorte que la vitesse de l'écoulement $\mathbf{v} = 0$ et son énergie cinétique $k = 0$. Le profil des vitesses est connue pour être logarithmique en fonction de la hauteur à la paroi, ainsi la condition de bords sans glissement imposerait une condition trop forte au profil. Nous utiliserons dans les simulations numériques proposées un modèle dit de Glaucker-Manning [Gauckler, 1867] pour le champ des vitesses. Nous allons aussi proposer une nouvelle condition de bords de type Neumann, obtenue à travers l'analyse dimensionnelle pour l'énergie cinétique. Les conditions de bords habituellement proposées pour l'énergie cinétique ainsi que pour les autres variables de modèles RANS sont de type Dirichlet [Blocken et al., 2007]. Nous proposons ici une condition de Neumann.

Avec une condition de bords de type Neumann pour la vitesse et pour l'énergie cinétique turbulente ; nous démontrons l'existence d'une solution faible au système d'équations découlant du problème :

$$\begin{cases} (\overline{\mathbf{v}} \cdot \nabla)\, \overline{\mathbf{v}} - \nabla \cdot \left[(2\nu + C_v \ell \sqrt{k})\, D\overline{\mathbf{v}} \right] + \nabla \overline{p} = \mathbf{f}, \\ \nabla \cdot \overline{\mathbf{v}} = 0, \\ \overline{\mathbf{v}} \cdot \nabla k - \nabla \cdot ((\mu + C_k \ell \sqrt{k}) \nabla k) = C_k \ell \sqrt{k} |D\overline{\mathbf{v}}|^2 - \ell^{-1} k \sqrt{|k|}, \\ \overline{\mathbf{v}} \cdot \mathbf{n} = 0, \quad -[(2\nu + \nu_t) D\overline{\mathbf{v}} \cdot \mathbf{n}]_\tau = \alpha_v |\overline{\mathbf{v}}| \overline{\mathbf{v}}, \\ \frac{\partial k}{\partial n} = A(k). \end{cases} \tag{3.1}$$

La preuve de l'existence d'une solution faible est rendue difficile par le terme source de l'équation résolvant l'énergie cinétique turbulente ; en effet ce terme est dans L^1 ce qui nous empêche d'utiliser le contexte variationnel habituel. Nous proposons donc une preuve pour un problème de Neumann elliptique avec un terme source dans L^1. [Andreu et al., 2007], [Andreu et al., 2008], [Chabrowski, 2007].

La validation de ce modèle avec ces lois de parois sera validée à travers des simulations numériques ayant pour objectif de reproduire des résultats de DNS.

3.1 Introduction

The simulation of a turbulent flow by a direct numerical simulation using the Navier-Stokes Equations (NSE) remains today out of reach for a high Reynolds number Re. Indeed, the Kolmogorov's laws imply that $O(Re^{9/4})$ degrees of freedom are neccessary to do so, which is too large in term of computing power for realistic turbulent flows, such as geophysical flows, the Reynolds number of which is larger than 10^8. This is why turbulence models are always essential until now. Among all turbulence models, two main classes can be distinguished : the Large Eddy Simulation models (LES), such as the Smagorinsky's model, and the Reynolds-Averaged Navier-Stokes (RANS) models, such as the $k-\varepsilon$ model [Chacòn Rebollo and Lewandowski, 2014, Mohammadi and Pironneau, 1994, Pope, 2000, Sagaut, 2006].

The aim of this paper is to investigate the ability of one of the most basic incompressible RANS model to faithfully reproduce a neutral boundary layer. The model under consideration is a by-product of the $k-\varepsilon$ model with only one closure equation, specified by the following PDE system :

$$\begin{cases} (\overline{\mathbf{v}}\cdot\nabla)\,\overline{\mathbf{v}} - \nabla\cdot\left[(2\nu + C_v\ell\sqrt{k})\,D\overline{\mathbf{v}}\right] + \nabla\overline{p} = \mathbf{f}, \\ \nabla\cdot\overline{\mathbf{v}} = 0, \\ \overline{\mathbf{v}}\cdot\nabla k - \nabla\cdot((\mu + C_k\ell\sqrt{k})\nabla k) = C_k\ell\sqrt{k}|D\overline{\mathbf{v}}|^2 - \ell^{-1}k\sqrt{|k|}, \end{cases} \tag{3.2}$$

where "$\nabla\cdot$" is the divergence operator and

i) $\overline{\mathbf{v}} = (\overline{u}, \overline{v}, \overline{w})$ is the long time average of the flow [Berselli and Lewandowski, 2018, Lewandowski, 2015] (or any stationnary statistical mean, which does not make any difference thanks to the ergodic assumption about turbulent flows, see for instance in [Frisch, 1995]), $\overline{p}$ the mean pressure, k the turbulent kinetic energy (TKE), $D\overline{\mathbf{v}} = (1/2)(\nabla\overline{\mathbf{v}} + \nabla\overline{\mathbf{v}}^T)$ the deformation tensor,

ii) $\nu > 0$ is the kinematic viscosity of the flow, $\mu > 0$ a diffusion coefficient, $\mathbf{f}$ a source term expressing possible external forces,

iii) $\nu_t = C_v\ell\sqrt{k}$ is the eddy viscosity, $\mu_t = C_k\ell\sqrt{k}$ the eddy diffusion, ℓ the Prandtl mixing length, $C_v > 0$ and $C_k > 0$ are dimensionless constants.

This type of one-closure equation model can be a good alternative to the full two-closure equations $k-\varepsilon$ model, which one is expensive and very hard to be implemented in a code, although very accurate and effective. Evolutionary versions of

(3.2) have been used for large scale oceanic simulations ([Blanke and Delecluse, 1993, Lewandowski, 1997a]), and also in marine engineering to simulate a 2D flow around a fishing net [Lewandowski and Pichot, 2007].

A natural question is : how far can such one-closure model be used instead of the full $k-\varepsilon$ model ? It depends strongly on how the mixing length ℓ and the boundary conditions are set.

In [Lewandowski and Pichot, 2007], simulations are performed at $Re = 10^5$. In this work, the mixing length $\ell = \ell_i$ is constant on each triangle $K_i \in \mathcal{T}_h$, where $\mathcal{T}_h$ is the mesh, ℓ_i the length of the longer edge of K_i. We have used in [Lewandowski and Pichot, 2007] the software FreeFEM++, `http://www.freefem.org/`, based on the finite element method. Data were provided by a measurement campaign performed in IFREMER Boulogne, France. At the domain input, $\overline{\mathbf{v}} = (\overline{u}_i, 0, 0)$ is given according to the data and $k = 0$, at the domain output $\overline{\mathbf{v}} \cdot \mathbf{n} = 0$ and $k = 0$. At the top, the bottom and the lateral boundaries, the boundary of the fishing net, $\overline{\mathbf{v}} = 0$ and $k = 0$, which is like doing a DNS in a 2D boundary layer. Although this strategy provided excellent results compared with the experimental data in this 2D framework, it will not work in a 3D case for high Reynolds numbers. Therefore, we must consider another approach.

To fix ideas, let us consider a 3D flow over a plate, placed at $z = 0$. The flow domain is the half space $\{z \geq 0\}$, divided in two regions :

i) the boundary layer $\{0 \leq z \leq z_0\}$, z_0 being the height of the boundary layer,

ii) $\{z_0 \leq z\}$, where a turbulent model is implemented.

At $z = z_0$, the boundary condition satisfied by the mean velocity is usually a wall law, one of the most popular being the Glaucker-Manning law (see in [Chacòn Rebollo and Lewandowski, 2014, Chapter 5]) [1] :

$$\overline{\mathbf{v}} \cdot \mathbf{n} = 0, \quad -[(2\nu + \nu_t) D\overline{\mathbf{v}} \cdot \mathbf{n}]_\tau = \alpha_v |\overline{\mathbf{v}}| \overline{\mathbf{v}}. \tag{3.3}$$

When the model involves the TKE, people used to set at $z = z_0$,

$$k = |\overline{\mathbf{v}}|^2. \tag{3.4}$$

The boundary layer is often modeled by a given continuous steady profile depending on z, most of the time linear in the viscous sublayer and then logarithmic. Howe-

1. Let $\mathbf{n}$ denotes the outward normal vector at the boundary, and for a given vector $\mathbf{w}$, $\mathbf{w}_\tau = \mathbf{w} - (\mathbf{w}\cdot\mathbf{n})\mathbf{n}$ its tangential part. We refer to ν_t as any eddy viscosity.

ver, there are several different models [Chacòn Rebollo and Lewandowski, 2014, Schlichting and Gersten, 2000, Spalding, 1961], more or less sophisticated, depending on the desired degree of accuracy and the available computing power. When stratification occurs, such as in the atmosphere, the Monin Obukhov theory [Monin and Obukhov, 1954] applies, yielding to add stabilizing functions to the log profile, which may be controversial [Pelletier, 2018]. Moreover, in the case of the ocean, there are many other boundary layer models, as for instance the Pacanowski-Philander model, based on closure equations with eddy viscosities, functions of the Richardson number [Bennis et al., 2010].

Therefore, there is no universal boundary layer model. This is what motivates that we aim to evaluate the performances of the model (3.2) in a boundary layer, which means taking z_0 at least of order of the height of the viscous sublayer. We will do so in the case of a flat bottom, then in the case of a non trivial topography as displaids in figure 3.1, called the rough case.

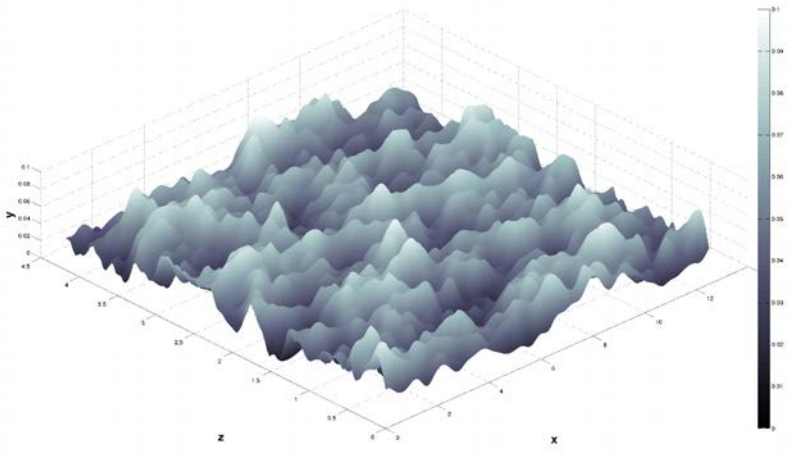

FIGURE 3.1 – Non trivial topography, the rough case

A natural option is solving (3.2) with the boundary conditions (3.3)-(3.4) inside the boundary layer, provided that the mixing length ℓ is specified. However, we know that the resulting boundary value problem, for a given smooth function $\ell = \ell(\mathbf{x})$, yields serious mathematical and numerical complications (see in [Chacòn Rebollo and Lewandowski, 2014, Chapters 7,8] and additional comments in section 3.5.1 below), mainly because of (3.4), that must be reconsidered. In this

perspective, we have modeled in this paper an alternative boundary condition for the TKE k, which is a non linear Neumann boundary condition, see (3.18) below. We get a more affordable mathematical struture than that provided by (3.4) (see section 3.5). The resulting model, (3.2)-(3.3)-(3.18), is appointed by the acronym NSTKE.

For running the NSTKE model, the mixing length ℓ must be determined. In the full $k-\varepsilon$ model, it is deduced from k and ε by the standard formula

$$\ell = \frac{k^{3/2}}{\varepsilon}, \tag{3.5}$$

which cannot be directly used in our NSTKE model, since we do not have an equation to compute ε. Noting $Re_\star$ the frictional Reynolds number (see definition (3.23) below), we choose to determine $\ell = \ell(z, Re_\star)$ from direct numerical simulation (DNS) and interpolations, based on the formula (3.5), in both flat and rough cases (see formula (3.39) and (3.40), complemented by (3.41), (3.43) and (3.44) for the calculation of the different coefficients)[2]. Our DNS are compared to the DNS of Moser et all [Lee and Moser, 2015, Moser et al., 1999], which serve as the benchmark for our results.

We could have checked the method of [Lewandowski and Pichot, 2007], taking ℓ equal to the size of the local mesh size, which is cheap in terms of computational cost. However, this would not have taken into account the structure of the flow that we study, although the comparison between both options could be interesting.

We have carried out several numerical simulations with the NSTKE model, up to $Re_\star = 10000$, in both flat and rough cases, with ℓ interpolated from the DNS. The first series of simulations yields mixed results. We finally get correct profiles in a large part of the boundary layer, but at the price of significant corrections in the formula for ℓ. This is what makes us think that this one-closure equation RANS model cannot be used as a universal model for more complex situations, like the turbulent ocean-atmosphere mixing layer, where buoyancy and stratification must be included. This suggests that a customized full $k-\varepsilon$ model should be designed for the ocean-atmosphere interaction, if one believes the Monin-Obukhov theory to be wrong, and if one prefers the RANS models to the LES models.

The organization of the paper follows the plan of the introduction : TKE boundary

2. In the process, we also calculate the values of the constants C_v and C_k involved in the eddy viscosities

condition modeling, DNS and mixing length formula, NSTKE simulations and analysis of the results and convergence. The paper ended by and apendice, in which one proves the existence of a weak solution to the NSTKE model, by a proof that can be extended to the evolutionnary case, which is a clear theoretical advantage of the model.

3.2 Boundary condition modeling

The aim of this section is the derivation of the boundary condition (3.17) for the turbulent kinetic energy, TKE in the following. Before doing this, we set up the geometrical framework and recall the log law.

3.2.1 Geometry and boundary layers assumptions

The computational box Ω is defined by (see figure 3.2)

$$\Omega = [0, L_x] \times [0, L_y] \times [0, L_z].$$

For the simplicity, we assume that the flow field $(\overline{\mathbf{v}}, \overline{p}, k)$ satisfies periodic boundary conditions in the x and y directions. To be more specific, $(\overline{\mathbf{v}}, \overline{p}, k)$ is defined on $\mathbb{R}^2 \times [0, L_z]$, and when it is at least of class C^2, for $\psi = \overline{\mathbf{v}}, \overline{p}, k$,

$$\forall\, (m, n) \in \mathbb{N}^2, \quad \forall\, (x, y, z) \in \Omega, \quad \psi(x + nL_x, y + mL_y, z) = \psi(x, y, z). \tag{3.6}$$

To carry out the modeling process, we assume that in the boundary layer, the mean velocity $\overline{\mathbf{v}}$ has a constant direction, $\overline{\mathbf{v}} = (\overline{u}, 0, 0)$, and is homogeneous in the x-y axes. Therefore, $\overline{u} = \overline{u}(z)$, which is a standard assumption.

It is generally accepted [Chacòn Rebollo and Lewandowski, 2014, Lewandowski, 1997a, Mohammadi and Pironneau, 1994, Pope, 2000] that there exists $0 < z_0 << z_1$ such that in the absence of stratification or buoyancy effects, $\overline{u}$ has in $[0, z_1]$ the following profil,

$$\forall\, z \in [0, z_0], \qquad \overline{u}(z) = \frac{u_\star}{\kappa} \frac{z}{z_0}, \tag{3.7}$$

$$\forall\, z \in [z_0, z_1], \qquad \overline{u}(z) = \frac{u_\star}{\kappa} \left(\log\left(\frac{z}{z_0} \right) + 1 \right), \tag{3.8}$$

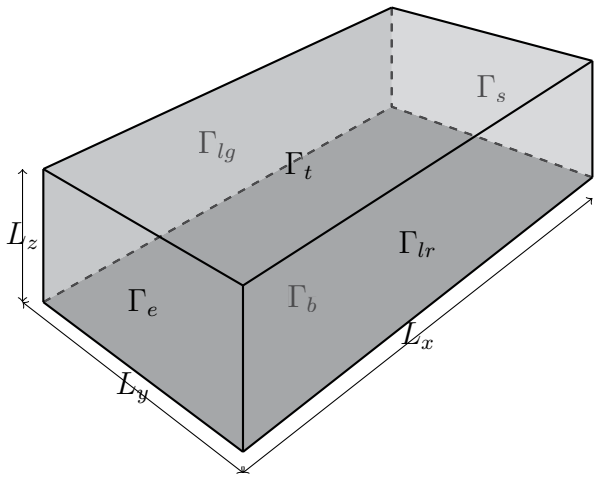

FIGURE 3.2 – 3D Representation of Ω

where $u_\star$ denotes the friction velocity, given by

$$u_\star = \sqrt{\nu \frac{\partial \overline{u}}{\partial z}(0)}, \tag{3.9}$$

and κ is the Van Karmàn constant, the numerical value of which is estimated between 0.35 and 0.42 [Foken, 2006]. Here z_1 denotes the height of the boundary layer.

3.2.2 Boundary condition for the TKE

We model in this section a boundary condition for the TKE at $z = z_0$, alternative to (3.4). In order to proceed, we first must :

i) Determine the eddy diffusion coefficient μ_t in $[0, z_0]$,

ii) Settle the profile of the TKE k in the same region, in which we assume $k = k(z)$.

i) According to standard uses, we assume that in $[0, z_0]$, the flow is driven by the mixing length ℓ and the friction velocity $u_\star$, and that

$$\ell = \kappa z.$$

Therefore, as z and $u_\star$ are dimensionaly independant, $(z, u_\star)$ is a dimensional basis (see [Chacòn Rebollo and Lewandowski, 2014, Chapter 3]). We deduce from straightforward

calculation based on dimensional analysis the usual formula :

$$\forall\, z \in [0, z_0], \quad \mu_t(z) = \kappa_\mu u_\star z, \tag{3.10}$$

where κ_μ is a dimensionless constant.

ii) It is natural to set $k(0) = 0$ and $k(z_0) = \overline{u}^2(z_0)$, which yields, by (3.7),

$$k(0) = 0, \quad k(z_0) = \frac{u_\star^2}{\kappa^2}. \tag{3.11}$$

Following (3.7) we enforce k to be linear in the viscous sublayer, which leads by (3.11) to

$$\forall\, z \in [0, z_0], \quad k(z) = \frac{u_\star^2}{\kappa^2}\frac{z}{z_0}. \tag{3.12}$$

We derive from these modeling hypotheses the following result.

Proposition 3.2.1. *Assume that (3.12) and (3.10) hold. Then the following expansion holds :*

$$\forall\, z \in]0, z_0], \quad \mu_t \frac{dk}{dz} = \kappa\kappa_\mu \left(\frac{z_0}{z}\right)^{\frac{1}{2}} k\sqrt{k} + o(z). \tag{3.13}$$

Démonstration. We expand $k(z)$ between 0 and z :

$$k(0) = k(z) - z\frac{dk}{dz}(z) + o(z). \tag{3.14}$$

By (3.12), we get

$$z\frac{dk}{dz}(z) = \frac{u_\star^2}{\kappa^2}\left(\frac{z}{z_0}\right) + o(z). \tag{3.15}$$

We combine (3.10) and (3.15), and we get

$$\mu_t \frac{dk}{dz}(z) = \frac{\kappa_\mu}{\kappa^2} u_\star^3 \left(\frac{z}{z_0}\right) + o(z). \tag{3.16}$$

The relation (3.12) can be rewritten for $z > 0$ as

$$u_\star = \kappa \left(\frac{z_0}{z}\right)^{\frac{1}{2}} \sqrt{k(z)},$$

that we insert in (3.16) to eliminate $u_\star$, which yields (3.13). □

When we neglect the remaining term in (3.13), we get at $\Gamma_{b,c} = \{z = z_0\}$ the following

boundary condition for k :

$$\mu_t \frac{dk}{dz} = \alpha_k k\sqrt{k}, \tag{3.17}$$

where $\alpha_k = \kappa\kappa_\mu$. By symmetry, a similar analysis can be carried out at the top of the computational box. Therefore, we can summarize the results in the following general setting :

$$-\mu_t \frac{\partial k}{\partial \mathbf{n}} = \alpha_k k\sqrt{k} \quad \text{at} \quad \mathbb{R}^2 \times (\{z = z_0\} \cup \{z = L_z - z_0\}) = G_c. \tag{3.18}$$

Let Om_c denotes the infinite strip

$$\mathsf{Om}_c = \mathbb{R}^2 \times [z_0, L_z - z_0]. \tag{3.19}$$

We are led to introduce the following boundary value problem :

$$\begin{cases} (\overline{\mathbf{v}} \cdot \nabla)\,\overline{\mathbf{v}} - \nabla \cdot [(2\nu + \nu_t(k))\, D\overline{\mathbf{v}}] + \nabla p &= \mathbf{f} & \text{in } \mathsf{Om}_c, \\ \nabla \cdot \overline{\mathbf{v}} &= 0 & \text{in } \mathsf{Om}_c, \\ \overline{\mathbf{v}} \cdot \nabla k - \nabla \cdot [(\mu + \mu_t(k) \nabla k] &= \nu_t(k)|D\overline{\mathbf{v}}|^2 - \ell^{-1} k\sqrt{|k|} & \text{in } \mathsf{Om}_c, \\ -[(2\nu + \nu_t(k))D\overline{\mathbf{v}} \cdot \mathbf{n}]_\tau &= \alpha_v |\overline{\mathbf{v}}|\overline{\mathbf{v}} & \text{on } G_c, \\ \overline{\mathbf{v}} \cdot \mathbf{n} &= 0 & \text{on } G_c, \\ -(\mu + \mu_t(k))\nabla k \cdot \mathbf{n} &= \alpha_k k\sqrt{|k|} & \text{on } G_c, \end{cases} \tag{3.20}$$

with periodic boundary conditions in the x and y axes, as defined by (3.6). The proof of the existence of a weak solution to the system (3.20) is postponed to appendice 3.5.

Remark 3.2.1. *We have replaced μ_t by $\mu + \mu_t$ to avoid degeneration issues in the TKE part of the system, where $\mu > 0$ is a small stabilizing mathematical parameter.*

Remark 3.2.2. *In the context of the modeling assumptions of this section, the wall law* (3.3) *becomes*

$$(2\nu + \nu_t)\frac{\partial \overline{u}}{\partial z} = \alpha_v \overline{u}^2 \quad \textit{at} \quad z = z_0, \tag{3.21}$$

$$(2\nu + \nu_t)\frac{\partial \overline{u}}{\partial z} = -\alpha_v \overline{u}^2 \quad \textit{at} \quad z = L_z - z_0 \tag{3.22}$$

Remark 3.2.3. *The coefficients $\alpha_v > 0$ and $\alpha_k > 0$ involved in the boundary conditions of* (3.20) *must be set. This point is discussed in section 3.4.1 below.*

3.3 Direct Numerical Simulations

We perform and validate in this section several DNS, in order to derive a universal formula for the mixing length ℓ as a function of the frictional Reynolds number

$$Re_\star = \frac{u_\star H}{\nu}, \tag{3.23}$$

the friction velocity $u_\star$ being given by (3.9), $H = L_z/2$. The frictional Reynolds number is the main control parameter in this study. To close the set of parameters, we enforce u to be equal to 1 at $z = H$. We will use the following standard relation between $u_\star$ and $Re_\star$:

$$u_\star = \left(\frac{1}{0.41}\log Re_\star + 5.5\right)^{-1}, \tag{3.24}$$

which is a byproduct of the log law. Therefore, $Re_\star$ yields $u_\star$ and then ν from (3.23) re-written as

$$\frac{\nu}{u_\star} = \frac{H}{Re_\star}. \tag{3.25}$$

Note that $\nu/u_\star$ is the natural length scale of the flow.

3.3.1 Settings and results

To begin with, we set data and parameters for the simulations.

i) Software and equations. The direct numerical simulations (DNS) are performed by using the parallelised flow solver Incompact3d (see at `https://www.incompact3d.com/`). The numerical shemes implemented in this software are detailed in [Laizet and Lamballais, 2009, Laizet and Li, 2011, Lele, 1992]. The equations, solved in $\Omega = [0, L_x] \times [0, L_y] \times [0, L_z]$, are [3] :

$$\begin{cases} \partial_t \mathbf{v} + \dfrac{1}{2}\left[\nabla\cdot(\mathbf{v}\otimes\mathbf{v}) + (\mathbf{v}\cdot\nabla)\mathbf{v}\right] - \nabla\cdot(\nu\nabla\mathbf{v}) + \nabla p = \mathbf{f}, \\ \nabla\cdot\mathbf{v} = 0, \\ \mathbf{v}|_{z=0} = \mathbf{v}|_{z=L_z} = 0, \quad \mathbf{v} \text{ periodic in the } x-y \text{ axes}, \\ \mathbf{v}|_{t=0} = \mathbf{v}_0. \end{cases} \tag{3.26}$$

3. numerically more convenient, theoretically equivalent to the standard Navier-Stokes equations

The source term $\mathbf{f}$ is constant and given by

$$\mathbf{f} = \left(\frac{u_*^2}{H}, 0, 0\right). \tag{3.27}$$

ii) The initial data. The initial data $\mathbf{v}_0$ is a random pertubation of the field

$$\mathbf{U}(x, y, z) = \left(\left(\frac{\widetilde{z}}{H}\right)^{\frac{1}{7}}, 0, 0\right), \tag{3.28}$$

where $\widetilde{z} = \min(z, 2H - z)$. The corresponding profile coincides more or less with the log profile, without the singularity at $z = 0$ and $z = L_z$. In order to get a flow that is not too trivial and looks like a turbulent flow, we take $\mathbf{v}_0$ such that

$$\mathbf{v}_0 = \mathbf{U} + 0.125\eta(x, y, \widetilde{z}, \omega)\left(\left(\frac{\widetilde{z}}{H}\right)^{\frac{1}{7}}, 1, 1\right). \tag{3.29}$$

The function $\eta \in [-1, 1]$ is a zero mean Gaussian random variable : at each point (x, y, z) and each run labelized by ω, the code randomly picks a number $\eta(x, y, z, \omega)$, thanks to a standard numerical random generator. This field is not divergence free, but the code automatically corrects this error at the first time step.

iii) Parameters of the simulations. They are the same as those of Moser et al [Moser et al., 1999], which is our benchmark. We have performed four DNS : three of them are in the flat case (see figure 3.2), for $Re_\star = 180, 360, 550$, and one in the rough case (see figure 3.1) for $Re_\star = 180$.

Let Δt denotes the time step, T the final time of the simulation, (n_x, n_y, n_y) determines the mesh size, which means that the discretization space-step Δa in the a-axis ($a = x, y, z$) is given by

$$\Delta a = \frac{L_a}{n_a}.$$

Run	(L_x, L_y, L_z)	(n_x, n_y, n_z)	Δt	T
DNS-FLAT-180	$(4\pi, 4/3\pi, 2)$	$(128, 128, 128)$	0.005	$3600\nu/u_\star^2$
DNS-FLAT-360	$(2\pi, 2/3\pi, 2)$	$(256, 128, 192)$	0.0025	$3600\nu/u_\star^2$
DNS-FLAT-550	$(2\pi, 2/3\pi, 2)$	$(256, 256, 257)$	0.00125	$1800\nu/u_\star^2$
DNS-ROUGH -180	$(4\pi, 4/3\pi, 2)$	$(128, 128, 128)$	0.005	$3600\nu/u_\star^2$

TABLE 3.1 – Parameters for each DNS

Since the Kolmogorov scale is getting smaller as $Re_\star$ increases, the computational cost is dramatically expensive for large $Re_\star$. This is why the dimensions of the computational boxes in DNS-FLAT-360 and 550 are smaller than the dimensions in DNS-FLAT-180.

iv) Results in the flat case.[4] Our results are reported in figure 3.3 where we have plotted the mean adimensionalized streamwise component of the velocity as well as the results of Moser et all [Moser et al., 1999]. In particular, if $\mathbf{v}_{\text{DNS}} = (u_{\text{DNS}}, v_{\text{DNS}}, w_{\text{DNS}})$ denotes the calculated field by the DNS,

$$\overline{u}(z) = \frac{1}{T n_x n_y} \sum_{n=0}^{T/\Delta t} \sum_{j=0}^{n_x} \sum_{k=0}^{n_y} u_{\text{DNS}} \left(n\Delta t, j\frac{L_x}{n_x}, k\frac{L_y}{n_y}, z \right). \tag{3.30}$$

We observe a very good correspondance between our results of those of

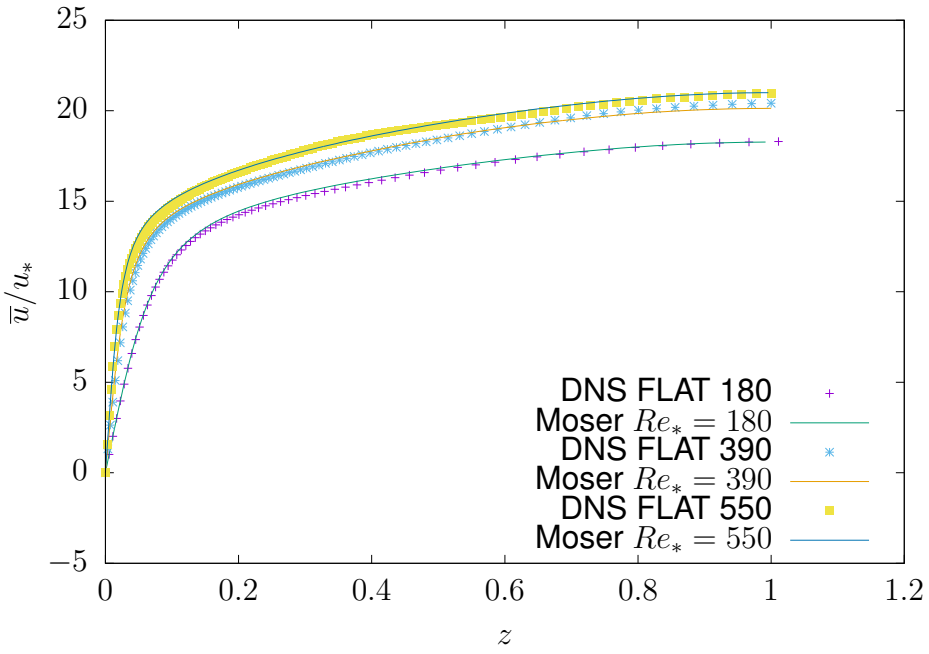

FIGURE 3.3 – Streamwise velocity profile compared to those of [Moser et al., 1999].

[Moser et al., 1999], at least in average. This validates our DNS in the flat case, which allows us to think that our DNS in the rough case[5], outlined below, is accurate.

4. For the simplicity, the overline always means an average which will be specified case by case, to avoid the risks of confusion. We also may use $\langle \cdot \rangle$ for time averages.

5. So far we know, there is no avaible data in the litterature for such a rough case.

v) The rough case. The rough topography displayed in figure 3.1 is built in three steps as follows.

1) We construct regularly spaced gaussian domes centered at (x_i, y_i) with random heights $\tilde{\Lambda}_i$ and variances σ_i, leading to the primary topography $z = \tilde{\Lambda}(x, y)$ given by

$$\tilde{\Lambda}(x,y) = \sum_{i=1}^{N} \tilde{\Lambda}_i e^{-[(x-x_i)^2+(y-y_i)^2)]/(4\sigma_i^2)}. \tag{3.31}$$

2) This topography remains regular. In order to make it more chaotic and we pick gaussian domes Λ_j again, as well as random angles θ_j and aspect ratio a_j. Then we perturb $\tilde{\Lambda}(x, y)$ as follows :

$$\Lambda(x,y) = \tilde{\Lambda}(x,y) + \sum_{j=1}^{N} \Lambda_j e^{-[[c_j(x-x_j)+s_j(y-y_j)]^2/a_j^2+[c_j(y-y_j)-s_j(x-x_j)]^2 a_j^2]/(4\sigma_j^2))}, \tag{3.32}$$

where $c_j = \cos(\theta_j)$, $s_j = \sin(\theta_j)$, a_j. The Λ_j's, the θ_j'a and the a_j's are all gaussian as well.

3) The roughness field is normalized such that $max(\Lambda(x, y)) = h_{max} = 0.1$. Therefore, the bottom is the surface given by : $z = \Lambda(x, y)$.

To perform the simulation, we use the “immersed boundary method" (IBM), initialy developed by Peskin [Peskin, 2002] (see also in [Lewandowski and Pichot, 2007]). This consists of solving the Navier-Stokes equation in $\Omega = [0, L_x] \times [0, L_y] \times [0, L_z]$, by adding in the Navier-Stokes equations (3.26) the additional source term

$$-\frac{1}{\varepsilon} \mathbb{1}_{\{0 \le z \le \Lambda(x,y)\}} \mathbf{v}, \tag{3.33}$$

for a small value of ε, which does not change the standard results and analysis about the Navier-Stokes equations [6]. This additional term enforces $\mathbf{v}$ to be negligible for $z \le \Lambda(x, y)$, and does not affect the system in the domain $\Lambda(x, y) \le z \le L_z$. The results of the simulation are reported in figure 3.4. We also have plotted on the same figure the log profil given by

$$h(z) = \frac{1}{0.31} \ln\left(\frac{z}{0.025}\right) + 7.0.$$

Our simulation yields a mean streamwise profile that perfectly matches with this log law

6. The comprehensive mathematical analysis of the IBM is carried out in [Lewandowski and Pichot, 2007].

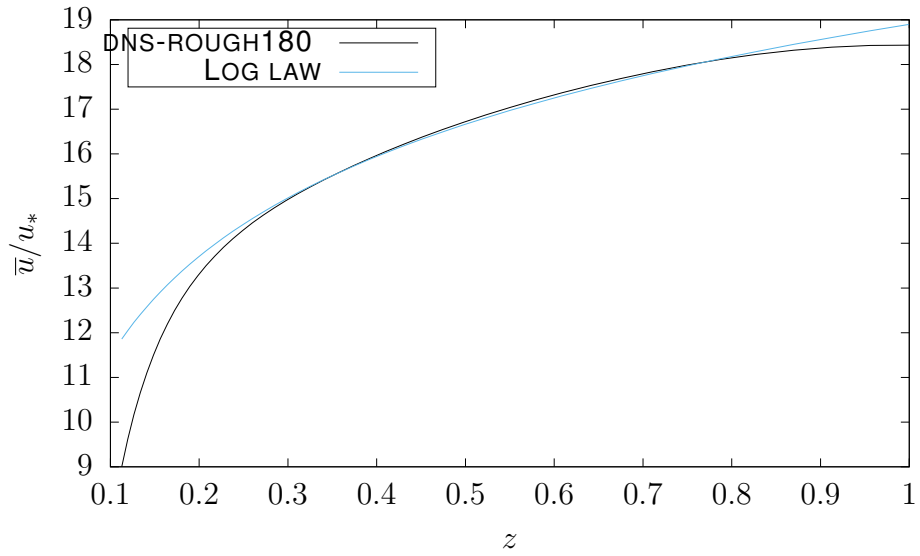

FIGURE 3.4 – Steamwise velocity profile compared to a log profil.

for $z \in [0.3, 0.8]$, thereby validating our DNS.

3.3.2 Determination of the mixing length and the constants

The aim of this section is to derive from the DNS a formula to determine the mixing length ℓ. We also settle the values of the constants C_v and C_k involved in the boundary conditions at Γ_c for $\mathbf{v}$ and k.

General methodology

Let $\mathscr{E}$ denotes the total mean dissipation, given by

$$\mathscr{E} = 2\nu\overline{|\nabla \mathbf{v}|^2}. \tag{3.34}$$

It is common in turbulence modeling to assume that ℓ is a function of k and $\mathscr{E}$, that is $\ell = \ell(k, \mathscr{E})$. A straightforward dimensional analysis yields the formula

$$\ell = \frac{k\sqrt{|k|}}{\mathscr{E}}, \tag{3.35}$$

on which the determination of ℓ is based. We assume that ℓ does not depend on x and y. Therefore in this framework, the means are calculated from the data by the same formula as (3.30). To be more specific, if Ψ is any field related to the flow, Ψ_{DNS} the corresponding calculated field, then

$$\overline{\Psi}(z) = \frac{1}{Tn_xn_y} \sum_{n=0}^{T/\Delta t} \sum_{j=0}^{n_x} \sum_{k=0}^{n_y} \Psi_{\text{DNS}} \left(n\Delta t, j\frac{L_x}{n_x}, k\frac{L_y}{n_y}, z \right). \tag{3.36}$$

Of course, only numerical values of $\overline{\Psi}$ at $z = qL_z/n_z$ ($q = 0, \cdots, n_z$) can be calculated by (3.36). Based on this, our procedure is the following :

i) we compute $\overline{\mathbf{v}} = \overline{\mathbf{v}}(z)$ by (3.36),

ii) at each grid point, we form the field $\mathbf{v}'_{vert} = \mathbf{v}_{\text{DNS}} - \overline{\mathbf{v}}$,

iii) we extract from the data the numerical TKE denoted by k_{vert}, given at each $z = qL_z/n_z$ by the quantity $k_{vert}(z) = (1/2)\overline{|\mathbf{v}'_{vert}|^2}(z)$,

iv) by the standard finite difference scheme, we calculate $\mathscr{E}_{vert} = \mathscr{E}_{vert}(z)$ by (3.34),

v) we get at each $z = qL_z/n_z$ the mixing length $\ell = \ell(z)$ by forming the quotient $k_{vert}(z)\sqrt{k_{vert}(z)}/\mathscr{E}_{vert}(z)$.

Remark 3.3.1. *The function $k_{vert}(z)$ calculated above is the horizontal mean of the TKE. This is the appropriate quantity for the determination of ℓ, according to the horizontal homogeneity assumption. To calculate the full TKE from the DNS, we must use the time average over the simulation time :*

$$\langle \psi \rangle(\mathbf{x}) = \frac{1}{T} \sum_{n=0}^{T/\Delta T} \psi_{DNS}(n\Delta T, \mathbf{x}). \tag{3.37}$$

Then the Reynolds decomposition is written as $\mathbf{v}_{DNS} = \langle \mathbf{v} \rangle + \mathbf{v}'_{DNS}$, yielding

$$k_{DNS}(\mathbf{x}) = (1/2)\langle |\mathbf{v}'_{DNS}|^2 \rangle. \tag{3.38}$$

We have plotted in figure 3.5 the curves of ℓ we have obtained by this way, in terms of the non dimensional variable $z' = z/H$.

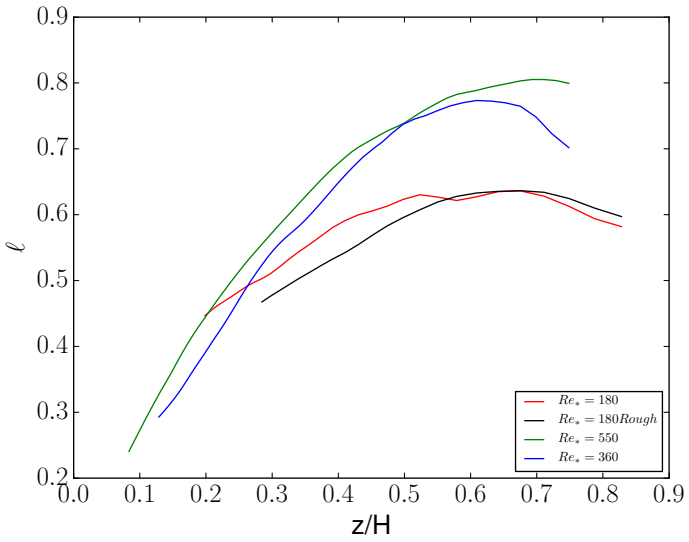

FIGURE 3.5 – Profiles of ℓ calculated from the DNS

Universal formula for the mixing length

We observe that the mixing length is increasing in the beginning of the turbulent layer (until $z \approx 0.6$) and slighly decreases until $z = 1$. Our goal is to interpolate these curves to get a universal formula in terms of the $Re_\star$ and z, by an empirical method.

Figure 3.5 suggests to seek for exponential profiles. However, it is usually accepted that near $z = 0$, ℓ is of the form $\ell = \kappa z$. Therefore, we multiply this exponential profile by a hyperbolic tangent function, which is an approximation of the Heaviside function. Finally, since ℓ is non-zero within the viscous sublayer, we add a term that depends on the natural length scale $\nu/u_\star = H/Re_\star$. These considerations have led us to introduce the following empirical formula by trial and error :

$$\ell = K \tanh\left(A\left(Re_\star \frac{z}{H} - B\right)\right) \exp\left(-Re_\star^2 \frac{\left(\frac{z}{H} - \frac{z_i}{H}\right)^2}{2\sigma}\right) + 75\frac{H}{Re_\star} \tag{3.39}$$

where $z_i = 0.6H\,m$. In the rough case, by comparing the red line to the dark line in figure 3.5 (DNS-FLAT 180 and DNS-ROUGH 180) we apply a correction that takes the

topography into account, which gives :

$$\ell = K \tanh\left(A\left(Re_\star \frac{z+z_R}{H} - B\right)\right) \exp\left(-Re_\star^2 \frac{\left(\frac{z+z_R}{H} - \frac{z_i}{H}\right)^2}{2\sigma}\right) + 75\frac{H}{Re_\star} \tag{3.40}$$

where $z_R = 0.5H\,m$ is the mean value of the roughness, estimated from Figure 3.5. It remains to settle the coefficients A, B, σ and K. They are sought to be function of $Re_\star$ only. As we shall show it in the following, we get the following laws for large values of $Re_\star$ (valid from $Re_\star = 900$, depending on the coefficients) :

$$A = 3.05 Re_*^{0.065}, \tag{3.41}$$

$$B = 0, \tag{3.42}$$

$$\sigma = 0.3 Re_*^{1.05}, \tag{3.43}$$

$$K = 0.32 Re_*^{0.12}. \tag{3.44}$$

Moreover, it is accepted that near $z = 0$, $\ell = \kappa z$ where κ is the von Kármán constant. However, according to figure 3.7, although ℓ follows well a linear law near $z = 0$, its slope looks non constant when $Re_\star$ varies. Indeed, we obtain from our graphs (see Figure 3.12 below) the following law, valid from $Re_\star \approx 800$:

$$\kappa = \kappa(Re_\star) = 0.25(Re_\star)^{0.32} \quad \text{hence} \quad \ell = 0.25(Re_\star)^{0.32} z. \tag{3.45}$$

However, we observe in Figure 3.12 that the usual law is valid for instance when $Re_\star = 180$. The law (3.39) must be checked for high values of $Re_\star$, which is done by applying the algorithm to the results of Moser and al in Figure 3.7, and also yields the laws satisfied by the coefficients A, B, σ and K for high values of $Re_\star$, also used in the rough case.

In Figures 3.8 and 3.9, we have plotted the values of the constants A and B.

Figure 3.10 shows that the coefficient σ follows a linear law for all $Re_\star$, hence (3.41).

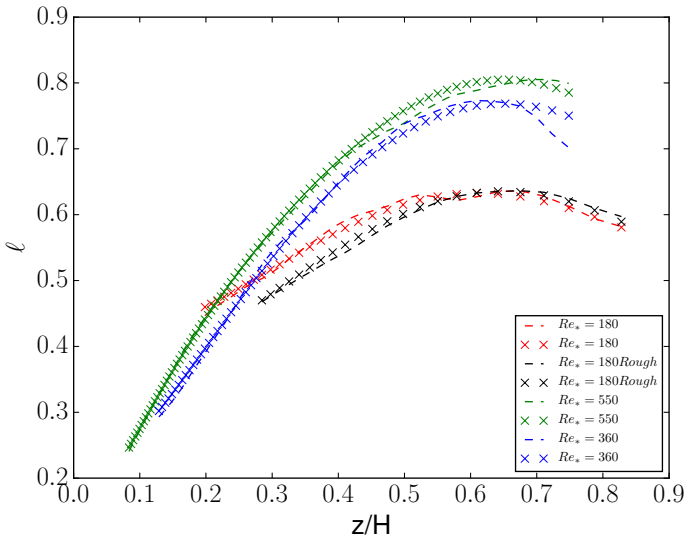

FIGURE 3.6 – Dotted lines draw the mixing length calculated from the DNS, Crosses draw curves from formula (3.39) and (3.40)

Determination of the constants

We recall that the eddy viscosities/diffusion ν_t and μ_t are given by

$$\nu_t(k) = C_v \ell \sqrt{k}, \quad \mu_t(k) = C_k \ell \sqrt{k}.$$

Now that we know how to compute ℓ thanks to (3.39), we are able to estimate the constants C_v and C_k as follows. In this section, $\langle \psi \rangle$ denotes the time average over the time simulation defined by (3.37), and the TKE k in the formulae below is given by (3.38). Because of the horizontal homogeneity, we focus on the vertical components of the Reynolds stress, linked to the eddy coefficients by :

$$\langle u'_{\text{DNS}} w'_{\text{DNS}} \rangle = \nu_t \frac{\partial \langle u_{\text{DNS}} \rangle}{\partial z} = C_v \ell \sqrt{k_{\text{DNS}}} \frac{\partial \langle u_{\text{DNS}} \rangle}{\partial z}, \tag{3.46}$$

and

$$\langle e'_{\text{DNS}} w'_{\text{DNS}} \rangle = \mu_t \frac{\partial k_{\text{DNS}}}{\partial z} = C_k \ell \sqrt{k_{\text{DNS}}} \frac{\partial k_{\text{DNS}}}{\partial z}. \tag{3.47}$$

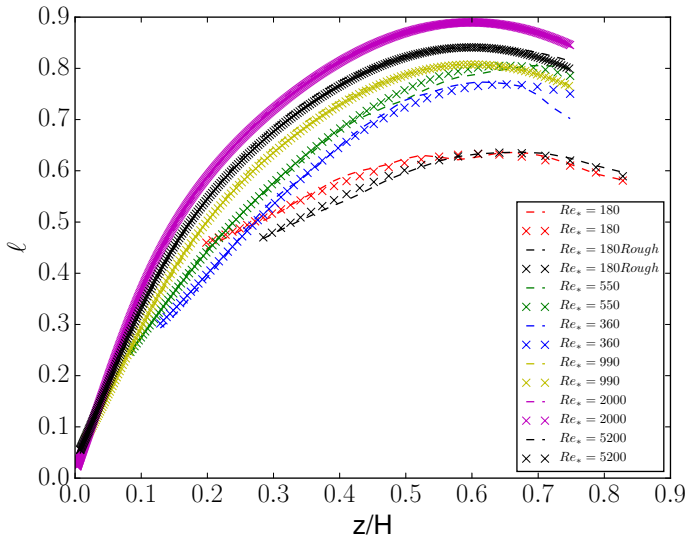

FIGURE 3.7 – Lines are results from Moser and al [Moser et al., 1999], Crosses results from formulae (3.39) and (3.40)

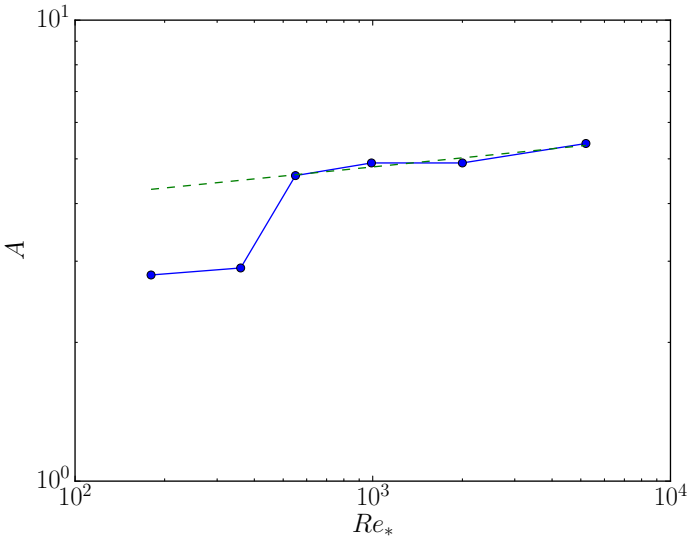

FIGURE 3.8 – $A = A(Re_\star)$. The green dotted line is the 0.065 slope.

Hence, C_v is the value that minimizes the error in (3.46) whereas C_k is the value that minimizes the error in (3.47). By the least square method, C_v is such that

$$\sum_{i=1}^{N} \left(\langle u'_{\text{DNS}} w'_{\text{DNS}} \rangle(\mathbf{x}_i) - C_v \ell(z_i) \sqrt{k_{\text{DNS}}(\mathbf{x}_i)} \frac{\partial \langle u_{\text{DNS}} \rangle}{\partial z}(\mathbf{x}_i) \right)^2 \tag{3.48}$$

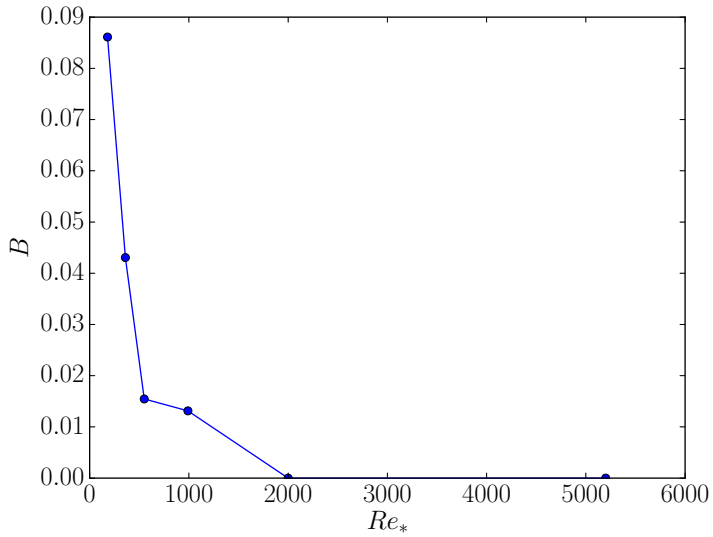

FIGURE 3.9 – $B = B(Re_\star)$

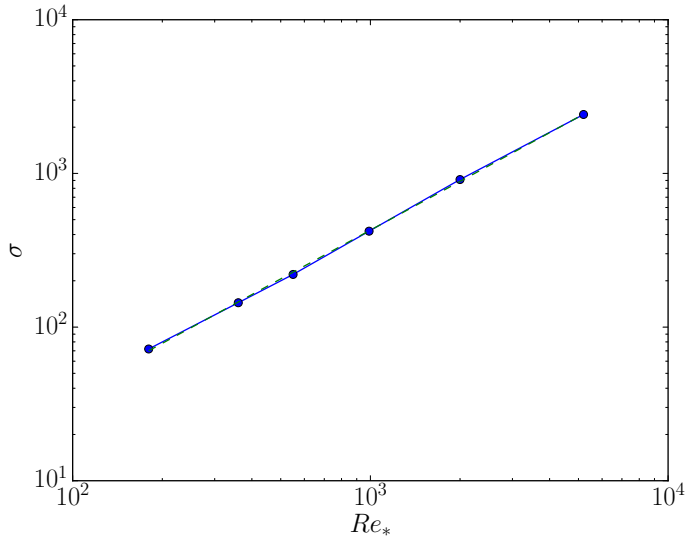

FIGURE 3.10 – $\sigma = \sigma(Re_\star)$. The green doted line is the 1.05 slope.

is minimum, and C_k is such that

$$\sum_{i=1}^{N} \left(\langle e'_{\text{DNS}} w'_{\text{DNS}} \rangle(\mathbf{x}_i) - C_k \ell(z_i) \sqrt{k_{\text{DNS}}(\mathbf{x}_i)} \frac{\partial k_{\text{DNS}}}{\partial z}(\mathbf{x}_i) \right)^2 \tag{3.49}$$

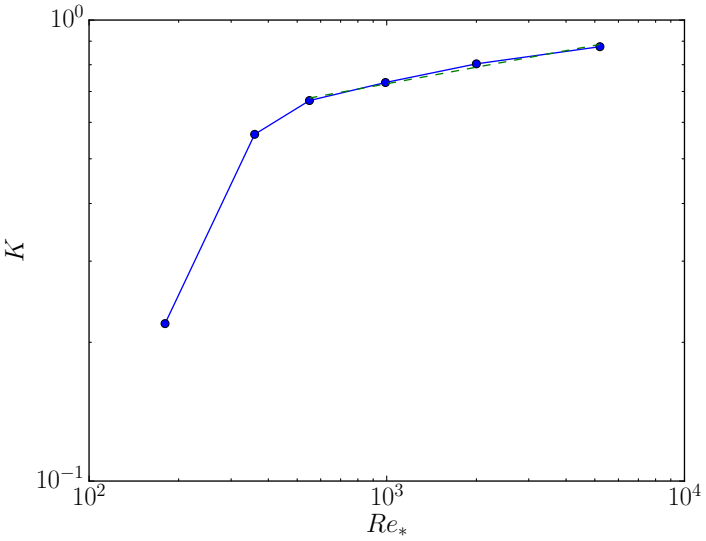

FIGURE 3.11 – $K = K(Re_\star)$. The green dotted line is the 0.12 slope.

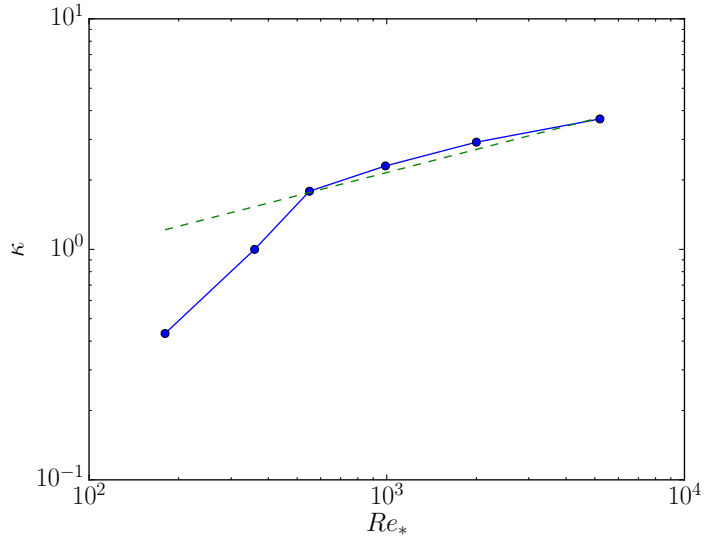

FIGURE 3.12 – $\kappa = \kappa(Re_\star)$. The green dotted line is the 0.32 slope.

is minimum, where $\{\mathbf{x}_1, \cdots, \mathbf{x}_N\}$ denotes the grid points set, $\mathbf{x}_i = (x_i, y_i, z_i)$. This optimization problem has been solved by the *brute-force* method, based on the results of DNS-FLAT 180, DNS-FLAT 550 and the corresponding profiles for ℓ. We get :

$$C_k = 0.15 \quad C_v = 0.105 \tag{3.50}$$

Remark 3.3.2. *We find in [Mohammadi and Pironneau, 1994, Chapter 4] :* $C_v = C_k = 0.09$*. However, these values have been calibrated for the full* $k - \mathscr{E}$ *model, which can explain the slight difference with our results.*

3.4 NSTKE simulations and conclusions

3.4.1 Algorithm and settings

Our code is based on the SIMPLEC algorithm (Patankar [Patankar, 1980], Issa [Issa, 1986]), that we have adapted to the NSTKE equations, leading to encode the following iterations. At step n, $(\mathbf{v}^{n-1}, p^{n-1}, k^{n-1})$ being known, we first solve the velocity equation

$$\left\{\begin{array}{rcll} (\overline{\mathbf{v}}^{n-1}\cdot\nabla)\,\overline{\mathbf{v}}^n - \nabla\cdot\left[(2\nu+\nu_t(k^{n-1}))\,D\overline{\mathbf{v}}^n\right] + \nabla p^{n-1} &=& \mathbf{f} & \text{in Om}_c, \\ \nabla\cdot\overline{\mathbf{v}}^n &=& 0 & \text{in Om}_c, \\ -[(2\nu+\nu_t(k^{n-1}))D\overline{\mathbf{v}}^n\cdot\mathbf{n}]_\tau &=& \alpha_v|\overline{\mathbf{v}}^{n-1}|\overline{\mathbf{v}}^n & \text{on } G_c, \\ \overline{\mathbf{v}}^n\cdot\mathbf{n} &=& 0 & \text{on } G_c, \end{array}\right. \tag{3.51}$$

which is a standard elliptic equation, with the added difficulties presented by the incompressibility constrain and the boundary condition $\overline{\mathbf{v}}^n\cdot\mathbf{n}|_{G_c} = 0$. Once $\mathbf{v}^n$ is calculated, we solve the TKE equation :

$$\left\{\begin{array}{rcll} \overline{\mathbf{v}}^n\cdot\nabla k^n - \nabla\cdot[(\mu+\mu_t(k^{n-1})\nabla k^n] &=& \nu_t(k^{n-1})|D\overline{\mathbf{v}}^n|^2 - \dfrac{k^n\sqrt{|k|^{n-1}}}{\ell} & \text{in Om}_c, \\ -(\mu+\mu_t(k^{n-1}))\dfrac{\partial k^n}{\partial\mathbf{n}} &=& \alpha_k k^n\sqrt{|k|^{n-1}} & \text{on } G_c. \end{array}\right. \tag{3.52}$$

Finally, the pressure is calculated by the Poisson equation :

$$\begin{cases} \Delta p^n &= -\nabla\cdot(\nabla\cdot(\mathbf{v}^n\otimes\mathbf{v}^{n-1}) - \nabla\cdot\left[(2\nu+\nu_t(k^{n-1}))\,D\mathbf{v}^n\right] - \mathbf{f}) & \text{in Om}_c, \\ \dfrac{\partial p^n}{\partial \mathbf{n}} &= 0 & \text{on } G_c. \end{cases} \tag{3.53}$$

System (3.51)-(3.52)-(3.53) for a given n, satisfies periodic boundary conditions in the $x-y$ axes. The source term $\mathbf{f}$ is given by (3.27). We implement this scheme in the OpenFoam solver (see at `https://www.openfoam.com`), based on the second order finite volumes method.

Remark 3.4.1. *Although we observe a good numerical convergence, we have no mathematical proof of the convergence of this scheme to the NSTKE model, which is a hard open question. Usually, we know that such scheme does converge when the eddy viscosity is close to a constant and when the source term is small enough in some sense (see in [Lewandowski and Odin, 2018]). However, It is likely that the homogeneous Neumann boundary condition for the pressure in the equation* (3.53) *may yield serious complications in a mathematical convergence analysis.*

We have carried out four simulations in the flat case for high Reynolds numbers, namely $Re_\star = 990, 2000, 5200, 10000$. Then we have tested the rough case for $Re_\star = 5200, 10000$. The mixing length is given by (3.39) and (3.40), the constants C_v and C_k by (3.50). The iterations (3.51)-(3.52)-(3.53) are initialized by

$$\mathbf{v}^0 = (u^0, 0, 0), \quad u^0 = 1\,ms^{-1}; \quad k^0 = 10^{-3}\,m^2s^{-2}; \quad p^0 = 0\,Pa \tag{3.54}$$

The parameter settings are given in Table 3.2. The coefficients α_v and α_k have been

Run	(L_x, L_y, L_z)	(n_x, n_y, n_z)	α_v	α_k
NSTKE-FLAT-990	$(6.28, 4.18, 2)$	$(16, 16, 32)$	0.000125	0.04
NSTKE-FLAT-2000	$(6.28, 4.18, 2)$	$(16, 16, 32)$	0.0000525	0.01
NSTKE-FLAT-5200	$(6.28, 4.18, 2)$	$(16, 16, 32)$	0.000035	0.0005
NSTKE-FLAT-10000	$(6.28, 4.18, 2)$	$(16, 16, 64)$	0.000035	0.0005
NSTKE-ROUGH-5200	$(6.28, 4.18, 2)$	$(32, 24, 64)$	0.000035	0.0005

TABLE 3.2 – Parameters settings

determined up to $Re_\star = 5000$ by solving the minimization problem

$$\min\{||\mathbf{v}_{\text{NSTKE}} - \mathbf{v}_{\text{DNS}}||_2^2 + ||k_{\text{NSTKE}} - k_{\text{DNS}}||_2^2\}. \tag{3.55}$$

The resolution of Problem (3.55) is based on a standard dichotomy algorithm (see for instance in [Teghem, 2012]). We have kept the same values for $Re_\star = 10000$, since the the obtained results are quite good. Moreover, we conjecture that these coefficients remain constant from a critical $Re_\star$. Notice that the mesh sizes in this case are much coarser than those used for the DNS, which is an undeniable advantage of the model. However, considering the height of the viscous sublayer compared to this resolution, we have taken $z_0 = 0$ in these simulations. The number of iterations is of order 1000.

3.4.2 Numerical Results in the flat case

Streamwise velocity

The results we get are compared to those of the high Reynolds numbers DNS provided in [Lee and Moser, 2015], up to $Re_\star = 5200$. For $Re_\star = 10000$, we have compared our result to the log law, in the absence of anything better. When $Re_\star = 990$,

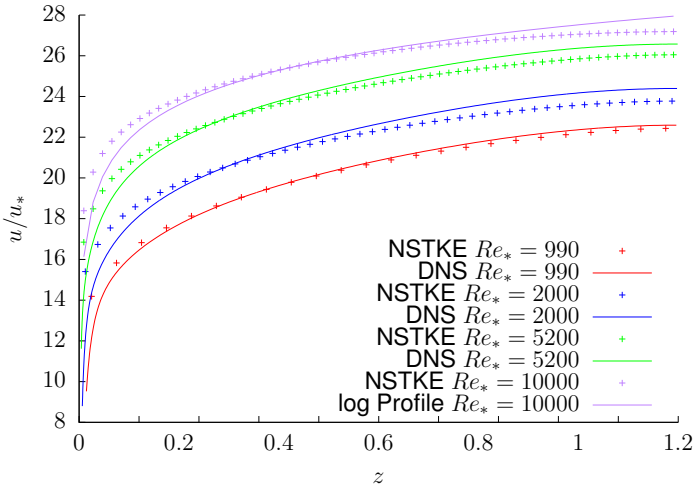

FIGURE 3.13 – Non dimensional streamwise velocity

the results seem to be close from those of the DNS. However, this is not the case for $Re_\star = 2000, 5200$. Moreover, the NSTKE model yields a significant departure from the log law when $Re_\star = 10000$. To corroborate these observations, we have calculated the non dimensional mean shear defined by

$$\Phi = \frac{\kappa z}{u_*}\frac{\partial \overline{u}}{\partial z}, \tag{3.56}$$

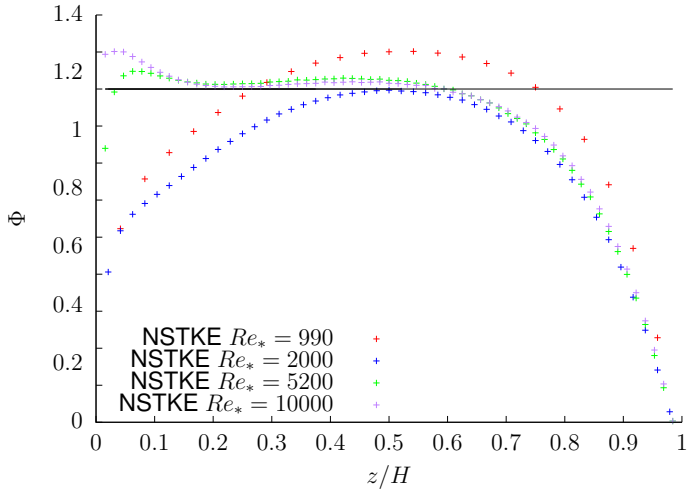

FIGURE 3.14 – Comparaison of the non dimensional mean shear Φ computed by the NSTKE model for the High Reynolds number simulations.

which is equal to 1 when the profile is logarithmic. The results are plotted in Figure 3.14. The streamwise velocity given by the NSTKE model has a serious lack of shear at the top and the bottom of the boundary layer.

Turbulent kinetic energy

The turbulent kinetic energy is plotted on Figure 3.15, compared with the DNS results.The model overestimates the TKE at the bottom of the boundary layer.

Convergergence analysis

The convergence of the SIMPLEC algorithm for the NSTKE problem is shown in figure 3.16 for the $Re_\star = 900, 2000, 5200$ cases. The black lines indicates the slope of the decreasing rate, which is proportionnal to $n^{-2/3}$ for the first 300 iterations and increases up to n^{-8} until $n = 1000$, which is a good convergence result.

Corrected mixing length

The previous sections show that the NSTKE model does not perfectly reproduce the standard boundary layer profiles. It may come from the mixing length formula (3.39) and the law (3.41) that determines the main coefficient in the formula for ℓ, denoted by

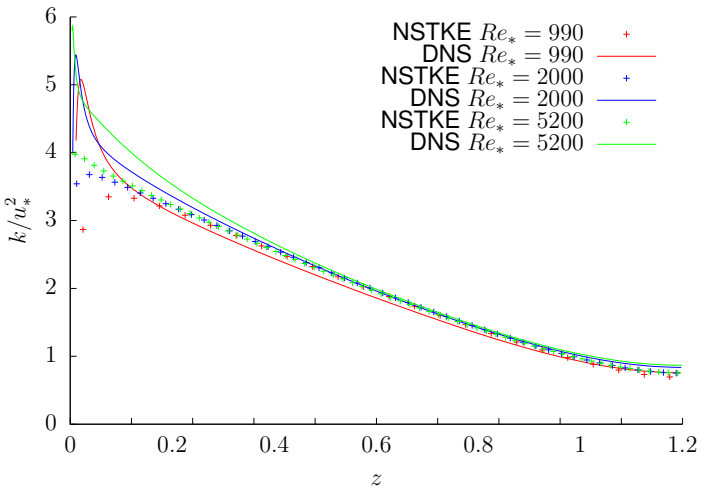

FIGURE 3.15 – Turbulent kinetic energy

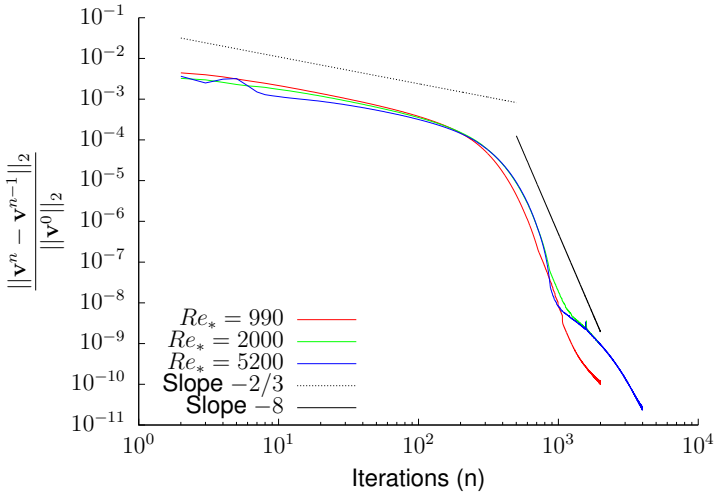

FIGURE 3.16 – Convergence analysis.

A. To fix this issue, we have replaced A by another coefficient of the form λA, the best choice of λ being equal to 0.608. As shown by the figure (3.17), the model reproduces accurately the log profile up to $z = 0.7H$, wich is quite satisfactory. Moreover, the TKE calculated from the NSTKE model matches with the one calculated from the DNS.

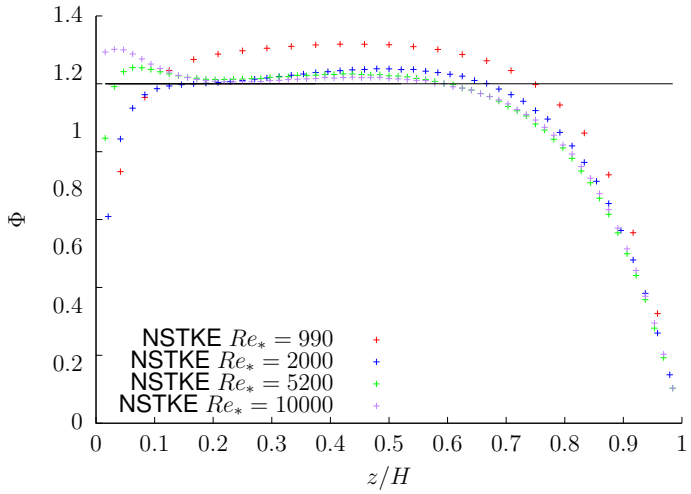

FIGURE 3.17 – Mean shear Φ with the corrected mixing length profile.

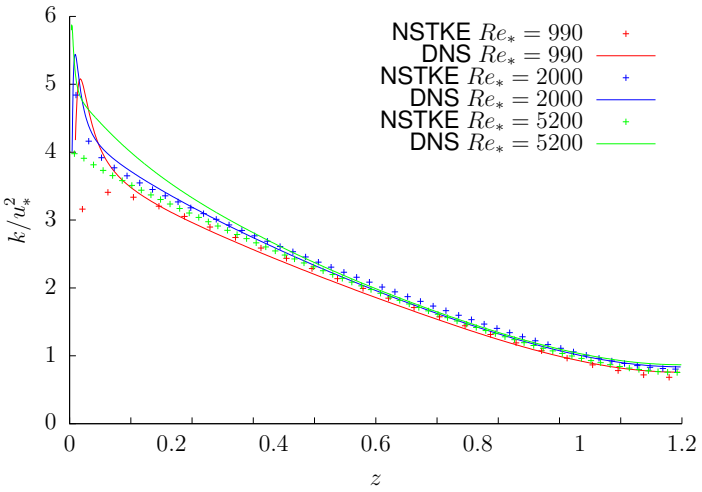

FIGURE 3.18 – Turbulent kinetic energy with the corrected mixing length profile.

3.4.3 Numerical results in the rough case

The simulation is carried out from $z_0 = 0.1$. This is as if we have put a flat plate over the domes, starting the simulation from z_0 as in the flat case, the information about the topography being contained in the formula for ℓ, the boundary condition and the corresponding coefficients. We have applied the same correction for the coefficicent A in formula (3.40) as in the flat case. The results are reported in Figure 3.19, Figure 3.20 and Figure 3.21, following the same order as in the flat case. Without any DNS, the only way to analyse the results is the comparison with log profiles. We observe a departure from the log law outside the interval $[0.5, 0.7]$. Considering the TKE profiles, the intensity of the turbulence for $Re_\star = 1000$ and $Re_\star = 5000$ looks to be different only from $z/H = 0.5$.

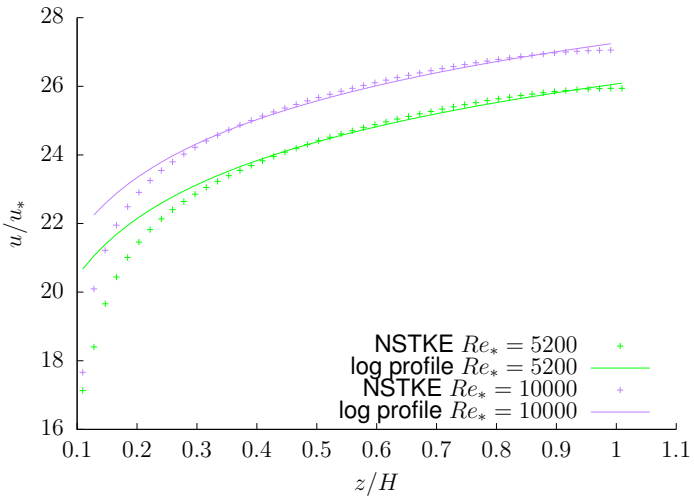

FIGURE 3.19 – NSTKE Rough case. Non dimensional streamwise velocity.

3.5 Theoretical analysis of the NSTKE model

We aim to prove the existence of a weak solution $(\overline{\mathbf{v}}, p, k)$ to the boundary value problem (3.20). Standard à priori estimates yield $\nu_t(k)|D\overline{\mathbf{v}}|^2 \in L^1(\Omega)$, so that (3.20) couples a steady-state Navier-Stokes like equation to an elliptic equation with a right hand side in L^1.

Throughout this theoretical section, the mixing length $\ell = \ell(\mathbf{x})$ is a given strictly non negative bounded continous function, $\nu > 0$, $\mu > 0$, $\alpha_v > 0$, $\alpha_k > 0$ are constants, the

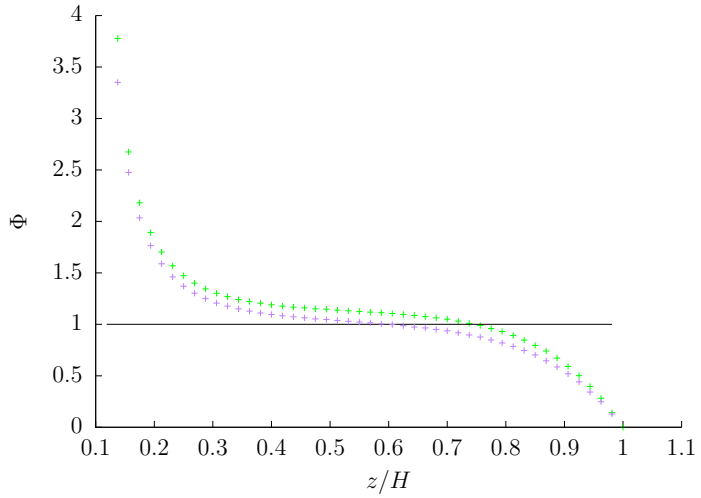

FIGURE 3.20 – NSTKE Rough case. Mean shear

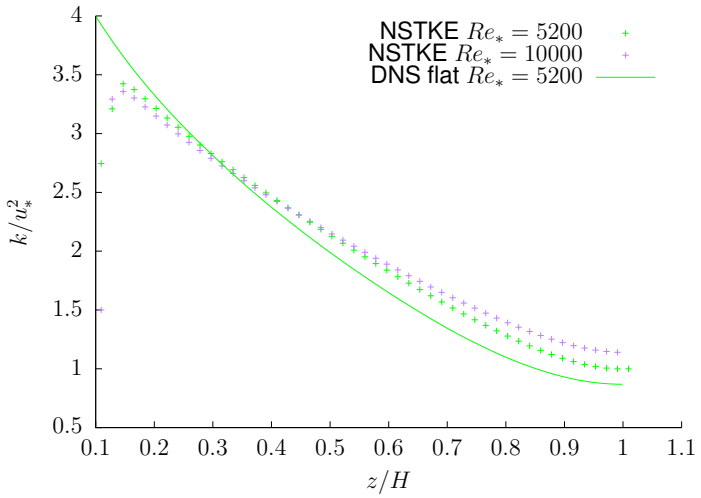

FIGURE 3.21 – NSTKE Rough case. Turbulent kinetic energy

eddy viscosity $\nu_t = \nu_t(k) \geq 0$ and $\mu_t = \mu_t(k) \geq 0$ are continuous function of k.

3.5.1 Brief state of the art

The NSTKE model was first studied in [Lewandowski, 1997b], where $\Omega \subset \mathbb{R}^d$ ($d = 2, 3$) is a smooth bounded domain, with homogeneous boundary condition in the whole boundary of Ω, that is $\overline{\mathbf{v}}|_{\partial\Omega} = 0$ and $k|_{\partial\Omega} = 0$, and where ν_t and μ_t are bounded continuous functions of k. Steady state and evolutionary cases were considered in this paper, in which various existence and stability results are proved.

In [Bulíček et al., 2011], the model was studied in $\Omega \subset \mathbb{R}^3$, $\overline{\mathbf{v}}$ satisfies the (linear) Navier Law at $\partial\Omega$, k satisfies mixed homegeneous Dirichlet/Neumann boundary condition at $\partial\Omega$, ν_t and μ_t are continuous functions of k, with growth condition at infinity, covering the case $\nu_t, \mu_t = O\left(k^{1/2}\right)$. In this paper, the k-equation is replaced by the equation for the total energy $e = 1/2|\overline{\mathbf{v}}|^2 + k$, and the existence of a weak solution to the $(\overline{\mathbf{v}}, p, e)$ system is proved.

In [Chacòn Rebollo and Lewandowski, 2014], we have studied the NSTKE model in $\Omega \subset \mathbb{R}^3$ with the boundary conditions (3.3) (wall law) and (3.4) ($k_{\partial\Omega} = |\overline{\mathbf{v}}|^2$) at the whole boundary. To carry out this study, we have set $k' = k - |\overline{\mathbf{v}}|^2$ and considered the equation for k' in place of that for k. The advantage is that k' satisfies an homogeneous Dirichlet boundary conditions at $\partial\Omega$, suggesting that the method developed in [Lewandowski, 1997b] might be adapted. The disavantage is that additional coupling terms appear in the equation for k'.

In the steady state case, we have proved in [Chacòn Rebollo and Lewandowski, 2014, Chapters 7] the existence of a weak solution to the $(\overline{\mathbf{v}}, \overline{p}, k')$ system when $\nu_t = \nu_t(k)$ and $\mu_t = \mu_t(k)$ are continuous bounded function of k, by a very long and technical proof. When $\nu_t, \mu_t = O\left(k^{1/2}\right)$ at infinity, we still get an existence result when the equality in the k' equation is replaced by a variational inequality. The method fails in the evolutionary case, which still remains an open problem. In this evolutionary case, we have been able to obtain existence results when $k|_{\partial\Omega} = 0$ and $\overline{\mathbf{v}}$ satisfies the wall law (3.3).

In comparison with the former studies, the boundary value problem (3.20) is characterized by

i) mixed boundary conditions, in the sense that they are periodic in the $x - y$ axes, and of flux type in the z-axis (wall law, Neumann),

ii) the non linear Neumann boundary condition (3.18) for k in the z axis.

In what follows, we will limit ourselves to focus on these special features, to avoid repeating arguments already written in former works. In particular, it will be enough to carrefully detail the functional setting, and to study the Laplace equation with a right hand side in L^1, periodic boundary conditions in the (x, y)-axes, and (3.18) in the z-axis, which was not already carried out elsewhere, up to our knowledge.

3.5.2 Functional spaces

This section is devoted to define the functional spaces we are working with, which will be done step by step. Let us first set

$$\Omega_c = [0, L_x] \times [0, L_y] \times [z_0, L_z - z_0], \tag{3.57}$$

$$\Gamma_{b,c} = [0, L_x] \times [0, L_y] \times \{z = z_0\} \quad \text{(bottom)}, \tag{3.58}$$

$$\Gamma_{t,c} = [0, L_x] \times [0, L_y] \times \{z = L_z - z_0\} \quad \text{(top)}, \tag{3.59}$$

$$\Gamma_c = \Gamma_{b,c} \cup \Gamma_{t,c}. \tag{3.60}$$

i) Suitable space for the periodic boundary conditions in the (x, y)*-axes.* It is natural to introduce the following functional space :

$$\begin{aligned} \mathcal{W} = \{&\psi \in C^\infty(\mathbb{R}^2 \times [z_0, L_z - z_0], \mathbb{R}) \text{ s.t.} \\ &\forall\, (m, n) \in \mathbb{N}^2,\ \forall\, (x, y, z) \in \Omega_c,\ \psi(x + nL_x, y + mL_y, z) = \psi(x, y, z)\Big\}, \end{aligned} \tag{3.61}$$

that means the smooth function defined in the strip $z_0 \leq z \leq L_z - z_0$, periodic in the (x, y)-axes by the $[0, L_x] \times [0, L_y]$ box. Given any $\psi \in \mathcal{W}$, we still denote by ψ its restriction to Ω_c, so far no risk of confusion occurs.

Let us consider on $\mathcal{W}$ the following norm :

$$||\psi||_{1,2} = \left(\int_{\Omega_c} |\nabla\psi|^2\right)^{\frac{1}{2}} + \left(\int_{\Omega_c} |\psi|^2\right)^{\frac{1}{2}} = ||\psi||_{1,2,\Omega_c}. \tag{3.62}$$

Generally speaking, for any $s \geq 0$, $1 \leq p \leq \infty$, we set

$$||\psi||_{s,p} = ||\psi||_{s,p,\Omega_c}, \tag{3.63}$$

where $||\psi||_{s,p,\Omega_c}$ denotes the $W^{s,p}$ norm of the restriction of ψ to Ω_c. Due to the periodicity in the (x, y)-axes, these are norms on $\mathcal{W}$. We denote by $W^{s,p}_\pi$ the completion of $\mathcal{W}$ with respect to the $||\cdot||_{s,p}$ norm.

Remark 3.5.1. *Let* $W^{s,p}_\pi|_{\Omega_c}$ *be the space of the restrictions to* Ω_c *of functions of* $W^{s,p}_\pi$*. Then* $W^{s,p}_\pi|_{\Omega_c}$ *is a closed subspace of* $W^{s,p}(\Omega_c)$*.*

We will write in the remainder :

$$H^1_\pi = W^{1,2}_\pi, \quad L^p_\pi = W^{0,p}_\pi. \tag{3.64}$$

ii) Vertical homogeneous space. We will need the following space :

$$\begin{aligned}\mathcal{W}_0 = \{&\psi \in \mathcal{W} \text{ s.t.} \\ &\exists\, \delta > 0,\ \forall\, (x,y) \in \mathbb{R}^2,\ \forall z \in [z_0, z_0+\delta] \cup [L_z - z_0 - \delta, L_z - z_0], \\ &\qquad\qquad \psi(x,y,z) = 0\}.\end{aligned} \tag{3.65}$$

In other word, $\mathcal{W}_0$ is the set of functions in $\mathcal{W}$ vanishing in a neighbourhood of the bottom $z = z_0$ and the top $z = L_z - z_0$. We denote by $W^{1,p}_{\pi,0}$ the adherence of $\mathcal{W}_0$ in $W^{1,p}_\pi$. It easy checked that given any $\psi \in W^{1,p}_\pi$, then $\psi \in W^{1,p}_{\pi,0}$ if and only if $\psi|_{\Gamma_c} = 0$ (see [Brezis, 2011]). Moreover, the following Poincaré's inequality holds

$$\forall\, \psi \in W^{1,p}_{\pi,0}, \quad ||\psi||_{0,p,\Omega_c} \leq C_{p,\Omega_c} ||\nabla\psi||_{0,p,\Omega_c}, \tag{3.66}$$

where C_{p,Ω_c} is a constant that only depends on p and Ω_c. Note that in view of the geometry of Ω_c, a straightforward calculation using Fubini's theorem allows to check that (3.66) can be improved by :

$$\forall\, \psi \in W^{1,p}_{\pi,0}, \quad ||\psi||_{0,p,\Omega_c} \leq C_{p,L_z} ||\frac{\partial\psi}{\partial z}||_{0,p,\Omega_c}, \tag{3.67}$$

iii) Norm with the trace. Because of the boundary conditions involved in problem (3.20), it is convenient to consider norms on $W^{1,p}_\pi$ that take the traces on Γ_c into account. The general framework is the following :

— Given any $1 \leq p < 3$, $p^\star = \dfrac{3p}{3-p}$ is the critical exponent for the space $W^{1,p}(\Omega_c)$,

— For all $\psi \in W^{1,p}_\pi$, $\mathrm{tr}_b\psi$ (resp. $\mathrm{tr}_t\psi$) denotes the trace of ψ at the bottom $\Gamma_{b,c}$ (resp. at the top $\Gamma_{t,c}$). In this case, according to the theory of traces (see in [Adams and Fournier, 2003]) $\mathrm{tr}_\alpha\psi \in W^{1-1/p,p}(\Gamma_{\alpha,c})$ for α = b,t. Because of the Sobolev embedding theorem, $\mathrm{tr}\psi \in L^q(\Gamma_c)$ for any

$$1 \leq q \leq \frac{2p}{3-p} = p^{\star\star}, \tag{3.68}$$

where $\mathrm{tr}\psi(\mathbf{x}) = \mathrm{tr}_\alpha\psi(\mathbf{x})$ if $\mathbf{x} \in \Gamma_{\alpha,c}$, for α = b,t.

Lemma 3.5.1. *Let $1 \leq p < 3$, $1 \leq q < p^{\star\star}$. Then the application*

$$N_{p,q} : \begin{cases} W^{1,p}_{\pi} \longrightarrow \mathbb{R}_+, \\ \psi \longrightarrow ||\nabla\psi||_{0,p,\Omega_c} + ||\mathrm{tr}\psi||_{0,q,\Gamma_c}, \end{cases} \tag{3.69}$$

is a norm on $W^{1,p}_{\pi}$, equivalent to the standard $W^{1,p}$-norm.

Démonstration. The application $N_{p,q}$ is obviously a semi norm. To check that it is a norm, let us consider $\psi \in W^{1,p}_{\pi}$ such that $N_{p,q}(\psi) = 0$. In particular $\psi|_{\Gamma_c} = 0$. Therefore, $\psi \in W^{1,p}_{\pi,0}$, hence as $||\nabla\psi||_{0,p,\Omega_c} = 0$, we get from Poincaré's inequality, $||\psi||_{0,p,\Omega_c} = 0$. Then $\psi|_{\Omega_c} = 0$, and by periodicity, $\psi = 0$.

To prove that $N_{p,q}$ is equivalent to the $W^{1,p}$ norm, it is enough to prove that there exists a constant C such that

$$\forall\, \psi \in W^{1,p}_{\pi}, \quad ||\psi||_{0,p,\Omega_c} \leq C N_{p,q}(\psi). \tag{3.70}$$

If (3.70) would not hold true, there would be a sequence $(\psi_n)_{n\in\mathbb{N}}$ in $W^{1,p}_{\pi}$ such that $||\psi_n||_{0,p,\Omega_c} = 1$ and $N_{p,q}(\psi_n) \to 0$ as $n \to \infty$. Such a sequence is bounded in $W^{1,p}_{\pi}$. Therefore, up to a subsequence, it converges weakly in $W^{1,p}_{\pi}$ to some ψ. By Remark 3.5.1 and the compact Sobolev embedding theorem, $\psi_n \to \psi$ in L^p_{π} strong (eventually up to another subsequence). In particular, $||\psi||_{0,p,\Omega_c} = 1$. By a similar argument, as $q < p^{\star\star}$, $\mathrm{tr}\psi_n \to \mathrm{tr}\psi$ strongly in $L^q(\Gamma_c)$, and from $N_{p,q}(\psi_n) \to 0$, we obtain $\psi \in W^{1,p}_{\pi,0}$. Finally, always by $N_{p,q}(\psi_n) \to 0$ and $||\nabla\psi||_{0,p,\Omega_c} \leq \liminf_{n\to\infty} ||\nabla\psi_n||_{0,p,\Omega_c}$ since $\psi_n \to \psi$ weakly in $W^{1,p}_{\pi}$, $||\nabla\psi||_{0,p,\Omega_c} = 0$, and by Poincaré's inequality, $||\psi||_{0,p,\Omega_c} = 0$, which is in contradiction with $||\psi||_{0,p,\Omega_c} = 1$, hence (3.70), ending the proof. □

Remark 3.5.2. *The application $N_{p,q}$ is also a norm on $W^{1,p}(\Omega_c)$, equivalent to the standard $W^{1,p}$ norm.*

Space for the velocity. The boundary condition $\overline{\mathbf{v}} \cdot \mathbf{n} = 0$ at $z = z_0$ and $z = L_z - z_0$ must be considerd in the functional setting. We remark that if $\mathbf{w} = (w_x, w_y, w_z)$ is a vector field defined over $\mathbb{R}^2 \times [z_0, L_z - z_0]$ that satisfies $\mathbf{w} \cdot \mathbf{n}|_{z=z_0} = \mathbf{w} \cdot \mathbf{n}|_{z=L_z-z_0} = 0$, then $w_z(x, y, z_0) = w_z(x, y, L_z - z_0) = 0$. In other words, $w_z|_{\Gamma_c} = 0$. Therefore, according to this fact and in view of the standard variational formulations involved in the general Navier-Stokes equations framework, we are led to seek for the mean velocity in the space

$$W = H^1_{\pi} \times H^1_{\pi} \times H^1_{\pi,0}, \tag{3.71}$$

Note that the proof of Lemma 3.5.1 combined with Korn's inequality (see [Chacòn Rebollo and Lewandowski, 2014, Appendice A]) shows that W equipped with the scalar product

$$(\mathbf{u},\mathbf{w}) = \int_{\Omega_c} D\mathbf{u} : D\mathbf{w} + \int_{\Gamma_c} \mathrm{tr}\mathbf{u}\cdot\mathrm{tr}\mathbf{w}, \tag{3.72}$$

is a Hilbert space, and that the norm $\mathbf{u} \to \sqrt{(\mathbf{u},\mathbf{u})}$ is a norm on W equivalent to the standard H^1 norm.

3.5.3 Weak solutions

Weak solutions are solutions of the variational problem deduced from the initial boundary value problem. They are usually deduced from *à priori estimates*, based on the Stokes formula and interpolation inequalities. Given the previous studies and the results already known, we must :

i) Study the action of general operator $\psi \to -\nabla\cdot(A\nabla\psi)$ on the $W^{1,p}_{\pi}$-spaces, for any positive definite matrix $A = A(\mathbf{x})$ of class C^1, periodic in the (x,y)-axes,

ii) Set the appropriate variational formulation for the system (3.20) and check that it falls within the framework of problems already studied before, in particular the one considered in [Chacòn Rebollo and Lewandowski, 2014, Chapter 7],

iii) Check if $W^{1,q}$ $(1 \le q < 3/2)$ estimates "à la Boccardo-Gallouët" (see the initial paper [Boccardo and Gallouët, 1989]) can be deduced from the equation satisfied by k.

From now, the source term $\mathbf{f}$ in (3.20) is in the dual space W'.

Turbulent operator

In this section, $A = A(\mathbf{x})$ is a C^1 (x,y)-periodic matrix, positive definite uniformly in $\mathbf{x} = (x,y,z) \in \Omega_c = \mathbb{R}^2 \times [z_0, L_z - z_0]$, that is

$$\forall\, \mathbf{u} \in \mathbb{R}^3, \quad \forall\, \mathbf{x} \in \Omega_c, \quad (A(\mathbf{x})\mathbf{u},\mathbf{u}) \ge \nu|\mathbf{u}|^2. \tag{3.73}$$

Let $\psi, \phi \in \mathcal{W}$. By the Stokes formula over Ω_c, which is a Lipchitz domain, we have

$$\int_{\Omega_c} -\nabla\cdot(A\nabla\psi)\phi = -\int_{\partial\Omega_c} \phi A\nabla\psi\cdot\mathbf{n} + \int_{\Omega_c} A\nabla\psi\cdot\nabla\phi. \tag{3.74}$$

Using the notations of figure 3.2, we decompose the integral on $\partial\Omega_c$ as

$$\int_{\partial\Omega_c} = \int_{\Gamma_c} + \int_{\Gamma_e} + \int_{\Gamma_s} + \int_{\Gamma_{lg}} + \int_{\Gamma_{lr}} \tag{3.75}$$

We have : $\mathbf{n}|_{\Gamma_e} = -\mathbf{n}|_{\Gamma_s}$ and $\mathbf{n}|_{\Gamma_{lg}} = -\mathbf{n}|_{\Gamma_{lr}}$. As $\phi A\nabla\psi$ is a C^1 function, periodic in the (x, y)-axes, we also have $\phi A\nabla\psi|_{\Gamma_e} = \phi A\nabla\psi|_{\Gamma_s}$ as well as $\phi A\nabla\psi|_{\Gamma_{lg}} = \phi A\nabla\psi|_{\Gamma_{lr}}$. Therefore, aside the term on Γ_c, all other terms in the boundary integral (3.75) are vanishing, hence (3.74) yields

$$(-\nabla\cdot(A\nabla\psi)\phi, \phi) = \int_{\Omega_c} -\nabla\cdot(A\nabla\psi)\phi = -\int_{\partial\Gamma_c} \phi A\nabla\psi\cdot\mathbf{n} + \int_{\Omega_c} A\nabla\psi\cdot\nabla\phi. \tag{3.76}$$

Unfortunately, the operator

$$\begin{cases} \mathcal{W} \to L^p(\Gamma_c), \\ \psi \to \mathrm{tr}(A\nabla\psi)\cdot\mathbf{n} \end{cases}$$

is not bounded, whatever the choice of $p \geq 1$. Therefore, Formula (3.76) cannot be extended for any ψ and ϕ in $W^{1,p}_\pi$ spaces. However, the structure of our problem suggests to introduce the following. Let $F : \mathbb{R} \to \mathbb{R}$ be a function which satisfies the growth condition

$$|F(\psi)| \leq C(1 + |\psi|^q), \tag{3.77}$$

for some q that be specified later, and let us consider

$$\mathcal{M}_F = \{\psi \in \mathcal{W};\ \mathrm{tr}(A\nabla\psi)\cdot\mathbf{n} = -F(\psi)\}.$$

Let M_F denotes the adherence of $\mathcal{M}_F$ with respect to the $W^{1,p}$ topology. For $\psi \in M_F$, $\phi \in W^{1,p'}_\pi$, the equality (3.76) becomes

$$(-\nabla\cdot(A\nabla\psi)\phi, \phi) = \int_{\partial\Gamma_c} \phi F(\psi) + \int_{\Omega_c} A\nabla\psi\cdot\nabla\phi. \tag{3.78}$$

We observe on one hand that as $\nabla\psi \in L^p(\Omega_c)$ and $\nabla\phi \in L^{p'}(\Omega_c)$, the volume integral in (3.78) is also well defined as soon as $A \in L^{p'}(\Omega_c)$. On a second hand, straightforward calculations based on Hölder and Sobolev inequalities, yield the following rules for the

right choice of q to make the boundary integral well defined in (3.78) :

$$\begin{cases} \text{if } 1 \leq p < 3/2, \quad q \leq p^{\star\star} = \dfrac{2p}{3-p} = q_c, \\ \text{if } p = 3/2, \quad q < 2 = q_c, \\ \text{if } 3/2 < p < 3, \quad q \leq \dfrac{3}{3-p} = q_c. \end{cases} \tag{3.79}$$

In the equation for $\overline{\mathbf{v}}$[7], $A = (2\nu + \nu_t(k))\mathrm{Id}$, $p = 2$ and

$$F(\overline{\mathbf{v}}) = \alpha_v |\overline{\mathbf{v}}| \overline{\mathbf{v}}. \tag{3.80}$$

then $q = 2$ and $q_c = 3$. This case is well covered by the classification (3.79). In the k-equation[8], $A = (\mu + \mu_t(k))\mathrm{Id}$, $p = 3/2^-$,

$$F(k) = \alpha_k k \sqrt{|k|}, \tag{3.81}$$

then $q = 3/2$ and $q_c = 2$, which is also well covered by the classification (3.79).

Variational formulation

For the sake of simplicity, we only consider the case of bounded eddy viscosities. We define the following operators, suggested by the results of the previous section :

$$\begin{cases} a(\mathbf{v},\mathbf{w}) = 2\nu \displaystyle\int_{\Omega_c} D\mathbf{v} : D\mathbf{w}, & a_e(k,l) = \mu \displaystyle\int_{\Omega_c} \nabla k \cdot \nabla l, \\ s(k;\mathbf{v},\mathbf{w}) = \displaystyle\int_{\Omega_c} \nu_t(k) D\mathbf{v} : D\mathbf{w}, & s_e(k;q,l) = \displaystyle\int_{\Omega_c} \mu_t(k) \nabla q \cdot \nabla l, \\ G(\mathbf{v},\mathbf{w}) = \alpha_v \displaystyle\int_{\Gamma_c} \mathbf{v}|\mathbf{v}|\mathbf{w}, & G_e(k,l) = \alpha_k \displaystyle\int_{\Gamma_c} k\sqrt{k}\, l. \end{cases} \tag{3.82}$$

As we are not working with a space of free divergence field, following [Chacòn Rebollo and Lewandowski, 2014, Chapter 6], we use the transport

7. Things are a little bit more technical with vector fields and laws such as (3.3), but the calculation and the final result are similar to the scalar case, changing ∇ by D, and thus we will not repeat it.

8. When we write $k \in W_\pi^{1,\frac{3}{2}^-}$, we mean $k \in \bigcap_{r<3/2} W_\pi^{1,r}$. When we write $q \in W_\pi^{1,3^+}$, we mean $q \in \bigcup_{\rho>3} W_\pi^{1,\rho}$

operator $b(\mathbf{z};\mathbf{v},\mathbf{w})$ defined by

$$b(\mathbf{z};\mathbf{v},\mathbf{w}) = \frac{1}{2}\left(\int_{\Omega_c}(\mathbf{z}\cdot\nabla)\mathbf{v}\cdot\mathbf{w} - \int_{\Omega_c}(\mathbf{z}\cdot\nabla)\mathbf{w}\cdot\mathbf{v}\right). \tag{3.83}$$

By similar calculations as those carried out in section (3.5.3) and arguments of the proof of Lemma 6.3 in [Chacòn Rebollo and Lewandowski, 2014], we easily get :

Lemma 3.5.2. *The form $(\mathbf{z},\mathbf{v},\mathbf{w}) \to b(\mathbf{z};\mathbf{v},\mathbf{w})$ verifies the following properties.*

i) b is trilinear and continuous on $(H^1_\pi)^3$, then on W, and in particular,

$$\forall\, \mathbf{z},\ \mathbf{v},\ \mathbf{w} \in (H^1_\pi)^3, \quad |b(\mathbf{z};\mathbf{v},\mathbf{w})| \le C\,\|\mathbf{z}\|_{1,2,\Omega_c}\,\|\mathbf{v}\|_{1,2,\Omega_c}\,\|\mathbf{w}\|_{1,2,\Omega_c}, \tag{3.84}$$

for some constants C only depending on Ω.

ii) b is antisymmetric,

$$\forall\, \mathbf{z},\ \mathbf{v},\ \mathbf{w} \in (H^1_\pi)^3, \quad b(\mathbf{z};\mathbf{v},\mathbf{w}) = -b(\mathbf{z};\mathbf{w},\mathbf{v}), \tag{3.85}$$

iii) we also have

$$\forall\, \mathbf{z},\ \mathbf{w}\ \in (H^1_\pi)^3, \quad b(\mathbf{z};\mathbf{w},\mathbf{w}) = 0. \tag{3.86}$$

iv) For any $\mathbf{z} \in W$ such that $\nabla\cdot\mathbf{z} = 0$ (in L^2_π), we have

$$\forall\, \mathbf{v},\ \mathbf{w}\ \in (H^1_\pi)^3, \quad b(\mathbf{z};\mathbf{v},\mathbf{w}) = \int_{\Omega_c}(\mathbf{z}\cdot\nabla)\,\mathbf{v}\cdot\mathbf{w}, \tag{3.87}$$

as well as

$$\forall\, \mathbf{w}\ \in (H^1_\pi)^3, \quad b(\mathbf{z};\mathbf{z},\mathbf{w}) = -\int_{\Omega_c}\mathbf{z}\otimes\mathbf{z} : \nabla\mathbf{w}. \tag{3.88}$$

We also introduce the following transport operator, with similar properties in the appropriate spaces :

$$b_e(\mathbf{z};k,l) = \frac{1}{2}\left[(\mathbf{z}\cdot\nabla k, l) - (\mathbf{z}\cdot\nabla l, k)\right], \tag{3.89}$$

where $\int_{\Omega_c}\phi\psi = (\phi,\psi)$. More generaly, given any Banach space E, $\psi\in E$, $\phi\in E'$, then so far no risk of confusion occurs, (ϕ,ψ) denotes the duality product between ϕ and ψ.

These results yield the following variational problem corresponding to the system

(3.20) (we write $\mathbf{v}$ instead of $\overline{\mathbf{v}}$ for the simplicity) :

$$\text{Find } (\mathbf{v},p,k)\in W\times L^2_\pi\times H^{1,\frac{3}{2}^-}_\pi \text{ s.t. for all } (\mathbf{w},q,l)\in W\times L^2_\pi\times H^{1,3^+}_\pi,$$

$$b(\mathbf{v};\mathbf{v},\mathbf{w})+a(\mathbf{v},\mathbf{w})+s(k;\mathbf{v},\mathbf{w})+G(\mathbf{v},\mathbf{w})-(p,\nabla\cdot\mathbf{w})=(\mathbf{f},\mathbf{w}), \tag{3.90}$$

$$(q,\nabla\cdot\mathbf{v})=0, \tag{3.91}$$

$$b_e(\mathbf{v};k,l)+a_e(k,l)+s_e(k;k,l)+G_e(k,l)=(\nu_t(k)|D\mathbf{v}|^2-\ell^{-1}k\sqrt{|k|},l). \tag{3.92}$$

Any solution to the variational problem (3.90)-(3.90)-(3.90) is a weak solution to the system (3.20). The calculation carried out before ensures that any strong solution to (3.20) is a weak solution. Conversely, it is easily checked that if $(\mathbf{v},p,k)$ is a weak solution which in addition satisfies $(\mathbf{v},p,k)\in(H^2_\pi)^3\times H^1_\pi\times H^2_\pi$, and ν_t, μ_t are C^1 functions, then $(\mathbf{v},p,k)$ is also a strong solution to (3.20).

Theorem 3.5.1. *The system* (3.20) *has a weak solution.*

The analysis carried out above shows that the weak formulation of system (3.20) is formulated as that considered in [Chacòn Rebollo and Lewandowski, 2014, Chapter 7], which was one of our goal. Therefore, the proof is similar to that of Theorem 7.1 in [Chacòn Rebollo and Lewandowski, 2014] [9], once we will have checked that estimates "*à la Boccardo-Gallouët*" hold in this case, which is the aim of the next section.

Remark 3.5.3. *When ν_t and μ_t are of order $k^{1/2}$ as it is the case in the real life, arguing by approximation like in section 7.5.3 in [Chacòn Rebollo and Lewandowski, 2014], we also get an existence result in which the equation for k is replaced by a variational inequality.*

Remark 3.5.4. *It is easily proved by standard arguments that the TKE k is non negative.*

3.5.4 Elliptic equation with a r.h.s in L^1

Basically, the k-equation is an elliptic equation with a r.h.s in L^1 (see for instance [Boccardo et al., 1989, Boccardo and Murat, 1994]). Indeed, taking $\mathbf{w}=\mathbf{v}$ in (3.90)

9. In fact it is much more simpler in this case, since we do not have many additional terms coming from the boundary condition, in which $\mathbf{v}$ is involved. These terms are replaced by the boundary term $G_e(k,l)$, which is easily treated, just as the term $G(\mathbf{v},\mathbf{w})$ in the $\mathbf{v}$-equation.

and using the result of Lemma 3.5.2, in particular $b(\mathbf{v};\mathbf{v},\mathbf{v})=0$, we get

$$\int_{\Omega_c}(2\nu+\nu_t(k))|D\mathbf{v}|^2+\alpha_v\int_{\Gamma_c}|\mathbf{v}|^3=(\mathbf{f},\mathbf{v}). \tag{3.93}$$

We deduce from Lemma 3.5.1 combined with Korn's inequality the existence of a constant C such that

$$C||\mathbf{v}||_W^2\leq 2\nu\int_{\Omega_c}|D\mathbf{v}|^2+\alpha_v\int_{\Gamma_c}|\mathbf{v}|^3. \tag{3.94}$$

Therfore, by Young inequality, (3.93) yields

$$\frac{C}{2}||\mathbf{v}||_W^2+\int_{\Omega_c}\nu_t(k)|D\mathbf{v}|^2\leq\frac{1}{2C}||\mathbf{f}||_{W'}. \tag{3.95}$$

Hence $\nu_t(k)|D\mathbf{v}|^2\in L^1(\Omega_c)$. The derivation of $W^{1,q}$ estimates for such an equation is based on taking $l=H(k)$ as test, for suitable continuous Lipchitz functions H. The term $-\ell^{-1}k\sqrt{|k|}$ has the correct sign, and is not involved in this process. Moreover, we also have $b_e(\mathbf{v};k,H(k))=0$. Finally as $\mu_t\in L^\infty$, the term $-\nabla\cdot[(\mu+\mu_t(k)]\nabla k)$ behaves as $-\Delta k$, at least from this viewpoint. Therefore, we are left with the following basic elliptic problem :

$$\left\{\begin{array}{l} -\Delta k=g\in L^1_\pi,\\ \dfrac{\partial k}{\partial\mathbf{n}}|_{\Gamma_c}=-\alpha_k k|k|^{\frac{1}{2}},\end{array}\right. \tag{3.96}$$

which has not been studied before, so far we know. We will have finished this section once we will have proved the following formal *à priori* estimate :

Lemma 3.5.3. *for all $1\leq q<3/2$, there exists a constant $C_q=C_q(||g||_{1,1,\Omega_c})$ such that any solution k to* (3.96) *satisfies*

$$||k||_{1,q,\Omega_c}\leq C_q. \tag{3.97}$$

Démonstration. The proof follows a formal procedure, which is standard in this context. Given any $n\in\mathbb{N}$, let $H_n:\mathbb{R}\to\mathbb{R}$ be the odd continuous Lipchitz function defined by

$$\left\{\begin{array}{ll} H_n(x)=0 & \text{if } x\in[0,n],\\ H_n(x)=x-n & \text{if } x\in[n,n+1],\\ H_n(x)=1 & \text{if } x\in[n+1,\infty[.\end{array}\right. \tag{3.98}$$

Taking $H_n(k)$ as test in (3.96) yields

$$\int_{\Omega_c} H_n'(k)|\nabla k|^2 + \alpha_k \int_{\Gamma_c} k|k|^{\frac{1}{2}} H_n(k) = \int_{\Omega_c} g H_n(k) \leq ||g||_{1,1,\Omega_c} \tag{3.99}$$

As H_n is odd, $k|k|^{\frac{1}{2}} H_n(k) \geq 0$. Therefore, (3.93) yields

$$\int_{n\leq|k|\leq n+1} |\nabla k|^2 \leq ||g||_{1,1,\Omega_c}. \tag{3.100}$$

From this estimate, we can use the result of Boccardo-Gallouët [Boccardo and Gallouët, 1989] turnkey to get the existence of $C_q = C_q(||g||_{1,1,\Omega_c})$ such that

$$||\nabla k||_{0,q,\Omega_c} \leq C_q, \tag{3.101}$$

for all $1 \leq q < 3/2$. To conclude, it is enough by Lemma 3.5.1 to find an L^r estimate at Γ_c, for whatever $r < 2 = (3/2)^{\star\star}$. To do so, given any $\varepsilon > 0$, let S_ε be the odd function defined by

$$\begin{cases} S_\varepsilon(x) = \varepsilon^{-1} x & \text{if } x \in [0, \varepsilon], \\ S_\varepsilon(x) = 1 & \text{if } x \in [\varepsilon, \infty[, \end{cases} \tag{3.102}$$

and take $S_\varepsilon(k)$ as test in (3.96), which leads to

$$\int_{\Omega_c} S_\varepsilon'(k)|\nabla k|^2 + \alpha_k \int_{\Gamma_c} k|k|^{\frac{1}{2}} S_\varepsilon(k) = \int_{\Omega_c} g S_\varepsilon(k) \leq ||g||_{1,1,\Omega_c} \tag{3.103}$$

As S_ε is non decreasing, $S_\varepsilon'(k)|\nabla k|^2 \geq 0$. Hence (3.103) yields

$$\alpha_k \int_{\Gamma_c} k|k|^{\frac{1}{2}} S_\varepsilon(k) \leq ||g||_{1,1,\Omega_c}, \tag{3.104}$$

which gives by Fatou's Lemma, since $S_\varepsilon(k) \to \text{sign}(k)$ where $k \neq 0$ as $\varepsilon \to 0$,

$$\int_{\Gamma_c \cap \{k\neq 0\}} |k|^{\frac{3}{2}} \leq \liminf_{\varepsilon\to 0} \int_{\Gamma_c\cap\{k\neq 0\}} k|k|^{\frac{1}{2}} S_\varepsilon(k) \leq ||g||_{1,1,\Omega_c},$$

leading to

$$\int_{\Gamma_c} |k|^{\frac{3}{2}} \leq ||g||_{1,1,\Omega_c}, \tag{3.105}$$

hence a $L^{3/2}$ estimate for k at Γ_c, which conludes the proof. □

CHAPITRE 4

A MODEL UNDER LOCATION UNCERTAINTY FOR THE MEAN VELOCITY IN WALL BOUNDED FLOWS

Dans le quatrième chapitre du manuscrit, nous revisitons le profil de vitesse dans la couche limite turbulente. Habituellement, les profils de vitesses sont obtenus par analyse dimensionnelle. Le schéma est le suivant : en considérant que l'écoulement dépend de la vitesse de friction u_*, la viscosité moléculaire ν et la hauteur z ; l'expression suivante est obtenue :

$$\frac{\kappa z}{u_*}\frac{\partial u}{\partial z} = F\left(\frac{z}{H}\right).$$

Si l'écoulement ne dépend pas d'un gradient de température, alors $F = 1$. Dans l'autre cas, le profil est obtenu par le développement en série entière de F, l'argument est inférieur à 1 ($z < H$).

Deux problèmes sont majeurs dans cette méthode, premièrement il se base sur l'hypothèse que la viscosité turbulente est linéaire en fonction de la hauteur, deuxièmement, il est impossible d'obtenir une loi unique dans l'ensemble de la couche limite, il y a bien une loi pour la zone visqueuse puis la zone logarithmique mais rien pour la zone intermédiaire. Jusqu'à ce jour, la référence mélant au mieux théorie et experimental est [Reichardt, 1951].

Nous allons utiliser le formalisme stochastique développé par Étienne Mémin [Mémin, 2014] pour développer une loi de paroi qui soit continue et dérivable dans toute la couche limite. Puis nous la validerons par rapport à des DNS.

Par des simulations lagrangiennes, il sera également démontré dans ce chapitre

que la modélisation de l'équivalent de la viscosité turbulente (ici un tenseur de variance) est cohérent. Il est remarqué que cette quantité est une distribution suivant une loi statistique log-normale à chacune des hauteurs.

Concernant les fluctuations dans la couche limite, les variances de vitesses sont parfaitement documentées [Jimenez and Moser, 2007]. Cependant, peu de théories sont disponibles pour caractériser ces variances sur des temps courts. Nous apportons un calcul de cette variance à temps court dans la zone visqueuse.

4.1 introduction

The study of mean velocity profiles in turbulent boundary layers (TBL) is generating an intense research effort. Their knowledge is as a matter of fact an immense source of information for many industrial applications and in geophysics to model the interface between atmosphere and ocean. Since the seminal work of [Prandtl, 1925] and [von Karman, 1930], the mean velocity profile is known to be linear in a viscous sublayer near the wall and logarithmic within a turbulent sublayer, located before a region of uniform mean profile. These models have been derived from different theoretical arguments and confirmed in a wide variety of experiments [Marusic et al., 2010, Klewicki, 2010, Marusic et al., 2013]. Between the viscous layer and the logarithmic layer, within an interfacial region, referred to as the buffer zone, no robust model is yet available.

The lack of a model with clear theoretical foundations for the buffer zone is essentially due to a change of the dynamical regime between the viscous and turbulent sublayers. In the former, the molecular friction dominates while in the latter it is a large-scale turbulent mixing dissipation which governs the flow. A transitional mechanism is necessarily acting in between these two regions. In this study we show that by taking properly into account the uncertainties associated to the unresolved (turbulent) components of the TBL dynamics, it is possible to introduce a theoretically well-defined model for the buffer zone. This model is directly associated to a statistical eddy-induced velocity. Such a drift correction corresponds to the so-called *turbophoresis* phenomenon associated with small-scale inhomogeneity, which drives inertial particles toward the regions of low turbulent diffusivity [Reeks, 1983]. It is also akin to the velocity correction introduced for tracer mean transport in oceanic or atmospheric circulation models [Andrews and McIntyre, 1976].

The model used in this study is derived from a large-scale stochastic representation recently proposed by [Mémin, 2014] and has been applied with success for various turbulent flows [Chandramouli et al., 2018, Kadri H. and Mémin, 2017, Resseguier et al., 2017]. The formulation referred to as modeling under location uncertainty (ULU) incorporates a random component as a model of the unresolved small-scale velocities. We briefly describe hereafter its principles.

The velocity is decomposed in a large-scale smooth component, $\widetilde{\boldsymbol{u}}$, and a highly

oscillating random component

$$\boldsymbol{u}(\boldsymbol{x},t) = \widetilde{\boldsymbol{u}}(\boldsymbol{x},t) + \boldsymbol{\sigma}(\boldsymbol{x},t)\frac{\mathrm{d}\mathbb{B}_t}{\mathrm{d}t}. \tag{4.1}$$

The first term represents the large-scale velocity component whereas the second one, written (formally) as the time derivative of a Brownian random field, stands for the small-scale velocity component. The divergence-free random field involved in this equation is defined over the fluid domain, Ω, through the kernel $\breve{\boldsymbol{\sigma}}(.,.,t)$ of the diffusion operator $\boldsymbol{\sigma}(.,t)$

$$\forall \boldsymbol{x} \in \Omega, \quad (\boldsymbol{\sigma}(\boldsymbol{x},t)\boldsymbol{f})^i \triangleq \sum_j \int_\Omega \breve{\sigma}^{ij}(\boldsymbol{x},\boldsymbol{y},t) f^j(\boldsymbol{y},t)\mathrm{d}\boldsymbol{y},\ i,j=1,\dots,d. \tag{4.2}$$

This operator is assumed to be of finite norm and function $\mathbb{B}_t$ denotes a d-dimentional Brownian function (formally an infinite dimensional vectorial Brownian motion). The covariance of the random turbulent component is defined as

$$Q_{ij}(\boldsymbol{x},\boldsymbol{x}',t,t') = \mathbb{E}\Big((\boldsymbol{\sigma}(\boldsymbol{x},t)\mathrm{d}\mathbb{B}_t)_i(\boldsymbol{\sigma}(\boldsymbol{x}',t')\mathrm{d}\mathbb{B}_t)_j\Big) = c_{ij}(\boldsymbol{x},\boldsymbol{x}',t)\delta(t-t')\mathrm{d}t,$$

and the diagonal of the covariance tensor, defined as $a_{ij}(\boldsymbol{x},t) = c_{ij}(\boldsymbol{x},\boldsymbol{x},t)$ is of crucial importance in the following. It has the dimension of a diffusion (m^2/s) and plays the role of a *generalized* matrix-valued eddy viscosity.

The evolution of the large-scale component follows a modified Navier-Stokes system of equations [Mémin, 2014]

Incompressible Navier-Stokes equations ULU

Momentum equations

$$\partial_t\widetilde{\boldsymbol{u}} + \left(\Big(\widetilde{\boldsymbol{u}} - \frac{1}{2}(\boldsymbol{\nabla}\cdot\boldsymbol{a})\Big)\cdot\boldsymbol{\nabla}\right)\widetilde{\boldsymbol{u}} - \frac{1}{2}\boldsymbol{\nabla}\cdot\Big((\boldsymbol{a}\boldsymbol{\nabla})\widetilde{\boldsymbol{u}}\Big) = -\frac{1}{\rho}\boldsymbol{\nabla}p + \nu\boldsymbol{\nabla}^2\widetilde{\boldsymbol{u}}, \tag{4.3a}$$

Pressure random contribution

$$\boldsymbol{\nabla}\mathrm{d}p_t = -\rho(\boldsymbol{\sigma}\mathrm{d}\hat{\mathbb{B}}_t\cdot\boldsymbol{\nabla})\widetilde{\boldsymbol{u}} + \nu\boldsymbol{\nabla}^2\boldsymbol{\sigma}\mathrm{d}\mathbb{B}_t, \tag{4.3b}$$

Mass conservation

$$\boldsymbol{\nabla}\cdot(\boldsymbol{\sigma}\mathrm{d}\mathbb{B}_t) = 0, \quad \boldsymbol{\nabla}\cdot\widetilde{\boldsymbol{u}} - \frac{1}{2}\boldsymbol{\nabla}\cdot(\boldsymbol{\nabla}\cdot\boldsymbol{a}) = 0. \tag{4.3c}$$

This system corresponds to a large-scale description of the flow with an unresolved random turbulent component. A quite intuitive representation results from this formulation. It includes in a neat theoretical basis both a generalized eddy-viscosity subgrid model, $(\boldsymbol{a}\boldsymbol{\nabla})\widetilde{\boldsymbol{u}}$, together with a correction of the advection term associated with turbulence inhomogeneity ($\boldsymbol{\nabla}\cdot\boldsymbol{a}$). These two terms depend on the variance tensor, $\boldsymbol{a}(\boldsymbol{x})$. The term $\mathrm{d}p_t$ corresponds to the pressure term associated to the random turbulent component, whereas p is the large scale pressure, ρ is the density and ν the kinematic viscosity. The last constraint stems from mass conservation and imposes a divergence-free effective advection.

In the next section, we recall the ideal flow conditions pertaining to the classical derivation of the TBL mean velocity profile and develop its expression for the model under location uncertainty. In this paper, the x direction is the streamwise direction, y the spanwise direction and z the wall normal direction.

4.2 Boundary layer and wall laws

The derivation of the wall laws relies on the following hypothesis : the large-scale component $\widetilde{\boldsymbol{u}}$ is parallel to the wall plane $\{z=0\}$; the large-scale and small-scale velocity components are stationary and depend only on the distance to the wall, z ; on the wall the whole flow velocity is zero ($\widetilde{\boldsymbol{u}}=0$ and $\boldsymbol{\sigma}=0$) ; the large-scale pressure p is constant. At fixed depth, the random field is homogeneous with a constant variance tensor. This assumption, which considers no particular dependence on the horizontal plane of the variance tensor seems reasonable.

The tangential cumulated friction exerted by the flow on the wall per time interval, Δt, is expressed from the shear stress at the wall, which according to our model involves a large-scale component and a small-scale random component

$$S_t = \rho\nu \int_t^{t+\Delta t} \Big(\frac{\partial \widetilde{\boldsymbol{u}}}{\partial n}\mathrm{d}t + \frac{\partial \boldsymbol{\sigma}}{\partial n}\mathrm{d}\mathbb{B}_t\Big)\Big|_{z=0}, \tag{4.4}$$

Invoking Ito isometry for the Brownian term, we infer that its mean magnitude reads

$$\mathbb{E}\|\boldsymbol{S}_t\|^2 = (\rho\nu)^2\Delta t\int|\partial_n\widetilde{\boldsymbol{u}}|^2\mathrm{d}t + (\rho\nu)^2\int tr\Big(\partial_n\boldsymbol{\sigma}(\boldsymbol{x})\;\partial_n\boldsymbol{\sigma}^T(\boldsymbol{x})\Big)\mathrm{d}t. \tag{4.5}$$

Assuming that both the normal derivative of the diffusion tensor $\partial_n\boldsymbol{\sigma}$ and velocity $\partial_n\widetilde{\boldsymbol{u}}$

are constant, we get

$$(\mathbb{E}\|\boldsymbol{S}_t\|^2)^{\frac{1}{2}} = (\rho\nu)\Big(|\partial_n\widetilde{\boldsymbol{u}}|^2(\Delta t)^2 + \epsilon^2\Delta t\Big)^{1/2}. \tag{4.6}$$

In this expression, $\epsilon^2 = tr\Big(\partial_n\boldsymbol{\sigma}(\boldsymbol{x})\ \partial_n\boldsymbol{\sigma}^T(\boldsymbol{x})\Big)$ stands for the variance of the small-scale shear stress (where the dimension of the normal derivative is $[\partial_n\boldsymbol{\sigma}] = [T]^{-1/2}$).

The friction velocity $U_\tau\boldsymbol{\delta}_{\widetilde{\boldsymbol{u}}}$ in the direction $\boldsymbol{\delta}_{\widetilde{\boldsymbol{u}}}$ is now defined from the shear stress as

$$U_\tau = \left(\frac{\mathbb{E}(\|S\|^2)^{1/2}}{\rho\Delta t}\right)^{1/2} = \left[\nu\left(|\partial_n\widetilde{\boldsymbol{u}}|^2 + \frac{1}{\Delta t}\epsilon^2\right)^{1/2}\right]^{1/2}. \tag{4.7}$$

It can be checked this quantity scales as a velocity ($\sim (L^2/T^2)^{1/2}$) and for a null uncertainty $\epsilon^2 = 0$, we obtain the usual definition of the friction velocity : $U_\tau^{std} = (\nu|\partial_n u|^{1/2})$. For a non null uncertainty, we get a modified expression with a deviation from the standard definition depending on Δt. It is immediate to observe that when $\Delta t \to \infty$, $\boldsymbol{U}_\tau \to \boldsymbol{U}_\tau^{std}$. However, for small time interval and large small-scale velocity stress at the wall, the deviation from the standard definition can be important. The friction velocity $\boldsymbol{U}_\tau \approx \boldsymbol{U}_\tau^{std}$ is recovered only when the shear stress variance is much smaller than the time interval : $\epsilon^2 \ll \Delta t$.

4.2.1 Boundary layer structure

As classically admitted, the boundary layer is formed of two main sublayers : the viscous sublayer and the turbulent layer. The former corresponds to a region of contact between the wall and the fluid, where the flow is driven mainly by the molecular shear stress. In the latter, the flow is dominated by the large-scale shear stress associated to the small-scale random field. For the flow dynamics ULU and the TBL ideal configuration described above, the stationary equations for the mean velocity component in these two sub-layers are described below

Viscous sublayer $z \in [0, z_0]$

Large-scale component

$$\nu \boldsymbol{\nabla}^2 \widetilde{\boldsymbol{u}} = 0 \Rightarrow \partial_z \widetilde{\boldsymbol{u}} = C_1 \quad (4.8a)$$

Small scale component

$$\nu \boldsymbol{\nabla}^2 \boldsymbol{\sigma} \mathrm{d}\mathbb{B}_t = 0 \Rightarrow \boldsymbol{\nabla}^2 \boldsymbol{\sigma}^{ij} = 0 \quad (4.8b)$$

Turbulent pressure

$$\mathrm{d}p_t = C_2 \quad (4.8c)$$

Incompressibility

$$\boldsymbol{\nabla} \cdot (\boldsymbol{\sigma} \mathrm{d}\mathbb{B}_t) = 0 \quad (4.8d)$$

Turbulent sublayer $z \in [z_0, z_1]$

Large-scale component

$$-\partial_z a_{zz} \partial_z \widetilde{\boldsymbol{u}} - \partial_z \Big((a_{zz} + 2\nu) \partial_z \widetilde{\boldsymbol{u}} \Big) = 0 \quad (4.9a)$$

Turbulent pressure horizontal gradients

$$\boldsymbol{\nabla}_H \mathrm{d}p_t = \partial_z \widetilde{\boldsymbol{u}} (\boldsymbol{\sigma} \mathrm{d}\mathbb{B}_t)_z + \nu \boldsymbol{\nabla}^2 (\boldsymbol{\sigma} \mathrm{d}\mathbb{B}_t)_H = 0 \quad (4.9b)$$

Turbulent pressure vertical gradient

$$\partial_z \mathrm{d}p_t = \nu \boldsymbol{\nabla}^2 (\boldsymbol{\sigma} \mathrm{d}\mathbb{B}_t)_z \quad (4.9c)$$

Incompressibility

$$\boldsymbol{\nabla} \cdot (\boldsymbol{\sigma} \mathrm{d}\mathbb{B}_t) = 0, \quad \boldsymbol{\nabla} \cdot (\boldsymbol{\nabla} \cdot \boldsymbol{a}) = 0 \quad (4.9d)$$

In the viscous sublayer molecular viscosity dominates at all scales. Therefore the large-scale drift component exhibits a constant variation depth. The small-scale component is spatially very smooth (harmonic) and the random turbulent pressure diffusion term is constant.

In the turbulent sublayer, the dynamics is driven by the combination of the large-scale diffusion with the molecular friction. The eddy-induced velocity term caused by an eventual inhomogeneity of the turbulence is also involved in equation (4.9a). The second term of this equation represents the diffusion due to the molecular friction and the small-scale mixing activity. From these two systems, the expressions of the mean velocity profile can be inferred for both regions.

4.2.2 Velocity expression in the viscous sublayer

At the interface between the two sublayers $(z = z_0)$, the large-scale normal derivative of the velocity being constant, a null advection of $\widetilde{\boldsymbol{u}}$ by the random field $(\partial_z \widetilde{\boldsymbol{u}} (\boldsymbol{\sigma} \mathrm{d}\mathbb{B}_t)_z = 0)$ in the turbulent pressure equation (4.8c) implies that $(\boldsymbol{\sigma} \mathrm{d}\mathbb{B}_t)_z|_{z=z_0} = 0$. The null boundary condition of the random field at the wall and the harmonic condition (4.8b and the strong maximum principle) indicates that the turbulent component is necessarily 2D $(i.e. (\boldsymbol{\sigma} \mathrm{d}\mathbb{B}_t)_z = 0)$ and incompressible (4.8d) everywhere in the viscous layer. Furthermore, integrating below the viscous layer depth the harmonic condition of this horizontal

random field ($\boldsymbol{\nabla}_H^2(\boldsymbol{\sigma}\mathrm{d}\mathbb{I}\mathrm{B}_t)_H = -\partial_{zz}^2(\boldsymbol{\sigma}\mathrm{d}\mathbb{I}\mathrm{B}_t)_H$) we get

$$\boldsymbol{\nabla}_H^2 \int_0^{z_0} (\boldsymbol{\sigma}\mathrm{d}\mathbb{I}\mathrm{B}_t)_H = -\,\partial_z(\boldsymbol{\sigma}\mathrm{d}\mathbb{I}\mathrm{B}_t)_H|_{z=z_0} + (\partial_n\boldsymbol{\sigma}\mathbb{I}\mathrm{B}_t)_H.$$

The left-hand side term corresponds to an empirical mean along the vertical direction. Since it is a zero-mean random variable, it tends to zero (discretizing the interval with enough points) and thus

$$\partial_z(\boldsymbol{\sigma}\mathrm{d}\mathbb{I}\mathrm{B}_t)_H|_{z=z_0} = (\partial_n\boldsymbol{\sigma}\mathbb{I}\mathrm{B}_t)_H.$$

The right-hand term is an homogeneous random field with variance $\epsilon^2\mathrm{d}t$. The left-hand side random field has the same characteristics. Again due to the harmonic constraint and the strong maximum principle, its variance increases linearly with z. Therefore, the whole random field can be defined from a unitary 2D divergence-free Gaussian random field, $\boldsymbol{\eta}_t$, on the whole viscous layer and can be expressed as

$$(\boldsymbol{\sigma}(\boldsymbol{x})\mathrm{d}\mathbb{I}\mathrm{B}_t) = \epsilon z\sqrt{\mathrm{d}t}\ \boldsymbol{\eta}_t(\boldsymbol{x}),\ \forall z \in [0, z_0]. \tag{4.10}$$

This allows us to state : *in the viscous sublayer the small-scale component is a 2D divergence free random field characterized by a variance, which depends on the wall shear stress variance with a linear increase in time and with the square of the sublayer depth. Its vorticity is slanted,* $\boldsymbol{\nabla}\times\boldsymbol{\sigma}(\boldsymbol{x})\mathrm{d}\mathbb{I}\mathrm{B}_t = \epsilon\sqrt{\mathrm{d}t}(-\eta_y, \eta_x, z(\partial_x\eta_y - \partial_y\eta_x))^T$ *and its mean magnitude intensifies linearly with the distance to the wall. As a result, it forms curved cones of vorticity*.

Besides, from the friction velocity definition (4.7), (4.8a) and because $\partial_z\widetilde{\boldsymbol{u}} = \partial_n\widetilde{\boldsymbol{u}} = C_1$ we have (with $\partial_z\widetilde{\boldsymbol{u}} > 0$)

$$\partial_z\widetilde{\boldsymbol{u}} = \Big(\frac{1}{\nu^2}U_\tau^4 - \frac{1}{\Delta t}\epsilon^2\Big)^{1/2}\boldsymbol{\delta}\widetilde{\boldsymbol{u}} = \frac{1}{\nu}\widetilde{U}_\tau^2\boldsymbol{\delta}\widetilde{\boldsymbol{u}}, \tag{4.11}$$

where $\widetilde{U}_\tau = (\nu|\partial_n\widetilde{\boldsymbol{u}}|)^{1/2}$ stands for the friction velocity associated to the large-scale component. Integrating along z and since $\widetilde{\boldsymbol{u}}(0) = 0$, we therefore get

$$\widetilde{\boldsymbol{u}}(z) = \frac{1}{\nu}\widetilde{U}_\tau^2 z\ \boldsymbol{\delta}\widetilde{\boldsymbol{u}}. \tag{4.12}$$

Gathering the large-scale and small-scale components, the whole infinitesimal displace-

ment field over time interval, Δt, in the viscous layer finally reads

$$\forall z \in [0, z_\tau] \;\; \boldsymbol{u}(z)\Delta t = \frac{1}{\nu}\widetilde{U}_\tau^2 z \; \boldsymbol{\delta\widetilde{u}}\Delta t + \epsilon z(\Delta t)^{1/2}\boldsymbol{\eta}. \tag{4.13}$$

The small-scale zero-mean random component has a variance $V = \epsilon^2 z^2 \Delta t$. The mean velocity profile is given by (4.12) and the usual linear expression is retrieved. It is interesting to note that this profile can be specified from the friction velocity associated to the long-time average velocity field (if it can be computed), or from (4.7) if only smooth velocity snapshots on a given period of time together with an estimation of the small-scale shear stress variance are available. This latter case corresponds to the situation often encountered for the study of oceanic or atmospheric flows.

4.2.3 Velocity expression in the buffer and turbulent sublayer

In the vicinity of the viscous sublayer the molecular friction still dominates whereas at the end of the turbulent sublayer the large-scale shear stress is predominant. This stress depends directly on the small-scale variance. We assume that at the end of the turbulent sublayer the turbulence is isotropic with no influence of the wall. According to this hypothesis, the variance tensor tends toward a constant diagonal expression. As a consequence, at the end of the turbulent layer the dynamics of the large-scale component (4.9a) corresponds to an eddy-viscosity formulation

$$\frac{1}{2}(\partial_z a_{zz})\partial_z \, w + \frac{1}{2}\partial_(z \cdot ((a_{zz} + 2\nu)\partial_z \boldsymbol{\widetilde{u}}) = 0, \tag{4.14}$$

which leads to the logarithmic profile. The log law is however known to poorly fits the transitional buffer region coming into play just after the viscous layer. For that reason, we choose to separate the turbulent layer into a logarithmic region and a buffer zone.

Buffer zone

In the buffer zone, we assume a strict independence of the variance tensor with respect to the horizontal directions. With this assumption, the small-scale component is a 3D homogeneous random field for a given depth. From the incompressibility constraint we get

$$\boldsymbol{\nabla} \cdot \boldsymbol{\nabla} \cdot a = 0 \implies \partial_{zz}^2 a = 0 \implies \partial_z a_{zz} = C'. \tag{4.15}$$

At the interface $a_{zz}(z_0) = 0$, which yields $a_{zz}(z) = C'(z - z_0)$ where C' scales as a velocity. From similarity principles and as the variance tensor is assumed stationary for all z in the turbulent sublayer, we define

$$a_{zz}(z) = \widetilde{\kappa}\widetilde{U}_\tau(z - z_0), \tag{4.16}$$

where $\widetilde{\kappa}$ denotes a constant, which is different from the usual von Karman constant attached to the logarithmic region.

At the interface $z = z_0$, let us recall that we have from (4.12)

$$\partial_z\widetilde{\boldsymbol{u}}(z_0) = \frac{1}{\nu}\widetilde{U}_\tau^2\boldsymbol{\delta}\widetilde{\boldsymbol{u}}, \tag{4.17}$$

and a null value for the vertical variance tensor $(a_{zz} = 0)$. Integrating (4.9a) with the above boundary condition (4.17) gives an expression for $\partial_z\widetilde{\boldsymbol{u}}$. A second integration of the same equation gives the following velocity profile within the buffer zone

$$\forall z \in [z_0, z_L] \;\; \widetilde{\boldsymbol{u}}(z) = \widetilde{\boldsymbol{u}}(z_0) - \widetilde{U}_\tau\frac{4\nu}{\widetilde{\kappa}}\left(\frac{1}{\widetilde{\kappa}\widetilde{U}_\tau(z - z_0) + 2\nu} - \frac{1}{2\nu}\right)\delta\widetilde{\boldsymbol{u}}. \tag{4.18}$$

It can be checked that $\widetilde{\boldsymbol{u}}(z)$ and $\partial_z\widetilde{\boldsymbol{u}}(z)$ are indeed positive and therefore verify the fundamental properties of the large-scale velocity in the TBL. The buffer zone is restricted to an area located between the end of the viscous zone (at $z = z_0$) and the beginning of the logarithmic region (at $z = z_L$).

Logarithmic region

To reach a logarithmic profile from two successive integrations of (4.9a) the variance tensor cannot be linear anymore. It necessarily scales as the square-root of the wall distance ($a_{zz} \sim \sqrt{z}$). Because the flow is continuous in the whole turbulent boundary layer, we get the following expression

$$a_{zz}(z) = \widetilde{\kappa}\widetilde{U}_\tau(z_L - z_0)\sqrt{\frac{z}{z_L}}, \;\; \forall z \in [z_L, z_1], \tag{4.19}$$

for the vertical variance tensor value. To satisfy the incompressibility condition (4.9d), such an expression comes to relax the strict independence on x and y of the crossed vertical variance terms (a_{xz} and a_{yz}). For the region located between the buffer zone

limit (z_L) and the end of the turbulent sublayer (z_1), we have

$$\widetilde{\boldsymbol{u}}(z) = \widetilde{\boldsymbol{u}}(z_L) + \partial_z \widetilde{\boldsymbol{u}}(z_L) z_L \ln\left(\frac{z}{z_L}\right) \delta\widetilde{\boldsymbol{u}}. \tag{4.20}$$

This profile differs slightly from the usual logarithmic law. We notice that the von Karman constant, which weights the usual log-law, has here a more complex expression that depends among other things on the separation limit between the buffer zone and the logarithmic region.

4.3 Numerical validation

This section is devoted to the numerical assessments of the velocity profiles and of the expressions of $a_{zz}(z)$. Benchmark flows have been built from Direct Numerical Simulations of turbulent channel flows for two Reynolds (tau) numbers, $Re_\tau = 182$ and 536, with $Re_\tau = \frac{\widetilde{U}_\tau H}{\nu}$ where H denotes the half of the channel's height and $\widetilde{U}_\tau$ is the long-time averaged friction velocity. The dimensions of the channel for the $Re_\tau = 182$ case are $(L_x, L_z, L_y) = (4\pi, 2, 4\pi/3)$ and the resolution is $(n_x, n_y, n_z) = (128, 129, 128)$. The dimensions of the channel used in the $Re_\tau = 536$ case are $(L_x, L_z, L_y) = (2\pi, 2, 2\pi)$ and the resolution is $(n_x, n_y, n_z) = (256, 257, 256)$. The simulations have been performed with the high order finite-difference solver Incompact3d [Laizet and Lamballais, 2009]. In addition to these three channel flow simulations, a turbulent boundary layer up to $Re_\theta = 1808$ – with $Re_\theta = U_\infty \theta/\nu$ based on the free-stream velocity U_∞ and the momentum thickness $\theta = \int_0^\infty U/U_\infty(1 - U/U_\infty)\mathrm{d}y$ – has been simulated in the same setup as [Diaz-Daniel et al., 2017].

Particles trajectories have been computed from the Eulerian velocity fields, and a set of 4096 particles have been launched at every computationnal $z-$points and at 5 different times. The integration of the Lagrangian velocities has been performed using a fifth-order 3D-Lagrangian interpolation of the Eulerian fields and a second-order Adam-Bashford temporal scheme.

4.3.1 Variance evaluation in the viscous sublayer

We first assess the expression of the small-scale component random field in the viscous sublayer (4.10). Figure 4.1 depicts the variance of the velocity (in log-log plot)

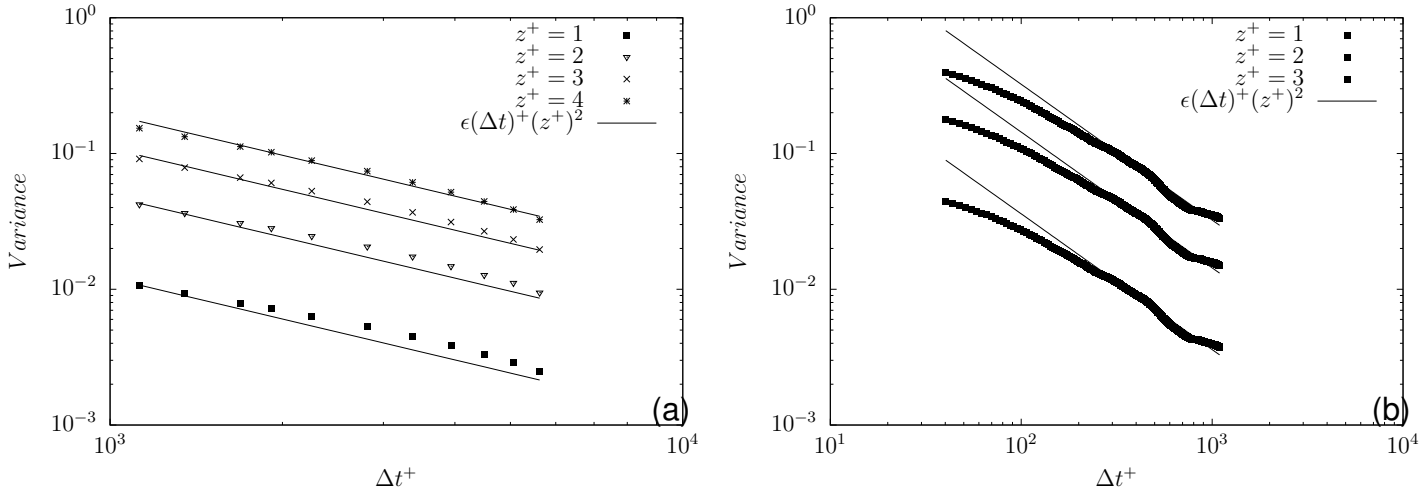

FIGURE 4.1 – Δ_t averaged streamwise velocity variances in the viscous sublayer for the channel flow $Re_\tau = 182$ (a) and the turbulent boundary layer at $Re_\tau \approx 550$ (b). The square, triangle, cross and star dots are the variance profiles at $z^+ = zU_\tau/\nu = 1, 2, 3$ and 4 respectively. The lines correspond to the theoretical profile $V = \epsilon z^2(\Delta_t)$.

in the streamwise direction for different time interval and different heights. Lagrangian velocity fields have been integrated on different windows of size Δ_t to provide different samples for these variances. The final variance corresponds to the empirical mean of these samples. The z^2 linear variance increase in the viscous sublayer is well recovered. The experimental rate is close to the one predicted by the model. The variance of the vertical velocity component is negligible (of the order from 10^{-5} to 10^{-3}, see also figure 4.3) as well as the vertical-horizontal cross correlation (not shown for concisness).

4.3.2 Variance tensor

The variance tensor can be evaluated through the integration of the Lagrangian velocity covariance up to the Lagrangian integral time scale T_i^L (for velocity component i) :

$$a_{ij}(z) = \int_0^{T_i^L(z) \wedge T_j^L(z)} < v_i'(t,z) v_j'(t,z) > \mathrm{d}t, \text{ with } a \wedge b = \max(a,b). \tag{4.21}$$

This definition is similar to the definition of the Prandtl mixing length from a Lagrangian free path [Prandtl, 1925]. In figure 4.2, we show an example of the probability density of the value of a_{zz} for a given distance to the wall. As it can be observed this empirical distribution roughly behaves as a log-normal distribution (with a sharp peak and a heavy

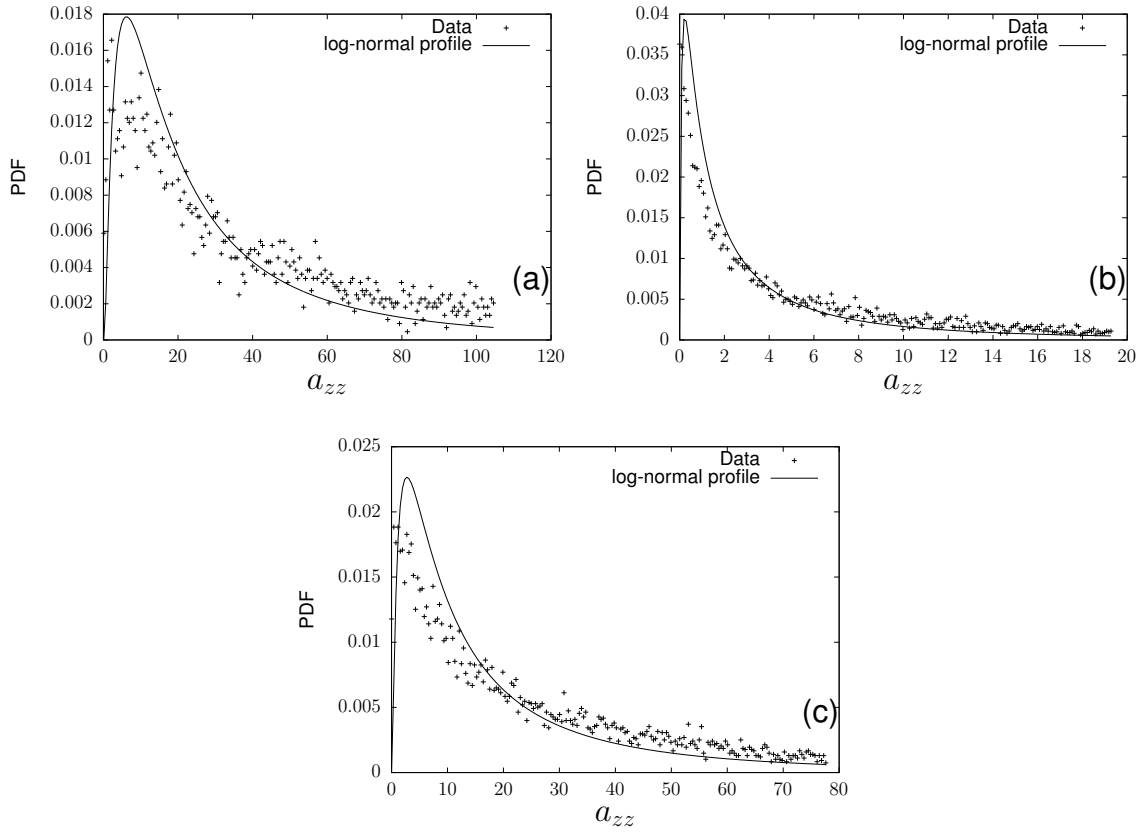

FIGURE 4.2 – Empirical probability density function of a_{zz} as crosses. The line is the log-normal profile which best fits to the data : (a) at the center of the turbulent boundary layer at $Re_\tau \approx 550$; (b) in the buffer of the channel $Re_\tau = 536$ and (c) at the center of the channel $Re_\tau = 536$.

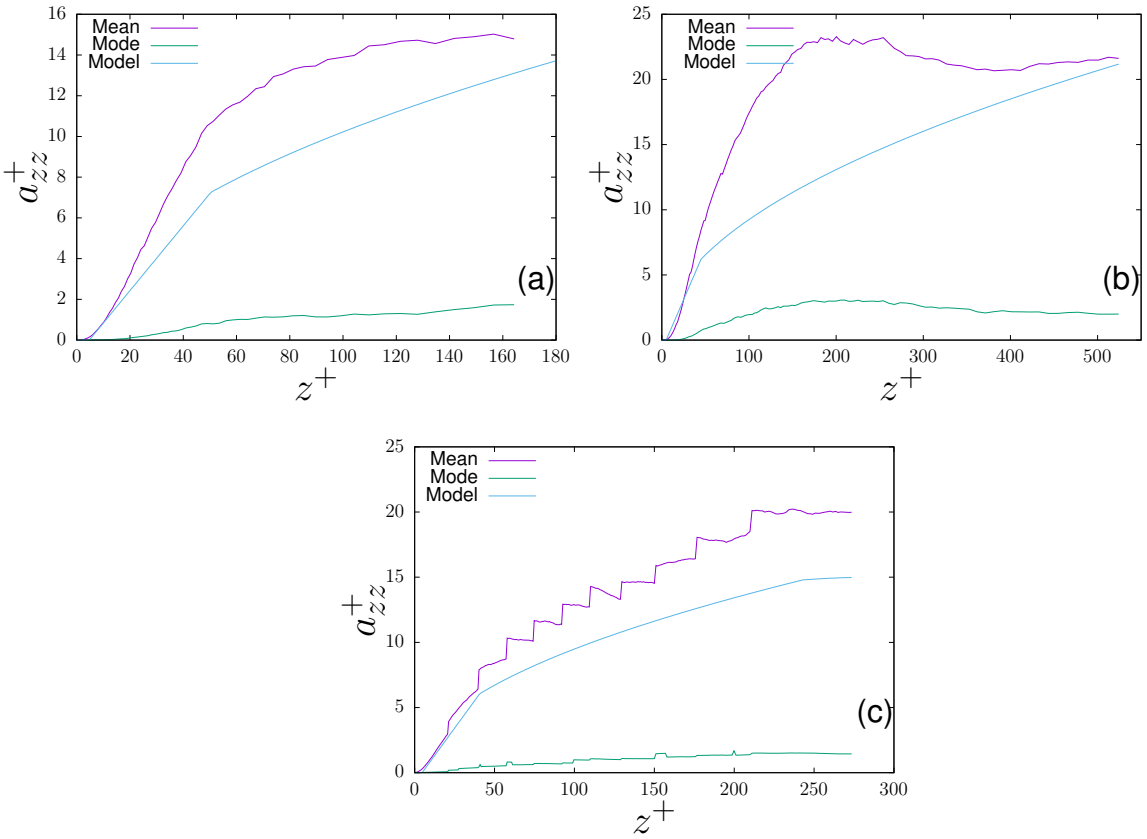

FIGURE 4.3 – Vertical component of the variance tensor for the channel flows (a) $Re_\tau = 182$, (b) $Re_\tau = 536$ and (c) the turbulent boundary layer $Re_\tau \approx 550$. The purple curve stands for the $a_{zz}(z)$ value at the distribution mean, the blue curves denote the theoretical model whereas the green curves show $a_{zz}(z)$ value at the distribution mode.

tail). In figure 4.3, we show, for each different flow configuration, the plot of the theoretical $a_{zz}(z)$ profile ($a_{zz} \propto 0$; $a_{zz} \propto z$; $a_{zz} \propto \sqrt{z}$ in the viscous, buffer and logarithmic zones respectively) and compare it to the empirical mean and mode distribution values. The theoretical curves lie in between the mean and the mode of the distribution but remains clearly closer to the mean. This indicates a reasonable approximation of the vertical value of the variance tensor.

4.3.3 Drifts profiles

The velocity profiles come from two different databases. The turbulent boundary layer simulation are provided from the Universidad Politecnica de Madrid. The

turbulent boundary layer lies to a range $Re_\theta \in [2780 - 6650]$ and an equivalent Reynolds friction number $Re_* \in [1000, 2000]$. More details are available in the articles [Sillero et al., 2013, M. P. Simens J. Jimenez, 2009, G. Borrell, 2013].

The velocity profiles of the pipe flow experiments are provided by the royal Institude of technolgy of Stockolm (KTH). We use the profiles from the experiment at $Re_* = 180, 360, 550, 1000$. The explanations of the simulations are noticed in the article [El Khoury et al., 2013].

Methodology The main issue is to fit the near wall profile, since the database provides more points inside this section, the designed objective function to minimize is :

$$f(z_0, z_l, \kappa) = \sum_{i=0}^{N} (u(z_i) - u_{ref}(z_i))^2. \tag{4.22}$$

In the equation (4.22), the function u is the profile computed with the set of variables (z_0, z_l, κ) whereas u_{ref} is the profile provided by the database. The limit N is the height where reference velocity profile does not fit to the logarithmic profile (the begin of the wake section).

We briefly explain the procedure. The starting point $x^0 = (z_0^0, z_l^0, \kappa^0)$ of the algorithm is a manually derived profile which fits the data. The fixed step α for each problem is setted at 10^{-8}. The gradient of the objective function is computed by a 1st order gradient scheme. At each step the next solution is

$$x^{n+1} = (z_0^{n+1}, z_l^{n+1}, \kappa^{n+1}) = x^n + \alpha \nabla f(z_0^n, z_l^n, \kappa^n).$$

The limit of the viscous zone (z_0) is estimated in a classical way as the first point departing from the linear velocity profile (with a relative error of 0.02). The constant $\widetilde{\kappa}$ and the limit of the buffer zone are estimated through a nonlinear least-squares procedure from (4.18) and (4.20) respectively. In figure 4.4, we show the mean velocity profiles for each flow configuration. We considered also a very high Reynolds number case ($Re_\tau \approx 5200$) provided by [Lee and Moser, 2015] (figure 4.4c). For each case, the parameters are $(z_0^+, z_L^+, \widetilde{\kappa}) = (4.75, 50, 0.145)$ at $Re_\tau = 182$; $(5, 52, 0.152)$, at $Re_\tau = 536$;

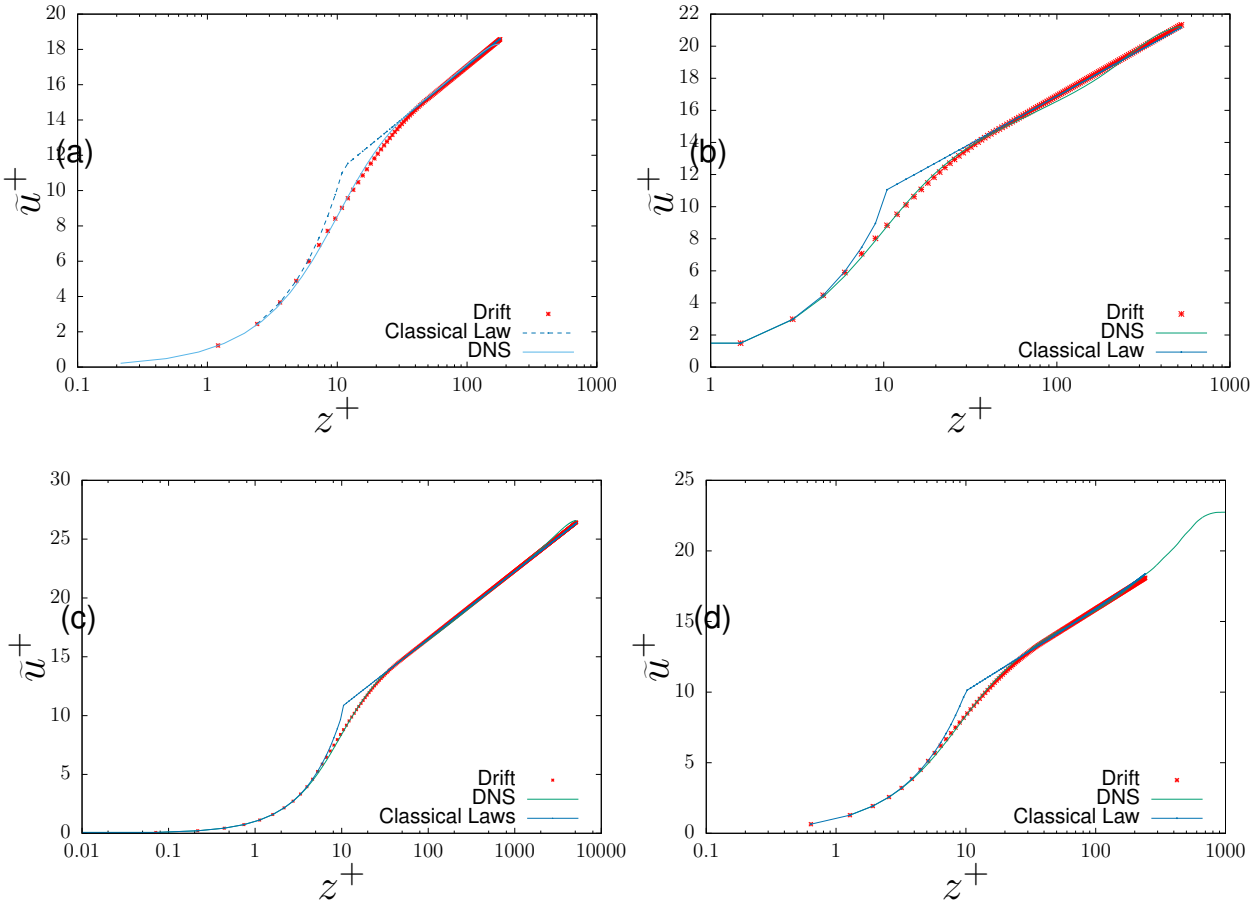

FIGURE 4.4 – Mean velocity profiles for the channels flow (a) $Re_\tau = 182$, (b) $Re_\tau = 536$, (c) $Re_\tau \approx 5200$ [Lee and Moser, 2015] and (d) the turbulent boundary layer at $Re_\tau \approx 550$. The green curves are the reference velocity profiles computed by the DNS ; the blue dot lines are the classical laws (linear then logarithmic) and the red dots corresponds to the profile of the model under location uncertainty.

$(5, 45, 0.16)$, at $Re_\tau \approx 5200$ and $(5, 45, 0.155)$ for the TBL at $Re_\tau \approx 550$. The profiles of the new model are compared to the classical wall laws : $\widetilde{\boldsymbol{u}} = z\widetilde{U}_\tau^2/\nu$ in the viscous sublayer, and $\widetilde{\boldsymbol{u}} = u_\tau \left(\frac{1}{\kappa} \ln(z\frac{\widetilde{U}_\tau}{\nu}) + B \right)$ above the viscous sublayer, where the constants κ and B are optimally set from the data. In the viscous sublayer, there is no difference between the classical models and the new one (4.12). Both of them perfectly superimpose with the experimental data.

In the buffer region, where $a_{zz}(z)$ is linear, there is no theoretically well grounded model available for the velocity profile. In this transition area both the linear profile or the logarithmic profile deviate significantly from the experimental profiles. At variance, the new model fits well the data. The modeling under location uncertainty, unlike adhoc formulation Spalding1961, enables us to devise a physically coherent model from a large-scale representation of the Navier-Stokes equation.

In the logarithmic region, both the classical log-law model and the modified one provide similar results. This highlights the validity of the connection between the linear and square-root profiles of $a_{zz}(z)$ as the velocity profile highly depends on $\partial_z \widetilde{\boldsymbol{u}}(z_l)$ (4.20).

Turbulent boundary layer The table 4.23 summarizes the optimal triplet of parameters for the tubulent boundary layer experimentation. First of all, for each experimentation, the values belongs to a tiny interval.

Re_*	z_0^+	z_l^+	κ
1306	4.94	48.22	0.158
1437	4.97	48.29	0.157
1709	5.08	49.01	0.161
1989	4.8976	50.38	0.15776

(4.23)

Pipe Flow In this paragraph the results for the pipe flow experimentations are shown. The optimal parameters are shown in the table 4.24. Few properties are shown, the value of z_0 is decreasing when the friction Reynolds number increases, z_l inscreases and κ is constant except for the first simulation.

Having a look to figures 4.9,4.10, 4.11, 4.12. Contrarly to the channel flow simulation, the pipe flow exhibits a larger deviation from the logarithmic profile at high Reynolds number, hence the range of validity of the current profiles is a few restricted. However,

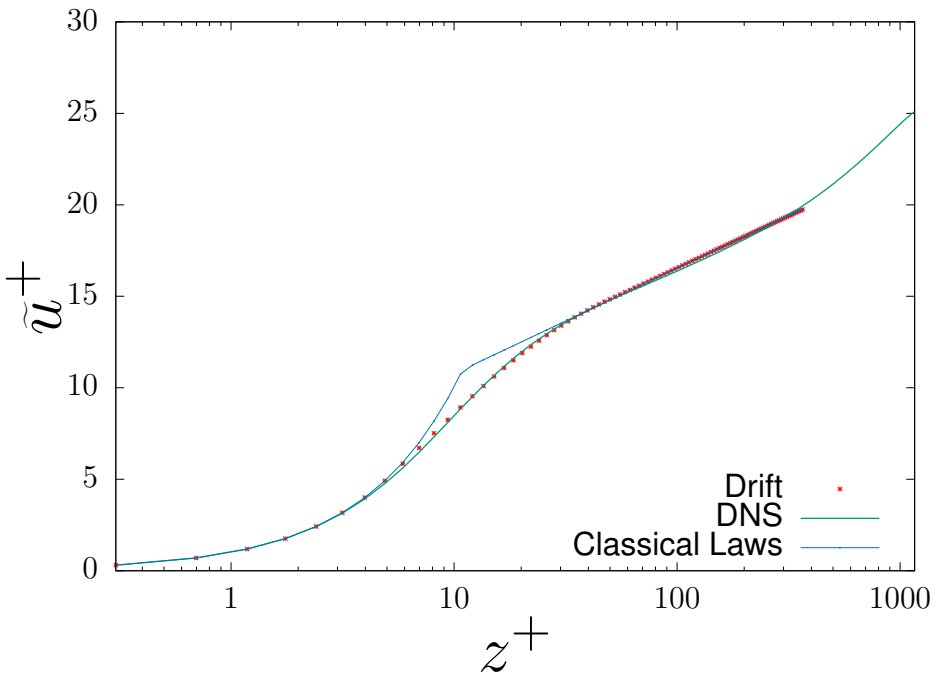

FIGURE 4.5 – Velocity profiles for the turbulent boundary layer at $Re_* = 1306$

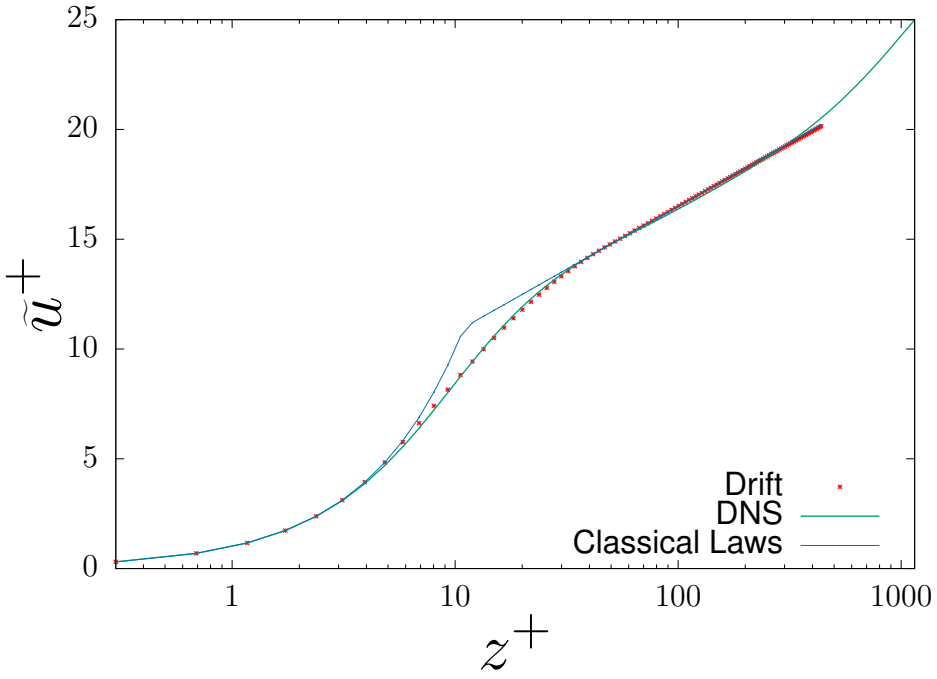

FIGURE 4.6 – Velocity profiles for the turbulent boundary layer at $Re_* = 1437$

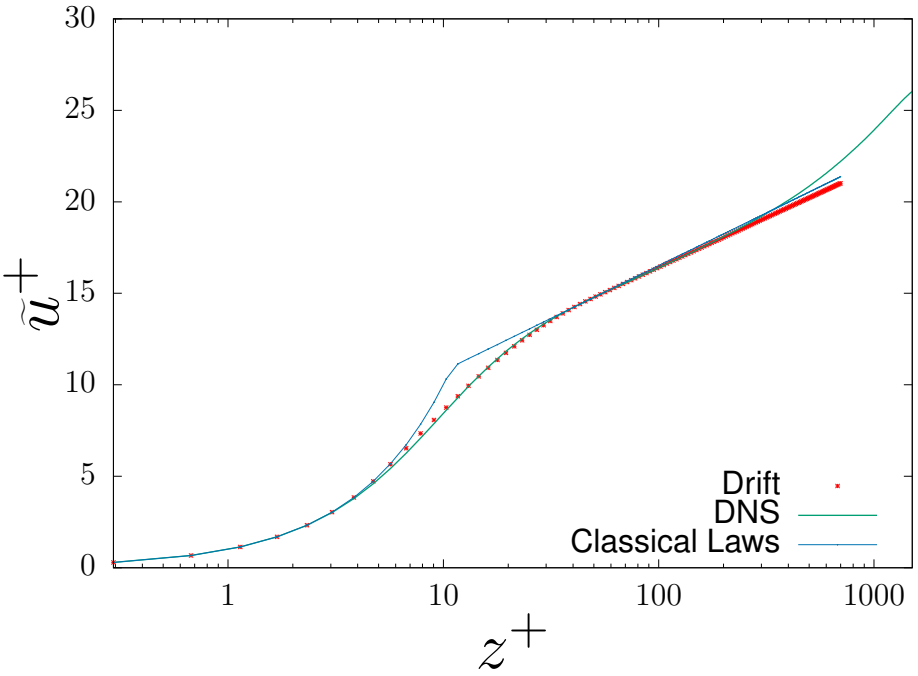

FIGURE 4.7 – Velocity profiles for the turbulent boundary layer at $Re_* = 1709$

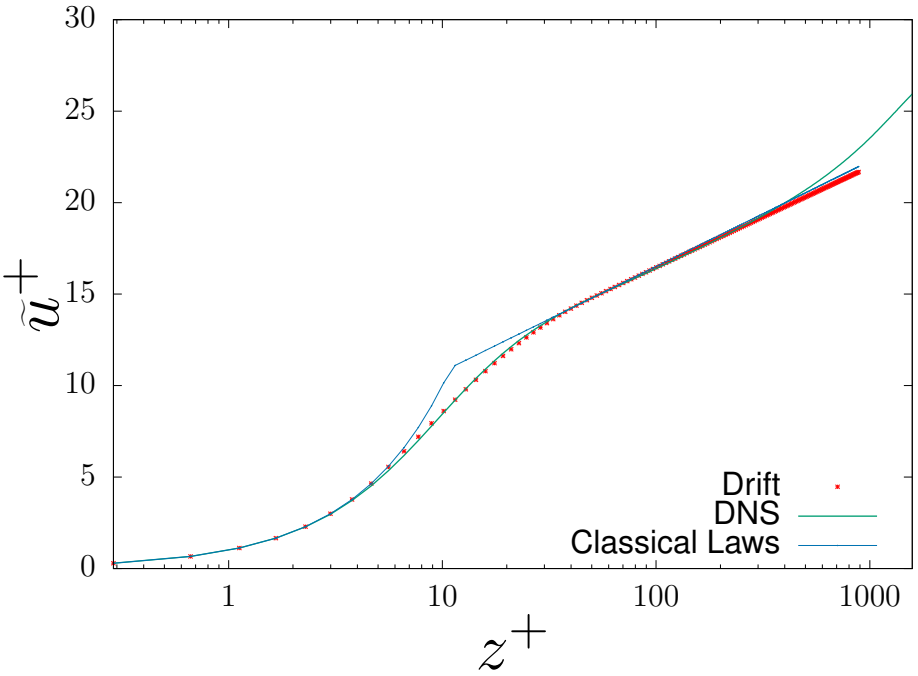

FIGURE 4.8 – Velocity profiles for the turbulent boundary layer at $Re_* = 1989$

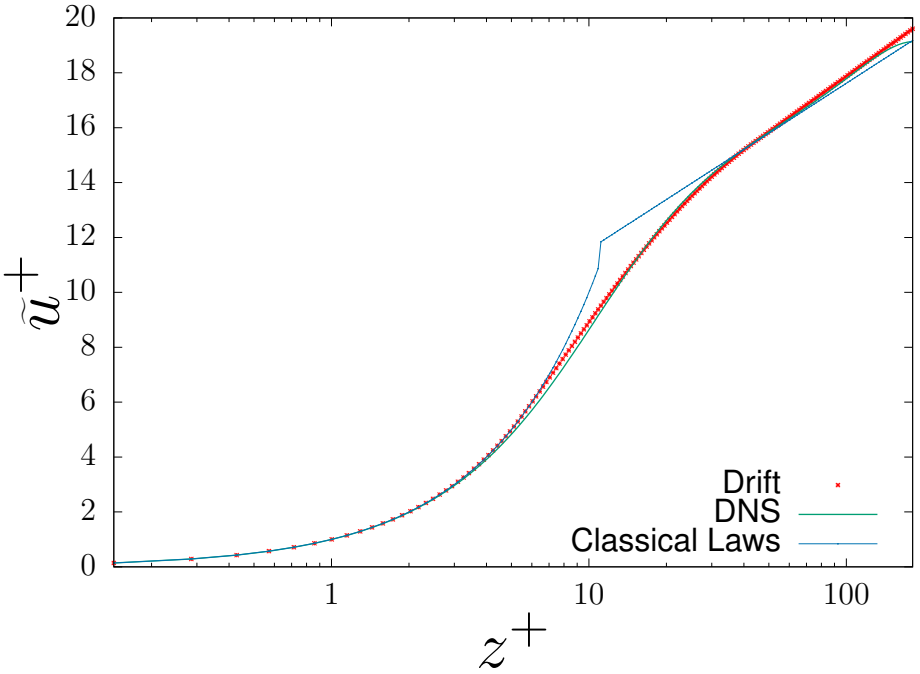

FIGURE 4.9 – Velocity profiles for the pipe flow at $Re_* = 180$

near wall, the velocity profiles fit well with the references.

Re_*	z_0^+	z_l^+	κ
180	5.61	43.754	0.15
360	5.27	43.85	0.158
590	5.11	46.31	0.158
1000	5.05	49	0.158

(4.24)

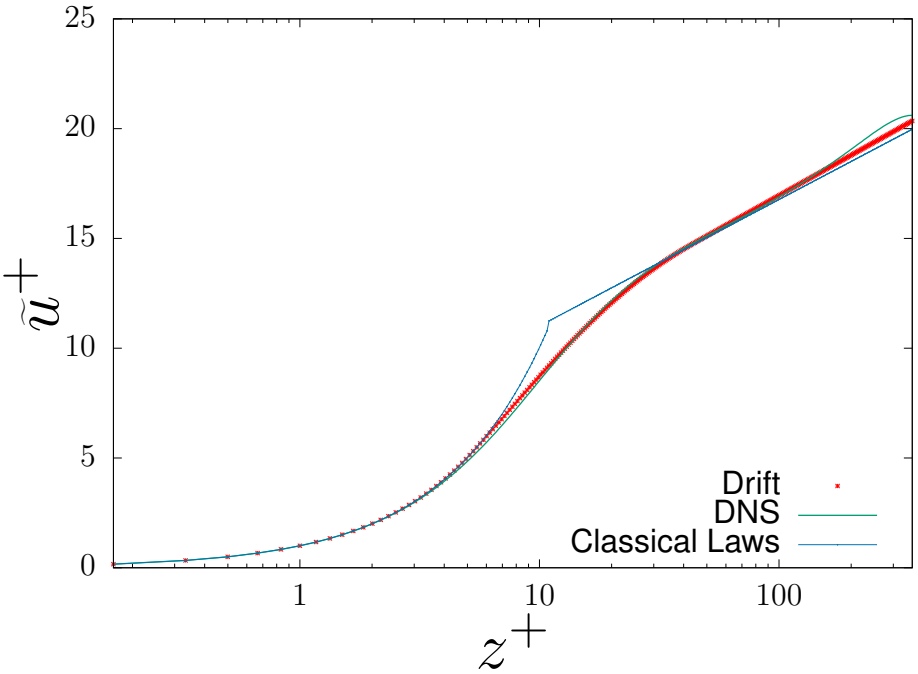

FIGURE 4.10 – Velocity profiles for the pipe flow at $Re_* = 360$

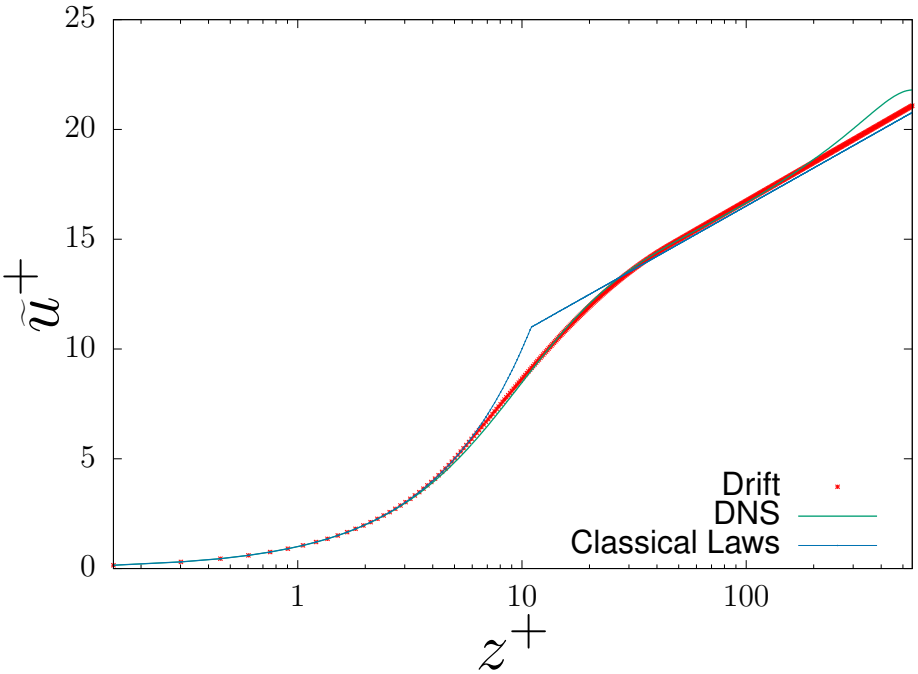

FIGURE 4.11 – Velocity profiles for the pipe flow at $Re_* = 590$

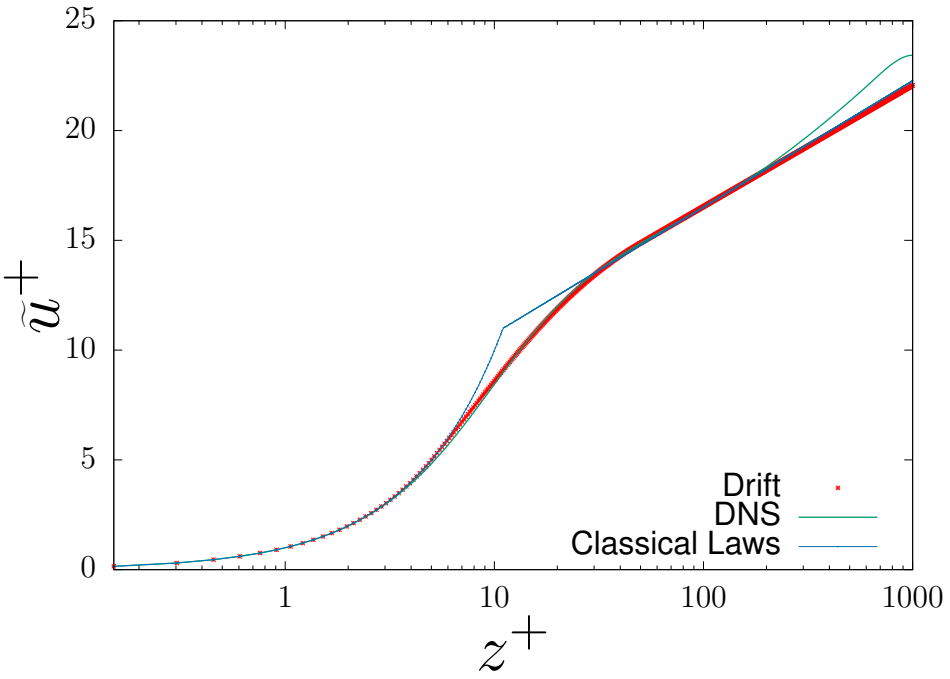

FIGURE 4.12 – Velocity profiles for the pipe flow at $Re_* = 1000$

CONCLUSION

Dans la première partie de ce manuscrit, nous nous sommes intéressé à une nouvelle formulation de la longueur de mélange de Prandtl. Cette dernière a la particularité de prendre en compte des simulations à très haut nombre de Reynolds. De plus, cette formule est universelle au sens où chacun de ces coefficients est une fonction du nombre de Reynolds. Via un ensemble de simulations numériques menées sur le solveur volumes finis OpenFoam, nous avons démontré que cette longueur de mélange était à même de reproduire l'énergie cinétique turbulente ainsi que le champ de vitesse moyen dans la couche limite. Nous avons poussé le Reynolds de friction à 10000 pour vérifier ces résultats. De plus, nous avons développé une modification prenant en compte un fond rugueux pour un canal. A partir de ce travail, nous avons montré que l'obtention d'une formule correcte pour la longueur de mélange malgré l'ensemble des données disponible est très sensible.

De plus, nous avons démontré l'existence d'une solution pour le problème mathématique associé en utilisant les techniques à la "Boccardo-Gallouet" pour des problèmes avec un terme source dans L^1. Il semble possible de faire une extension au cas parabolique.

Il est possible de pousser le raisonnement écrit ici pour un écoulement stratifié. Des DNS existent à haut nombre de Reynolds depuis les 5 dernières années. Il est probable qu'un paramètre de stratification β modifie légèrement la formule de la longueur de mélange. Mathématiquement, le problème associé (à première vue en imposant une condition mixte sur un champ de température) semble lui aussi démontrable.

La modélisation under location uncertainty a donc apporté un profil de vitesse moyenne qui colle parfaitement bien avec les données obtenues par des DNS y compris à haut nombre de Reynolds. Nous avons vérifié cette expression pour des couches limites ainsi que des écoulements de canal. Il est important de noter le caractère C^1 du profil obtenu y compris dans la zone de buffer.

Les lois utilisées pour obtenir ce profil sont mathématiquement et physiquement cohérentes. En effet, les hypothèses faites sur le tenseur des variances ont été vérifiées. Contrairement à ce qui est souvent admis, cet équivalent à la viscosité turbulente n'est pas limité à une valeur, c'est une distribution qui suit une loi log-normale. Le tenseur de variance est compris pour toutes les altitudes entre le mode et la moyenne de cette distribution. Dans la zone de buffer, la croissance linéaire de a_{zz} suit le mode et converge vers la moyenne en se rapprochant du sommet de la zone turbulente.

La démonstration utilisée met en avant le rôle de l'advection modifiée, en effet, c'est ce terme qui permet de faire le lien entre la zone visqueuse et la zone logarithmique.

Nous nous sommes également intéressé à l'expression de la variance à temps court dans la zone visqueuse qui suit une loi inversement proportionnelle au temps, cela permet de générer des profils de vitesses à temps court physiquement cohérents. Les corrélations spatiales (streak) sont gérées par le noyau $\boldsymbol{\sigma}$.

Les perspectives ouvertes sont intéressantes pour l'obtention de profil à temps court dans le cas neutre mais aussi dans le cas d'un fluide stratifié, en effet, le système atmosphérique ne conserve pas assez longtemps sa propriété thermique pour converger vers une moyenne uniforme.
Enfin, il sera intéressant de tester ce modèle sur des écoulements industriels (pipeline, ailes d'avions ...).

Appendices

ANNEXE A

DETERMINATION OF THE NUMERICAL VISCOSITY AND DIFFUSIVITY INHERENT TO THE DISCRETIZATION FOR THE ADVECTION TERM IN OPENFOAM

A.1 Numerical framework

We introduced some useful notations summarized in the figure 2.5 :

— Let a family of convexe opens of dimension d , $\{K_i, \forall i \in \{1, N\} = I\}$ such that $\overline{\Omega} = \overline{\cup_{i \in I} K_i}$, we notice $\mathscr{T} = \{K_i, \forall i \in I\}$ the mesh.
— Each $K \in \mathscr{T}$ denotes a control volume,
— $\forall K \in \mathscr{T}$, we notice $\mathbf{x}_k$ coordinates of the gravity center of K,
— $\forall K \in \mathscr{T}$, we notice ϵ_K the set of its faces, that is $\epsilon_K = \partial K = \overline{K} \setminus K = \cup_{\sigma \in \epsilon_K} \overline{\sigma}$,
— $\forall K \in \mathscr{T}$, we notice $\mathscr{N}_K = \{L \in \mathscr{T} \setminus \overline{K} \cap \overline{L} \neq \emptyset\}$, the set of control volumes which are the neighbourhood of K,
— $\forall (K, N) \in (\mathscr{T}, \mathscr{N}_K)$,we notice the common face $\sigma_{K,L}$ such that $\overline{K} \cap \overline{N} = \overline{\sigma}_{K,N}$
— $\forall (K, N) \in (\mathscr{T}, \mathscr{N}_K)$, we notice $\mathcal{D}_{K,L}$ the line between x_K and x_N. We associate the distance $d_{K,\sigma}$ between x_K and the face $\sigma = \{\sigma \in \epsilon_K | \epsilon_K \cap \mathcal{D}_{K,N} \neq 0\}$.

In this study, we make an important assumption about the mesh, $\forall (K, L) \in (\mathscr{T}, \mathscr{N}_K), \mathcal{D}_{K,L}$ is orthogonal to σ such that the classical scheme used to compute the gradient is second-order.

We consider in this study two problems, a transport of a scalar field and a fluid problem computed by a Navier Stokes equations.

The Navier Stokes problem expressed in finite volume framework is :

$$\begin{cases} \frac{d}{dt}(|K|\mathbf{v}_K) + \sum_{\sigma\in\epsilon_K} \psi_\sigma \mathbf{v}_\sigma - \sum_{\sigma\in\epsilon_K} |\sigma|(2\nu+\nu_t)\nabla\mathbf{v}_\sigma + |K|\nabla p_K &= |K|\mathbf{f}_K + R_2 \quad \Omega, \\ \sum_{\sigma\in\epsilon_K} \psi_\sigma &= 0 \quad \Omega, \end{cases} \tag{A.1}$$

Because the convection term is nonlinear, we notice $\psi_\sigma = |\sigma|\mathbf{v}_\sigma \cdot \mathbf{n}_{K,\sigma}(\mathbf{x})$ as the interfacial flux, the pressure gradient is considered as a data since it is computed during another step of the algorithm to ensure the divergence free constraint. The issue raised from the spatial interpolation to express the $\mathbf{v}_\sigma$ in term of $\mathbf{v}_K, K \in \mathscr{T}$ essential to determine the convention term and diffusion. Furthermore, the term R_2 denotes the error inherent to the schemes.

In our framework, the interpolation schemes are expressed as :

$$T_\sigma = (T_\sigma)^{(U)} + \Psi(r)[(T_\sigma)^{(L)} - (T_\sigma)^{(U)}] \tag{A.2}$$

and

$$\mathbf{v}_\sigma = (\mathbf{v}_\sigma)^{(U)} + \mathbf{\Psi}(r)[(\mathbf{v}_\sigma)^{(L)} - (\mathbf{v}_\sigma)^{(U)}] \tag{A.3}$$

where $(\mathbf{v}_\sigma)^{(U)}$ is the interpolated value computed by the spatial upwind scheme as $(\mathbf{v}_\sigma)^{(U)} = \alpha_u(\mathbf{v}_K - \mathbf{v}_N) + \mathbf{v}_N$ where $\alpha_u = 1$ if $\psi_\sigma > 0$ and 0 otherwise. This scheme is well known to be bounded but it brings a huge amount of numerical diffusion. The other term $(\mathbf{v}_\sigma)^{(L)}$ denotes the interpolated value computed by the linear interpolation such that $(\mathbf{v}_\sigma)^{(L)} = d_\sigma\mathbf{v}_K + (1-d_\sigma)\mathbf{v}_N$, this is a third order scheme, however it produces spurious oscillations. According to the previous observations, theses schemes make the computed solution less physical.

The determination of the limiter functions $\Psi(r)$ is divided in two ways, a first one devoted to the scalar field and another one to the vectorial fields.

Let T being a scalar field. The parameter r of the flux limiter is

$$r = 2\frac{\mathbf{d}_{K,L} \cdot (\nabla T)_J}{T_N - T_K} - 1 \tag{A.4}$$

where $\mathbf{d}_{K,L} = \mathbf{x}_K - \mathbf{x}_N$ and

$$(\nabla T)_J = \begin{cases} \nabla T_K & if \quad \psi_\sigma > 0 \\ \nabla T_N & else \end{cases} \tag{A.5}$$

This formulation derived from the original method presented in [Sweby, 1984]. A first modification for unstructured grid was provided in [Bruner and Walters, 1997] and another improvement was brough in [Darwish and Moukalled, 2003].
Now, let $\mathbf{v}$ a vector, the parameter could be obtained by the same way as a scalar field, in that case, one can consider $T = ||\mathbf{v}||^2$. This is the way used when a numerical scheme like 'SuperBee', 'MUSCL', 'Minmod' are used for a vector field. The specific way to compute the parameter of a the limiter function is :

$$r = 2\frac{(\mathbf{v}_N - \mathbf{v}_K) \cdot (\mathbf{d}_{K,L} \cdot (\nabla \mathbf{v})_J)}{||\mathbf{v}_N - \mathbf{v}_K||^2} - 1 \tag{A.6}$$

where $\mathbf{d}_{K,L} = \mathbf{x}_K - \mathbf{x}_N$, and

$$(\nabla \mathbf{v})_J = \begin{cases} \nabla \mathbf{v}_K & if \quad \psi_\sigma > 0 \\ \nabla \mathbf{v}_N & else \end{cases} \tag{A.7}$$

The equation A.6 is used for the numerical schemes called with the suffixe 'V" e.g. 'MinmodV','SuperBeeV' etc. In this study, we will deal with the SuperBee scheme [Roe, 1986]

$$\psi(r) = max(min(1, 2r), min(2, r)), \tag{A.8}$$

the MUSCL scheme [Van Leer, 1979] :

$$\psi(r) = \frac{r + |r|}{1 + r^2}, \tag{A.9}$$

The vanLeer schemes [Van Leer, 1974]

$$\psi(r) = \frac{r + |r|}{1 + r}, \tag{A.10}$$

The MinMod scheme [Harten, 1983] :

$$\psi(r) = min(1, r), \tag{A.11}$$

and the vanAlbada scheme [van Albada et al., 1997]

$$\psi(r) = \frac{r + r^2}{1 + r^2}, \tag{A.12}$$

A.2 Expression of the numerical viscosity

In the case of an interpolation process described as in A.3, a numerical viscosity is obtained and as a consequence, we get a modified system explained in the next proposition.

Proposition A.2.1. *If the scheme uses for the interpolation of* $\mathbf{v}_\sigma$ *d admit a form as in A.3 in the convection discretization, so the first equation of* **??** *becomes :*

$$\frac{d}{dt}(|K|\mathbf{v}_K) + \sum_{\sigma\in\epsilon_K} |\sigma|(\mathbf{v}_\sigma)^{(L)} \cdot \mathbf{n}_{K,\sigma}\mathbf{v}_\sigma - \sum_{\sigma\in\epsilon_K} |\sigma|(2\nu + \nu_t + \nu_{\mathbf{num}})\nabla\mathbf{v}_\sigma + |K|\nabla p_K = |K|\mathbf{f}_K + R_2 \quad \Omega \tag{A.13}$$

where

$$\nu_{\mathbf{num}} = \frac{\psi_\sigma}{|\sigma|} d_{K,L} \left(\mathbf{I_3} - \mathbf{\Psi}(r)\right)(\alpha_u - d_\sigma), \tag{A.14}$$

$\mathbf{I_3}$ *is the three dimensionned identity matrix and*

$$\mathbf{\Psi}(r) = \begin{pmatrix} \Psi(r) & 0 & 0 \\ 0 & \Psi(r) & 0 \\ 0 & 0 & \Psi(r) \end{pmatrix}. \tag{A.15}$$

Démonstration. To get the expression of the numerical viscosity, we need to get an expression like

$$\mathbf{v}_\sigma = (\mathbf{v}_\sigma)^{(L)} + \nu_{\mathbf{num}}(\nabla\mathbf{v})_\sigma \cdot \mathbf{n}_{K,\sigma}$$

.

We begin by modifying A.3 to get

$$\mathbf{v}_\sigma = (\mathbf{v}_\sigma)^{(L)} + (\mathbf{I_3} - \mathbf{\Psi}(r))[(\mathbf{v}_\sigma)^{(U)} - (\mathbf{v}_\sigma)^{(L)}] \tag{A.16}$$

We combine with $(\mathbf{v}_\sigma)^{(U)} = \alpha_u(\mathbf{v}_K - \mathbf{v}_N) + \mathbf{v}_N$ and $(\mathbf{v}_\sigma)^{(L)} = d_\sigma\mathbf{v}_K + (1 - d_\sigma)\mathbf{v}_N$ to

get :

$$\mathbf{v}_\sigma = (\mathbf{v}_\sigma)^{(L)} + (\mathbf{I_3} - \mathbf{\Psi}(r))[(\mathbf{v}_K) - (\mathbf{v}_N)]\,(\alpha_u - d_\sigma) \tag{A.17}$$

Since the mesh is orthogonal, the approximation $(\nabla\mathbf{v})_\sigma \cdot \mathbf{n}_{K,\sigma} = (\mathbf{v}_K - \mathbf{v}_N)/(\mathbf{d}_{K,L} \cdot \mathbf{n}_{K,\sigma})$ admits a second order error, we can note :

$$\mathbf{v}_\sigma = (\mathbf{v}_\sigma)^{(L)} + (\mathbf{I_3} - \mathbf{\Psi}(r)) d_{K,L} (\nabla\mathbf{v})_\sigma \cdot \mathbf{n}_{K,\sigma}\,(\alpha_u - d_\sigma) \tag{A.18}$$

Now, coming back to the convection term in **??**

$$\sum_{\sigma\in\epsilon_K} \psi_\sigma \mathbf{v}_\sigma = \sum_{\sigma\in\epsilon_K} \psi_\sigma \left[(\mathbf{v}_\sigma)^{(L)} + (\mathbf{I_3} - \mathbf{\Psi}(r)) d_{K,L} (\nabla\mathbf{v})_\sigma \cdot \mathbf{n}_{K,\sigma}\,(\alpha_u - d_\sigma)\right] \tag{A.19}$$

We focus on the second part and the right hand side of the previous equation,

$$\sum_{\sigma\in\epsilon_K} \psi_\sigma (\mathbf{I_3} - \mathbf{\Psi}(r)) d_{K,L}\,(\alpha_u - d_\sigma)\,(\nabla\mathbf{v})_\sigma \cdot \mathbf{n}_{K,\sigma} = \sum_{\sigma\in\epsilon_K} |\sigma| \frac{\psi_\sigma}{|\sigma|} (\mathbf{I_3} - \mathbf{\Psi}(r)) d_{K,L} (\nabla\mathbf{v})_\sigma\,(\alpha_u - d_\sigma) \cdot \mathbf{n}_{K,\sigma} \tag{A.20}$$

such that

$$\sum_{\sigma\in\epsilon_K} \psi_\sigma (\mathbf{I_3} - \mathbf{\Psi}(r)) d_{K,L}\,(\alpha_u - d_\sigma)\,(\nabla\mathbf{v})_\sigma \cdot \mathbf{n}_{K,\sigma} = \sum_{\sigma\in\epsilon_K} \int_\sigma \left(\frac{\psi_\sigma}{|\sigma|} (\mathbf{I_3} - \mathbf{\Psi}(r)) d_{K,L}\,(\alpha_u - d_\sigma)\,(\nabla\mathbf{v})_\sigma \cdot \mathbf{n}_{K,\sigma} \right) \tag{A.21}$$

And so

$$\sum_{\sigma\in\epsilon_K} \psi_\sigma (\mathbf{I_3} - \mathbf{\Psi}(r)) d_{K,L}\,(\alpha_u - d_\sigma)\,(\nabla\mathbf{v})_\sigma \cdot \mathbf{n}_{K,\sigma} = \int_K \nabla \cdot \left(\frac{\psi_\sigma}{|\sigma|} (\mathbf{I_3} - \mathbf{\Psi}(r)) d_{K,L}\,(\alpha_u - d_\sigma)\,(\nabla\mathbf{v})_K \right) \tag{A.22}$$

then, we are able to identify

$$\nu_{num} = \frac{\psi_\sigma}{|\sigma|} (\mathbf{I_3} - \mathbf{\Psi}(r)) d_{K,L}\,(\alpha_u - d_\sigma) \tag{A.23}$$

The modified equation is obtained considering $\sum_{\sigma\in\epsilon_K} \psi_\sigma (\mathbf{v}_\sigma)^{(L)} = \int_K \mathbf{v}_K \otimes \mathbf{v}_K$ with a second order error. □

According to the same procedure, on can get a proposition for the scalar problems :

Proposition A.2.2. *If the interpolated value T_σ between the cells K and L in the convection term is A.2, equation* **??** *becomes :*

$$\frac{d}{dt}(|K|T_K) + \sum_{\sigma\in\epsilon_K} |\sigma|(\psi_\sigma)\cdot\mathbf{n}_{K,\sigma}T_\sigma^{(L)} - \sum_{\sigma\in\epsilon_K} |\sigma|\nu_{num}\nabla T_\sigma = 0 \quad \Omega \tag{A.24}$$

where $T_\sigma^{(L)}$ is the interpolated value of T by a linar method and

$$\nu_{num} = \frac{\psi_\sigma}{|\sigma|} d_{K,L}\left(1-\Psi(r)\right)(\alpha_u - d_\sigma). \tag{A.25}$$

A.3 Verification of the expression

In order to test the validity of the formulation obtained for the numerical viscosity, we compare results obtained from a solver computing the classical transport equation where the convection term is computed as in A.3 and another solver which compute the solution a transport-diffusion problem where the convection term is discretized by CDS and the viscosity for the diffusion term is leaded by the numerical viscosity.

The code used to validate our result is an implementation of a Runge Kutta projection method presented in [Vuorinen et al., 2014] and used in an atmospheric boundary layer simulation [Vuorinen et al., 2015].

A.3.1 Scalar case

1 step profile

The benchmark is based on the 2D-step profile, it consists of a 2D square with side of length unity. The tested resolution is $46\times46\times1$. The advected quantity is initialized as 1 at the left and top and 0 at the bottom and right boundaries. The scalar quantity is advected by a constant velocity $\mathbf{u} = (1,1,0)^T$. The problem converges to a step profile. We will test the CDS, Upwind and the TVD schemes based on the superbee, minMod and VanLeer limiter functions.

In figure A.1, we present the contour plot of the solution for the 2D step-profile problem where the interpolation schemes are upwind (A.1a) and Minmod (A.1b).

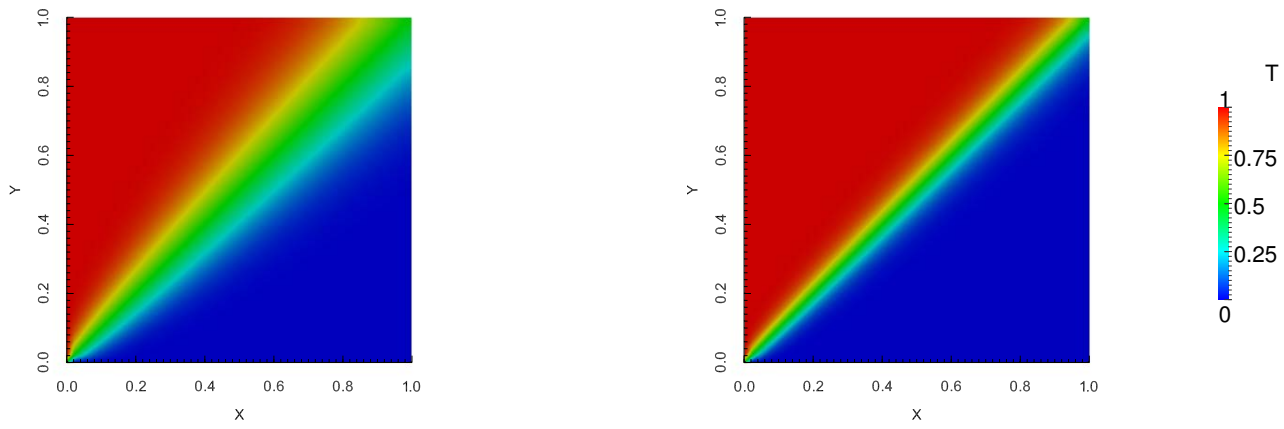

(a) Upwind

(b) Minmod

FIGURE A.1 – Plot of the solution for the 2D Step profile problem, left : Upwind, right : minMod

Since the upwind scheme is described by $\psi_\sigma(r) = 0$, it corresponds to the maximum numerical viscosity, as a consequence, the diffusion in maximum and it is illustrated by the smoothness of the solution. In the case of the Minmod limiter, $0 < \Psi(r) < 1$ so the diffusion is weaker as in the upwind scheme and according to A.23, the numerical viscosity remains positive, there is no anti-diffusion added to the problem. As a consequence, the smoothness of the solution is lower as the upwind case.

We present on figure A.2 the profile of the advected quantity for both the transport-diffusion and the transport problems. The profile correspond to the values at the arbitrary chosen cutting plane $y = 0.5$. With both solutions perfectly matches for every tested schemes (other schemes were also tested), we can conclude that for the benchmark problem, the numerical viscosity A.23 is correct.

The numerical viscosity are presented in figure A.3a at the line $y = 0.5$ for the schemes upwind, Minmod, superb and MUSCL. It shows the numerical viscosity is higher far away from the discontinuity and reduce until the reaches its minimum at the discontinuity. Furthermore, it is interesting to notice the numerical viscosity is high for region where the gradient is null, this curiosity has no effect since the diffusion term $\nabla \cdot (\nu_{num} \nabla T) = 0$. The limiter functions presented in figure A.3b shows the region

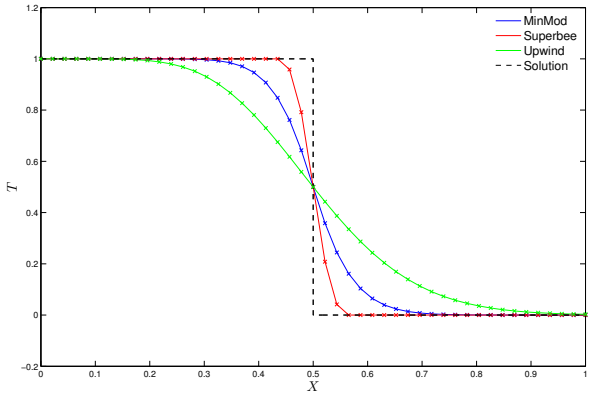

FIGURE A.2 – Comparison of the advected quantity profile T for the cutting plane $y = 0.5$, the lines correspond to the solution computed for the transport-diffusion problem and the cross correspond to the solution for the transport problem using upwind, Minmod, superBee schemes for the interpolation

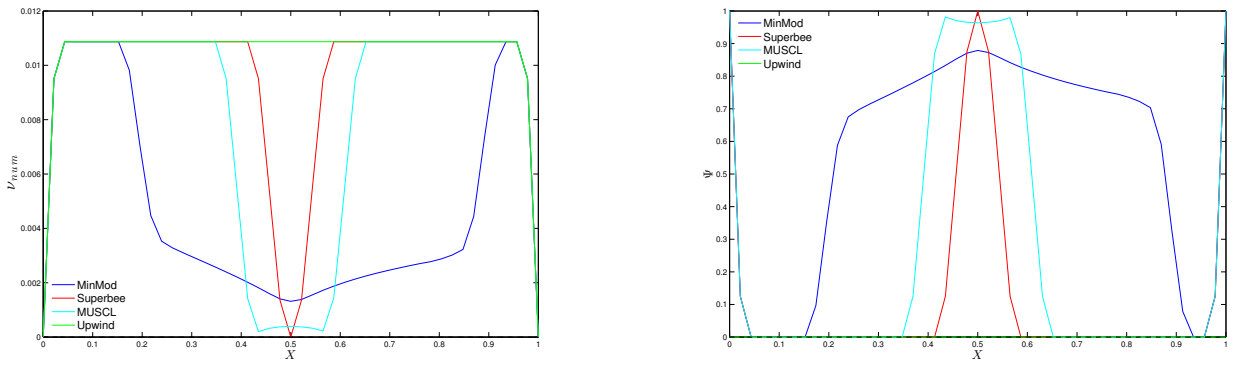

(a) Numerical Viscosity

(b) Limiters function

FIGURE A.3 – Plot of the solution for the numerical viscosity and the limiters function at the line $y = 0.5$ for the schemes upwind, Minmod, superb and MUSCL

where the gradient is null since the function depends on the variations of the gradient.

Furthermore, in this problem, the gradient are not high enough to make the limiter function superior to 1 for the superBee and MUSCL, because theses functions are bounded by 2, they could bring numerical anti-diffusivity and do not ensure a monotone solution. A modification in the interpolation process where the limiter function is divided by 2 ensure a positive numerical viscosity and as a consequence the absence of spurious oscillations, it is illustrated in [Bidadi and Rani, 2014] in the context of the Roe-MUSCL schemes.

A.3.2 Vectorial cases in 2D

We now turn to the study of the numerical viscosity and effect of the numerical schemes for the incompressible Navier Stokes equation. In the first experimentation, we will focus in the shear layer experience and then, we will be interested in 2D Taylor Green experience.
For both shear layers and taylor-Green experience, we will be interested in some statistics. First of all, the total kinetic energy in computed as

$$E_k = \frac{1}{2|\Omega|}\int_\Omega \mathbf{v}\cdot\mathbf{v}dx \tag{A.26}$$

The viscous dissipation is

$$\epsilon_{viscous} = \frac{\nu}{|\Omega|}\int_\Omega \mathbf{v}\cdot\Delta\mathbf{v}dx \tag{A.27}$$

and the numerical dissipation induced by the numerical schemes is :

$$\epsilon_{num} = \frac{1}{|\Omega|}\int_\Omega \mathbf{v}\cdot\nabla\cdot\left(\nu_{\mathbf{num}}\nabla\mathbf{v}\right)dx \tag{A.28}$$

We recall that the equations A.26, A.27 and A.28 come from the procedure known to compute the kinetic energy equation. It is derived by taking the scalar product of $\mathbf{v}$ with Navier Stokes equation.

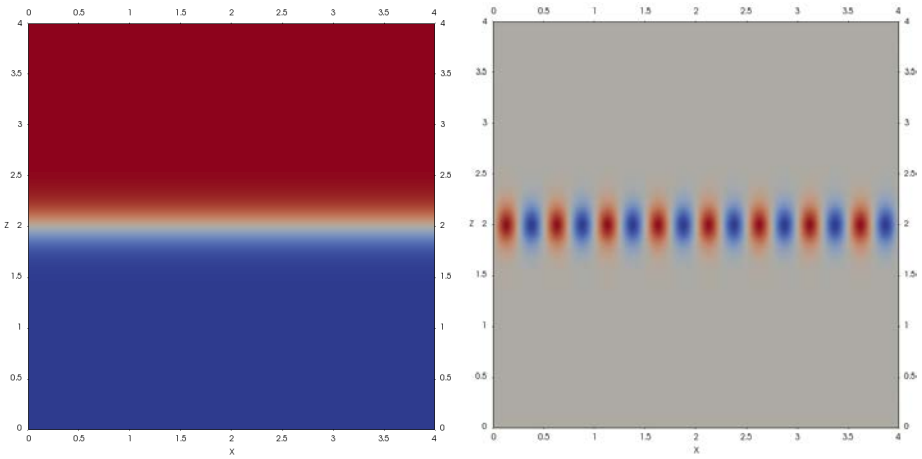

FIGURE A.4 – Initial profile of the velocity field (left : u, right : v) for the shear stress experimentation. In the red section $u(x,z) = U_0$ and in the blue section $u(x,z) = -U_0$. The intermediate section, which is the regularization to get a derivative $u-$profile, is dependant on the Reynolds number.

Shear layer flow

The first problem to study the numerical dissipation induced by the discretization of the convection term is the shear layer flow. This problem is known to generate vorticies at the shear interface [Lesieur et al., 1988]. The problem takes place in a numerical blox with size $(L_x, L_z) = (4H, 4H)$. The initial condition for the velocity field is :

$$u(x,z) = U_0 tanh\left(\frac{z-2H}{\delta}\right) \tag{A.29}$$

and

$$v(x,z) = \alpha sin(4\pi x)\frac{\partial u}{\partial z} \tag{A.30}$$

where $\alpha = 0.04\delta$. We use the length δ to generate a Reynolds number as $Re = \frac{U_0\delta}{\nu}$. In this study, the Reynolds number is setted as 202500. We show an example of the initial flow in figure A.4. In the current simualtion $U_0 = 10$. The timestep is $\Delta t = 0.001$ to ensire that the maximum Courant number in less than 1. The simulations are runned until $t = 10$.

In the figures A.5, we show the dissipation in the simulations. The top picture summarize every run including the extrem case upwind. The highly diffusive characteristic of the upwind scheme is clear, at $t = 10$, the simulation dissipates

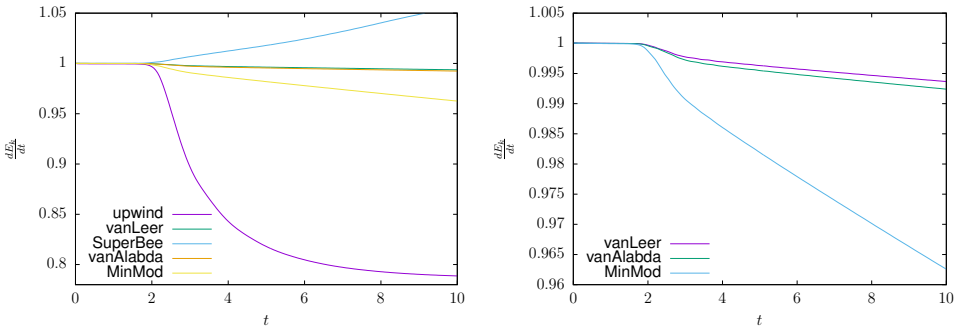

FIGURE A.5 – Normalized dissipation for the shear layer flow. At the top, we show the results with the upwind and SuperBee problems (purple and blue respectively) and at the bottom, we focus on the solution from the vanLeer, vanAlbada and MinMod problem.

around 22% whereas the MinMod schemes, which is the second more dissipative scheme, disspiates only 3.75% of the initial kinetic energy. Contrary the upwind scheme, the anti-dissusivity of the SuperBee scheme is visible while $\frac{dE_k}{dt} > 0$. Furthermore, according to the plot, $\frac{d^2E_k}{d^2t} > 0$, which proves the high instability of the solution.

At the bottom of the figure A.5, we focus on the effect of the stable TVD-schemes on the dissipation according to the time. It was clear that the MinMod scheme was more dissipative than the vanLeer and vanAlbada schemes from the previous picture. With the bottom one, we can conclude that thhe vanLeer scheme brings less dissipation than the vanAlbada one.

In the figure A.6, we show the decomposition of the diffusity into the viscous and the numerical parts. For this experimentation, the numerical viscosity is very higher than the molecular viscosity when the vortices are organized. At the beginning of the simulation, when the Kelvin Helmotz vortices are not organized, it is the modelcular one which dominates. Because the numerical viscosity needs strong gradients to increase, this fact is explained by the abscence of strong gradient in the initialization period.

Having a look to the particular SuperBee case in figure **??**, it is clear that the negative viscosity is brough by the numerical scheme which is (in magnitude) also very stronger than the molecular viscosity. The same feature than the other schemes is visible at the beginning of the simulation, the physical diffusion dominates the numerical one.

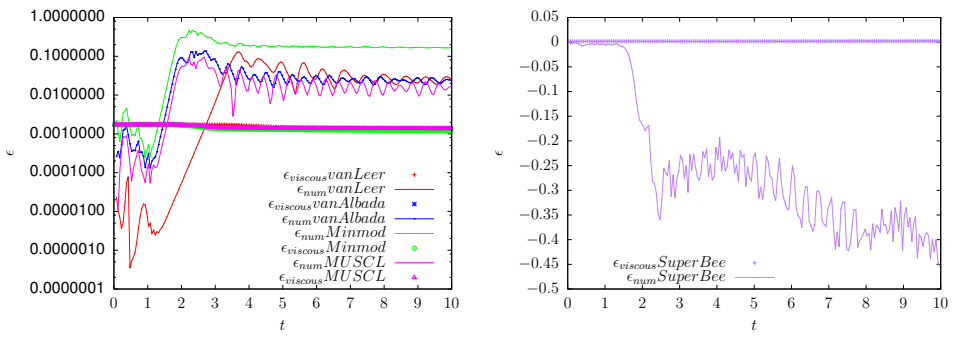

FIGURE A.6 – Viscous (crosses) and numerical (lines) dissipation, of the shear layer experience, induced by a vanLeer, vanAlbada, MinMod and MUSCL schemes. In this case, the numerical viscosity are positive unlike in the SuperBee case.

BIBLIOGRAPHIE

[Adams and Fournier, 2003] Adams, R.-A. and Fournier, J. F. (2003). *Sobolev spaces*, volume 140 of *Pure and Applied Mathematics (Amsterdam)*. Elsevier/Academic Press, Amsterdam, second edition.

[Andreu et al., 2007] Andreu, F., Igbida, N., Mazón, J., and Toledo, J. (2007). L1 existence and uniqueness results for quasi-linear elliptic equations with nonlinear boundary conditions. *Annales de l'Institut Henri Poincare (C) Non Linear Analysis*, 24(1) :61–89.

[Andreu et al., 2008] Andreu, F., Igbida, N., Mazón, J., and Toledo, J. (2008). Renormalized solutions for degenerate elliptic–parabolic problems with nonlinear dynamical boundary conditions and L1-data. *Journal of Differential Equations*, 244(11) :2764–2803.

[Andrews and McIntyre, 1976] Andrews, D. and McIntyre, M. (1976). Planetary waves in horizontal and vertical shear : the generalized Eliassen- Palm relation and the zonal mean acceleration. *J. Atmos. Sci.*, 33 :2031–2048.

[Argyropoulos and Markatos, 2015] Argyropoulos, C. and Markatos, N. (2015). Recent advances on the numerical modelling of turbulent flows. 39 :pp.693–732.

[Barenblatt et al., 1997] Barenblatt, G., Chorin, A., and Prostokishin, V. (1997). Scaling laws for fully developed turbulent flow in pipes. *Applied Mechanics Reviews*, 50(7) :413–429.

[Barenblatt and Chorin, 1998] Barenblatt, G. and Chorin, J. (1998). Scaling of the intermediate region in wall-bounded turbulence : The power law. *Physics of Fluids*, 10(4) :1043–1044.

[Batchelor, 1959] Batchelor, G. K. (1959). *The theory of homogeneous turbulence*. Cambridge Monographs on Mechanics and Applied Mathematics. Cambridge University Press, New York.

[Behrendt et al., 2015] Behrendt, A., Wulfmeyer, V., Hammann, E., Muppa, S., and Pal, S. (2015). Profiles of second-to fourth-order moments of turbulent temperature

fluctuations in the convective boundary layer : first measurements with rotational raman lidar. *Atmospheric Chemistry and Physics*, 15(10) :5485–5500.

[Bennis et al., 2010] Bennis, A.-C., Chacón-Rebollo, T., Gómez-Mármol, M., and Lewandowski, R. (2010). Numerical modelling of algebraic closure models of oceanic turbulent mixing layers. *M2AN Math. Model. Numer. Anal.*, 44(6) :1255–1277.

[Berselli and Lewandowski, 2018] Berselli, L. and Lewandowski, R. (2018). On the reynolds time-averaged equations and the long-time behavior of leray-hopf weak solutions, with applications to ensemble averages. *Preprint : https://arxiv.org/abs/1801.08721*.

[Bidadi and Rani, 2014] Bidadi, S. and Rani, S. (2014). Quantification of numerical diffusivity due to tvd schemes in the advection equation. *Journal of Computational Physics*, 261 :65 – 82.

[Blanke and Delecluse, 1993] Blanke, B. and Delecluse, P. (1993). Variability of the tropical atlantic ocean simulated by a general circulation model with two different mixed-layer physics. *J. Phys. Oceanogr.*, 23 :1363–1388.

[Blocken et al., 2007] Blocken, B., Stathopoulos, T., and Carmeliet, J. (2007). CFD simulation of the atmospheric boundary layer : wall function problems. *Atmospheric Environment*, 41(2) :238–252.

[Boccardo et al., 1989] Boccardo, L., Diaz, J. I., Giachetti, D., and Murat, F. (1989). Existence of a solution for a weaker form of a nonlinear elliptic equation. In *Recent advances in nonlinear elliptic and parabolic problems (Nancy, 1988)*, volume 208 of *Pitman Res. Notes Math. Ser.*, pages 229–246. Longman Sci. Tech., Harlow.

[Boccardo and Gallouët, 1989] Boccardo, L. and Gallouët, T. (1989). Nonlinear elliptic and parabolic equations involving measure data. *J. Funct. Anal.*, 87(1) :149–169.

[Boccardo and Murat, 1994] Boccardo, L. and Murat, F. (1994). A property of nonlinear elliptic equations when the right-hand side is a measure. *Potential Anal.*, 3(3) :257–263.

[Boussinesq, 1877] Boussinesq, J. (1877). Theorie de l'écoulement tourbillant. *Mém. prés par div. savants á la Acad. Sci.*, 23 :46–50.

[Brezis, 2011] Brezis, H. (2011). *Functional analysis, Sobolev spaces and partial differential equations*. Universitext. Springer, New York.

[Brossier and Lewandowski, 2002] Brossier, F. and Lewandowski, R. (2002). Impact of the variations of the mixing length in a first order turbulent closure system. *M2AN Math. Model. Numer. Anal.*, 36(2) :345–372.

[Bruner and Walters, 1997] Bruner, C. and Walters, R. (1997). Parallelization of the Euler equations on unstructured grids. In *13th Computational Fluid Dynamics Conference*, Fluid Dynamics and Co-located Conferences. American Institute of Aeronautics and Astronautics. DOI : 10.2514/6.1997-1894.

[Bulíček et al., 2011] Bulíček, M., Lewandowski, R., and Málek, J. (2011). On evolutionary Navier-Stokes-Fourier type systems in three spatial dimensions. *Comment. Math. Univ. Carolin.*, 52(1) :89–114.

[Businger et al., 1971] Businger, J. A., Wyngaard, J. C., Izumi, Y., and Bradley, E. F. (1971). Flux-Profile Relationships in the Atmospheric Surface Layer.

[Busse et al., 2015] Busse, A., Lützner, M., and Sandham, N. D. (2015). Direct numerical simulation of turbulent flow over a rough surface based on a surface scan. *Computers & Fluids*, 116 :129–147.

[Cammilleri et al., 2013] Cammilleri, A., Guéniat, F., Carlier, J., Pastur, L., Mémin, E., Lusseyran, F., and Artana, G. (2013). Pod-spectral decomposition for fluid flow analysis and model reduction. *Theoretical and Computational Fluid Dynamics*, 27(6) :787–815.

[Cannone, 2004] Cannone, M. (2004). Harmonic analysis tools for solving the incompressible Navier-Stokes equations. In *Handbook of mathematical fluid dynamics. Vol. III*, pages 161–244. North-Holland, Amsterdam.

[Carlier and Stanislas, 2005] Carlier, J. and Stanislas, M. (2005). Experimental study of eddy structures in a turbulent boundary layer using particle image velocimetry. *Journal of Fluid Mechanics*, 535 :143–188.

[Chabrowski, 2007] Chabrowski, J. (2007). On the Neumann problem with L1 data. *Colloq. Math.*, 107(2) :301–316.

[Chacòn Rebollo and Lewandowski, 2014] Chacòn Rebollo, T. and Lewandowski, R. (2014). *Mathematical and Numerical Foundations of Turbulence Models and Applications*. Modeling and Simulation in Science, Engineering and Technology. Springer New York.

[Chandramouli et al., 2018] Chandramouli, P., Heitz, D., Laizet, S., and Mémin, E. (2018). Coarse large-eddy simulations in a transitional wake flow with flow models under location uncertainty. *Computer and Fluids*, 168 :170–189.

[Chemin and Gallagher, 2009] Chemin, J.-Y. and Gallagher, I. (2009). Wellposedness and stability results for the Navier-Stokes equations in $\mathbf{R}^3$. *Ann. Inst. H. Poincaré Anal. Non Linéaire*, 26(2) :599–624.

[Cheng and Porté-agel, 2016] Cheng, W. and Porté-agel, F. (2016). Large-eddy simulation of flow and scalar dispersion in rural-to-urban transition regions. *International Journal of Heat and Fluid Flow*, 60 :47–60.

[Chow, 2007] Chow, P. (2007). *Stochastic partial differential equations*. Chapman and Hall/CRC.

[Cipra, 1996] Cipra, B. (1996). A new theory of turbulence causes a stir among experts. *Science*, 272(5264) :951–951.

[Clark et al., 1979] Clark, R. A., Ferziger, J. H., and Reynolds, W. C. (1979). Evaluation of subgrid-scale models using an accurately simulated turbulent flow. *Journal of Fluid Mechanics*, 91(1) :1–16.

[Coleman et al., 1992] Coleman, G. N., Ferziger, J. H., and Spalart, P. R. (1992). Direct simulation of the stably stratified turbulent Ekman layer. *Journal of Fluid Mechanics*, 244(-1) :677.

[Coles, 1956] Coles, D. (1956). The law of the wake in the turbulent boundary layer. *Journal of Fluid Mechanics*, 1(January) :191–226.

[Constantin and Foias, 1988] Constantin, P. and Foias, C. (1988). *Navier-Stokes equations*. Chicago Lectures in Mathematics. University of Chicago Press, Chicago, IL.

[Darwish and Moukalled, 2003] Darwish, M. S. and Moukalled, F. (2003). TVD schemes for unstructured grids. *International Journal of Heat and Mass Transfer*, 46 :599–611.

[Deardorff, 1970] Deardorff, J. W. (1970). A numerical study of three-dimensional turbulent channel flow at large reynolds numbers. *Journal of Fluid Mechanics*, 41(2) :453–480.

[Del Alamo et al., 2004] Del Alamo, J. C., Jiménez, J., Zandonade, P., and Moser, R. D. (2004). Scaling of the energy spectra of turbulent channels. *Journal of Fluid Mechanics*, 500 :135–144.

[Diaz-Daniel et al., 2017] Diaz-Daniel, C., Laizet, S., and Christos Vassilicos, J. (2017). Wall shear stress fluctuations : Mixed scaling and their effects on velocity fluctuations in a turbulent boundary layer. *Physics of Fluids*, 29(5).

[Ducros et al., 1998] Ducros, F., F., N., and Poinsot, T. (1998). Wall-adapting local eddy-viscosity models for simulations in complex geometries. *Numerical Methods for Fluid Dynamics VI*.

[Dyer, 1974] Dyer, A. J. (1974). A review of flux-profile relationships. *Boundary-Layer Meteorology*, 7(3) :363–372.

[Eitel-Amor et al., 2014] Eitel-Amor, G., Örlü, R., and Schlatter, P. (2014). Simulation and validation of a spatially evolving turbulent boundary layer up to reθ= 8300. *International Journal of Heat and Fluid Flow*, 47 :57–69.

[El Khoury et al., 2013] El Khoury, G., Schlatter, P., Noorani, A., Fischer, P., and Brethouwer, G.and Johansson, A. V. (2013). Direct numerical simulation of turbulent pipe flow at moderately high reynolds numbers. *Flow, turbulence and combustion*, 91(3) :475–495.

[Eymard et al., 2000] Eymard, R., Gallouët, T., and Herbin, R. (2000). Finite volume methods. In *Solution of Equation in Rn (Part 3), Techniques of Scientific Computing (Part 3)*, volume 7 of *Handbook of Numerical Analysis*, pages 713 – 1018. Elsevier.

[Fang and Porté-Agel, 2015] Fang, J. and Porté-Agel, F. (2015). Large-Eddy Simulation of Very-Large-Scale Motions in the Neutrally Stratified Atmospheric Boundary Layer. *Boundary-Layer Meteorology*, 155(3) :397–416.

[Feireisl, 2004] Feireisl, E. (2004). *Dynamics of viscous compressible fluids*, volume 26 of *Oxford Lecture Series in Mathematics and its Applications*. Oxford University Press, Oxford.

[Ferziger and Peric, 2001] Ferziger, J. and Peric, M. (2001). *Computational Methods for Fluid Dynamics*. Springer Berlin Heidelberg.

[Foken, 2006] Foken, T. (2006). 50 years of the Monin-Obukhov similarity theory. *Boundary-Layer Meteorology*, 119(3) :431–447.

[Frehlich and Kelley, 2008] Frehlich, R. and Kelley, N. (2008). Measurements of wind and turbulence profiles with scanning doppler lidar for wind energy applications. *IEEE Journal of Selected Topics in Applied Earth Observations and Remote Sensing*, 1(1) :42–47.

[Frisch, 1995] Frisch, U. (1995). *Turbulence*. Cambridge University Press, Cambridge. The legacy of A. N. Kolmogorov.

[Fujita and Kato, 1964] Fujita, H. and Kato, T. (1964). On the navier-stokes initial value problem. i. *Archive for Rational Mechanics and Analysis*, 16(4) :269–315.

[Fulgosi et al., 2003] Fulgosi, M., Lakehal, D., Banerjee, S., and De Angelis, V. (2003). Direct numerical simulation of turbulence in a sheared air–water flow with a deformable interface. *Journal of fluid mechanics*, 482 :319–345.

[G. Borrell, 2013] G. Borrell, J.A. Sillero, J. J. (2013). A code for direct numerical simulation of turbulent boundary layers at high reynolds numbers in bg/p supercomputers. *Computers & Fluids*, 80 :37–43.

[Gallouët et al., 2003] Gallouët, T., Lederer, J., Lewandowski, R., Murat, F., and Tartar, L. (2003). On a turbulent system with unbounded eddy viscosities. *Nonlinear Anal.*, 52(4) :1051–1068.

[Gauckler, 1867] Gauckler, P. (1867). *Etudes Théoriques et Pratiques sur l'Ecoulement et le Mouvement des Eaux*. Gauthier-Villars.

[Gautier et al., 2014] Gautier, R., Laizet, S., and Lamballais, E. (2014). A dns study of jet control with microjets using an immersed boundary method. *Int. J. Comput. Fluid Dyn.*, 28(6-10) :393–410.

[George and Castillo, 1997] George, W. and Castillo, L. (1997). Zero-pressure-gradient turbulent boundary layer. *Applied Mechanics Reviews*, 50(12) :689–729.

[Germano, 1986] Germano, M. (1986). A proposal for redefinition of the turbulent stresses in the filtered navier-stokes equations. *Physics of Fluids*, 29(7) :2323–2324.

[Germano, 1992] Germano, M. (1992). Turbulence : the filtering approach. *Journal of Fluid Mechanics*, 238 :325–336.

[Germano, 2000] Germano, M. (2000). Fundamentals of large eddy simulation. In *Advanced turbulent flow computations (Udine, 1998)*, volume 395 of *CISM Courses and Lectures*, pages 81–130. Springer, Vienna.

[Germano et al., 1991] Germano, M., Piomelli, U., Moin, P., and Cabot, W. H. (1991). A dynamic subgrid scale eddy viscosity model. *Physics of Fluids A : Fluid Dynamics*, 3(7) :1760–1765.

[Gorji et al., 2014] Gorji, S., Seddighi, M., Ariyaratne, C., Vardy, A., O'Donoghue, T., Pokrajac, D., and He, S. (2014). A comparative study of turbulence models in a transient channel flow. *Computers & Fluids*, 89 :111–123.

[Gullbrand and Chow, 2003] Gullbrand, J. and Chow, F. (2003). The effect of numerical errors and turbulence models in large-eddy simulations of channel flow, with and without explicit filtering. *Journal of Fluid Mechanics*, 495 :323–341.

[Hambleton et al., 2006] Hambleton, W., Hutchins, N., and Marusic, I. (2006). Simultaneous orthogonal-plane particle image velocimetry measurements in a turbulent boundary layer. *Journal of Fluid Mechanics*, 560 :53–64.

[Harten, 1983] Harten, A. (1983). High resolution schemes for hyperbolic conservation laws. *Journal of Computational Physics*, 49(3) :357 – 393.

[Herbin, 2011] Herbin, R. (2011). Analyse numérique des équations aux dérivées partielles.

[Högström, 1988] Högström, U. (1988). Non-dimensional wind and temperature profiles in the atmospheric surface layer : A re-evaluation. *Boundary-Layer Meteorology*, 42(1-2) :55–78.

[Holm, 2015] Holm, D. D. (2015). Variational principles for stochastic fluid dynamics. *Proc. R. Soc. A*, 471(2176) :20140963.

[Holzmann, 2016] Holzmann, T. (2016). Mathematics, numerics, derivations and openfoam®.

[Hopf, 1951] Hopf, E. (1951). Über die Anfangswertaufgabe für die hydrodynamischen Grundgleichungen. *Math. Nachr.*, 4 :213–231.

[Hrvoje, 1996] Hrvoje, J. (1996). Error analysis and estimation for finite volume method with applications to fluid flow. Technical report.

[Issa, 1986] Issa, R. I. (1986). Solution of the implicitly discretised fluid flow equations by operator-splitting. *Journal of Computational Physics*, 62(1) :40–65.

[Jasak, 1996] Jasak, H. (1996). *Error analysis and estimation for the finite volume method with applications to fluid flows*. PhD thesis, Imperial College London (University of London).

[Jeong et al., 1997] Jeong, J., Hussain, F., Schoppa, W., and Kim, J. (1997). Coherent structures near the wall in a turbulent channel flow. *Journal of Fluid Mechanics*, 332 :185–214.

[Jimenez and Moser, 2007] Jimenez, J. and Moser, R. D. (2007). What are we learning from simulating wall turbulence ? *Phil. Trans. R. Soc. A*, (January) :715–732.

[Juneja and Brasseur, 1999] Juneja, A. and Brasseur, J. G. (1999). Characteristics of subgrid-resolved-scale dynamics in anisotropic turbulence, with application to rough-wall boundary layers. *Physics of Fluids*, 11(10) :3054–3068.

[Kadri H. and Mémin, 2017] Kadri H., S. and Mémin, E. (2017). Stochastic representation of the Reynolds transport theorem : revisiting large-scale modeling. *Computers and Fluids*, 156 :456–469.

[Kalitzin et al., 2005] Kalitzin, G., Medic, G., Iaccarino, G., and Durbin, P. (2005). Near-wall behavior of RANS turbulence models and implications for wall functions. *Journal of Computational Physics*, 204(1) :265–291.

[Kawamura, 2000] Kawamura, T. (2000). Numerical investigation of turbulence near a sheared air–water interface. part 2 : Interaction of turbulent shear flow with surface waves. *Journal of marine science and technology*, 5(4) :161–175.

[Kim et al., 1987] Kim, J., Moin, P., and Moser, R. (1987). Turbulence statistics in fully developed channel flow at low reynolds number. *Journal of fluid mechanics*, 177 :133–166.

[Kirkil et al., 2012] Kirkil, G., Mirocha, J., Bou-Zeid, E., Chow, F., and Kosović, B. (2012). Implementation and Evaluation of Dynamic Subfilter-Scale Stress Models for Large-Eddy Simulation Using WRF*. *Monthly Weather Review*, 140(1) :266–284.

[Klebanoff, 1955] Klebanoff, P. (1955). Characteristics of turbulence in a boundary layer with zero pressure gradient. Technical report, NATIONAL BUREAU OF STANDARDS GAITHERSBURG MD.

[Klewicki, 2010] Klewicki, J. C. (2010). Reynolds number dependence, scaling, and dynamics of turbulent boundary layers. *Trans. ASME J. Fluids Eng.*, 132(094001) :1–48.

[Kline et al., 1967] Kline, S. J., Reynolds, W., Schraub, F., and Runstadler, P. (1967). The structure of turbulent boundary layers. *Journal of Fluid Mechanics*, 30(4) :741–773.

[Kolmogorov, 1941] Kolmogorov, A. (1941). Equations of turbulent motion in an incompressible fluid. In *Dokl. Akad. Nauk SSSR*, volume 30, pages 299–303.

[Kravchenko and Moin, 1997] Kravchenko, A. and Moin, P. (1997). On the effect of numerical errors in large eddy simulations of turbulent flows. *Journal of Computational Physics*, 131(2) :310 – 322.

[Krell, 2010] Krell, S. (2010). *Schémas Volumes Finis en mécanique des fluides complexes*. PhD thesis, Université de Provence-Aix-Marseille I.

[Kunita, 1997] Kunita, H. (1997). *Stochastic flows and stochastic differential equations*, volume 24. Cambridge university press.

[Laizet and Lamballais, 2009] Laizet, S. and Lamballais, E. (2009). High-order compact schemes for incompressible flows : A simple and efficient method with quasi-spectral accuracy. *Journal of Computational Physics*, 228(16) :5989–6015.

[Laizet and Li, 2011] Laizet, S. and Li, N. (2011). Incompact3d : A powerful tool to tackle turbulence problems with up to O(105) computational cores. *International Journal for Numerical Methods in Fluids*, 67 :1735–1757.

[Lederer and Lewandowski, 2007] Lederer, J. and Lewandowski, R. (2007). A RANS 3D model with unbounded eddy viscosities. *Ann. Inst. H. Poincaré Anal. Non Linéaire*, 24(3) :413–441.

[Lee and Moser, 2015] Lee, M. and Moser, R.-D. (2015). Direct numerical simulation of turbulent channel flow up to $re_\tau = 5200$. *Journal of Fluid Mechanics*, 774 :395–415.

[Lele, 1992] Lele, S. K. (1992). Compact finite difference schemes with spectral-like resolution. *Journal of Computational Physics*, 103 :16–42.

[Lemarie, 2008] Lemarie, F. (2008). Algorithmes de Schwarz et couplage ocean-atmosphere.

[Lemarié-Rieusset, 2002] Lemarié-Rieusset, P.-G. (2002). *Recent developments in the Navier-Stokes problem*, volume 431 of *Chapman & Hall/CRC Research Notes in Mathematics*. Chapman & Hall/CRC, Boca Raton, FL.

[Leonard, 1975] Leonard, A. (1975). Energy cascade in large-eddy simulations of turbulent fluid flows. In Frenkiel, F. and Munn, R., editors, *Turbulent Diffusion in Environmental Pollution*, volume 18 of *Advances in Geophysics*, pages 237 – 248. Elsevier.

[Leray, 1934] Leray, J. (1934). Sur le mouvement d'un liquide visqueux emplissant l'espace. *Acta Math.*, 63(1) :193–248.

[Lesieur et al., 1988] Lesieur, M., Staquet, C., Le Roy, P., and Comte, P. (1988). The mixing layer and its coherence examined from the point of view of two-dimensional turbulence. *Journal of Fluid Mechanics*, 192 :511–534.

[Lewandowski, 1997a] Lewandowski, R. (1997a). *Analyse Mathématique et océanographie*. Elsevier-Masson, Paris.

[Lewandowski, 1997b] Lewandowski, R. (1997b). The mathematical analysis of the coupling of a turbulent kinetic energy equation to the Navier-Stokes equation with an eddy viscosity. *Nonlinear Anal.*, 28(2) :393–417.

[Lewandowski, 2015] Lewandowski, R. (2015). Long-time turbulence model deduced from the Navier-Stokes equations. *Chin. Ann. Math. Ser. B*, 36(5) :883–894.

[Lewandowski, 2016] Lewandowski, R. (2016). *The Kolmogorov-Taylor Law of turbulence : what can rigorously be proved ?* Handbook of applications of chaos theory. Taylor and Francis.

[Lewandowski and Odin, 2018] Lewandowski, R. and Odin, E. (2018). Turbulent systems for fluids analysed by fixed point theorems. *To appear in Pure and Applied Functional Analysis*.

[Lewandowski and Pichot, 2007] Lewandowski, R. and Pichot, G. (2007). Numerical simulation of water flow around a rigid fishing net. *Comput. Methods Appl. Mech. Engrg.*, 196(45-48) :4737–4754.

[Lilly, 1992] Lilly, D. K. (1992). A proposed modification of the germano subgrid[U+2010]scale closure method. *Physics of Fluids A : Fluid Dynamics*, 4(3) :633–635.

[Lions, 1996] Lions, P.-L. (1996). *Mathematical topics in fluid mechanics. Vol. 1*, volume 3 of *Oxford Lecture Series in Mathematics and its Applications*. The Clarendon Press, Oxford University Press, New York. Incompressible models, Oxford Science Publications.

[Lombardi et al., 1996] Lombardi, P., De Angelis, V., and Banerjee, S. (1996). Direct numerical simulation of near-interface turbulence in coupled gas-liquid flow. *Physics of Fluids*, 8(6) :1643–1665.

[López Castaño et al., 2018] López Castaño, S., Armenio, V., and Geurts, B. J. (2018). An investigation of strong backflow events at the interface of air–water systems using large-eddy simulation. *Journal of Turbulence*, pages 1–17.

[Lu and Porte-Agel, 2013] Lu, H. and Porte-Agel, F. (2013). A modulated gradient model for scalar transport in large-eddy simulation of the atmospheric boundary layer. *Physics of Fluids*, 25(1) :015110.

[Lu and Porte-Agel, 2014] Lu, H. and Porte-Agel, F. (2014). On the Development of a Dynamic Non-linear Closure for Large-Eddy Simulation of the Atmospheric Boundary Layer. *Boundary-Layer Meteorology*, 151(3) :429–451.

[M. P. Simens J. Jimenez, 2009] M. P. Simens J. Jimenez, S. Hoyas, Y. M. (2009). A high-resolution code for turbulent boundary layers. *Journal of Computational Physics*, 228(11) :4218–4231.

[Marlatt et al., 2011] Marlatt, S., Waggy, S., and Biringen, S. (2011). Direct Numerical Simulation of the Turbulent Ekman Layer : Evaluation of Closure Models. *Journal of the Atmospheric Sciences*, 69(3) :1106–1117.

[Marusic et al., 2010] Marusic, I., McKeon, B., Monkevitz, P., Smits, H. N. A., and Sreenivasan, K. (2010). Wall-bounded turbulent flows : recent advances and key issues. *Phys. Fluids*, 22(065103).

[Marusic et al., 2013] Marusic, I., Monty, J., Hultmark, M., and Smits, A. (2013). On the logarithmic region in wall turbulence. *J. Fluid Mech.*, 716(R3) :1–11.

[Mckeon et al., 2004] Mckeon, B. J., Li, J., Jiang, W., Morrison, J. F., and Smits, A. (2004). Further observations on the mean velocity distribution in fully developed pipe flow. *Journal of Fluid Mechanics*, 501 :135–147.

[Mémin, 2014] Mémin, E. (2014). Fluid flow dynamics under location uncertainty. *Geophysical & Astrophysical Fluid Dynamics*, 108(2) :119–146.

[Métais and Lesieur, 1992] Métais, O. and Lesieur, M. (1992). Spectral large-eddy simulation of isotropic and stably stratified turbulence. *Journal of Fluid Mechanics*, 239 :157–194.

[Millikan, 1938] Millikan, C. B. (1938). A critical discussion of turbulent flows in channels and circular tubes. In *Proc. 5th Int. Congr. Appl. Mech*, volume 386.

[Mizuno and Jiménez, 2011] Mizuno, Y. and Jiménez, J. (2011). Mean velocity and length-scales in the overlap region of wall-bounded turbulent flows. *Physics of Fluids*, 23(8).

[Mohammadi and Pironneau, 1994] Mohammadi, B. and Pironneau, O. (1994). *Analysis of the k-epsilon turbulence model*. RAM : Research in Applied Mathematics. Masson, Paris ; John Wiley & Sons, Ltd., Chichester.

[Monin et al., 2007] Monin, A., Yaglom, A., and Lumley, J. (2007). *Statistical Fluid Mechanics : Mechanics of Turbulence*. Number vol. 1 in Dover books on physics. Dover Publications.

[Monin and Obukhov, 1954] Monin, A. S. and Obukhov, A. M. (1954). Basic laws of turbulent mixing in the surface layer of the atmosphere. *Tr. Akad. Nauk. SSSR Geophiz. Inst.*, 24(151) :163–187.

[Moser et al., 1999] Moser, R.-D., Kim, J., and Mansour, N. (1999). Direct numerical simulation of turbulent channel flow up to Re_τ=590. *Physics of Fluids*, 11(4) :943–945.

[Moukalled et al., 2016] Moukalled, F., Mangani, L., Darwish, M., et al. (2016). The finite volume method in computational fluid dynamics.

[Øksendal, 2003] Øksendal, B. (2003). Stochastic differential equations. In *Stochastic differential equations*, pages 65–84. Springer.

[Onsager, 1949] Onsager, L. (1949). Statistical hydrodynamics. *Nuovo Cimento (9)*, 6(Supplemento, 2(Convegno Internazionale di Meccanica Statistica)) :279–287.

[Orlandi and Leonardi, 2006] Orlandi, P. and Leonardi, S. (2006). Dns of turbulent channel flows with two-and three-dimensional roughness. *Journal of Turbulence*, (7) :N73.

[Parente et al., 2011] Parente, A., Gorlé, C., Van Beeck, J., and Benocci, C. (2011). Improved k–ε model and wall function formulation for the rans simulation of abl flows. *Journal of wind engineering and industrial aerodynamics*, 99(4) :267–278.

[Patankar, 1980] Patankar, S. (1980). *Numerical Heat Transfer and Fluid Flow*. Series in computational methods in mechanics and thermal sciences. Taylor & Francis.

[Pelletier, 2018] Pelletier, C. (2018). *Étude mathématique du problème de couplage océan-atmosphère incluent les échelles turbulentes*. PhD thesis, Communauté Université Grenoble Alpes.

[Peskin, 2002] Peskin, C. (2002). The immersed boundary method. *Acta Numerica*, 11 :479–517.

[Podvin and Fraigneau, 2011] Podvin, B. and Fraigneau, Y. (2011). Synthetic wall boundary conditions for the direct numerical simulation of wall-bounded turbulence. *Journal of Turbulence*, (12) :N4.

[Pope, 2000] Pope, S.-B. (2000). *Turbulent flows*. Cambridge University Press, Cambridge.

[Porté-agel and chi C., 2015] Porté-agel, F. and chi C., W. (2015). Adjustment of Turbulent Boundary-Layer Flow to Idealized Urban Surfaces : A Large-Eddy Simulation Study. pages 249–270.

[Porté-agel et al., 2000] Porté-agel, F., Meneveau, C., and Parlange, M. B. (2000). A scale-dependent dynamic model for large-eddy simulation : application to a neutral atmospheric boundary layer. *J. Fluid Mech*, 415 :261–284.

[Prandtl, 1925] Prandtl, L. (1925). Über die ausgebildeten turbulenz. *Zeitschrift für angewandte Mathematik und Mechanik*, 5 :136–139.

[Protter, 2005] Protter, P. (2005). Stochastic differential equations. In *Stochastic integration and differential equations*, pages 249–361. Springer.

[Reeks, 1983] Reeks, M. (1983). The transport of discrete particles in inhomogeneous turbulence. *J. Aerosol Sci.*, 14(6) :729–739.

[Reichardt, 1951] Reichardt, H. (1951). Vollständige darstellung der turbulenten geschwindigkeitsverteilung in glatten leitungen. *ZAMM-Journal of Applied Mathematics and Mechanics/Zeitschrift für Angewandte Mathematik und Mechanik*, 31(7) :208–219.

[Resseguier et al., 2017] Resseguier, V., Mémin, E., Heitz, D., and Chapron, B. (2017). Stochastic modelling and diffusion modes for proper orthogonal decomposition models and small-scale flow analysis. *Journ. Fluid Mech.*, 828 :29.

[Reynolds, 1883] Reynolds, O. (1883). An experimental investigation of the circumstances which determine whether the motion of water shall be direct or sinuous, and of the law of resistance in parallel channels. *Philosophical Transactions of the Royal Society of London*, 174 :935–982.

[Rhie and Chow, 1983] Rhie, C. M. and Chow, W. L. (1983). Numerical study of the turbulent flow past an airfoil with trailing edge separation. *AIAA Journal*, 21 :1525–1532.

[Richards and Hoxey, 1993] Richards, P. and Hoxey, R. (1993). Appropriate boundary conditions for computational wind engineering models using the k-ε turbulence model. In *Computational Wind Engineering 1*, pages 145–153. Elsevier.

[Roe, 1986] Roe, P. L. (1986). Characteristic-based schemes for the euler equations. *Annual Review of Fluid Mechanics*, 18(1) :337–365.

[Sagaut, 2006] Sagaut, P. (2006). *Large eddy simulation for incompressible flows*. Scientific Computation. Springer-Verlag, Berlin, third edition. An introduction, Transla-

ted from the 1998 French original, With forewords by Marcel Lesieur and Massimo Germano, With a foreword by Charles Meneveau.

[Sarkar and So, 1997] Sarkar, A. and So, R. (1997). A critical evaluation of near-wall two-equation models against direct numerical simulation data. *International Journal of Heat and Fluid Flow*, 18(2) :197–208.

[Schlatter et al., 2010] Schlatter, P., Li, Q., Brethouwer, G., Johansson, A. V., and Henningson, D. S. (2010). Simulations of spatially evolving turbulent boundary layers up to reθ= 4300. *International Journal of Heat and Fluid Flow*, 31(3) :251–261.

[Schlichting and Gersten, 2000] Schlichting, H. and Gersten, K. (2000). *Boundary-layer theory*. Springer-Verlag, Berlin, enlarged edition. With contributions by Egon Krause and Herbert Oertel, Jr., Translated from the ninth German edition by Katherine Mayes.

[Shah and Bou-zeid, 2014] Shah, S. K. and Bou-zeid, E. (2014). Direct numerical simulations of turbulent Ekman layers with increasing static stability : modifications to the bulk structure and second-order statistics. *J. Fluid Mech.*, 760 :494–539.

[Shamsoddin and Porté-agel, 2017] Shamsoddin, S. and Porté-agel, F. (2017). Large-Eddy Simulation of Atmospheric Boundary-Layer Flow Through a Wind Farm Sited on Topography. *Boundary-Layer Meteorology*, 163(1) :1–17.

[Sillero et al., 2013] Sillero, J., Jiménez, J., and Moser, R. (2013). One-point statistics for turbulent wall-bounded flows at reynolds numbers up to $\delta^+ \approx 2000$. *Physics of Fluids*, 25(10) :105102.

[Skamarock et al., 2005] Skamarock, W. C., Klemp, J. B., Dudhia, J., Gill, D. O., Barker, D. M., Wang, W., and Powers, J. G. (2005). A description of the advanced research wrf version 2. Technical report, National Center For Atmospheric Research Boulder Co Mesoscale and Microscale Meteorology Div.

[Smagorinsky, 1963] Smagorinsky, J. (1963). General Circulation Experiments With the Primitive Equations. *Monthly Weather Review*, 91(3) :99–164.

[Smith and Metzler, 1983] Smith, C. and Metzler, S. (1983). The characteristics of low-speed streaks in the near-wall region of a turbulent boundary layer. *Journal of Fluid Mechanics*, 129 :27–54.

[Sogachev et al., 2012] Sogachev, A., Kelly, M., and Leclerc, M. Y. (2012). Consistent two-equation closure modelling for atmospheric research : buoyancy and vegetation implementations. *Boundary-layer meteorology*, 145(2) :307–327.

[Spalart et al., 2008] Spalart, P. R., Coleman, G. N., and Johnstone, R. (2008). Direct numerical simulation of the ekman layer : a step in reynolds number, and cautious support for a log law with a shifted origin. *Physics of Fluids*, 20(10) :101507.

[Spalding, 1961] Spalding, D. B. (1961). A single formula for the “law of the wall”. *Journal of Applied Mechanics*, 28 :455–458.

[Speziale, 1985] Speziale, C. (1985). Galilean invariance of subgrid-scale stress models in the large-eddy simulation of turbulence. *Journal of Fluid Mechanics*, 156 :55–62.

[Stokes, 1851] Stokes, G. G. (1851)). On the effect of the internal friction of fluids on the motion of pendulums. *Transactions of the Cambridge Philosophical Society*, 9 :8–106.

[Sweby, 1984] Sweby, P. K. (1984). High Resolution Schemes Using Flux Limiters for Hyperbolic Conservation Laws. *SIAM Journal on Numerical Analysis*, 21(5) :995–1011.

[Taylor, 1935] Taylor, G. I. (1935). Statistical theory of turbulence. part i-iv. *Proc. Roy. Soc. A.*, 151 :421–478.

[Taylor and Sarkar, 2008] Taylor, J. R. and Sarkar, S. (2008). Stratification Effects in a Bottom Ekman Layer. *American Meteorological Society*, 38 :2535–2555.

[Teghem, 2012] Teghem, J. (2012). *Recherche opérationnelle Tome1*. Ellipses, Paris.

[Temam, 2001] Temam, R. (2001). *Navier-Stokes equations*. AMS Chelsea Publishing, Providence, RI. Theory and numerical analysis, Reprint of the 1984 edition.

[Tikhomirov, 1992] Tikhomirov, V. (1992). *Selected Works of A.N. Kolmogorov : Volume I : Mathematics and Mechanics*. Tikhomirov, V.M.(ed.) Kluwer Academic Publishers, Dordrecht, Boston, London.

[van Albada et al., 1997] van Albada, G. D., van Leer, B., and Roberts, W. W. (1997). *A Comparative Study of Computational Methods in Cosmic Gas Dynamics*, pages 95–103. Springer Berlin Heidelberg, Berlin, Heidelberg.

[Van Doormaal and Raithby, 1984] Van Doormaal, J. and Raithby, G. (1984). Enhancements of the simple method for predicting incompressible fluid flows. *Numerical heat transfer*, 7(2) :147–163.

[Van Leer, 1974] Van Leer, B. (1974). Towards the ultimate conservative difference scheme. ii. monotonicity and conservation combined in a second-order scheme. *Journal of Computational Physics*, 14(4) :361 – 370.

[Van Leer, 1979] Van Leer, B. (1979). Towards the ultimate conservative difference scheme. v. a second-order sequel to godunov's method. *Journal of Computational Physics*, 32(1) :101 – 136.

[von Karman, 1930] von Karman, T. (1930). Meckanishe ähnlichkeit und turbulenz. *Gött. Nachr.*, pages 58–76.

[Von Storch et al., 2013] Von Storch, H., Güss, S., and Heimann, M. (2013). *Das klimasystem und seine modellierung : eine einführung*. Springer-Verlag.

[Vuorinen et al., 2015] Vuorinen, V., Chaudhari, a., and Keskinen, J.-P. (2015). Large-eddy simulation in a complex hill terrain enabled by a compact fractional step OpenFOAM® solver. *Advances in Engineering Software*, 79 :70–80.

[Vuorinen et al., 2014] Vuorinen, V., Keskinen, J. P., Duwig, C., and Boersma, B. J. (2014). On the implementation of low-dissipative Runge-Kutta projection methods for time dependent flows using OpenFOAM. *Computers and Fluids*, 93 :153–163.

[Wang et al., 2012] Wang, Z., Akhtar, I., Borggaard, J., and Iliescu, T. (2012). Proper orthogonal decomposition closure models for turbulent flows : a numerical comparison. *Computer Methods in Applied Mechanics and Engineering*, 237 :10–26.

[Wosnik et al., 2000] Wosnik, M., Castillo, L., and George, W. K. (2000). A theory for turbulent pipe and channel flows. *Journal of Fluid Mechanics*, 421 :115–145.

[Wu and Moin, 2008] Wu, X. and Moin, P. (2008). A direct numerical simulation study on the mean velocity characteristics in turbulent pipe flow. *Journal of Fluid Mechanics*, 608 :81–112.

[Zagarola et al., 1997] Zagarola, M., Perry, A., and Smits, A. (1997). Log laws or power laws : The scaling in the overlap region. *Physics of Fluids*, 9(7) :2094–2100.

[Zagarola and Smits, 1998] Zagarola, M. and Smits, A. J. (1998). Mean-flow scaling of turbulent pipe flow. *Journal of Fluid Mechanics*, 373 :33–79.

[Zhang et al., 2013] Zhang, W., Markfort, C. D., and Porté-Agel, F. (2013). Wind-Turbine Wakes in a Convective Boundary Layer : A Wind-Tunnel Study. *Boundary-Layer Meteorology*, 146(2) :161–179.

[Zhou and Chow, 2011] Zhou, B. and Chow, F. (2011). Large-Eddy Simulation of the Stable Boundary Layer with Explicit Filtering and Reconstruction Turbulence Modeling. *Journal of the Atmospheric Sciences*, 68(9) :2142–2155.

[Zhou and Chow, 2014] Zhou, B. and Chow, F. (2014). Nested Large-Eddy Simulations of the Intermittently Turbulent Stable Atmospheric Boundary Layer over Real Terrain. *Journal of the Atmospheric Sciences*, 71(3) :1021–1039.

UNIVERSITE BRETAGNE LOIRE MATHSTIC

UNIVERSITÉ DE RENNES 1

Titre : Application de la théorie des similitudes en turbulences

Mot clés : Couche limite, lois de parois, Analyse fonctionnelle

Resumé : Le modèle RANS à une équation de fermeture est utilisée avec une nouvelle longueur de mélange. par interpolation, notre loi est universelle. Nous avons étendue ce résultat pour considérer les fonds rugueux. L'existence d'une solution au système d'équation associée est montrée, c'est un problème elliptique avec un terme source dans L^1. Nous utilisons le modèle "under location uncertainty" pour obtenir un profil de vitesse cohérent dans toute la couche limite turbulente. Le raisonnement que nous apportons ici lie un terme sous-grille à ce profile. Nous apportons également une estimation des variances à temps courts dans la zone visqueuse

Title : Application of the similitude theory in turbulence.

Keywords : Turbulent boundary layer, wall laws, Functionnal analysis

Abstract : The RANS one-closure equation is tested with a new formulation of the turbulent mixing length. By interpolation, the law is universal. It also take account of any roughness of the ground. The existence of solution of the RANS model is also proven and bring a new proof of elliptic problem with source term in L^1. We use the model under location uncertainty to derive a velocity profile in the whole boundary layer. An expression of the small-scale velocity component is also provided in the viscous zone